

**Electronic Properties  
of Single Crystal CVD Diamond  
and its Suitability for  
Particle Detection  
in Hadron Physics Experiments**

Dissertation  
zur Erlangung des Doktorgrades  
der Naturwissenschaften

vorgelegt beim Fachbereich Physik  
der Johann Wolfgang Goethe — Universität  
in Frankfurt am Main

von  
**Michał Pomorski**  
aus Skarżysko-Kamienna

Frankfurt 2008  
(D 30)

vom Fachbereich Physik der  
Johann Wolfgang Goethe Universität als Dissertation angenommen.

Dekan: Prof. Dr. Dirk-Hermann Rischke  
Gutachter: Prof. Dr. Joachim Stroth  
Prof. Dr. Wim de Boer  
Datum der Disputation: 7 August 2008



# Contents

<b>Contents</b>	<b>i</b>
<b>1 Introduction</b>	<b>1</b>
1.1 Motivation . . . . .	1
<b>2 Single Crystal CVD Diamond a Novel Wide-Bandgap Semiconductor</b>	<b>5</b>
2.1 Physical Properties of Diamond . . . . .	5
2.1.1 Diamond Lattice . . . . .	5
2.1.2 Band Structure and Lattice Vibrations . . . . .	6
2.1.3 Electronic transport . . . . .	8
2.1.4 General Electromagnetic Absorbtion Spectrum of Diamond . . . . .	13
2.1.5 Thermal Conductivity . . . . .	13
2.1.6 Dielectric Constant . . . . .	14
2.2 Chemical Vapor Deposition (CVD) . . . . .	14
2.2.1 Historical Background . . . . .	14
2.2.2 Basics of the CVD . . . . .	14
2.2.3 Homoepitaxial Growth . . . . .	17
2.3 Diamond Surfaces and Metal Diamond Interface . . . . .	17
2.3.1 Surface Termination . . . . .	17
2.3.2 Ohmic and Schottky Contact . . . . .	18
<b>3 Principles of Radiation Detection Using Solid State Detectors</b>	<b>21</b>
3.1 Particle Interaction with Matter . . . . .	21
3.1.1 Charged Particles - Stopping Power . . . . .	21
3.1.2 X-ray and Gamma Interaction . . . . .	25
3.2 Diamond as a Solid-State Particle Detector . . . . .	27
3.2.1 The Concept of a Solid-State Ionization Chamber . . . . .	27
3.2.2 Primary Ionization Cascades and Fano Factor . . . . .	27
3.2.3 Charge Carriers Transport - A Macroscopic View . . . . .	28
3.2.4 Influence of Lattice Defects . . . . .	29
3.2.5 Detectors of a Parallel Plate Geometry - Analytical Equations . . . . .	31
3.2.6 Trapping Related Phenomena . . . . .	33
<b>4 A Crystal Quality Study</b>	<b>37</b>
4.1 Material Used in This Work . . . . .	37
4.2 Atomic Impurities in scCVD Diamond . . . . .	37
4.3 Microscopic Structural Defects . . . . .	40

---

4.3.1	White Beam X-ray Topography . . . . .	41
4.3.2	Birefringence - Cross Polarized Visible Light Microscopy . . . . .	43
4.4	Surface Characterization . . . . .	47
4.4.1	Surfaces Roughness at Sub-micrometer Scale . . . . .	47
4.4.2	Macroscopic Morphology of the Surfaces . . . . .	48
4.5	Summary of the Crystal Quality Study . . . . .	50
<b>5</b>	<b>Detector Preparation</b>	<b>51</b>
5.1	Cleaning Procedure . . . . .	51
5.2	Electrodes Fabrication . . . . .	52
<b>6</b>	<b>Electronic Properties Characterization</b>	<b>55</b>
6.1	Dark Conductivity - I-E(V) Characteristics . . . . .	55
6.1.1	Setup and Methodology . . . . .	56
6.1.2	Results and Discussion . . . . .	57
6.2	Transient Current Technique . . . . .	64
6.2.1	Setup and Methodology . . . . .	64
6.2.2	Results and Discussion . . . . .	67
6.3	Charge Collection Efficiency and Energy Resolution . . . . .	73
6.3.1	Set-up and Methodology . . . . .	74
6.3.2	Results and Discussion . . . . .	75
6.4	Detector Response to Minimum Ionizing Electrons . . . . .	77
6.4.1	Set-up and Methodology . . . . .	77
6.4.2	Results and Discussion . . . . .	79
6.5	X-ray Microbeam Mapping . . . . .	81
6.5.1	Set-up and Methodology . . . . .	81
6.5.2	Results and Discussion . . . . .	83
6.6	Summary of the Electronic Properties Characterization . . . . .	90
<b>7</b>	<b>An Insight into Radiation Tolerance</b>	<b>93</b>
7.1	Non-Ionizing Energy Loss and Radiation Damage to Diamond . . . . .	93
7.1.1	Defects Creation . . . . .	93
7.1.2	Types of Radiation Induced Defects in Diamond . . . . .	96
7.1.3	Effects on Diamond Bulk Properties . . . . .	97
7.2	Irradiation Procedures . . . . .	100
7.2.1	26 MeV Proton Irradiation . . . . .	100
7.2.2	20 MeV Neutron Irradiations . . . . .	102
7.3	Radiation-Induced Defects Identification . . . . .	106
7.3.1	UV-VIS Absorbption Spectroscopy . . . . .	106
7.3.2	Photoluminescence Spectroscopy . . . . .	108
7.4	Electronic Properties of Irradiated scCVD-DDs . . . . .	110
7.4.1	I-E(V) Characteristics . . . . .	110
7.4.2	Transient Current Signals . . . . .	111
7.4.3	Priming and Polarization Phenomena . . . . .	118
7.4.4	Charge Collection Properties of Irradiated Detectors . . . . .	119
7.4.5	High-Temperature Annealing . . . . .	125
7.4.6	Discussion . . . . .	127

---

7.5	Summary of the Radiation-Tolerance Study . . . . .	127
<b>8</b>	<b>In-beam Performance</b>	<b>131</b>
8.1	Timing Properties . . . . .	131
8.1.1	Setup and Methodology . . . . .	132
8.1.2	Results and Discussion . . . . .	133
8.2	Spectroscopic Properties . . . . .	138
8.2.1	Experimental Environment . . . . .	138
8.2.2	Detector Response to $^{132}\text{Xe}$ Projectiles at SIS Energies . . . . .	140
8.2.3	Fragments Spectra . . . . .	141
8.2.4	Transient Current Signals . . . . .	145
8.3	Summary of the In-beam Tests . . . . .	147
<b>9</b>	<b>Summary and Outlook</b>	<b>149</b>
	<b>Deutsche Zusammenfassung</b>	<b>153</b>
	<b>APPENDIX</b>	<b>161</b>
	<b>List of Figures</b>	<b>167</b>
	<b>List of Tables</b>	<b>173</b>
	<b>Bibliography</b>	<b>175</b>



# Chapter 1

## Introduction

### 1.1 Motivation

Advances in hadron and nuclear physics have always been linked to innovations in the accelerator technology and the detector design - the gadgets of experimental particle physics. In order to explore new phenomena like the origin of the hadron mass or the properties of compressed, dense hadronic matter, large communities (FAIR, LHC) are preparing next generation experiments. The detectors operating in these experiments, have to be capable of withstanding very high radiation levels and cope with the high particle flux arising from extremely high event rates of up to  $10^8$  events/second of a charged particle multiplicity of about 1000 per central event [Sen02]. Therefore, radiation hard, low-mass detectors of high rate capability are required. The integral fluence closest to the particles interaction point will exceed  $10^{15} n_{eq}/cm^2$  over the projected time of operation, which is presently beyond the radiation tolerance of the standard silicon technology. Thus, a more robust detector material must be realized and efforts were started to improve the radiation hardness of silicon by material engineering [rose] or by cryogenic operation [rd39]. Another approach to the solution of this problem is the search for new radiation hard detector materials, which may replace silicon in the future detector developments. Materials like SiC and polycrystalline CVD (pcCVD) diamond have been widely studied in the past by [rd50] and [rd42], respectively. The intense R&D programm on pcCVD diamond at GSI Darmstadt, has already enabled the replacement of classical detectors in several beam-diagnosis as well as in Heavy-Ion (HI) timing applications with pcCVD-DDs [Mor01, Ber01]. However, the inhomogeneity of the pcCVD diamond material due to the presence of grain boundaries, leads to serious disadvantages limiting the implementation of such devices in a broader field of detector applications [Ber01a]. Recent progress in the growth of high purity single-crystal CVD diamond (scCVD) of extraordinary charge carriers mobility and lifetime [Isb02] has opened perspectives to high-performance radiation sensors based on this novel type of artificial diamond.

The main objectives of this thesis is thus, to study the feasibility of this novel material for the use as a particle detector in a wide range of particle species and beam energies available at GSI and FAIR as well as to confirm its radiation hardness. The work presented in the following chapters was performed in the framework of the NoRHDia collaboration (Novel Radiation Hard Diamond Detectors for Hadron Physics) [NoR]. Several international groups are involved in this project aiming at the fabrication of scCVD diamond detectors for

heavy-ion energy loss spectroscopy and minimum-ionizing particles timing with dedicated Front-End (FE) electronics. In order to achieve this goal, an interdisciplinary R&D program was applied including the improvement of the scCVD diamond growth processes with a research group of CEA in Saclay. The following technological steps have been pursued over the four years period of the project:

1. feasibility study of enlargement of the detector area (1x1 cm at present);
2. optimization of the thickness of the epitaxial mono-crystalline layers ;
3. study and optimization of the growth process parameters;
4. characterization of the quality of the crystal lattice, defect spectroscopy, concentration of residual impurities and their influence on the electrical transport properties of the excess charge carriers in this material. In this context, the charge collection distance, the mobility and the lifetime of the charge carriers;
5. optimization of the contact properties using various metals and surface treatments such as oxygen plasma treatment and annealing;
6. evaluation and development of suitable fast low-noise front-end (FE) electronics for spectroscopy and timing purposes;
7. systematic in-beam studies of the time, and the energy resolution of scCVD-DD as well as the pulse-shape parameters, which gives an insight into the signal formation in the detectors for an operation range from the 'small-signal' case, up to the space-charge limited regime, where plasma effect degrades the detector performance;
8. test of the radiation hardness of scCVD-DD by irradiation with neutrons and all kind of charged particles (electrons, protons, pions and heavy ions) as well as X-rays.

The experimental effort presented in this thesis is mainly focused on 4-8 points from the presented list. The studied diamond material was exclusively supplied by Element Six, Ascot, UK and has been tested in laboratory- and in-beam measurements applying various preparation- and characterization techniques. An exceptional material quality with respect to atomic impurities was confirmed by spectroscopic techniques including UV-VIS, IR absorption as well as, with ESR and TYPs measurements. The crystal structure was probed using 'white beam' X-ray topography, and cross-polarized light microscopy (Chapter 4). Particular attention is given to the I-E(V) characteristics, which is a standard technique probing both, the sample quality and the contact technology. The pulse shape of the transient-current signals predicting the signal formation, charge propagation and collection in the sensors was investigated. The homogeneity of the scCVD-DDs response was probed with radioactive sources as well as with spatially resolved X-ray microbeam microscopy (Chapter 6). In order to confirm the expected radiation hardness, the degradation of the charge transport properties was studied after neutron and proton irradiation up to highest integral fluence of  $10^{16}$  particle/cm<sup>2</sup> (Chapter 7). Fabricated diamond detector prototypes were tested using dedicated FE electronics in various in-beam experiments regarding start detectors for relativistic light ions and minimum-ionizing particles and spectroscopy detectors for slowed-down and relativistic heavy ions. The performance of charged-particle detectors made of these samples is compared to competitive solid-state sensors, for instance

---

to silicon detectors with respect to their spectroscopic properties and to pcCVD-DDs concerning the time resolution (Chapter 8). This work aims to deliver a complete picture of the present status of scCVD-DDs as well as perspectives for future developments.

Although the title of the thesis states 'scCVD-DDs for hadron physics', a large so called 'diamond community' can profit from the scCVD-DD development. The versatility of diamond devices allows their use in other fields. In particular, radiotherapy [Reb07, Des07], space applications [Hib07] for instance UV-detection [Ben06], synchrotron X-ray beam monitoring [Mor07a, Mor07b], neutron measurements in fusion experiments [Pil07], as well as the management of radioactive waste [Ber02].





# Chapter 2

## Single Crystal CVD Diamond a Novel Wide-Bandgap Semiconductor

The Greek word *αδάμα*, meaning unconquerable and indestructible, is the root word of diamond. By every measure, diamond is a unique material. Its supreme hardness, singular strength, high thermal conductivity, chemical inertness, excellent optical, infrared, and X-ray transparency, as well as extraordinary semiconductor properties of the material attracts scientific and technological interest worldwide ever since decades. However, only the recently developed CVD technique and in particular the homoepitaxial growth allowed reproducible synthesis of high quality single-crystal (scCVD) diamond. Thus scCVD diamond can be referred to as a novel material.

### 2.1 Physical Properties of Diamond

#### 2.1.1 Diamond Lattice

The diamond structure is equivalent to a face-centred cubic (FCC) lattice, with a motif of two atoms at each lattice point: one at (0 0 0) and the other at  $(\frac{1}{4} \frac{1}{4} \frac{1}{4})$ , where the coordinates are fractions along the cube sides. This is equivalent to two interpenetrating FCC lattices, offset from one another along a body diagonal by one-quarter of its length. The cubic unit cell of normal diamond (Figure 2.1) has a side length  $a = 3.567 \text{ \AA}$ .

The closest carbon atoms covalent bond length is equal to one-quarter of the cubic body diagonal, that is  $1.54 \text{ \AA}$ . The unit cell contains the equivalent of eight C atoms, and the atomic number density is therefore  $1.76 \times 10^{23} \text{ cm}^{-3}$ . It is interesting to mention that this is the highest atomic density of any matter on earth. Multiplying the atomic density by the average atomic mass of the C atom results in a theoretical mass density for diamond of  $3.52 \text{ g/cm}^3$ . A unique feature of carbon atoms in the diamond lattice is the strength of their bonds. The cohesive energy in diamond is 3.62 eV/bond or 7.24 eV, respectively. That is the reason for the relatively high energy necessary to displace an atom from its site under particle irradiation.

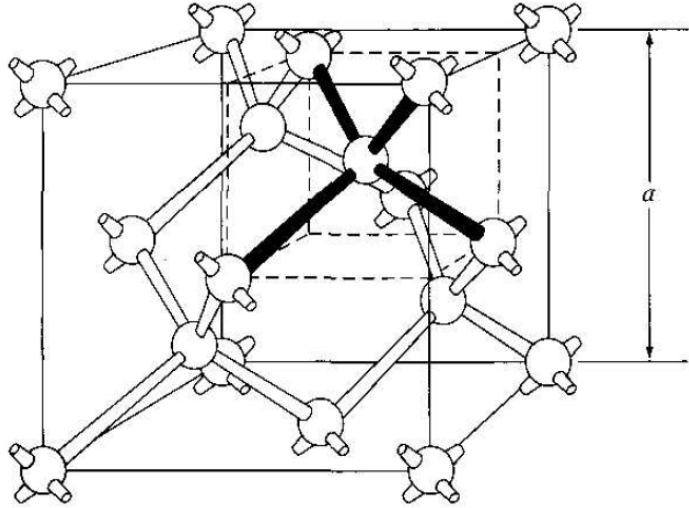


Figure 2.1: The unit cell of diamond, where  $a = 3.567 \text{ \AA}$  is the cubic lattice constant.

### 2.1.2 Band Structure and Lattice Vibrations

The allowed energy states of electrons in solids are structured in energy bands, separated by a forbidden energy region. These energy bands can be calculated by solving the Schrödinger equation:

$$\left[ -\frac{\hbar^2}{2m} \Delta^2 + V(r) \right] \Phi_k(r) = E_k \Phi_k(r) \quad (2.1)$$

for a single electron problem. Using the Bloch theorem, which states that for a periodic potential energy  $V(r)$  as given by the lattice periodicity, the solutions of the Schrödinger equation are of the form:

$$\Phi_k(r) = e^{ikr} U_n(k, r) \quad (2.2)$$

where  $k$  is the wave vector,  $n$  gives the band index and  $U_n(k, r)$  is a periodic function in  $r$  with the periodicity of the lattice.

Fig. 2.2 (a) shows energy dispersion curves for diamond as a function of the wave vector calculated using the discrete variational method in an *ab initio* approach with linear combination of atomic orbitals (LCAO) Bloch basis set [Pai71].

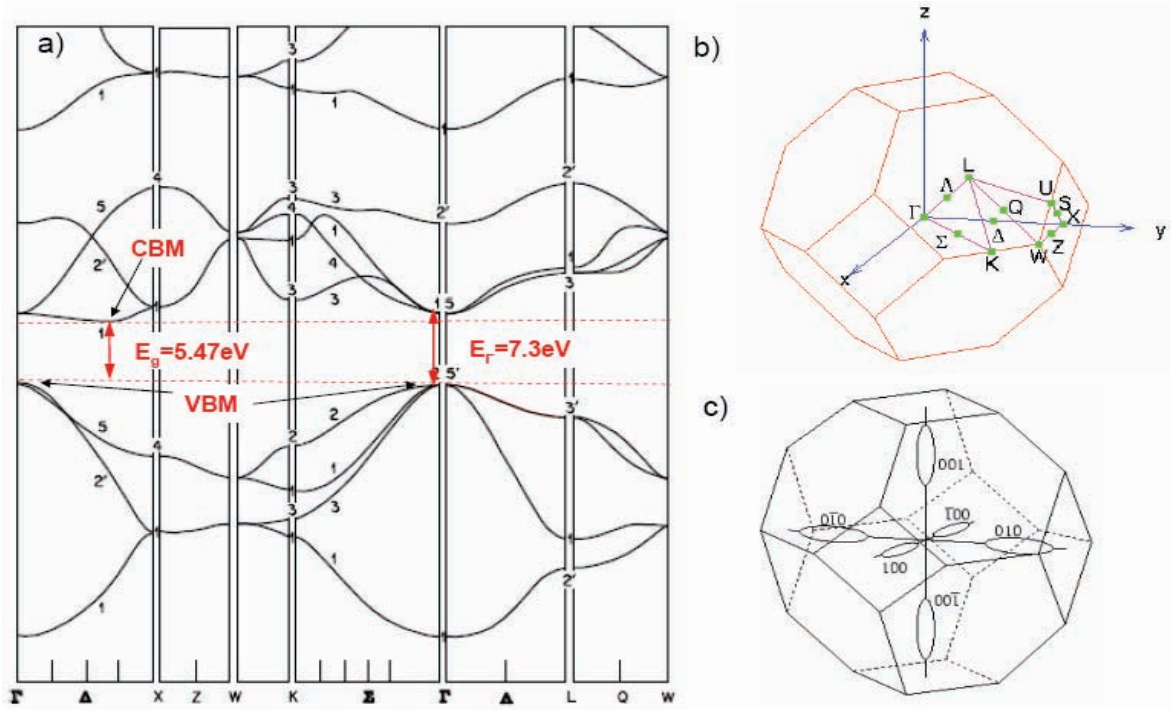
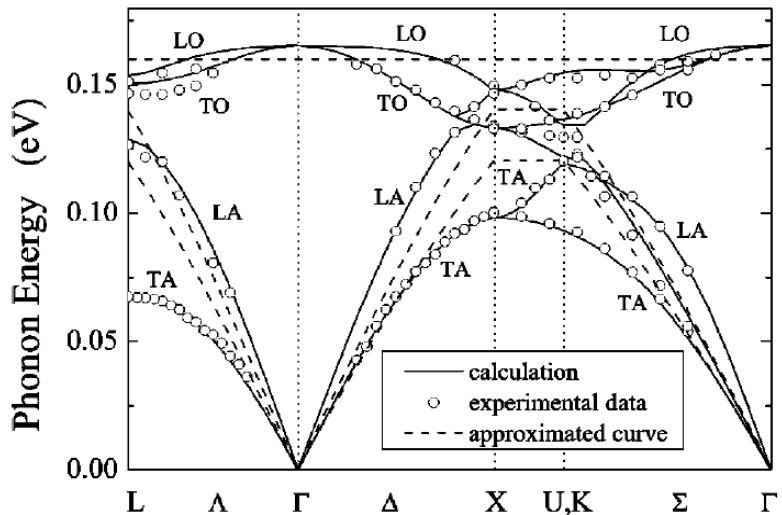


Figure 2.2: The band structure of diamond calculated 'ab initio' [Pai71]. Dashed red lines mark the energy difference between Valence Band Maximum (VBM) and Conduction Band Minimum (CBM) at 300 K. The indirect band gap of diamond is 5.47 eV. The direct band gap of 7.3 eV is marked as well. b) Symmetry points in the first Brillouin zone corresponding to the band diagram. c) Constant energy ellipsoids near the CBM; there are six equivalent valleys located along the  $\langle 100 \rangle$  directions.

The dispersion curves are shown for wave vectors along a path in the first Brillouin zone. Here, the path is described by the wave vectors,  $\Gamma$ ,  $X$ ,  $W$ ,  $K$ ,  $L$  which are points in the Brillouin zone (Figure 2.2 (b)). The energy of the valence band (VB) at  $\Gamma$  is the highest energy in the VB and is called valence band maximum (VBM). The energy of the conduction band (CB) localized at  $(0.7, 0, 0)$  from  $\Gamma$  is the lowest energy in the CB and is called conduction band minimum (CBM). Due to the crystal symmetry, the CB of diamond contains six equivalent minima (valleys) located along the  $\langle 100 \rangle$  crystallographic directions (Figure 2.2 (c)), which is similar to silicon.

The small size of C atoms allows them to get close to each other before experiencing net repulsive forces, and so relaxed  $C - C$  bonds are considered to be relatively short. The corresponding large overlap of the orbitals of adjacent C atoms in a  $C - C$  covalent bond causes a large energy separation between the occupied bonding orbitals and the unoccupied antibonding orbitals. This effect ultimately gives rise to a very large forbidden energy gap between the VB and CB states in the electronic structure of bulk diamond. As a result, the diamond is often considered to be a wide-bandgap semiconductor, if not an insulator. The minimal bandgap is indirect, with a value of 5.47 eV at 300 K, which can be compared to corresponding values of 1.12 and 0.66 eV, respectively, for the group-IV semiconductors silicon and germanium.

Figure 2.3: Phonon dispersion relation of diamond, calculated from an adiabatic bond-charge model. Dashed lines show the approximated dispersion relations used in the numerical calculations of the transport properties. The symbols TO, LO, LA, and TA indicate, transverse optical, longitudinal optical, longitudinal acoustic, and transverse acoustic branches, respectively [Tom04].



**Phonon dispersion curves** Figure 2.3 shows phonon dispersion curves. Since there are two atoms in the unit cell, there are six branches: three acoustic, and three optic branches. As the two atoms in the cell are identical, there is no intrinsic one-phonon infra-red absorption in diamond. In intrinsic semiconductors phonon scattering governs the saturation drift velocity of carriers, therefore due to the highly energetic optical phonons ( $E \approx 0.16 \text{ eV}$ ) diamond is one of the material of highest saturation drift velocity ( $v_{sat} = 2.7 \times 10^7 \text{ cm/s}$ ) [Fer75].

### 2.1.3 Electronic transport

**The concept of the effective mass** A localized electron in a crystal is described by a wave packet which may be seen as composed of plane waves of different wave lengths. The movement of such a wave packet is given by the group velocity:

$$v = \frac{1}{\hbar} \nabla E(k) \quad (2.3)$$

where  $E(k)$  is the energy of the electron depending on its wave vector  $k$  and the energy band in which it is situated.

Without any electric field applied, carriers underlie thermal motion only. Thermal motion has the same probability in each direction and therefore the average displacement is zero. When an external force  $f$ , for instance an electric field  $f = q\varepsilon$ , is applied to a band electron, it will do work:

$$dE = -q\varepsilon v \delta t \quad (2.4)$$

in a time  $\delta t$ . In addition it is:

$$\delta E = \frac{dE}{dk} \delta k = \hbar v \delta k \quad (2.5)$$

Equating equations 2.4 and 2.5, dividing through by  $\delta t$  and considering the limit  $\delta t \rightarrow 0$  gives:

$$\hbar \frac{dk}{dt} = -q\varepsilon \quad (2.6)$$

The equivalent three-dimensional formula is

$$\hbar \frac{d\mathbf{k}}{dt} = -q\boldsymbol{\varepsilon} \quad (2.7)$$

The rate of change of velocity with time is

$$\frac{dv}{dt} = \frac{1}{\hbar} \frac{d}{dt} (\nabla_{\mathbf{k}} E(\mathbf{k}))_i = \frac{1}{\hbar} \sum_j \frac{2E(\mathbf{k})}{k_i k_j} \frac{dk_j}{dt} = \frac{1}{\hbar^2} \sum_j \frac{2E(\mathbf{k})}{k_i k_j} (-q\varepsilon_j) \quad (2.8)$$

By analogy to the the classical equation of motion of a free-electron  $\frac{dv}{dt} = -q\varepsilon/m_0$

$$\left( \frac{1}{m^*} \right)_{ij} = \frac{1}{\hbar} \frac{2E(\mathbf{k})}{k_i k_j} \quad (2.9)$$

where  $m^*$  is called the effective mass. In general  $m^*$  is a tensor but in states close to the minima and maxima of  $E(\mathbf{k})$ , for instance CBM or VBM, it can be approximated parabolically and this tensor becomes a scalar. Depending on the band curvature  $\frac{d^2E}{dk^2}$  in which the electron is located, the effective mass of the charge carrier may be smaller or larger than the free electron mass,  $m_0$ , and also for the case of holes negative.

**Scattering** The energy distribution of the electrons in equilibrium is given by the Fermi-Dirac equation. For a gas of free electrons it would be spherical. In a crystal on the other hand it can be deformed by the varying  $E(\mathbf{k})$  dependencies for different directions e.g., it might have ellipsoidal shape. An external electric field shifts the Fermi surface and electrons acquire a small amount of extra velocity in the direction of the field. A new equilibrium is established by the collisions of the electrons with lattice imperfections. In linear approximation, this is described by the Boltzmann equation:

$$-\frac{f}{t} + c\nabla_r f - \frac{e}{\hbar} E \nabla_k f = \left( \frac{f}{t} \right)_{coll} \quad (2.10)$$

where  $f(r, v, t)$  is the distribution function of the charge carriers. This problem is very often simplified by the relaxation-time-approach, in which it is assumed that the rate of collisions bringing the system back to the equilibrium state is proportional to the deviation from the equilibrium state:

$$\left( \frac{f}{t} \right)_{coll} = \frac{f(\mathbf{k}) - f_0(\mathbf{k})}{\tau(\mathbf{k})} \quad (2.11)$$

where  $\tau(\mathbf{k})$  is the relaxation time. The relaxation time is usually independent of the position in the crystal but not of the position in the  $\mathbf{k}$ -space. If more than one mechanism is responsible for the relaxation time, it follows the Matthiessen's rule:

$$\frac{1}{\tau} = \frac{1}{\tau_{phonon}} + \frac{1}{\tau_{defects}} \quad (2.12)$$

where in this example,  $\tau_{phonon}$  is the relaxation time of phonon scattering and  $\tau_{defects}$  is the relaxation time of scattering at lattice imperfections.

**Drift-Diffusion equation** Taking the microscopic picture of an electron within crystal lattice into account, it follows that at low electric field the current density is given by the simple drift-diffusion equation:

$$j = qn\mu_0 E + qD\nabla n \quad (2.13)$$

where  $q$  is the electronic charge,  $n$  the carrier concentration,  $E$  the electric field,  $D$  is the diffusion coefficient, and  $\mu_0$  is the ohmic (or low-field) mobility expressed as:

$$\mu_0 = \frac{q\tau(k)}{m^*} \quad (2.14)$$

The transport parameters  $\mu_0$  and  $D$  are related to each other, in thermal equilibrium, by the Einstein relation,  $D = \mu_0 kT/q$ , where  $k$  is the Boltzmann constant.

**Transport in high fields** At high electric field the temperature of the excess charge carriers is not anymore in thermal equilibrium with the lattice temperature. This transport is often referred as a 'hot' transport, since the charge carriers' temperature is higher than the lattice temperature. Carriers undergo scattering processes, and if sufficiently high energy is transferred by a phonon, they can be scattered between particular bands or equivalent bands minima (inter-valley scattering) [Lon60]. The mean value for the effective mass  $m^*$  of carriers must then be calculated for different positions of the charge carriers within the valleys in the band structure, respectively. Consequently,  $\mu_0$  in equation 2.14 is not anymore constant. Therefore, to obtain a correct description of the carriers' transport in a semiconductor at high electric fields, detailed knowledge of the band structure and the scattering mechanisms is required. Although the description of transport at high fields has been attempted with analytical techniques, it has often been found to be far from correct [Can75]. Better results for the propagation of charge carriers in solids can be achieved using numerical techniques. The most widely used direct approach is the Monte Carlo method, by which a possible history of a single particle is stochastically simulated [Jac83, Tom04].

One of the consequence of the 'hot' carrier transport is the anisotropy of drift velocities in diamond caused by the valley repopulation effect, which is described in the following.

**The repopulation effect** The electrons which contribute to the conductivity in diamond are those in the six equivalent valleys which are located around the VBM in the  $\langle 100 \rangle$  directions (Figure 2.2 (c)). The constant energy surface (Fermi surface) is an ellipsoid, and the relationship between the energy  $E$  and the wave vector  $k$  is expressed as:

$$E_\alpha = \frac{1}{2} \left[ \frac{(k - k_{0\alpha})_l^2}{m_l} + \frac{(k - k_{0\alpha})_t^2}{m_t} \right] \quad (2.15)$$

where  $1/m_l$  and  $1/m_t$  are the longitudinal and transverse components of the inverse effective-mass tensor  $1/m^*$ , and  $k_{0\alpha}$  indicates the position in the Brillouin zone of the center of the  $\alpha$ -th valley. The effective mass of the electrons in an ellipsoid valley is anisotropic, and its inverse value for a given direction is determined by:

$$(1/m^*)_{\alpha k} = \frac{2E_{\alpha k}}{k^2} \quad (2.16)$$

For certain applied electric field, the conductivity effective mass  $m^*$  for the  $\alpha$ -th valley depends on the angle between its major axis and the direction of the applied field. For an applied field oriented along the  $\langle 1\ 0\ 0 \rangle$ , the  $m^*$  of the carriers in the two valleys whose major axes are along  $\langle 1\ 0\ 0 \rangle$  is  $m_l$  and that of the rest four valleys is  $m_t$ . For the electric field applied parallel to the  $\langle 110 \rangle$ , the  $m^*$  of two valleys, whose major axes are along  $\langle 001 \rangle$ , is  $m_t$ , and rest four valleys is  $2(1/m_t + 1/m_l)^{-1}$ . When the applied field is  $\langle 111 \rangle$  oriented, it is a special case. Here, the  $m^*$  of six valleys has the same value,  $3(2/m_t + 1/m_l)^{-1}$ . In the hot valleys (smaller effective masses), electrons are more efficient 'heated' by the field thus the electron temperature is higher than in the cold valleys (larger effective masses). The scattering rate of carriers from hot valleys to cold valleys is larger than in the reverse direction. Therefore the equilibrium population at a certain electric field of hot valleys is smaller than that of cold valleys. The anisotropy increases at decreasing lattice temperature, and it tends to vanish at extreme fields (very low or very high ones). This phenomenon is called valley repopulation effect, resulting in anisotropic drift velocity in multi-valley semiconductors like diamond or silicon. More detailed theoretical description of this phenomenon can be found in [Liu88, Tsh72].

**Resistivity** Intrinsic single-crystal diamond, with a bandgap of 5.47 eV, is one of the best solid electrical insulators. The high strength of the electron bond makes it unlikely that an electron would be excited out of the VB. In pure diamond, resistivity greater than  $10^{18}\ \Omega$  has been measured. However, the presence of impurities can drastically alter its electronic properties and the inclusion of  $sp^2$  (graphite) bonds e.g., in form of grain boundaries or dislocations, will considerably decrease the resistivity and render the material useless for electronic applications.

**Charge carriers mobility** The drift mobility of natural diamond shown in Figure 2.4, exhibits the typical  $T^{-1.5}$  dependence at temperatures below 400 K, which is related to acoustic phonon scattering, while above about 400 K the slope becomes steeper towards a  $T^{-2.8}$  dependence. This transition indicates an onset of optical (holes) or inter-valley (electrons) phonon scattering. The typical mobility in IIa natural diamond at RT amounts to  $\mu_e=2300\ \text{cm}^2\text{V}^{-1}\text{s}^{-1}$  and  $\mu_h=1800\ \text{cm}^2\text{V}^{-1}\text{s}^{-1}$  for electrons and holes respectively. High and almost equal mobilities for both charge carriers makes diamonds an outstanding material for high frequency devices, including particle detectors.

The recently measured extremely high mobilities in scCVD diamond of  $\mu_e=4500\ \text{cm}^2\text{V}^{-1}\text{s}^{-1}$  and  $\mu_h=3800\ \text{cm}^2\text{V}^{-1}\text{s}^{-1}$  by Isberg et al. [Isb02] are still controversial and thus widely discussed in literature. New results on low field mobilities in scCVD diamond are presented in Chapter 6.

**Charge carriers drift velocity** As a result of the multi-valley band structure, the anisotropy of the charge carriers' drift velocity is expected in diamond with respect to the three main crystallographic directions. This effect is illustrated in Figure 2.5, showing measurements of natural IIa diamond performed by Nava [Nav80] and Reggiani [Reg81]. The saturated carrier velocity, that is, the velocity at which electrons move in high electric fields, is higher than in silicon, gallium arsenide, or silicon carbide. Unlike other semiconductors, this velocity maintains its high rate in high-intensity electric fields.

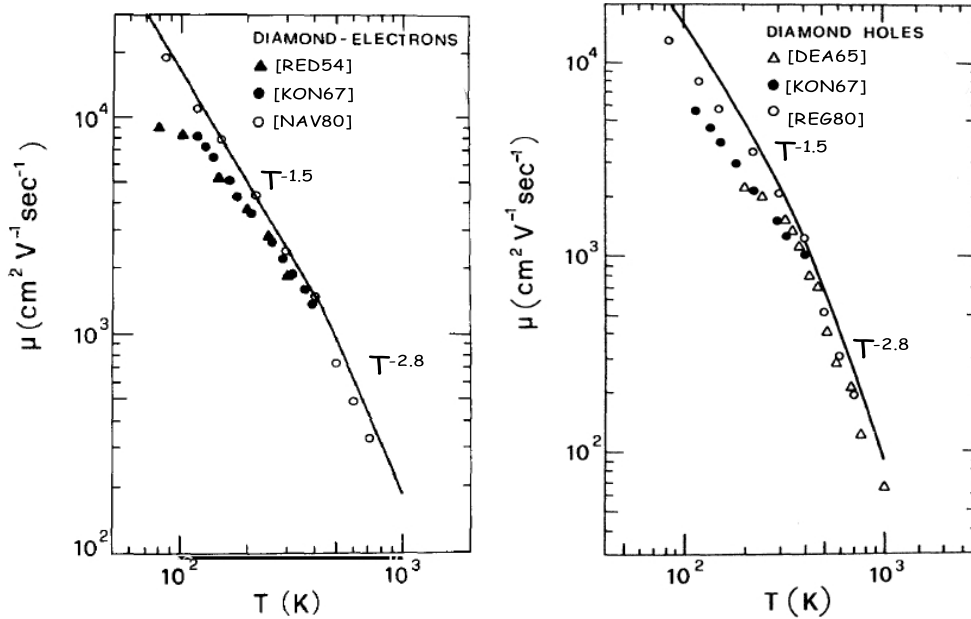


Figure 2.4: Charge carriers' mobility as a function of temperature in IIA natural diamond. (Left panel) electrons, (Right panel) holes. Data points represent different methods of measurement: triangles - Hall mobility [Red54, Dea66], full dots - Hall mobility [Kon67], open dots - drift mobility [Nav80, Reg81].

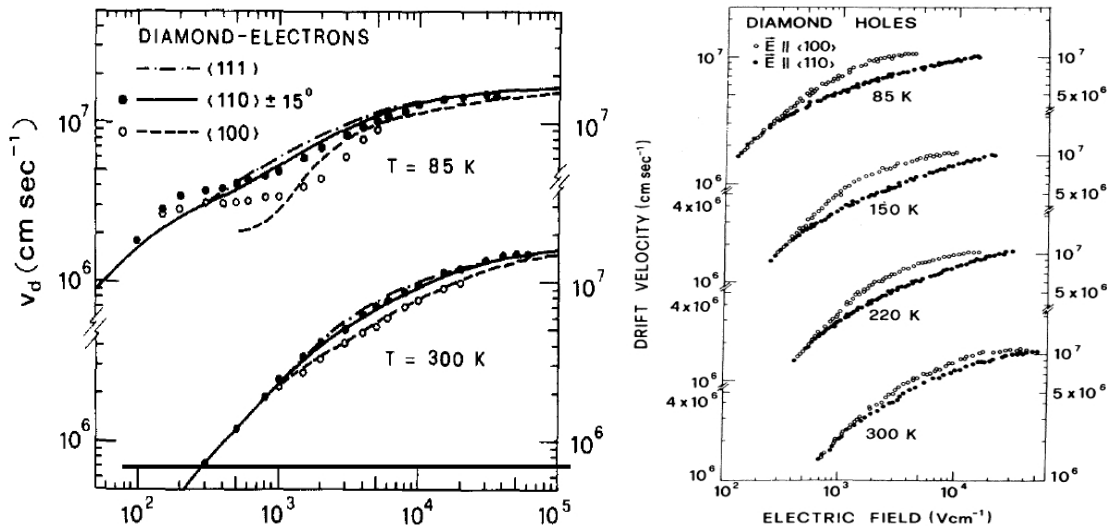


Figure 2.5: Charge carriers drift velocity in natural IIA diamond measured in main crystallographic directions at various temperatures. (Left panel) Electrons drift after [Nav80]. (Right panel) Holes drift after [Reg81]. For both, anisotropy of the drift velocity is observed originating from valley repopulation effect.



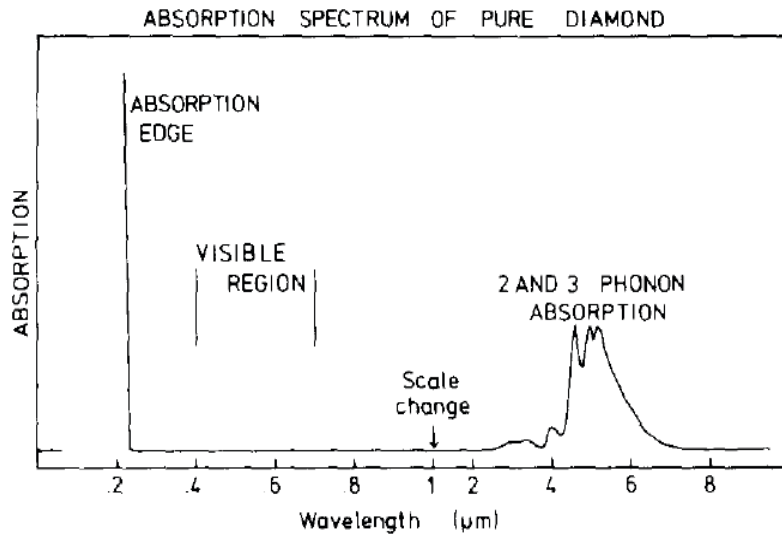


Figure 2.6: Theoretical electromagnetic absorption spectrum of intrinsic diamond after [Col93].

### 2.1.4 General Electromagnetic Absorption Spectrum of Diamond

Intrinsic diamond - which has never been found in nature and has been only recently synthesized by the CVD technique - would have only two intrinsic absorption bands as follows:

- At the short wavelength end of the optical spectrum, an ultraviolet absorption due to the electron transition across the bandgap. This corresponds to an absorption edge of 230 nm and, in the ideal crystal, there should be no absorption due to electronic excitation up to that level
- An infrared absorption which lies between 1400 and 2350 wave number ( $\text{cm}^{-2}$ ). The IR absorption is related to the creation of phonons and the intrinsic multiphonon absorption.

Due to the transparency in the VIS range, particle detectors made of high purity diamond are solar-blind. Therefore, no light-tight packaging or screening is needed for such detectors if diamond is employed.

### 2.1.5 Thermal Conductivity

Since diamond is a wide bangap semiconductor, there are almost no free electrons up to high temperatures in the range of the Debye temperature. Consequently almost all of the heat is transferred by phonons. Carbon atoms are small and have low mass and, in the diamond structure, are tightly and isotropically bonded to each other. As a result, the quantum energies necessary to make these atoms vibrate is large, which means that their vibrations occur mostly at high frequencies with a maximum of approximately  $40 \times 10^{12}$  Hz. Consequently, at ordinary temperatures, few atomic vibrations are present to impede the passage of thermal waves and thermal conductivity is unusually very high. For the highest quality single-crystal, type IIa diamonds the thermal conductivity is about  $25 \text{ W cm}^{-1} \text{ K}^{-1}$  at room temperature, or more than six times that of copper ( $4 \text{ W cm}^{-1} \text{ K}^{-1}$ ). Due to the high thermal conductivity, diamond detectors can be operated directly without cooling as beam monitors in high intensity heavy ion beams [Bol07].

## 2.1.6 Dielectric Constant

The static dielectric constant together with the device geometry defines the capacitance of a detector, which is important for the noise level in readout electronics. The low dielectric constant ( $\epsilon_r = 5.7$ ) of diamond is interesting in the reduction of capacitance when compared with silicon diodes of equivalent volume. Furthermore, dielectric losses in diamond are negligible ( $< 0.0001$ ) and as a consequence the dielectric constant of diamond is quoted to 5.6 at high frequencies (25 MHz-20 GHz) .

The discussed physical parameters of diamond and other semiconductors are gathered in Table 2.1

## 2.2 Chemical Vapor Deposition (CVD)

### 2.2.1 Historical Background

One of the most important developments in diamond synthesis is Chemical Vapor Deposition (CVD). In contrast to the HPHT method, it allows the synthesis of diamond of reproducible physical properties in a high purity environment. The first attempt at creating diamond using a CVD process was reported by Eversole in 1949 [Liu95]. A milestone in the diamond CVD technique was the discovery by Soviet researchers of the role of atomic hydrogen in removing unwanted graphitic phase but leaving diamond unaffected [Der75a,Der77b]. Although the Soviet successes were largely ignored in the U.S., this discovery launched a significant period of exploration of various CVD techniques for synthesizing diamond films and coatings in the 1980s in the Soviet Union and Japan [Spi81,Kam83]. In 1982, a group at the National Institute for Research in Inorganic Materials (NIRIM), Japan, had built a first reactor dedicated for diamond growth and reported growth rates for diamond films of up to 10  $\mu\text{m}/\text{h}$  [Mat82]. Also at NIRIM, the first investigation of homoepitaxial diamond films using the microwave plasma enhanced CVD (MWPECVD) method was undertaken by Kamo et al. [Kam88], following his demonstration of MWPECVD for polycrystalline diamond growth [Kam83]. The first high quality 'electronic grade' scCVD diamonds of extraordinary carrier mobilities and lifetimes were grown by Element Six in 2002 [Isb02]. Although nowadays electronic grade scCVD diamond is commercially available [e6] it is still considered as an R&D material.

### 2.2.2 Basics of the CVD

As its name implies, chemical vapor deposition involves a gas phase chemical reaction occurring above a solid surface, which causes deposition onto that surface. All CVD techniques for producing diamond films require a means of activating gas phase containing carbon precursor molecules. The activation can involve thermal methods (e.g., a hot filament), electric discharge (e.g., DC, RF or microwave), or a combustion flame (such as an oxy-acetylene torch). While each method differs in detail, they all share a few features in common: the precursor gas (usually  $\text{CH}_4$ ) is diluted in excess of hydrogen, in a typical mixing ratio of 1-15 % vol.  $\text{CH}_4$ . Also, the temperature of the substrate is usually greater than 700  $^\circ\text{C}$  to ensure the formation of diamond rather than amorphous carbon. The schematic in Figure 2.7 (Left panel) shows the basics of CVD chemistry. The process gases first mix in the chamber before diffusing toward the substrate surface. En route, they pass through

Table 2.1: Properties of some semiconductor materials that could be used as detector bulk material [Mol06, Owe04a, ioffe]. For the values marked with stars new experimental data and discussion on scCVD diamond are given in this work (see Chapter 6).

property	diamond	silicon	Ge	GaAs	4H-SiC	detector operation
band gap [eV]	5.48	1.12	0.67	1.43	3.26	+ high T operation
dielectric strength [V/cm]	$10^{7*}$	$3 \times 10^5$	$10^5$	$4 \times 10^5$	$5 \times 10^6$	+ high field operation
intrinsic resistivity [ $\Omega/cm$ ]	$>> 10^{11}$	$2.3 \times 10^5$	50	$10^7$	$> 10^5$	+ low leakage current
electron mobility [ $cm^2/Vs$ ]	1900 – 4500*	1350	3900	8000	1000	+ fast signal
hole mobility [ $cm^2/Vs$ ]	1800 – 3500*	480	1900	400	115	+ fast signal
electron lifetime [s]	$10^{-10}$ – $10^{-6**}$	$> 10^{-3}$	$> 10^{-3}$	$10^{-8}$	$5 \times 10^{-7}$	+ full charge collection
hole lifetime [s]	$10^{-10}$ – $10^{-6**}$	$10^{-3}$	$2 \times 10^{-3}$	$10^{-7}$	$7 \times 10^{-7}$	+ full charge collection
saturation velocity [cm/s]	$1.2 - 2.7 \times 10^{7*}$	$1 \times 10^7$	$6 \times 10^6$	$2 - 1 \times 10^7$	$3.3 \times 10^6$	+ fast signal
density [ $g/cm^3$ ]	3.52	2.33	5.33	5.32	3.21	+ therapy - tissue equiv.
average atomic number	6	14	32	31.5	10	+ low capacitance
dielectric constant	5.72	11.9	16	12.8	9.7	+ radiation hardness
displacement energy [eV]	43	13 – 20	28	10	20 – 35	+ heat dissipation
thermal conductivity [ $Wm^{-1}K^{-1}$ ]	2000	150	60.2	55	120	- lower signal
energy to create e-h [eV]	11.6 – 16*	3.62	2.96	4.2	7.8	+ low background
radiation length, $X_0$ [cm]	12.2	9.36	2.3	2.3	8.7	+ lower signal
Energy loss for MIPs [MeV/cm]	4.69	3.21	7.36	5.6	4.32	
Aver. Signal Created / 100 $\mu m$	3602	8892	24860	13300	5100	
e-h pairs/ $X_0$ ( $10^6 cm^{-1}$ )	5.7	10	5.67	2.99	4.5	

<sup>a</sup>

negative absolute drift velocity

an activation region (e.g. electric discharge), which causes molecules to fragment into reactive radicals and atoms and heats the gas up to temperatures approaching a few thousand Kelvins. When species reach the substrate a surface reaction occurs, where one of possible outcome, if all the conditions are suitable, is diamond.

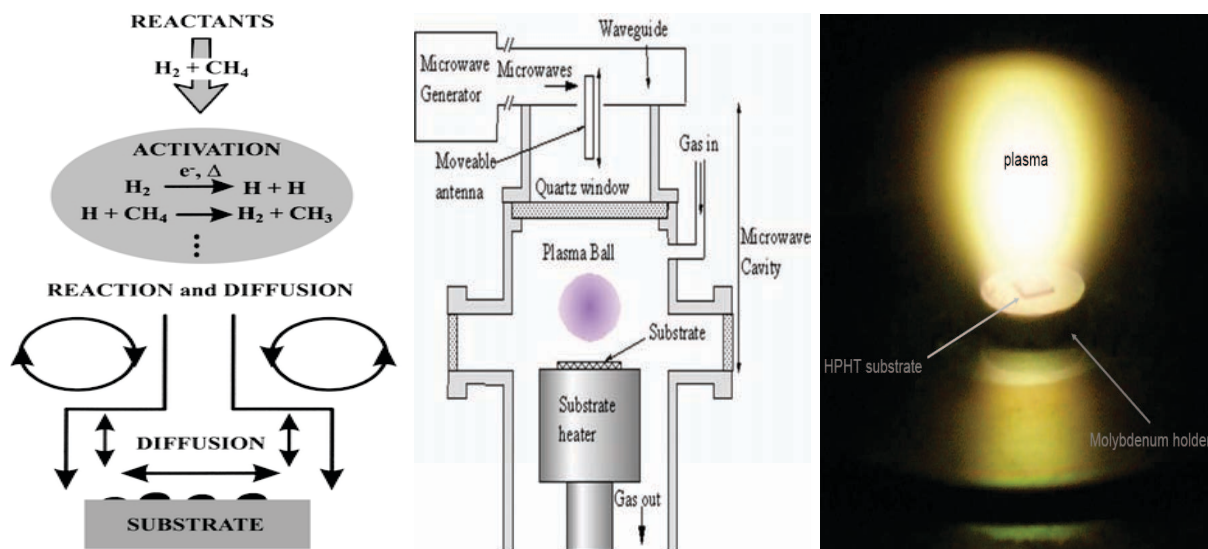


Figure 2.7: (Left panel) A schematic illustrating some of the more important physico-chemical processes occurring during diamond CVD using a  $CH_4/H_2$  input gas mixture after [Ash01]. (Middle panel) A schematic of the most popular ASTEX-type research reactor for microwave plasma enhanced chemical vapour deposition (MWPECVD) diamond growth. (Right panel) A photograph of scCVD diamond growth process in a MWPECVD ASTEX-type reactor (courtesy N. Tranchant).

Atomic hydrogen plays an essential role in the surface and plasma chemistry of diamond deposition. Two effects are believed crucial to the growth of CVD diamond:

- The bulk of diamond is fully  $sp^3$  bonded. However at the surface there is effectively a dangling bond, which needs to be terminated in order to prevent reconstruction of the surface to graphite. This surface termination is performed by hydrogen, which keeps the  $sp^3$  diamond lattice stable.
- Atomic H is known to etch graphitic  $sp^2$  carbon many times faster than diamond-like  $sp^3$  carbon. Diamond growth could thus be considered as five steps forward, but four steps back, with the net result being a (slow) build-up of diamond.

Additionally in the chemistry of the plasma:

- H atoms are efficient scavengers of long-chained hydrocarbons, breaking them up into smaller pieces. This prevents the build-up of polymers in the gas phase, which might deposit onto the substrate and inhibit diamond growth.
- H atoms react with neutral species such as  $CH_4$  to create reactive radicals, such as  $CH_3$ , which can then attach to suitable surface sites.

A detailed review of the various methods used for fabricating diamond can be found in [May00].

### 2.2.3 Homoepitaxial Growth

Homoepitaxial growth of single crystal diamonds uses diamond as the substrate material. Usually it is a  $\langle 1\ 0\ 0 \rangle$  oriented, type Ib HPHT synthetic single crystal diamond with carefully processed atomically flat surfaces. The growth process occurs usually by the step-flow mechanism [Bog05]. Microwave-plasma assisted CVD is the major method for the homoepitaxial growth at present. A typical ASTEX-type MWPECVD reactor is shown in Figure 2.7 (Middle panel). Microwave generators of 2.5 GHz, which are popularly used, have a maximum power output of ca. 5 kW, although generators with higher output power are recently applied for diamond growth. Microwaves are injected to a chamber on the upper side after. High-purity (6-7 N) methane is widely used as a source gas of homoepitaxial diamond CVD. The substrate temperature and the total gas pressure are typically 700 – 1000 °C and 20 – 100 Torr, respectively. The growth rate varies from 1  $\mu\text{m}/\text{h}$  to 150  $\mu\text{m}/\text{h}$  depending on the pressure and the mixture of gases used. However, the growth rate of high quality electronic grade scCVD are still rather low 1-10  $\mu\text{m}/\text{h}$ . A review article [Tok06] describes in more details homoepitaxial growth of scCVD diamond.

## 2.3 Diamond Surfaces and Metal Diamond Interface

For detector applications of diamond as a wide band gap semiconductor, the properties of its surfaces are of fundamental importance. These properties depend on the kind of passivation of the surface's dangling bonds, either by chemisorbed adsorbates or by the formation of mutual chemical bonds as a consequence of surface reconstruction. Although possible, the clean diamond surface with mutual bonds between carbon atoms is highly unstable in ambient conditions. Therefore, diamond surfaces are processed after growth to obtain more stable surface termination, namely: oxygen or hydrogen termination. In the present work scCVD samples with (100) surfaces have been used. Therefore, the short discussion presented below is limited only to this type of surface. More details on diamond surfaces can be found in [Neb04]

### 2.3.1 Surface Termination

**The hydrogen terminated (100)  $2 \times 1 : 2H$  surface** Hydrogen is the dominating gas species in the CVD process of diamond and after termination of deposition process CVD diamond surfaces are found in the hydrogen terminated state. Hydrogen surfaces' atoms remain arranged in dimer rows as shown in Figure 2.8 (a). Surface hydrogenation induces p-type surface conduction, even in undoped diamond. This conductivity shows a strong dependence on the ambient in which diamond is situated e.g., hydrogenated surface is conductive in air, whereas in vacuum is insulating. The most probable explanation of this behavior is a surface transfer doping mechanism [Ris01]. Due to the electronegativity difference between carbon (2.5) and hydrogen (2.1), the H-terminated diamond surface is positively charged. As a result, hydrogenated diamond surfaces are hydrophobic, and have negative electron affinity (-1.3 eV). The hydrogenation of the diamond surfaces can be obtained by diamond exposure to a hydrogen plasma.

**The oxygen terminated diamond (100)  $1 \times 1$  : O surface** As a divalent atom oxygen can saturate two surface dangling bonds simultaneously and thus for a full covalent termination of the surface only half the density of adsorbate atoms than for hydrogen is required (Figure 2.8 (b)). Oxygenated diamond surface is highly insulating. The O-terminated surface is negatively charged because oxygen has a larger electronegativity value (3.5). As a result oxygenated diamond surface is hydrophilic, and have positive electron affinity (+1.73 eV). The oxygenation of the diamond surfaces can be obtained by e.g., strong wet chemical oxidizing agents (see Chapter 6).

Due to the dipole structure of both types of diamond surfaces, prolonged exposure of the diamond to ambient conditions results in contamination of the diamond surface with the main impurities being various hydrocarbons [Mic08]. This can change the resistivity of the diamond surface, consequently diamond detectors should be operated in clean conditions or not metallized surface regions should be encapsulated.

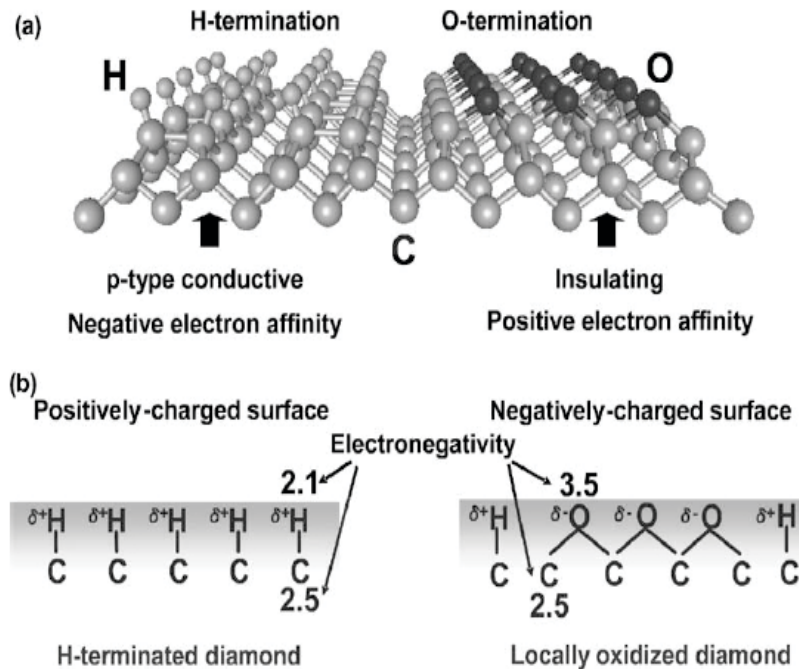


Figure 2.8: (a) Schematic illustration of the H- and O-terminated (100) diamond surfaces and their properties. (b) Schematics of the surface dipole of the H- and O-terminated diamond surfaces due to the electronegativity difference after [Tac05].

### 2.3.2 Ohmic and Schottky Contact

In order to get a signal from the detector, the free charge carriers generated by ionizing particles have to move towards the collecting electrodes. Thus the detector has to be metallized from two sides to apply a voltage and create an electric field, to force the electrons and holes to drift through the detector. The contacts have to be done in such a way that no free charge carriers can enter the diamond from the metal (non-injecting contacts) when a bias voltage is applied, but at the same time, excess charge carriers must be efficiently extracted from the diamond bulk.

In general two types of metal contacts to semiconductor are distinguished:

- **ohmic** An ohmic contact is defined as the metal-semiconductor contact that has negligible contact resistance relative to the bulk resistance of the semiconductor (bulk limited conductivity). Since diamond is inert and has a wide band gap, there are not so many techniques and metals which provide a good ohmic contact.
- **schottky** The Schottky barrier arises as a consequence of a mismatch between the semiconductor and metal Fermi levels and depends on the metal work function ( $\Phi_m$ ), the electron affinity of the semiconductor ( $\chi$ ) and surface state density of the semiconductor. For a n-type semiconductor electrons coming from metal to semiconductor see a barrier height of  $q\Phi_{Bn} = q(\Phi_m - \chi)$  and for p-type  $q\Phi_{Bp} = E_g - q(\Phi_m - \chi)$ , respectively.

Figure 2.9 shows band diagram of two hypothetical diamond devices with aluminium contacts in the sandwich geometry. The electron affinity is assumed to  $\chi = 1.7 \text{ eV}$  (oxygenated surfaces), and Aluminium work function is  $\Phi_m^{Al} = 4.08 \text{ eV}$ . This results in a Schottky barrier of about  $\Phi_{Bp} = 3 \text{ eV}$  height. The band structure of two devices with different amount of ionized acceptors (rest p-type conductivity of diamond is assumed) was simulated using the SimWindows semiconductor device simulation program [SimWi]. In the first case, the ionized acceptors' concentration amounts to  $N_A = 0.5 \times 10^{13} \text{ cm}^{-3}$  (black curves), in the second device it is  $N_A = 0.5 \times 10^{11} \text{ cm}^{-3}$  (red curves). In both cases, the bands edges of diamond are bent downwards giving about this same barrier height, however the barrier widths is fundamentally different (Figure 2.9 (Left panel)). The band diagrams are shown in Figure 2.9 (Right panel) when applying external bias of +30 to the left electrode. After biasing in the case of device with low ionized acceptor concentration band bending is negligible. Although electrons cannot be injected from the metal to the CB in diamond (non-injecting contacts), both excess electrons and holes created within the diamond bulk by e.g., ionizing particles can be effectively extracted by the aluminium contacts.

The corresponding internal electric field profiles are shown in Figure 2.10. For the device of higher ionized acceptor concentration, notable build-in potential is observed (gray dashed line). After applying the bias to the left electrode, the voltage drop occurs in the short range, due to depletion layer of the junction (gray solid line). In contrast to this, the build-in potential within low doped devices is negligible (black dashed line). After biasing, the electric field profile of this device approaches the constant value of the applied field in a perfect insulator with ohmic contacts, at which no voltage drop occurs (red dashed line).

The transient current measurements presented in Chapter 6 suggest the contact character of intrinsic scCVD-DD similar to the simulation result presented for the device of low ionized acceptor concentration.

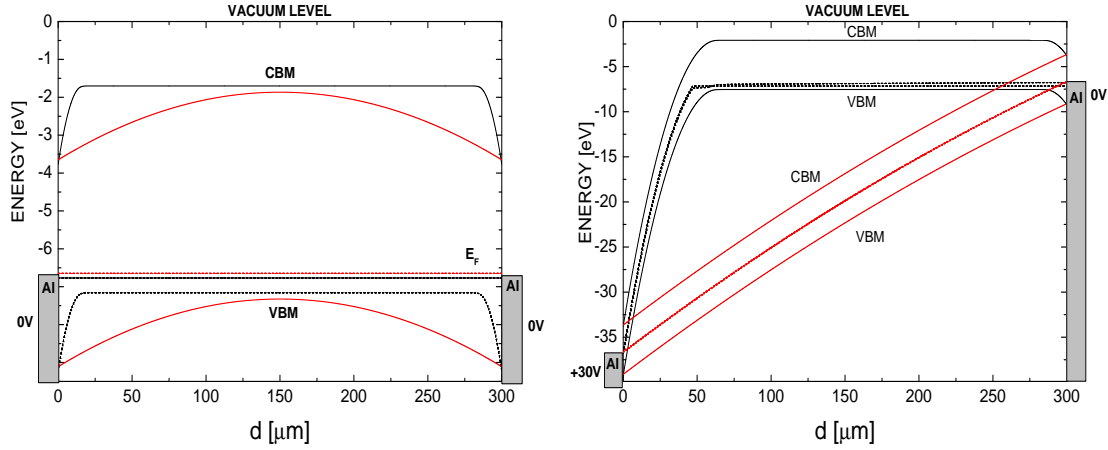
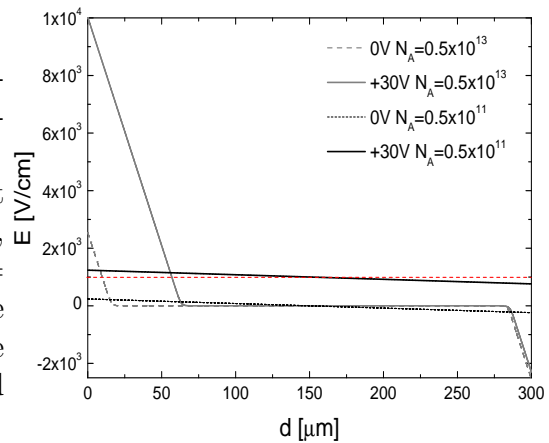


Figure 2.9: Band diagrams of two hypothetical oxygenated diamond devices with aluminium Schottky contacts of 3 eV barrier height. The concentration of ionized acceptors amounts to  $N_A = 0.5 \times 10^{13} \text{ cm}^{-3}$  (band diagrams in black),  $N_A = 0.5 \times 10^{11} \text{ cm}^{-3}$  (band diagrams in red). (Left panel) no bias is applied, (Right panel) +30V ( $E = 10^3 \text{ V/cm}$ ) applied to the left contact. Band diagrams have been simulated in SimWindows32 [SimWi].

Figure 2.10: Electric field profiles corresponding to the band diagrams from Figure 2.9. For the device with  $N_A = 0.5 \times 10^{13} \text{ cm}^{-3}$  voltage drop occurs mainly at the metal diamond interface (in gray), whereas in the case of device with  $N_A = 0.5 \times 10^{11} \text{ cm}^{-3}$ , the electric field profile (in black) approaches the profile of the device with ohmic contacts (red dashed line).





# Chapter 3

## Principles of Radiation Detection Using Solid State Detectors

### 3.1 Particle Interaction with Matter

#### 3.1.1 Charged Particles - Stopping Power

When a charged particle passes through matter, it loses energy mainly by its electromagnetic interaction with the atomic electrons in the material through which it is moving. The specific loss of energy  $dE$  for a charged particle that crosses a medium for a distance  $dx$  is given by the Equation 3.1

$$-\frac{dE}{dx} = Kz^2 \frac{Z}{A} \frac{1}{\beta^2} L(\beta) \quad (3.1)$$

where  $K/A = 4\pi N_A r_e^2 m_e c^2 = 0.307075 \text{ MeV g}^{-1} \text{ cm}^2$ ,  $z$  is projectile charge,  $A$  and  $Z$  are the target atomic mass and number, respectively;  $m_e$  and  $r_e$  are the electron mass and its classical radius;  $N_A$  is the Avogadro's number;  $c$  is the speed of light in vacuum. The parameter  $L(\beta)$ , is presented in the following form:

$$L(\beta) = L_0(\beta) + \sum_i \Delta L_i \quad (3.2)$$

$$L_0(\beta) = \ln\left(\frac{2m_e c^2 \beta^2 \gamma^2 T_{max}}{I^2}\right) - \beta^2 - \frac{\delta(\beta\gamma)}{2} \quad (3.3)$$

$$\text{with } \gamma = \frac{E_{kin} + m_0 c^2}{m_0 c^2} \text{ and } \beta = \sqrt{1 - 1/\gamma^2} \quad (3.4)$$

where  $T_{max}$  is the maximum kinetic energy which can be transferred to a free electron in a single collision,  $I$  and  $\delta$  are the mean excitation energy and the density correction, respectively;  $E_{kin}$  is the kinetic energy of the projectile and  $m_0$  is its rest mass. Taking into account only  $L_0(\beta)$ , while neglecting the rest of the corrections  $\sum \Delta L_i$ , the expression 3.1 is referred to as Bethe-Bloch equation [Blo97]. At non-relativistic energies the ionization energy loss has a  $1/\beta^2$  energy dependence, whereas at relativistic energies the energy loss is slightly growing. Thus, the ionization energy loss has a minimum at a certain energy. A particle of this energy is called a 'minimum ionizing particle' (MIP). The Bethe-Bloch formula describes quite precisely the energy losses of projectiles of  $z = 1$ , however it fails

when applied to heavy ions at both low and high energies. Therefore, further corrections  $\sum \Delta L_i$  to energy losses must be applied which are listed below.

**Lindhard-Sørensen (LS) Correction** Lindhard and Sørensen [Lin96] derived a relativistic expression for electronic stopping power of heavy ions taking into account a finite nuclear size. They used the exact solution of the Dirac equation with spherically symmetric potential, which describes the scattering of a free electron by an ion. At moderately relativistic energies ( $E_{kin} > 500 \text{ MeV}/u$ ) the following expression derived for point-like ions is valid:

$$\begin{aligned} \Delta L_{LS} = & \sum_{k=1} \left[ \frac{k}{\eta^2} \frac{k-1}{2k-1} \sin^2(\delta_k - \delta_{k-1}) \right. \\ & + \frac{k}{\eta^2} \frac{k+1}{2k+1} \sin^2(\delta_{-k} - \delta_{-k-1}) \\ & \left. + \frac{k}{4k^2-1} \frac{1}{\gamma^2 k^2 + \eta^2} - \frac{1}{k} \right] + \frac{\beta^2}{2} \end{aligned} \quad (3.5)$$

where  $\eta = \alpha z/\beta$  with  $\alpha$  the fine structure constant,  $\delta_k$  is a relativistic Coulomb phase shift expressed with the argument of the complex Gamma function, and  $k$  is a parameter used in the summation over partial waves. At ultra-relativistic energies, where the de Broglie wave length is much smaller than the projectile nucleus, an asymptotic expression for  $L(\beta)$  is valid:

$$L_{ultra} = L_0(\beta + \Delta L_{LS}) = \ln\left(\frac{2c}{R_p}\right) - 0.2 \quad (3.6)$$

where  $R_p = \sqrt{4\pi n e^2/m_e}$  is the plasma frequency, and  $n$  is the average density of target electrons. The value of  $L_{ultra}$  reveals a weak dependence on target and projectile parameters.

**Partially ionized ions** The LS correction gives perfect agreement with the experimental data for bare projectiles. However at lower energies ( $< 500 \text{ MeV}/u$ ) the heavy ions are no longer completely stripped. Therefore, in the energy loss description,  $z$  is replaced by the effective charge ( $q_{eff}$ ) using [Pie68]:

$$q_{eff} = z \left[ 1 - \exp\left(\frac{-0.95v}{z^{2/3}v_0}\right) \right] \quad (3.7)$$

where  $v/v_0$  is the projectile velocity in units of the Bohr velocity.

**Barkas correction** The Barkas effect [Bar63], associated with a  $z^3$  correction to the stopping power, is well pronounced at low energies. The correction is due to target polarization effects for low-energy distant collisions and can be accounted for by the following expression:

$$L_0(\beta) + \delta/2 \rightarrow (L_0(\beta) + \delta/2) \left( 1 + 2 \frac{z}{\sqrt{Z}F(V)} \right) \quad (3.8)$$

where  $V = \beta\gamma/\alpha\sqrt{Z}$ . The function  $F(V)$  is the ratio of two integrals within a Thomas-Fermi model of the atom.

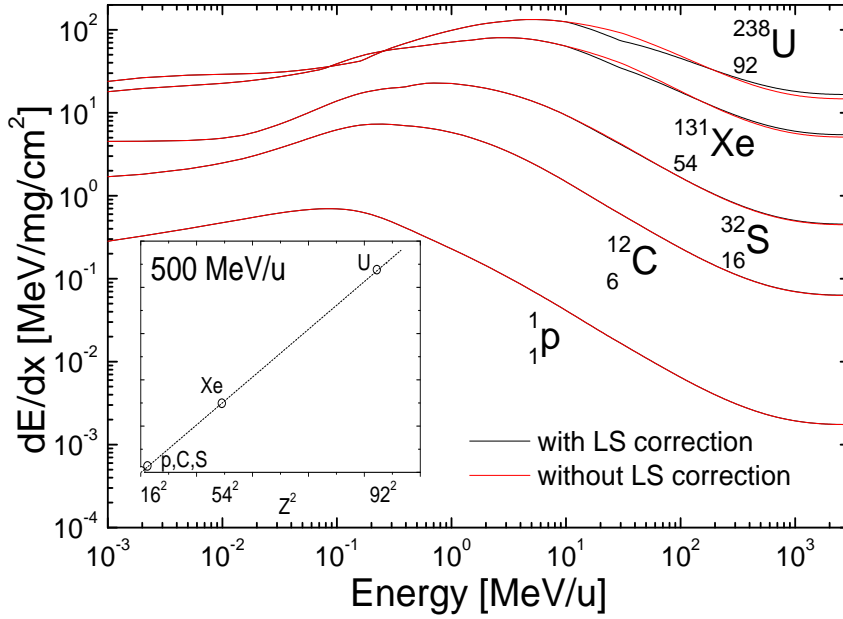


Figure 3.1: The electronic stopping power of several ions in diamond (density  $3.52 \text{ g/cm}^3$ ) in the projectile energy range  $1 \text{ keV/amu} - 3 \text{ GeV/amu}$ . The energy loss curves were calculated using the ATIMA program [ATIMA]. The figure inset shows the  $z^2$  dependence of the stopping power for ions of same velocity  $\beta$ .

**Shell corrections** Shell corrections [Bar64] should be taken into account at lower projectile velocities, when these approaches the velocity of the shell electrons of the target. The total shell correction can be presented as:

$$\Delta L = -\frac{C}{Z} \quad (3.9)$$

where  $C$  is equal to  $C_K + C_L + \dots$  and thus, it takes into account the contributions from different atomic shells.

Figure 3.1 presents the electronic stopping power  $dE/dx$  of several ions in diamond ( $\rho_{\text{diam}} = 3.52 \text{ g/cm}^3$ ) in the range of  $1 \text{ keV/amu} - 3 \text{ GeV/amu}$ . The curves are calculated using ATIMA software [ATIMA], which was developed at GSI for the calculation of various physical quantities characterizing the slowing-down of heavy ions in matter including all presented corrections.

**Energy loss of electrons** When electrons or positrons pass through matter, they lose energy by ionization like all other charged particles. In addition, they lose energy by bremsstrahlung as a consequence of their small mass.

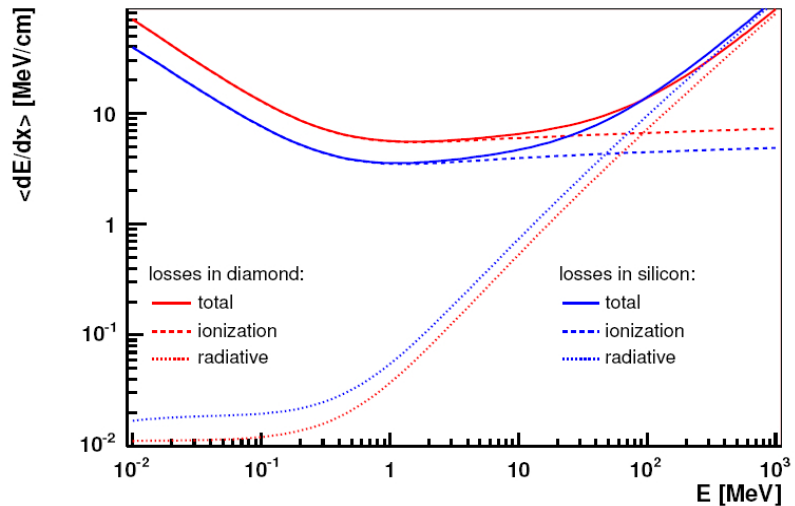
$$\frac{dE}{dx} = \left( \frac{dE}{dx} \right)_{\text{ion}} + \left( \frac{dE}{dx} \right)_{\text{rad}} \quad (3.10)$$

The bremsstrahlung process is caused by the electromagnetic interaction of the electrons with an atomic nucleus, where a photon is radiated from the decelerated electron or positron. The critical energy ( $E_c$ ), the energy above which bramsstrahlung dominates above the ionization loss can be estimated from the simplified relation:

$$E_c = \frac{600 \text{ MeV}}{Z} \quad (3.11)$$

For diamond ( $Z = 6$ ), the critical energy is about  $100 \text{ MeV}$ . Figure 3.2 shows the mean energy losses of an electron in diamond and silicon calculated using the ESTAR database

Figure 3.2: The mean energy losses of an electron in diamond (red curves) and silicon (blue curves) versus its kinetic energy. The solid curves show the total energy loss, the dashed ones correspond to the ionization loss and the dotted correspond to the radiative energy loss. The plot is obtained using the ESTAR database, after [Kuz06]



[ESTAR]. The minimum energy loss of an electron in diamond is about 1.6 MeV and in silicon about 1.3 MeV .

**Restricted energy loss** A part of the energy loss by a fast charged particle in matter is converted in fast secondary electrons or high energy photons, which leave the volume of the track. For thin films, the created secondary particles carry out a part of the deposited energy, thus the measured energy deposition within the detector material is smaller than the real energy lost by a primary particle. The restricted energy loss can be expressed in:

$$-\left(\frac{dE}{dx}\right) = Kz^2 \frac{Z}{A} \frac{1}{\beta^2} \left[ \frac{1}{2} \ln \left( \frac{2mc^2 \beta^2 \gamma^2 T_{upper}}{I^2} \right) - \frac{\beta^2}{2} \left( 1 + \frac{T_{upper}}{T_{max}} \right) - \frac{\delta(\beta\gamma)}{2} \right] \quad (3.12)$$

with  $T_{upper} = \min(T_{cut} T_{max})$ , and  $T_{cut}$  the cut-off energy above which the secondary particles escape the material. When  $T_{cut} > T_{max}$  the equation 3.12 meets the normal Bethe-Bloch function 3.1.

For standard-diamond thin films of 300-500  $\mu m$  thick, often a value  $T_{cut} = 7.5 \text{ keV}$  is assumed [Zha94], which is the energy at which the photons absorption length amounts to  $\lambda \approx 500 \mu m$ . Using this value the ionization yield for MIPs  $Q_{MIP}^{T_{cut}=7.5 \text{ keV}}/l$  can be calculated for diamond:

$$Q_{MIP}^{T_{cut}=7.5 \text{ keV}}/l = \rho_{diam} \frac{1}{\epsilon_{avg}} \frac{dE}{dx} \approx 36.7 \frac{e-h}{\mu m} \quad (3.13)$$

where  $\rho_{diam} = 3.52 \text{ g/cm}^3$  is the density of diamond,  $\epsilon_{avg} \approx 12.86 \text{ eV}/e-h$  is the average energy needed for e-h pair creation in diamond.

**Fluctuations of the energy loss - straggling functions** In the measurement of  $dE/dx$ , there are fluctuations of the average value caused by a small number of collisions that cause large energy transfers. In a thin layer of material the distribution of  $dE/dx$  will be asymmetric, with some measurements giving large energy losses. A first description of the energy straggling for thin absorbers was given by Landau resulting in so called Landau energy straggling function which depends only on one parameter [Lan44]. One of

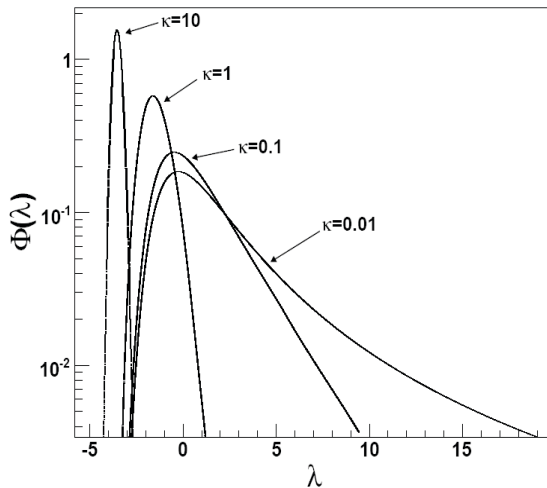


Figure 3.3: The Vavilov distribution function  $\Phi$  as a function of the scaled energy loss  $\lambda$  for various parameter  $\kappa$  and  $\beta = 0.98$ , calculated numerically using the the algorithm given in [Sch74]

the assumptions of the Landau distribution is that incoming particle can transfer all its energy to a single shell electron, which can be described by infinite energy transfer. A generalization of the Landau distribution was given by Vavilov [Vav57]. This distribution takes into account the maximum allowed energy transfer in a single collision of a particle with an atomic electron. The Vavilov distribution is a function of two parameters  $\kappa > 0$  and  $0 < \beta = \frac{v^2}{c^2} < 1$ .  $\kappa$  is proportional to the ratio of the mean energy loss over the path length of the particle to the largest energy transfer possible in a single collision with an atomic electron. The Vavilov distribution converges to the Landau distribution as  $\kappa \rightarrow 0$  for thin absorbers and large energy transfer. For thick absorbers and/or limited energy transfer,  $\kappa > 1$  and the Vavilov distribution can be replaced by a Gaussian. Figure 3.3 presents numerical calculation of the Vavilov density function for various  $\kappa$  and  $\beta = 0.98$  using algorithm of [Sch74].

A comprehensive overview of straggling functions as well as the methods of its numerical calculations can be found in several publications [Bic88, Ait69, Erm77]

### 3.1.2 X-ray and Gamma Interaction

The predominant interaction of photons with matter depends on the photon energy. Three major types of interactions are distinguished: photoelectric absorbtion, Compton scattering (coherent and incoherent) and pair production.

For energies  $E_\gamma < 100 \text{ keV}$  the predominant interaction is absorbtion via the photoelectric effect. From 100 keV to 2 MeV coherent (Rayleigh) and incoherent (Compton) scattering become more important and if the gamma energy exceeds twice the rest-mass energy of an electron (1.02 MeV), the process of pair production dominates. The conversion of a photon into a lepton pair is constrained by the momentum conservation and requires the field of an atom, thus pair conversion only occurs in matter. In Figure 3.4 the total photon cross section for carbon is shown together with the individual contributions.

After passing of a collimated gamma ray beam through an absorber e.g., scCVD-DD of variable thickness, the result will be a simple exponential attenuation of the number of gamma rays. Each of the interaction processes removes the gamma-ray photon from the beam either by absorbtion or by scattering away from the beam direction and can be characterized by a fixed probability of appearance per unit path length in the absorber. The

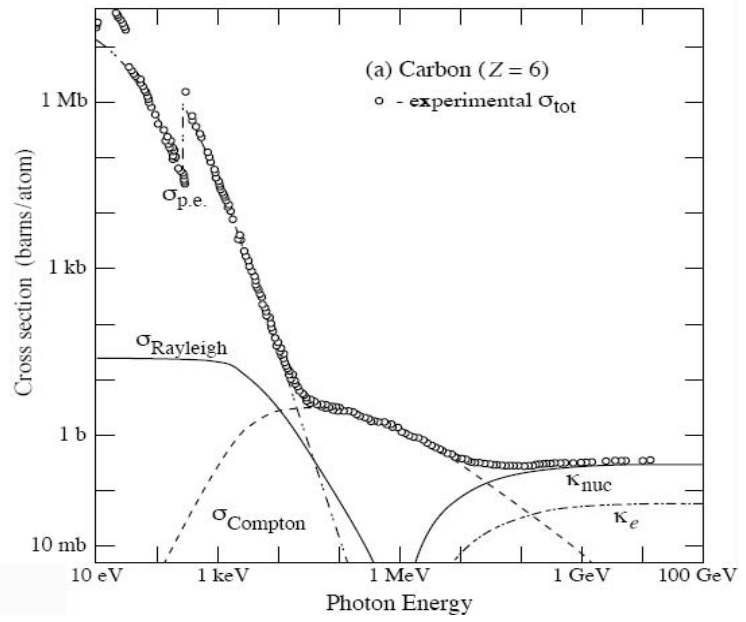


Figure 3.4: Photon total cross sections as a function of energy in carbon, showing the contributions of different processes, after [Bic06].

sum of these probabilities is the probability per unit path length the gamma-ray photon will be removed from the beam:

$$\mu = \sigma_{\text{photoelectric}} + \sigma_{\text{scattering}} + \sigma_{\text{pair}} \quad (3.14)$$

where  $\mu$  is the linear attenuation coefficient.

The number of transmitted photons  $I$  is then given in terms of the number without an absorber  $I_0$  as

$$\frac{I}{I_0} = e^{-\mu x} \quad (3.15)$$

Due to the low  $Z$  (6) diamond is a highly transparent material for X and gamma rays. Therefore, it is a favorable detector material for X-ray beam monitoring in synchrotrons or for neutron detection with high gamma background e.g., in nuclear reactors.

## 3.2 Diamond as a Solid-State Particle Detector

### 3.2.1 The Concept of a Solid-State Ionization Chamber

Particle detectors are usually composed of a sensitive volume and an amplification stage. The sensitive volume of high-quality solid-state sensor is usually characterized by a low intrinsic carrier density. In the case of narrow-band gap semiconductors e.g., silicon, PN-junction must be formed in order to obtain a sensitive volume with low carrier concentration. In the case of wide-band gap semiconductors like diamond, the sensitive volume is given only by the geometry of the electrodes. A charged particle impinging the sensitive volume, produces e-h pairs by the ionization process. After fast thermalization - order of a few ps - the carriers start to drift under the influence of an external applied electric field. The induced current is read-out either directly using broadband electronics or it is integrated by charge sensitive electronics, giving a signal proportional to the deposited energy. The drift length of the excess carriers is limited by their lifetime and their velocity. If the lifetime is much longer than the drift time of the carriers within the sensitive volume, the total charge measured is equal to the number of primary created e-h pairs. In order to optimize the detector signal is it important to improve the carrier lifetime and thus the crystal quality at the best.

### 3.2.2 Primary Ionization Cascades and Fano Factor

Ionizing radiation absorbed in the material excites electron-hole pairs in direct proportion to the energy deposited i.e.,  $n = \Delta E / \epsilon_{avg}$ ; where  $n$  is the number of electron-hole pairs generated,  $\Delta E$  is the energy deposited and  $\epsilon_{avg}$  is the average energy needed to create an electron-hole pair. The energy loss events are correlated by energy conservation. This causes the variance in the generated signal to be smaller than the value predicted by Poisson statistics. The energy loss per event depends strongly on the properties of the absorber such as band gap  $E_g$  in semiconductors. The variance in the number of generated charge carriers is expressed according to Fano [Fan46, Fan47] as:

$$\langle (n - \bar{n})^2 \rangle = F\bar{n} = F \frac{\Delta E}{\epsilon_{avg}} \quad (3.16)$$

where  $F$  is the Fano factor and  $0 < F < 1$

Thus the intrinsic energy resolution - with no variance due to the signal collection - of a detector material can be expressed as:

$$\sigma_{intr} = \sqrt{F E_0 / \epsilon_{avg}} \quad (3.17)$$

For semiconductor detectors Lappe [Lap61] proposed the empirical relationship that  $\epsilon_{avg}$  is approximately three times the band gap energy  $E_g$ . Shockley [Sho61] predicted  $\epsilon_{avg}$  in terms of  $E_g$  and optical phonon losses as  $\epsilon_{avg} = A E_g + B$ , where  $A$  is a constant calculated to be 2.2, and  $B = r(\bar{h}_r)$ , where  $r$  is the average number of optical phonons per ionization and  $\bar{h}_r$  is the average energy of the phonons. The comprehensive review of the theoretical method of calculation and experimental data can be found in [Ali80, Dev07, Alk67, Jor08].

Figure 3.5 (Right panel) shows  $\epsilon_{avg}$  as a function of the band-gap energy for a selection of semiconductors. Two main branches are apparent: the main branch found by Klein [Kle68]

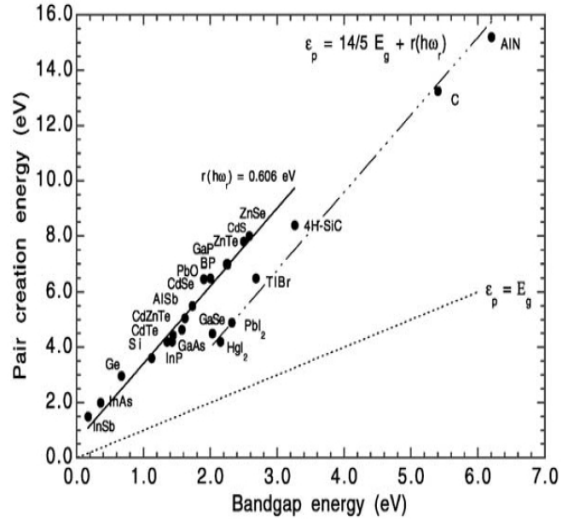


Figure 3.5: Average energy to create an e-h pair as a function of the band-gap energy for a selection of semiconductors [Owe04a].

(solid line) and the n-VIIB branch (dashed-dotted line). The dotted line denotes the limiting case when  $\epsilon_{avg} = E_g$ . In both cases the solid lines are the best fit 'Klein functions' of the form  $2.8E_g + B$  in which  $B$  is a free parameter. In order to obtain good fits the diamond and AlN values were fit as a part of the second branch.

The Fano factor of the most semiconductor materials is in the range of 0.08-0.14 as confirmed by theoretical calculations [Ali80] and experimental data. Due to the fact that the diamond detectors energy resolution had been mainly limited by the incomplete charge collection in the past, no reliable experimental data are available for the Fano factor in diamond. However, according to the theoretical predictions [Ali80], a rather low value is expected ( $F_{diam}=0.08$ ). The low predicted value results from the large band gap and the high energy of optical phonons in diamond. In general, the experimentally measured values of  $\epsilon_{avg}$  and  $F$  in semiconductors undergo downward with the detector development due to considerable improvements in the investigated material charge collection efficiency as well as electronics noise reduction. E.g., the measured  $F$  value for silicon decreased by a factor of 5 between the years 1964 and 2005. Similarly, the  $\epsilon_{avg}$  for diamond decreased from 18.6 eV in 1951 [Fre51] to 12.86 eV in 2005 [this work]. However, some authors have published recently almost equally high values of  $\epsilon_{avg}$  for scCVD diamond as in the year 1951 [Per05, Kan03].

### 3.2.3 Charge Carriers Transport - A Macroscopic View

A microscopic picture of drifting charge carriers in a semiconductor has been described in the preceding chapter. In this subsection, the relation between drifting charge and induced current is presented.

The induced current can be described by the Shockley-Ramo theorem, which states that the charge  $Q$  and the current  $i$  on an electrode induced by a moving point like charge  $q$  are given by:

$$Q_{ind} = -q\phi_0(x) \quad (3.18)$$

$$i_{ind} = q\nu \cdot \mathbf{E}_0(\mathbf{x}) \quad (3.19)$$



where  $\nu$  is the local drift velocity of charge,  $\phi_0$  dimensionless weighting potential and  $\mathbf{E}_0(\mathbf{x}) = \frac{d\phi_0}{dx}$  is the dimensionless weighting field. The last two parameters are the electric potential and field that would exist at  $q$ 's instantaneous position  $x$  under the following conditions: the selected electrode is at unit potential, all other electrodes are at zero potential and no space charge is present within the device. In the more general form the Schockley-Ramo theorem can be written as:

$$Q_{ind} = -q[\phi_0(x_f) - \phi_0(x_i)] \quad (3.20)$$

Where  $\phi_0(x_f)$  is the value of the weighting field at the stop point of the drifting charge and  $\phi_0(x_i)$  is the corresponding value at the start point of the generated charge. Consequently, the trajectory and the velocity of the charge  $q$  are determined by the real operating electric field, but the induced charge can be calculated only using the weighting potential.

Originally, this theorem has been used to describe induced signals by moving electrons in vacuum tubes. Later on, it has been confirmed also for others systems. A proof of the Schockley-Ramo theory using the energy conservation law or the mirror-charges method as well as its validity for semiconductors can be found in several publications [Dab89, Kot05, He01, Mar69].

In semiconductors, where charge particles create pairs of negatively-charged electrons and positively charged holes, both types of carriers contribute to the signal formation.

$$Q_{ind}^k = -q(\phi_0(x_f^h) - \phi_0(x_i)) + q(\phi_0(x_f^e) - \phi_0(x_i)) \quad (3.21)$$

$$i_{inst} = -q\nu_e \cdot \mathbf{E}_0(\mathbf{x}) + q\nu_h \cdot \mathbf{E}_0(\mathbf{x}) \quad (3.22)$$

with  $q$  the elementary charge.

In an ideal case both charge carriers reach the electrodes independently of the number of electrodes and their geometrical arrangement. When the read-out electrode collects one of the charge carriers (negatively biased - hole collection, positively biased- electron collection), the induced charge is equal to  $Q_{ind} = -q(1 - \phi_0(x_i)) + q(0 - \phi_0(x_i)) = q$ . When the charges reach any other electrode but the read-out electrode,  $Q_{ind} = -q(0 - \phi_0(x_i)) + q(0 - \phi_0(x_i)) = 0$ . An illustration of the Ramo theorem for a hypothetical semiconductor device surrounded by four electrodes is presented in Figure 3.6

In multi-electrode devices with complicated 3D electrodes geometry the calculation of the weighting potential and field as well as the charge velocity vector is not an easy task. Usually such calculations are done by solving numerically the Poisson equation, which relates the charge concentration to the electrostatic potential (or weighting potential) and the charge carriers continuity equations (see the Appendix).

### 3.2.4 Influence of Lattice Defects

In a real semiconductor device the charge-carriers drift length is limited by the finite carriers lifetime, due to either: recombination processes or charge trapping. There are several charge carrier recombination mechanisms [Sze81]. In general, the effective lifetime of excess electrons  $\tau_e$  and holes  $\tau_h$  for an intrinsic semiconductor can be expressed by Equation 3.23

$$\frac{1}{\tau_{e,h}} = \frac{1}{\tau_{direct}} + \frac{1}{\tau_{trap}} \quad (3.23)$$

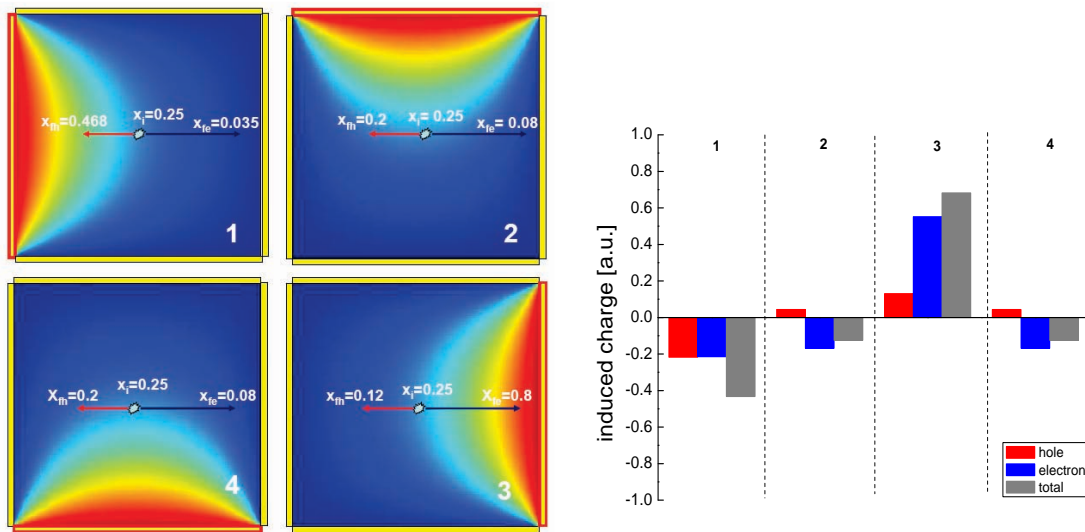


Figure 3.6: (Left panel) An illustration of the Ramo theorem for a hypothetical semiconductor device surrounded by four collecting electrodes (in yellow). The color maps correspond to four configurations of the weighting potential, where the read-out electrode at  $\Phi_0 = 1$  is marked in red, the rest of the electrodes are at  $\Phi_0 = 0$ . An e-h pair is created in the middle of the device, under applied electric field (not shown here) an electron (black arrow) drifts towards the right electrode and a hole (red arrow) towards the left electrode. Both carriers are stopped before arrival to the collecting electrodes. The weighting-field values at the start and the stop points are indicated in white. (Right panel) The corresponding induced charge at the read-out electrode for the four presented configurations.

For semiconductors with indirect wide band-gap, the direct band-to-band recombination  $\tau_{direct}$  is negligible. Thus, the lifetime of the charge carriers is mainly limited by trapping and trap assisted recombination. The trapping time for trap assisted recombination is given by:

$$\tau_{trap} = \frac{1}{\sigma_{e,h}\nu_{th}N_{def}} \quad (3.24)$$

where  $\sigma_{e,h}$  is the trapping cross-section. Depending on the nature of the defects, the usual values of  $\sigma_{e,h}$  vary from  $1 \times 10^{-16} \text{ cm}^2$  for neutral defects to  $1 \times 10^{-14} \text{ cm}^2$  for charged defects. The parameter  $\nu_{th} \approx 1 \times 10^7 \text{ cm/s}$  is the thermal velocity of the carriers, and  $N_{def}$  the defects density given by the purity of the semiconductor. For extremely pure intrinsic semiconductors  $N_{def}$  amounts to  $1 \times 10^{12} \text{ cm}^{-3}$ , whereas for bad quality materials it is  $N_{def} \approx 1 \times 10^{20} \text{ cm}^{-3}$ .

Introducing the effective lifetime of the charge carriers  $\tau_{eff}$ , the change of the excess carriers concentration with time can be written as:

$$\frac{dn}{dt} = n_0 \exp\left(-\frac{t}{\tau_{eff,e}}\right) \quad (3.25)$$

$$\frac{dp}{dt} = p_0 \exp\left(-\frac{t}{\tau_{eff,h}}\right) \quad (3.26)$$

Drifting carriers decays, therefore only electrons or holes reaching the collecting electrode contribute fully to the charge signal formation. It is important to optimize the detector geometry and the operation conditions in such a way that the carrier drift time is much shorter than the lifetime.

### 3.2.5 Detectors of a Parallel Plate Geometry - Analytical Equations

In the particular case of two parallel plate contacts at a distance  $d$  (sandwich geometry), where the longitudinal dimensions of the electrodes is much larger than the detector thickness, the weighting field  $E_k$  has the same geometrical shape as the external electric field and it is equal to  $1/d$ . The induced current from one single carrier (assume an electron) is then given by:

$$i_i = \frac{q \cdot v^e(E)}{d} \quad (3.27)$$

The drift time of the electron is defined by its effective lifetime  $\tau_e$  or/and by the distance  $z$  to the anode. If  $\tau_e$  is known, the collected charge from one electron is calculated according to the Equation 3.28

$$Q_{coll}^e = \frac{q}{d} \int_0^{\tau_e} v^e(E) dt = \frac{q}{d} v^e(E) \tau_e \equiv q \frac{\delta^e}{d} \quad (3.28)$$

with the constrain  $\tau_e \leq t_{tr}^e$ , where  $t_{tr}^e = z/v^e(E)$  is the electron transit time.

$$\delta^e = v^e(E) \tau_e \quad (3.29)$$

The parameter  $\delta^e$  is the electron drift length, also called Schubweg [Hec32]. It describes the distance between the point of creation and the point of stopping of the electron, which occurs due to carrier trapping or recombination. The collected charge from one electron is proportional to the ratio of the Schubweg to the distance between electrodes, i.e., the thickness of the detector. The drift velocity  $v^e(E)$  in equation 3.29 increases as a function of the applied electric field  $E$ . At high  $E$   $v^e(E)$  tends to saturate due to the scattering processes (discussed in the previous chapter). At saturated drift velocity  $\delta^e$  is independent of  $E$ .

In order to calculate the collected charge from a bunch of  $n_0$  electrons created in a point-like region within a detector volume, the relation 3.25 is used. The term  $t/\tau_e$  is replaced by  $\Delta z/\delta^e$  with  $\Delta z$  the drift distance. Equation 3.28 is then written as

$$\begin{aligned} Q_{coll} &= \frac{q}{d} \int_0^z v^e(E) n(t) v^e(E) dt \\ &= n_0 \frac{q}{d} \tau_e \left[ 1 - \exp\left(-\frac{z/v^e(E)}{\tau_e}\right) \right] \\ &= n_0 q \frac{\delta^e}{d} \left[ 1 - \exp\left(-\frac{z}{\delta^e}\right) \right] \end{aligned} \quad (3.30)$$

For the general case where the electrons are distributed within the detector volume with  $\rho^e(z)$  and  $\int_0^d \rho^e(z) dz = n_0$ , the expression for  $Q_{coll}$  changes to

$$\begin{aligned} Q_{coll} &= \frac{q}{d} \int_0^d \rho^e(z) \int_0^{(d-z)} v^e(E) \frac{n(t)}{n_0} v^e(E) dt dz \\ &= \frac{q}{d} \int_0^d \rho^e(z) \tau_e \left[ 1 - \exp\left(\frac{(z-d)}{v^e(E)\tau_e}\right) \right] dz \\ &= q \frac{\delta^e}{d} \int_0^d \rho^e(z) \left[ 1 - \exp\left(\frac{(z-d)}{\delta^e}\right) \right] dz \end{aligned} \quad (3.31)$$

Analogue expressions can be derived for holes. The total collected charge is the sum of the holes and the electrons contributions:

$$Q_{coll} = \frac{q}{d} \int_0^d \left[ \delta^e \rho^e(z) \left[ 1 - \exp\left(\frac{(z-d)}{\delta^e}\right) \right] + \delta^h \rho^h(z) \left[ 1 - \exp\left(\frac{(-z)}{\delta^h}\right) \right] \right] dz \quad (3.32)$$

For ionization process  $\rho_e(z) \equiv \rho_h(z) \equiv \rho_Q(z)$ , and  $Q_{gen} = \int_0^d \rho_Q(z) dz$ .

**Charge Collection Distance (CCD)** For a defective semiconductor of short lifetime charge carriers, it is often  $\delta_{e,h} \ll d$ , and equation 3.32 simplifies to:

$$Q_{coll} = Q_{gen} \frac{\delta^e + \delta^h}{d} \quad Q_{coll} = \frac{\delta^Q}{d} \quad (3.33)$$

where  $\delta_Q$  is called the Charge Collection Distance (CCD). In order to measure the CCD, the values of  $Q_{coll}$ ,  $Q_{gen}$ , and  $\rho^Q(z)$  must be known. For  $\rho^Q(z) = const$ ,  $\delta^Q$  is written as:

$$\delta^Q = v_d^e \tau_{eff}^e + v_d^h \tau_{eff}^h \quad (3.34)$$

**Charge Collection Efficiency (CCE)** A more detector relevant value, which does not need any approximation is the charge collection efficiency (CCE) defined as

$$CCE = \frac{Q_{coll}}{Q_{gen}} \quad (3.35)$$

Considering the generated charge  $Q_{gen}$ , the CCE is measured by the collected charge  $Q_{coll}$ . The CCE is independent from the generated charge distribution  $\rho^Q$ .

If free charge carriers are created in the vicinity of one electrode close to the surface ( $z \ll d$ ), only one type of charge carriers contributes to the signal formation, while for the other the charge drift length is close to zero. The induced current is expressed by:

$$i_{e,h} = \frac{Q_0 v_{e,h}(E)}{d} \exp(-t/\tau_{e,h}) \quad (3.36)$$

and the collected charge by:

$$Q_{coll}^{e,h} = Q_{gen} \frac{\delta^{e,h}}{d} \left[ 1 - \exp\left(-\frac{d}{\delta^{e,h}}\right) \right] \quad (3.37)$$

where  $Q_0 = q \int_0^d \rho_{e,h} dz$  is the generated charge due to the ionization process. If the transit time  $t_{tr}^{e,h} = \frac{d}{v(E)^{e,h}}$  is known, Hecht's equation is written as

$$Q_{col}^{e,h} = Q_0 \frac{\tau_{e,h}}{t_{tr}^{e,h}} \left[ 1 - \exp\left(-\frac{t_{tr}^{e,h}}{\tau_{e,h}}\right) \right] \quad (3.38)$$

For a homogenously ionizing particle with  $dE/dx = \text{const}$ , like relativistic particles in a solid-state detector of a typical thickness 300-500  $\mu m$ , the induced current is the sum of the holes and the electron currents

$$i(t) = Q_{gen} \frac{v(E)^e}{d} \left( 1 - \frac{t}{t_{tr}^e} \right) \exp(-t/\tau_e) + Q_0 \frac{v(E)^h}{d} \left( 1 - \frac{t}{t_{tr}^h} \right) \exp(-t/\tau_h) \quad (3.39)$$

and the collected charge  $Q_{coll}$

$$Q_{coll} = Q_{gen} \frac{\overline{\delta Q}}{d} \left[ 1 - \exp\left(-\frac{d}{\overline{\delta Q}}\right) \right] \quad \text{and} \quad \overline{\delta Q} = \frac{v^e(E)\tau_e + v^h(E)\tau_h}{2} \quad (3.40)$$

The graphical representation of the Hecht equation, relating the charge collection efficiency (CCE) to the charge collection distance (CCD) is presented in Figure 3.7.

### 3.2.6 Trapping Related Phenomena

In the previous sections the signal, generation process was discussed and the importance of the CCD was underlined. The ideal case that all charge is collected (CCE $\approx$ 100%) is only given for CCD $\gg$ d. Although recent scCVD diamond results are excellent [Pom05,Pom06], the lifetime of the charge carriers seems to be still limited by the presence of lattice defects. The defects may be of intrinsic (e.g., vacancy and carbon interstitial atom), or of extrinsic origin impurity atoms (typically H, N, B), forming so-called point defects. During the

Figure 3.7: The graphical representation of the Hecht equation relating the charge collection efficiency (CCE) to the charge collection distance (CCD). Although close to 100%, a full charge collection efficiency is never reached. For a detector of a short drift length of carriers a linear approximation  $CCE = CCD/d$  can be made.

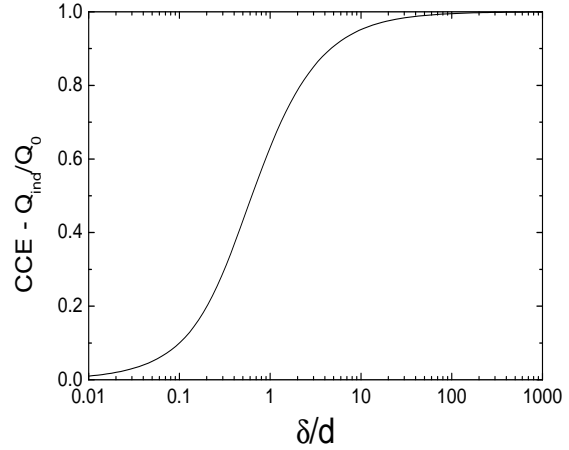
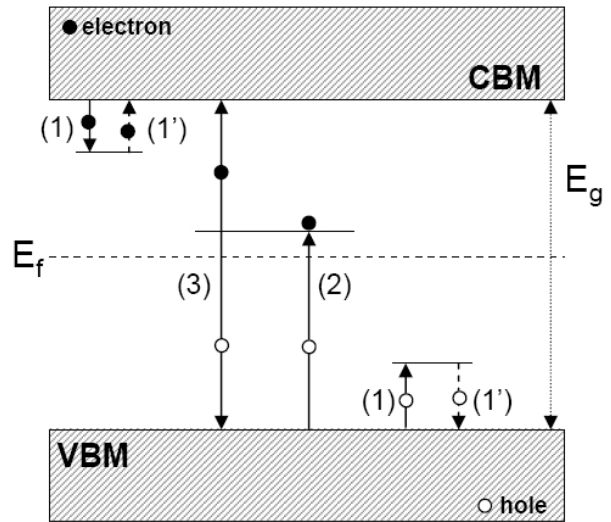


Figure 3.8: The simplified mechanism of (1) trapping, (2) recombination, (3) generation (1') re-emission of charge carriers.  $E_f$  is the Fermi level,  $E_g$  the band gap.



diamond growth, microscopic extended defects like dislocations or grain boundaries (pcCVD diamonds) can be formed, where the defect density is locally very high [Zhu95].

The defects are characterized by their position in the band-gap, and their cross section to capture charge carriers. The energy of the trap ( $E_d$ ) determines in conjunction with the temperature  $T$  and the Fermi level  $E_f$  the occupation state

$$F(E_d) = \frac{1}{e^{\frac{E_d - E_f}{kT}} + 1} \quad (3.41)$$

where  $k$  is the Boltzmann constant. Trap levels with  $(E_d - E_f)$  of a few eV are therefore practically not occupied at room temperature, but can be filled by excess carriers generated for instance by ionization.

According to the Shockley-Read-Hall theory [Sho52, Hal52], traps can act via three processes: (1) trapping, (2) recombination, (3) generation of charge carriers. These mechanisms are shown in Figure 3.8.

A trap can capture a free carrier (1) from the valence or conduction band. The rate per volume for this process is given by the density of non-occupied traps  $n_t$  and the density of

free carriers  $n_{fc}$ , the capture cross section  $\sigma_t$ , and the thermal velocity of the carrier,  $v_{th}$ , as:

$$r_t = n_t \cdot n_{fc} \cdot \sigma_t \cdot v_t \quad (3.42)$$

An occupied trap can capture a carrier of opposite sign which recombines (2) with the trapped charge. The rate is then given by:

$$r_r = n_r \cdot n_{fc} \cdot \sigma_r \cdot v_{th} \quad (3.43)$$

where  $n_r$  is the density of occupied traps and  $\sigma_r$  the capture cross section for charges of opposite sign. In the case of quasi-equilibrium with  $n_t \gg n_{fc}$  and  $n_r \gg n_{fc}$  a life-time  $\tau$  can be defined from Equation 3.44

$$\tau = \frac{n_{fc}}{r_t + r_r} = \frac{1}{v_{th}(\sigma_t n_t + \sigma_r n_r)} \quad (3.44)$$

A trapped charge can be thermally re-emitted (1'). The probability for thermal emission depends on the activation energy  $E_a$  defined as a distance of the trap level to the CBM or VBM in the case of electrons and holes respectively. The temperature dependence of the emission rate per volume is given by:

$$r_{re} = s \cdot n_f \cdot \exp\left(-\frac{E_a}{kT}\right) \quad (3.45)$$

with  $n_f$  the density of occupied traps and  $s$  the attempt to escape factor. Typically,  $s$  is in the range  $10^{12} \text{ s}^{-1}$  to  $10^{14} \text{ s}^{-1}$ . The thermal-emission rate is for deep defects levels ( $E_\Delta \gg kT$ ) very low, hence the charge is stored for a long time in the trap.

Trapped carriers give rise to space charge. In Figure 3.9, this effect is illustrated for negative and positive detector bias. After illumination, excess charge carriers are created which drift in the presence of an external electric field a), c). In the presented configuration one type of the carriers is rapidly extracted through the left electrode, whereas the second type ( a) electrons, c) holes ) is captured in deep traps during the long drift to the right electrode. Trapped charge gives rise to an internal electric field. After short illumination of a detector containing space charge, a carrier drift and thus an induced current can be observed even if no external field is applied b), d).

Fixed space charge gives rise to two phenomena important for the detector operation:

- **polarization**, which occurs by an inhomogenous filling of the traps as produced by short-range ionization (e.g.,  $\alpha$ -particles or UV-light absorbtion). In this case, the charge carriers are effectively separated and in the region of deposition strong polarized space charge develops. The polarized space charge creates an internal electric field which is opposed to the applied external field. As a result, progressive deterioration and finally loss of the measured pulse-height is observed.
- **priming (or pumping)**, which occurs when the filling of traps is more homogeneous e.g., for traversing particles. The polarization effect in this case is much less pronounced. If traps are occupied, the free-trap density is decreased, and thus the lifetime of the charge carriers increases. This leads to an enhancement of the detector signal.

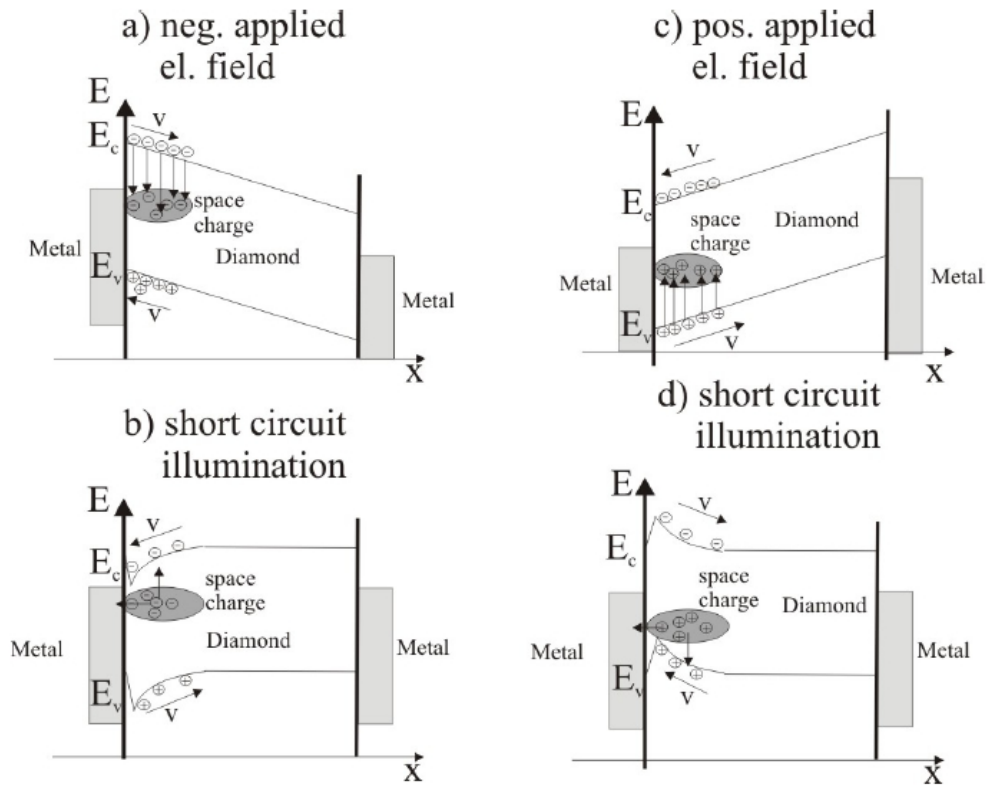


Figure 3.9: Diagrams illustrating the space charge generation within pcCVD sample after [Neb98] - see text.

The persistence of the space charge depends on the position of the defect level in the band gap. In the case of diamond most of the defect levels (both intrinsic and extrinsic) are located in the band gap as deep as  $E_d > 1$  eV. Therefore, polarization or priming are stable at room temperature. The depopulation of the deep traps (thus reestablishment of the non-polarized state) can be obtained by the samples heating or illumination with the visible light of a sub-band gap energy (1-3 eV). The priming effect is often exploited in the case of highly defective pcCVD-DDs. To improve their charge collection properties, the detectors are exposed, prior to the main experiment to high-doses of homogenous radiation. For a perfect crystal with extremely low density of defects no priming and no polarization should be observed.



# Chapter 4

## A Crystal Quality Study

The electronic properties of any semiconductor material, strongly depend on the presence of atomic impurities and structural defects within the crystal lattice. In the case of diamond, the most common atomic impurities are boron and nitrogen. Both atoms have a size, which is comparable to the carbon atom. Therefore they are easily incorporated into the diamond lattice during the CVD process, giving rise to electrically active defects. Structural defects in a microscopic scale (like dislocations) can be formed during the growth process, introducing extended electrical defects and strain into the crystal. Additionally, defective surfaces (e.g., resulting from polishing) may significantly change the characteristics of metal-semiconductor interfaces. Such imperfections can negatively affect the scCVD-DD operation through a significant reduction of the charge carriers lifetime or/and the safe range detector bias due to a decreased dielectric strength of the diamond film.

### 4.1 Material Used in This Work

The single crystal diamond material used in this work was supplied by Element Six (E6), King's Ride Park, Ascot, UK. All crystals had been grown with the microwave assisted CVD technique on  $\langle 1\ 0\ 0 \rangle$  oriented high-pressure high-temperature (HPHT) diamond substrates. After separation from the substrate by laser cutting, the surfaces of the diamond had been polished using variety of different techniques. Over a three years period, more than thirty samples of various thicknesses (50 - 500  $\mu\text{m}$ ), sizes ( $3 \times 3$  -  $5 \times 5$   $\text{mm}^2$ ), as well as different surface preparations were tested with respect to their detector properties, using diverse characterization techniques. The results are presented and discussed in the following sections.

### 4.2 Atomic Impurities in scCVD Diamond

In order to evaluate the chemical purity of scCVD diamond films, several randomly chosen samples were characterized by spectroscopic techniques: in the infrared (IR), visible (VIS) and ultraviolet (UV) range as well as by electron spin resonance (ESR) and finally by total photoelectron emission yield spectroscopy (TPYS).

**Nitrogen impurity:** Nitrogen incorporated into the diamond lattice, due to five valence electrons, becomes a deep donor with an ionization energy of 1.7 to 2 eV. Therefore it

acts as a deep trapping center, reducing significantly the average lifetime of excess charge carriers [Loh07]. Nitrogen is usually present in a form of substitutional atoms, which may appear isolated or, alternatively, form aggregates. Such defects form various electrically active states within the diamond band-gap, giving rise to absorption in the VIS or the IR range.

- The single substitutional nitrogen (called type C center) was observed in all synthetic diamonds, HPHT and CVD crystals. It gives rise to a characteristic IR spectrum with a broad peak around  $1130\text{ cm}^{-1}$  and a sharp local mode peak at  $1344\text{ cm}^{-1}$  [Zai01]. As a non-ionized donor at RT, it gives rise to a continuous absorption in UV-VIS spectroscopy starting at  $\sim 2\text{ eV}$ . As element with unpaired valence electrons it gives rise to the P1 ESR signal [Nok01].
- The nearest neighbor pair of substitutional nitrogen atoms, called the A aggregate, is present in the majority of natural diamonds (type IaA) and can be also incorporated into CVD films in form of  $N_2$  molecules [Neb00]. Its IR spectrum reveals a major peak at  $1282\text{ cm}^{-1}$  and another one at  $1212\text{ cm}^{-1}$  [Zai01].

Figure 4.1 (Left panel) shows an ESR spectrum measured with two scCVD samples: a) a high purity IIa diamond and b) a diamond produced by E6. The concentration of P1 centers was about  $\sim 10^{15}\text{ cm}^{-3}$  for the IIa sample (top spectrum). Despite of a 15 times longer scan for the E6 sample, no detectable ESR signal could be registered (bottom spectrum). The conclusion is that the concentration of the single-substitutional nitrogen within this sample is below  $10^{14}\text{ cm}^{-3}$ , i.e., the detection limit of the ESR method.

Examples of IR absorption spectra of three synthetic diamonds are shown in Figure 4.1 (Right panel). Characteristic nitrogen absorption bands (A and C centres) in the one-phonon region can be observed for two HPHT diamonds (black and red curves). No signature of nitrogen impurity in form of A or C centers is found for the E6 scCVD diamond, within the sensitivity of the IR absorption method, (i.e., 1 ppm).

**Boron impurity:** Boron is present in the very rare type IIb natural diamonds. In CVD diamond growth, boron is deliberately added in order to obtain p-conductive films [Col79]. However, due to pollution from the steel chambers of the growth reactors, unwanted contamination with boron can occur during the growth process even of intrinsic diamond films.

If boron, containing three valence electrons, is incorporated into the diamond lattice, it behaves approximately as a 'hydrogenic' acceptor with relatively low ionization energy of 0.368 eV. It gives rise to photoconductivity above this energy threshold. The diamond appears bluish due to absorption in the red region of the visible light spectrum. Boron acts as a shallow trapping center for excess charge carriers, affecting the operation of diamond detectors negatively.

Figure 4.2 presents the results of total photoelectron emission yield spectroscopy (TPYS) of a scCVD produced by E6 (black curve) and a high quality IIa CVD diamond (red curve). The measurement was carried out at 300 °C. At this temperature, most of the boron acceptors are ionized, gaining electrons from the valence band (VB). The band-gap at 573 K is estimated from  $E_g = 5.48\text{ eV} - \Delta E(T) = 5.48\text{ eV} - 0.06\text{ eV} = 5.42\text{ eV}$ . By subtracting the energy level of the boron acceptor from the band gap, one gets the energy difference of the electron transition from the acceptor level to the CBM, which is

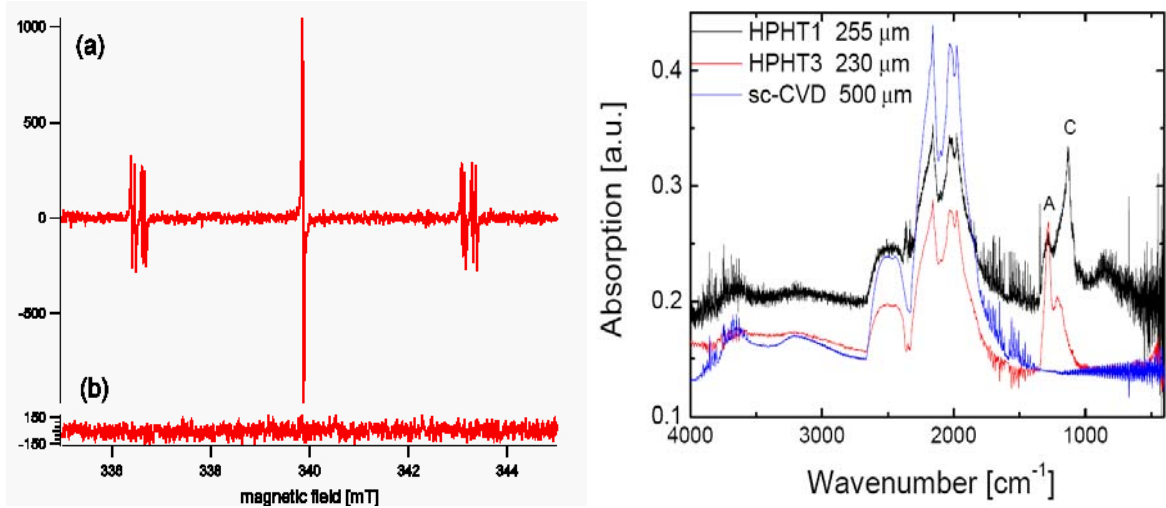


Figure 4.1: (Left panel) ESR spectra of two scCVD diamonds a) a high purity IIa diamond and b) a scCVD diamond sample produced by E6 (courtesy Ch. Nebel). No detectable ESR signal was found for the E6 sample within the sensitivity range of the method of  $\sim 10^{14} \text{ cm}^{-3}$ . (Right panel) IR absorption spectra of three synthetic diamonds, showing absorption in the one-phonon range by nitrogen impurities (A and C centers) in a HPHT diamond (red and black curves). No absorption could be detected for the E6 scCVD diamond (blue curve).

$\Delta E = 5.06 \text{ eV}$ . This transition is marked as *I* in the band diagram of Figure 4.2 (Right panel). The next onsets above 5.2 eV are due to exciton ground states and the absorption edge with phonon-absorption at 573 K, (marked in the band diagram as *II*). For both samples, boron related excitation is present. However, in the case of the E6 sample, the measured photoelectron emission yield is about one order of magnitude smaller. From cross calibration with a sample of known boron impurity concentration, the amount of boron for the E6 sample was estimated to  $\leq 10^{15} \text{ cm}^{-3}$ .

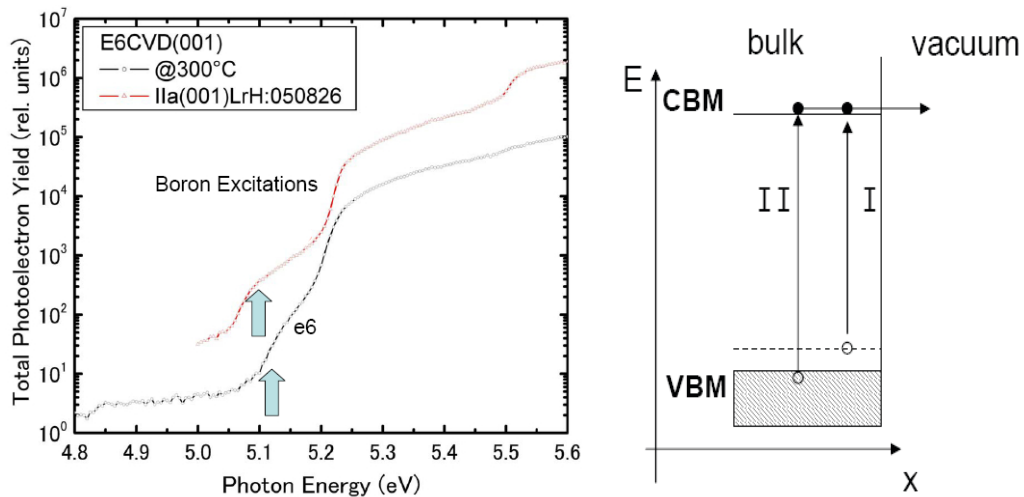


Figure 4.2: (Left panel) TPYS spectra of two scCVD diamonds measured at 300 °C (courtesy Ch. Nebel). In both cases onset at  $\sim 5.06 \text{ eV}$  is visible suggesting, transition from the boron impurity level (0.36 eV) to CBM as indicated in the band diagram (Right panel).

**Optical absorption spectra** Figure 4.3 (Left panel) shows UV - VIS absorption spectra of a scCVD diamond produced by E6 (red curve) measured at RT. For comparison, a spectrum of an HPHT Ib (containing nitrogen impurities) is displayed in black, where the absorption starts around 2 eV (photo-ionization onset of nitrogen impurities). No absorption is registered for the scCVD diamond up to the fundamental edge absorption at the band gap energy of diamond  $\sim 5.46$  eV (at RT). The right graph of Figure 4.3 presents the edge absorption of a scCVD diamond in expanded energy scale. Since, diamond is an indirect semiconductor, three thresholds in the absorption spectrum can be distinguished. The first and the second threshold correspond to the creation of an exciton ( $E_{gx} = 5.406$  eV) with the absorption of a transverse optic (TO) or a transverse acoustic (TA) phonon, respectively, whereas the third threshold corresponds to the creation of an exciton with the emission of a TA phonon. The absence of absorption in the near red region of visible light and an edge absorption with exciton creation is typical only for high purity IIa diamonds.

The UV - VIS absorption spectra of about six scCVD samples measured have shown the same characteristic.

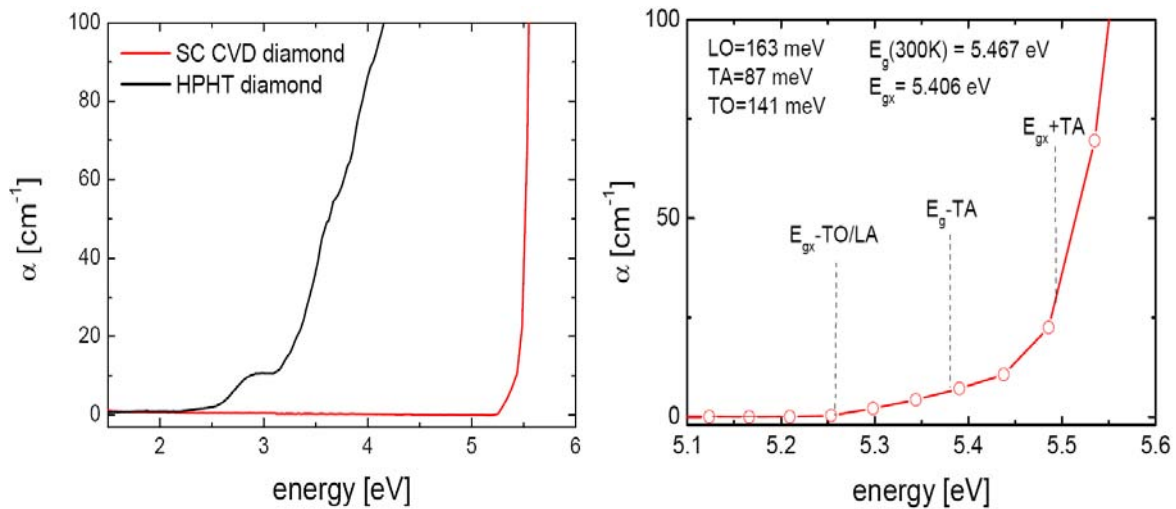


Figure 4.3: (Left panel) Absorption spectra in the VIS - UV range of an intrinsic scCVD and an Ib HPHT diamond measured at room temperature. (Right panel) Fundamental absorption edge at the band-gap energy of e6 scCVD diamond. The thresholds (1) and (2) involve creation of an exciton with the absorption of a TO or a TA phonon, and threshold (3) involves the emission of a TA phonon.

### 4.3 Microscopic Structural Defects

In order to judge the quality of the crystal structure of scCVD diamond, two imaging methods were employed. Several scCVD diamond samples were characterized by means of 'white beam' X-ray topography at the ID19 line [ID19] at electron synchrotron (ESRF) in Grenoble. In addition, cross polarized light microscopy was used to visualize strain fields induced by structural defects within the diamond bulk.

### 4.3.1 White Beam X-ray Topography

**Basics of white beam X-ray topography** White beam X-ray topography is a non-destructive characterization method for the imaging of defects and strain in crystals, electronic devices and epitaxial layers. The advantage of the method is easy operation in combination with high resolution. The basics of the method are sketched in Figure 4.4. A white beam is diffracted by a crystal according to Bragg's law:

$$2d\sin\Theta = \lambda \quad (4.1)$$

where  $d$  is the crystal planes spacing,  $\Theta$  is the Bragg angle, and  $\lambda$  denotes the incident wavelength.

Every diffraction vector which fulfils Bragg's law results in one topograph of the same sample area, called Laue pattern. By using X-ray films one can record a Laue pattern of topographs with one single exposure. Every inhomogeneity (i.e., variations in lattice spacing  $\Delta d$ ) of the crystal structure leads to a violation of Bragg's law and therefore to an intensity decrease of the diffracted beam, thus to a contrast modification in the corresponding topograph.

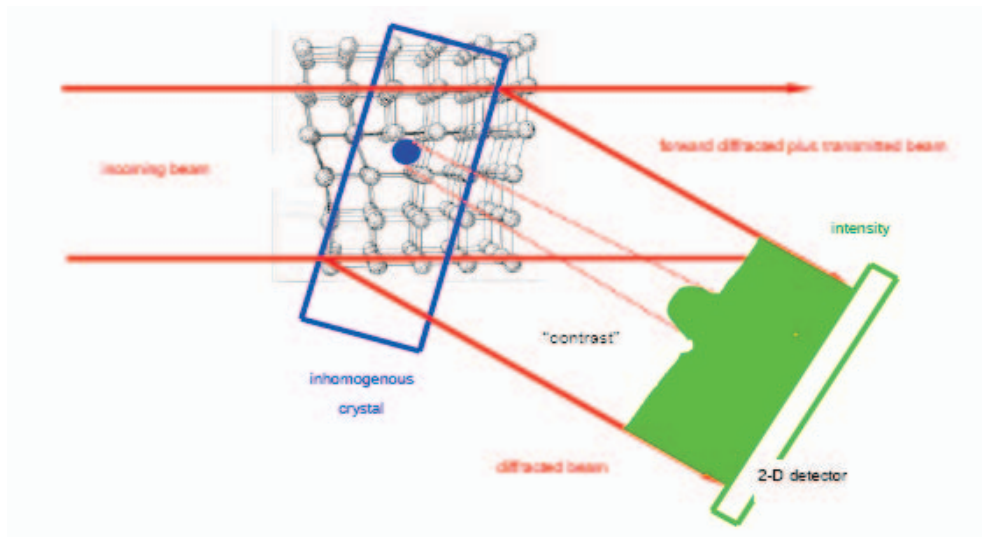


Figure 4.4: Contrast in X-ray topography: defects in a single-crystal material do not fulfil the Bragg condition for a selected diffracted beam, leading to an intensity change of diffracted beam, thus contrast modification in the corresponding topograph, after [ID19]

In contrast to the monochromatic case, no accurate sample adjustment is necessary in order to reach the diffraction conditions. The Bragg equation is always fulfilled in the case of a white X-ray beam with a wide enough spectrum. Although white-beam topography is useful for a fast and comprehensive visualization of crystal defects and distortions, it is rather difficult to analyze quantitatively (e.g., to estimate the absolute density of defects). More details on crystal structure investigations by diffraction methods can be found in [Bla04].

**Set-up** The schematic of the experimental set-up is presented in Figure 4.5.

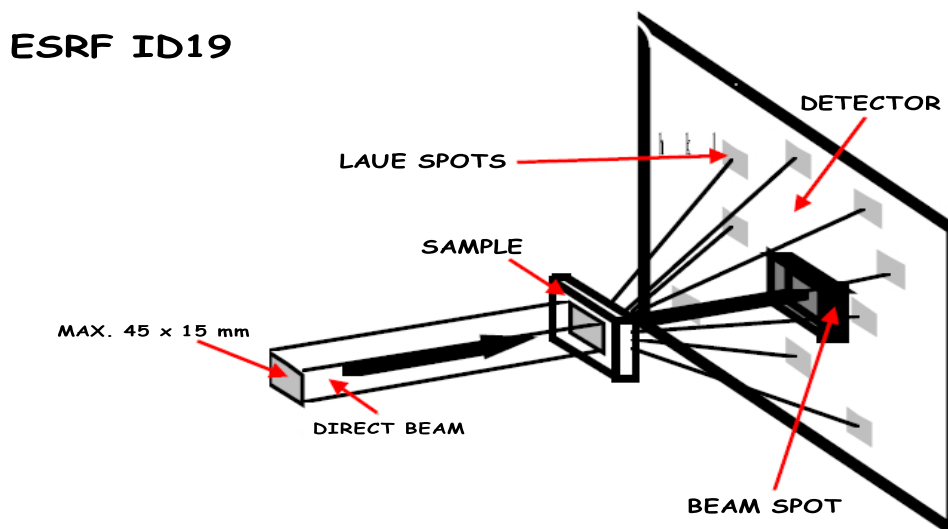


Figure 4.5: Experimental arrangement of X-ray topography measurements at the ID19 line of ESRF, after [ID19]

Transmission mode (Laue mode) of diffraction is chosen. The sample is enclosed in a plastic box and it is placed on a gyratory stage between the detector and the incoming X-ray beam. Kodak SR X-ray sensitive films with grain size 4-5  $\mu\text{m}$  are used as 2D detector to record the diffraction patterns. The correct time of exposition, which may vary from 0.1 s to several seconds, must be set before taking topographs. During the exposure, the particular wavelength, which fulfils the Bragg diffraction law is diffracted on the crystal lattice and, depending on the crystal orientation, it produces several diffraction Laue spots. In the case of scCVD diamond samples three main spots are produced at coordinates corresponding to the  $\langle 1\ 0\ 0 \rangle$  orientation of the crystal. The fine structure of each single Laue spot is related to defects and distortions within the sample. After exposure the X-ray film is developed at place in a Kodak developing machine. Next, the film regions containing Laue spots are digitalized using a conventional scanner.

**Results and discussion** In general, structural defect free samples give homogenous Laue spots without contrast. An example of a high structural quality IIa HPHT diamond prepared for use as an X-ray beam monochromator in a future generation of synchrotrons is presented in Figure 4.6 (Left panel). However, although this sample is of perfect structural quality, it cannot be used as a particle detector due to the bulk contamination with atomic nitrogen. The right plot of Figure 4.6 shows a quasi-3D X-ray topograph of a scCVD diamond. This topograph was obtained using the more sophisticated Lang's technique, where the sample is scanned with a sliced beam [Lan59]. Characteristic bundles of threading dislocations are visible, which diverge from isolated points localized on the substrate side of the sample. Such structures result from surface defects of the HPHT diamond substrate. During the CVD growth, the imperfections of the substrate are reproduced in the CVD film. As suggested in [Gau08], such agglomerated defects tend to be made up of  $\langle 0\ 0\ 1 \rangle$  edge dislocations.

Figure 4.7 shows 'white-beam' X-ray topographs of nine scCVD diamonds which are envisioned for the use as particle detectors. Bundles of threading dislocations appear in



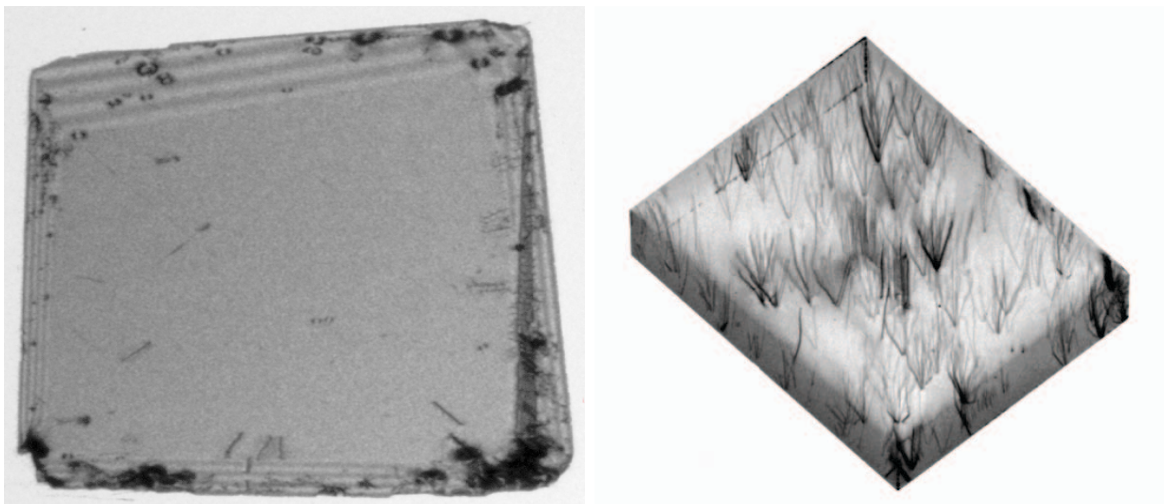


Figure 4.6: (Left panel) 'White beam' X-ray topograph of high crystal quality IIa HPHT diamond (courtesy J. Härtwig). (Right panel) Quasi-3D topograph of a scCVD diamond measured using Lang's technique after [Gau08] showing threading dislocations.

almost all investigated samples, particularly visible in samples SC2 and SC3 (red circles). In addition, due to the rough polishing, possibly applied for the preparation of the HPHT substrates, extended defects are formed in CVD films (e.g., agglomeration of dislocations diverging from linear scratches). Such extended defects introduce high strain fields (dark areas), where single dislocations are not resolved. Clusters of structural defects are visible in the topographs of the samples SC1, s0256-02-06 and SC2B.

The circular line structure in the topographs of samples SC2, SC3 and SC6A, as well as a quadrant motive indicated in sample SC8BP, are permanently introduced by stress during metal electrodes sputtering when producing scCVD-DD (see Chapter 5). Large defects in the corners of the samples (visible in sample SC14BP) originate from growth sectors of the HPHT substrate [Sec07]. The bright areas on these topographs are free of structural defects indicating perfect quality of the diamond lattice. The quality of recent samples (2007) is commonly superior to the quality of early samples (2005), showing the rapid progress in the CVD diamond growth and post processing technologies.

### 4.3.2 Birefringence - Cross Polarized Visible Light Microscopy

As a cubic crystal diamond is usually not birefringent but optically isotropic, meaning that its refraction index is equal in all directions throughout the crystalline lattice. However, strain in diamond caused by impurities, dislocations or external stress, introduces anisotropy resulting in birefringence, which can be detected by cross-polarized light imaging. Because intrinsic IIa type diamond is fully transparent in the visible range, this method is a cheap and efficient tool to judge the quality of the diamond lattice.

**Principles of cross polarized light microscopy** A schematic of the principle of cross-polarized microscopy is shown in Figure 4.8.

A sample is placed between two crossed polarizers. The first, nominated the polarizer, selects only one mode of the light wave from the unpolarized light source, whereas the

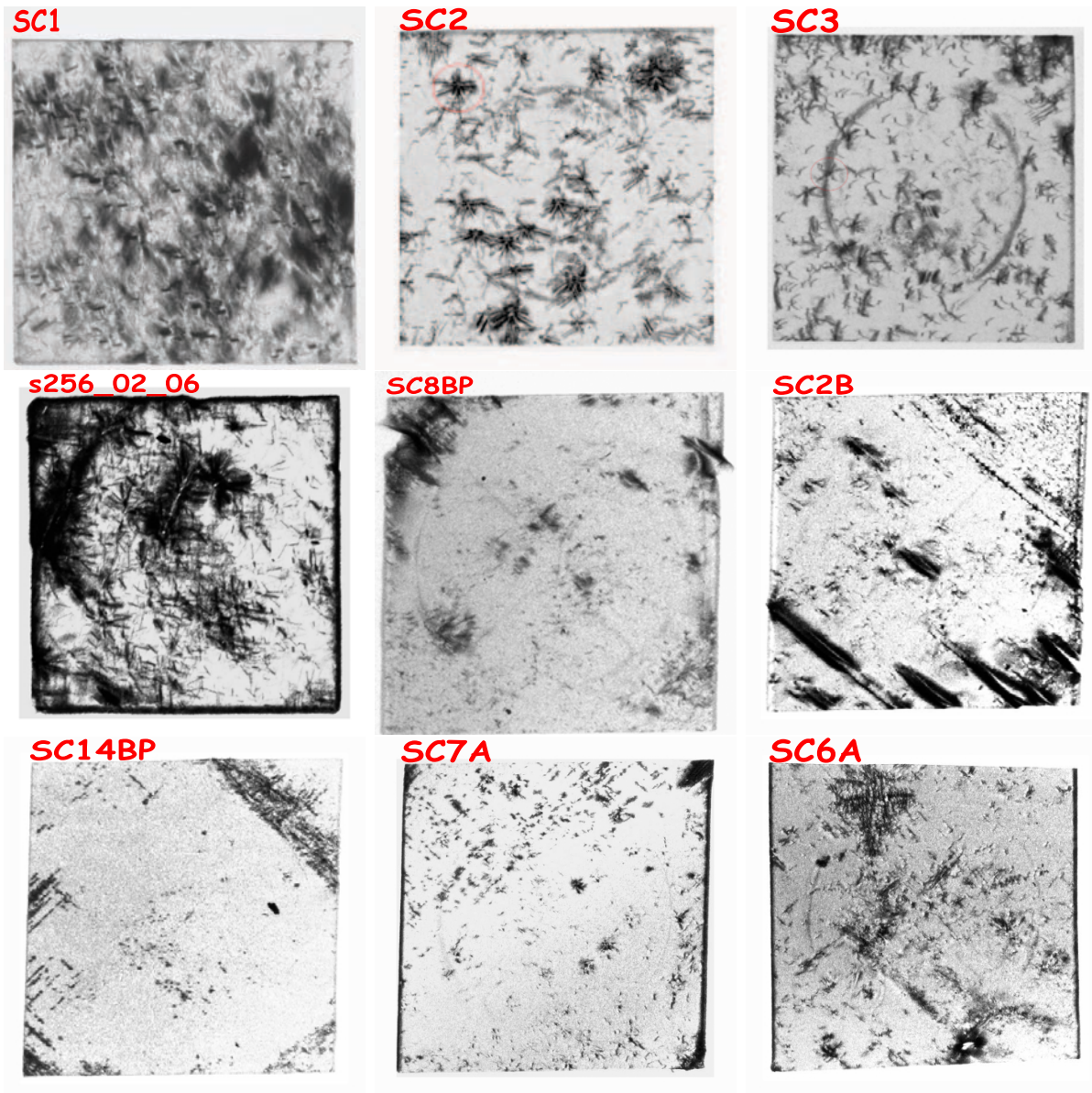


Figure 4.7: 'Witbe-beam' X-ray topographs of various scCVD diamonds prepared for the use in particle detection. The size of the individual topographs corresponds to the sample size of 3 mm  $\times$  3 mm up to 5 mm  $\times$  5 mm, respectively (see text).



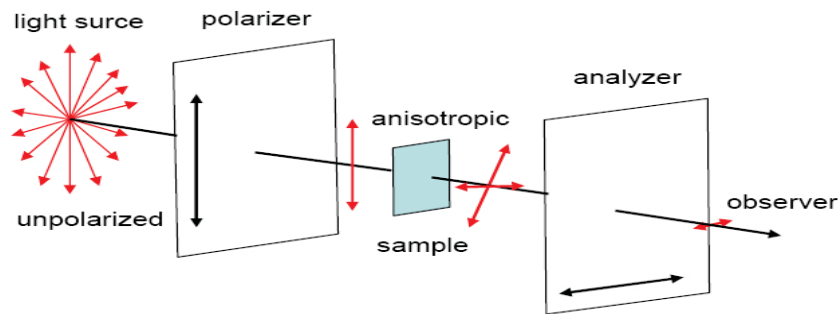


Figure 4.8: Principle of birefringence measurements using cross polarized light.

second, referred to as the analyzer, blocks the previously polarized light. When a homogeneous and isotropic material is present between the polarizers, very little light reaches the observer or the recording device. In contrary, when an anisotropic and/or inhomogeneous material is placed between the polarizers, birefringence causes a slight rotation of the axis of light polarization. Light traveling through the sample, encounters two (or more) refractive indices. It therefore splits into two parts: one part is resolved onto an ordinary direction (ordinary ray), the other is resolved onto an extraordinary direction (extraordinary ray). These parts travel with different velocities due to their different refractive indices. The overall wave of light emerging from the crystal is different from the incident one, and there is some component of the wave parallel to the analyzer. Therefore, some light may pass through, which can be observed or registered. The regions where birefringence occurs (in defective sites of an isotropic material), appear as bright areas, whereas the strain-free regions are dark.

**Results and discussion** Figure 4.9 shows birefringence images of nine scCVD diamonds recorded with a digital camera using crossed-polarizer light microscopy. The size of the individual images corresponds to the samples areas of  $3\text{-}5 \times 3\text{-}5 \text{ mm}^2$ . Almost no strain is visible for the samples of the bottom row, indicating isotropic material with perfect bulk quality, whereas for the rest of the samples the homogeneous dark area is interrupted by spots of strongly fluctuating birefringence. In particular, for the samples of the top row, the bright strained areas are rather intensive.

In Figure 4.10 the correlation between 'white-beam' X-ray topographs and the birefringence images of the sample s256-02-06 and SC14BP are presented.

It is obvious that the extended structural defects as well as bundles of dislocations, which are visualized in the X-ray topographs, correlate with high strain fields causing birefringence. The cross-like characteristic dark lines surrounded by bright areas (strain) in the birefringence images, correspond to the bundles of threading dislocations visible in the X-ray topographs. The cross-polarized light microscopy can be considered as an easily accessible and fast technique allowing a pre-selection of diamond samples of superior lattice quality, which is among others helpful for detector development.

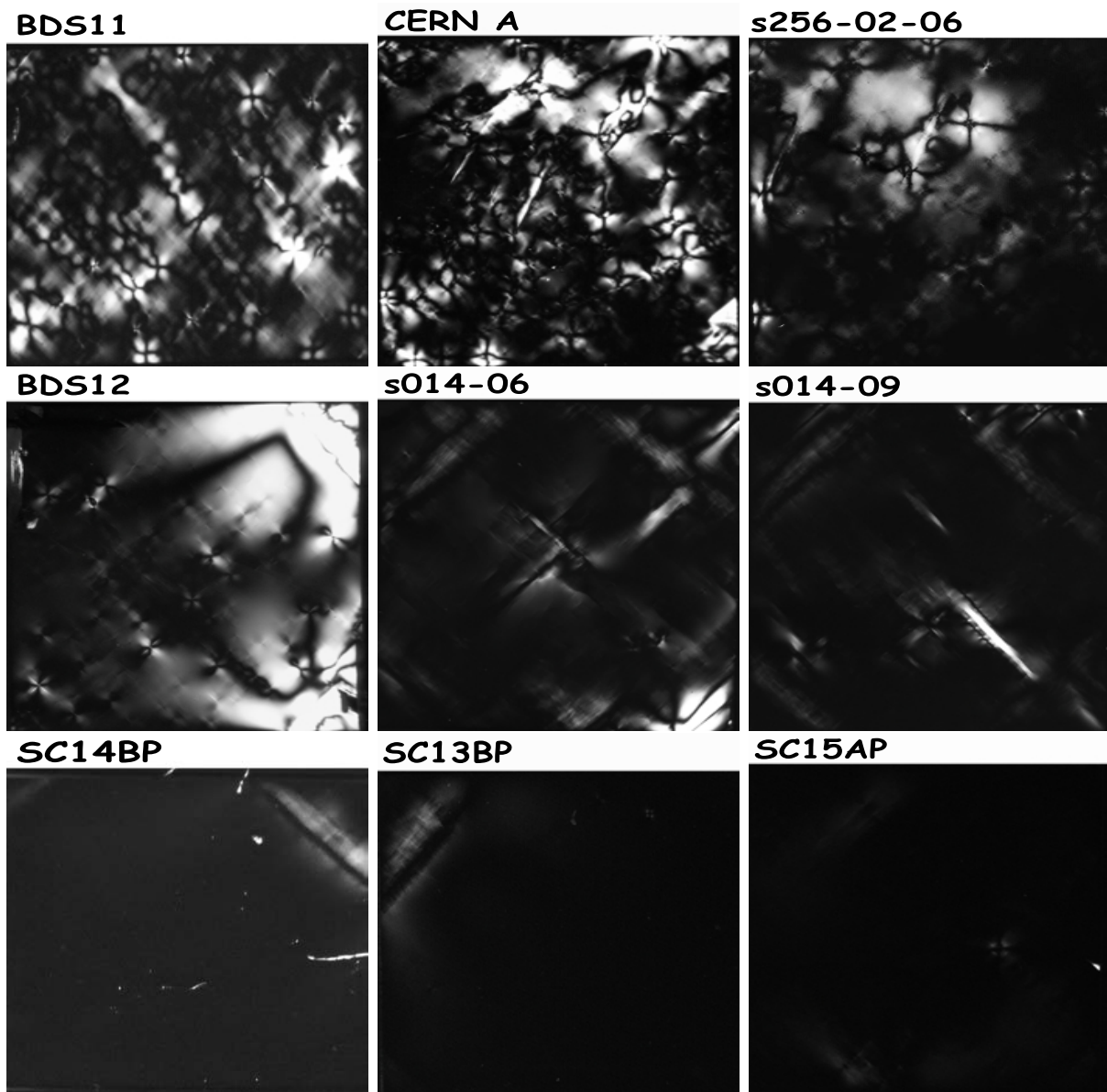


Figure 4.9: Crossed-polarizer images of nine scCVD diamonds. The size of the individual images corresponds to the full sample area  $3\text{-}5 \times 3\text{-}5 \text{ mm}^2$ .

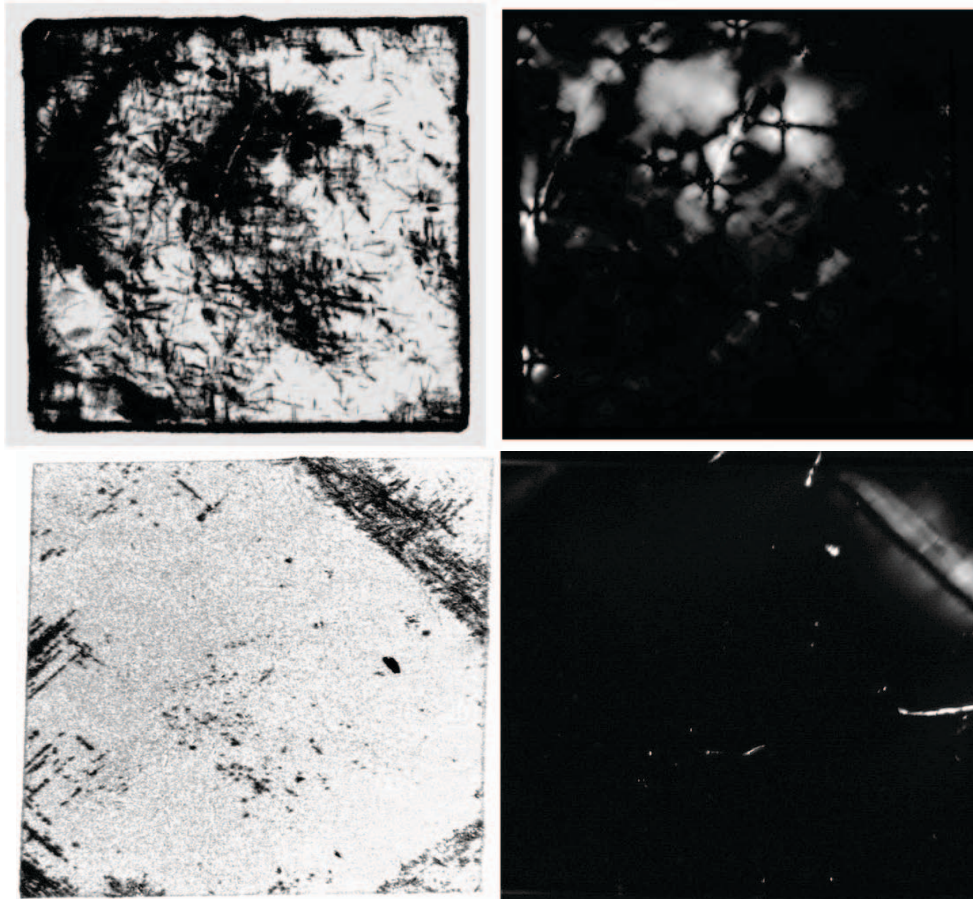


Figure 4.10: Correlation between X-ray topographs and birefringence pictures for samples s256-02-06 (top) and SC14BP (bottom).

## 4.4 Surface Characterization

After the crystal growth, the CVD films are separated from the HPHT substrates by laser cutting. During the last three years, the subsequent polishing of the surfaces has been performed, applying three different techniques:

- resin wheel polishing [Gri97]
- scaife polishing [Gri97]
- ion beam polishing [Han07]

Depending on the method used, the samples surfaces exhibit different morphology, which influences the properties of the electrode-diamond interface and thus diamond detector operation.

### 4.4.1 Surfaces Roughness at Sub-micrometer Scale

The surface morphology has been probed by Atomic Force Microscopy (AFM) in contact mode. Figure 4.11 shows maps of two opposite sides of an early received sample (BDS14),

which was resin wheel polished. Two surfaces (A, B) of different morphology were observed, where side A shows terrace-like structures of  $\sim 1.4$  nm (rms) roughness and side B an amorphous view of  $\sim 6$  nm (rms) roughness. It is known [private communication with the producer] that during resin-wheel or scaife polishing, the samples are brazed to the sample holder and have to be removed chemically afterwards. Thus consequently, one side of the samples remains amorphous and of the roughness limited by this procedure. The different surface structure, results in different electrical properties of the detectors electrodes (Chapter 6).

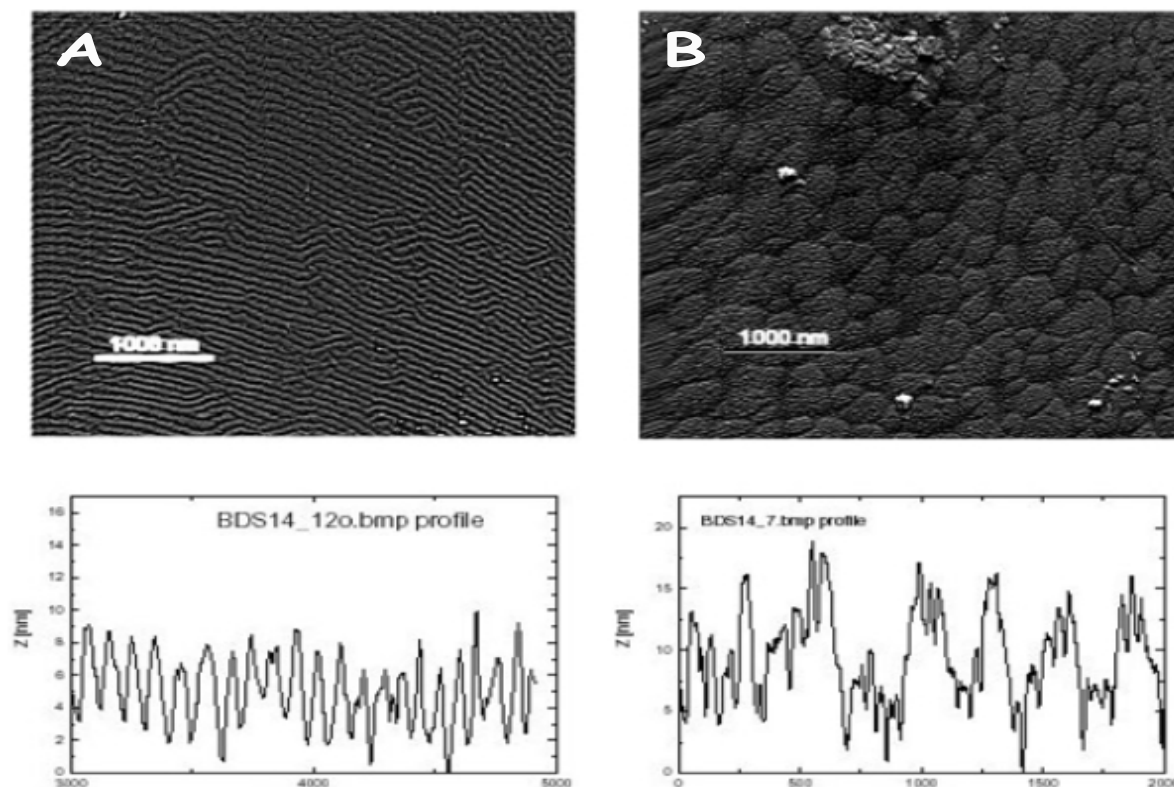


Figure 4.11: (Top) A typical example of the surfaces morphology of a resin wheel polished scCVD (BDS14) measured by AFM in contact mode. (Left panel) polished side A, (Right panel) brazed side B. (Bottom) The corresponding roughness profiles.

Figure 4.12 shows the surface morphology of a scaife polished sample with a characteristic parallel-groove scarring of a roughness of about 2 nm (rms). Similar to the resin wheel polished samples, an amorphous surface morphology has been obtained for the opposite side, indicating also in this case the sample brazing to the sample holder. In contrast, the ion beam polishing technique results in almost atomically flat surfaces of  $> 0.5$  nm (rms) roughness. A typical AFM topograph of an ion beam polished sample (SC8BP) is shown in Figure 4.13.

#### 4.4.2 Macroscopic Morphology of the Surfaces

Figure 4.14 shows optical microscopy images of the resin wheel polished sample BDS14 after 10 minutes of annealing at 600 °C in air. In a low magnification image, line scratches

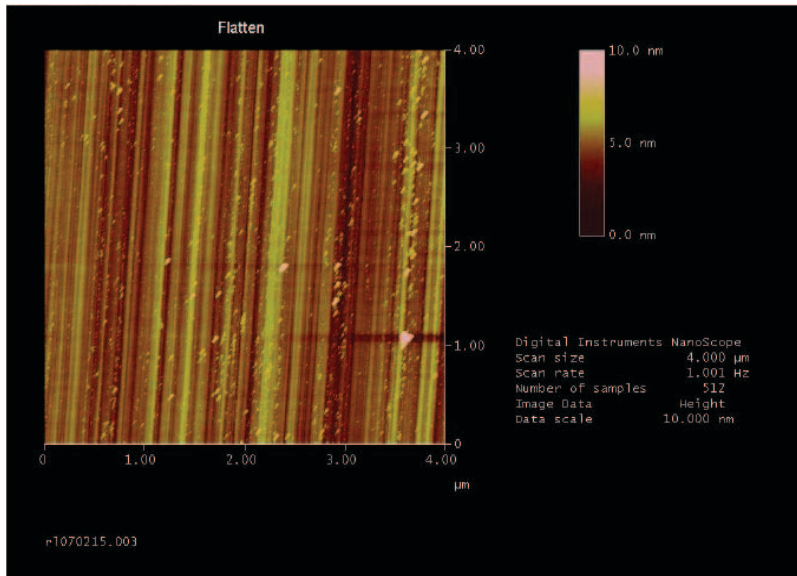


Figure 4.12: A typical example of the surface morphology of a scaife polished scCVD diamond measured using AFM in contact mode (courtesy R. Lovrincic).

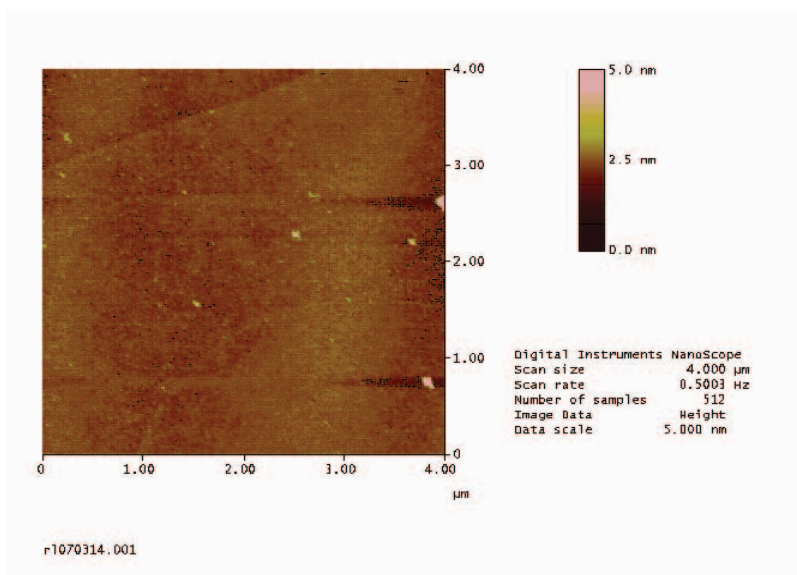


Figure 4.13: A typical example of the surface morphology of an ion beam polished scCVD diamond measured using AFM in contact mode (courtesy R. Lovrincic).



are visible. Zooming in, the structure of the scratches appears as crescent shaped indentations. The depth of indentations has been estimated in the range from  $1\ \mu\text{m}$  to a few micrometers. These indentations are known to correspond to impact damage arising from the diamond grit being released from the resin wheel during the polishing process. Curiously, it appears only after annealing due to an erosion process. Such defects have been found on all early resin wheel polished samples. Possible effects on the diamond-detector operation are discussed in Chapter 6.

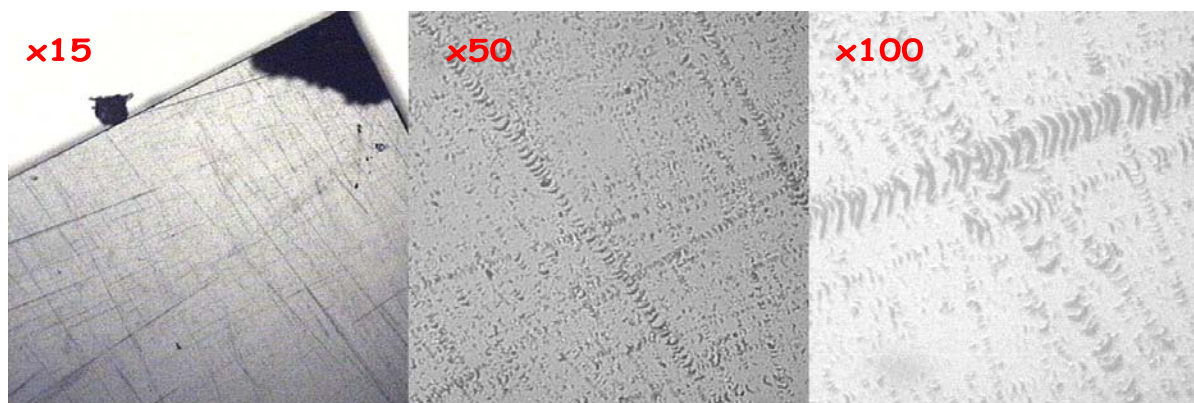


Figure 4.14: The defective diamond surface showing crescent indentations, the result of resin wheel polishing process (see text). The defects reveal after annealing at  $600\ \text{°C}$  in air.

## 4.5 Summary of the Crystal Quality Study

The investigated samples show extremely low concentration of nitrogen ( $\text{N}^0 \leq 10^{14}\ \text{cm}^{-3}$ ) and boron ( $\text{B}^0 \leq 10^{15}\ \text{cm}^{-3}$ ) related defects. According to the official classification of diamond, E6 scCVD samples can be assigned to the ultra-high purity type IIa diamonds.

Due to the reproducibility of the CVD technique, this impurity level is expected to be typical for all samples supplied by this producer. In 2007, E6 officially started to offer so called 'electronic grade' scCVD films of nitrogen concentration  $< 5\ \text{ppb}$  and boron concentration  $< 1\ \text{ppb}$  concentration [e6].

In contrast to the atomic purity of the crystals, the 'white beam' X-ray topography has revealed microscopic structural defects in almost all tested samples. Isolated bundles of threading dislocations and extended defects are the main forms of structural micro-defects, which introduce high-strain fields, visualized by cross polarized light microscopy. The defects originate from the defective surfaces of the HPHT diamond substrates. Depending on the polishing method, diamond surfaces exhibit various characteristics. Surfaces of resin wheel polished samples are rough ( $6\ \text{nm}$  (rms)) and highly defective. On a macroscopic scale, the defects appear as submicroscopic indentations. Two different types of surfaces are found, due to the sample mounting during the mechanical polishing, which may result in out-of-control electrode-diamond properties. Ion beam polishing avoids such an asymmetry in the surfaces morphology. Here, almost perfect, atomically flat surfaces of  $\leq 1\ \text{nm}$  (rms) roughness are achieved on both sides of the samples.

# Chapter 5

## Detector Preparation

Compared with silicon technology, the fabrication of a diamond detector is a relatively easy task. The high resistivity of intrinsic CVD diamond eliminates the need for a reverse-biased junction as well as the associated material doping to suppress thermally generated currents. Theoretically, it is possible to obtain an active device with extremely low leakage currents, by simply applying metal electrodes to the diamond surfaces.

### 5.1 Cleaning Procedure

The post processing of CVD diamond films after growth introduces surfaces contamination. For instance, laser cutting of CVD diamond surfaces introduces graphitic phases. Also, due to a highly polar surface (both, hydrogen and oxygen terminated), diamond is rapidly polluted by airborne contamination or hydrocarbons which are strongly bonded to the surface. Frequently, during the CVD process, surfaces are exposed to hydrogen plasma at the end of the growth, aiming to smooth the surfaces [Tok06]. Such a treatment results in hydrogen termination of the surface which is known to be p-type conductive in ambient atmosphere, and can be described by the electrochemical transfer doping model [Neb04]. Both, the graphite contamination and the hydrogen termination lead to undesirable surface leakage currents. On the other hand, oxygen-termination provides a strongly insulating diamond surface [Tac05], as required for particle detectors. To remove surface contaminations and to oxidize the samples, the following wet chemical cleaning protocol is performed before the electrodes deposition:

1.  $3 \text{H}_2\text{SO}_4 + 1 \text{HNO}_3$  at  $260 \text{ }^\circ\text{C}$  for  $\sim 30$  minutes - removal of organic impurities and partial oxidation of the surfaces;
2. a rinse with deionized (DI) water;
3.  $\text{H}_2\text{O}_2 + \text{HCl}$  at  $70 \text{ }^\circ\text{C}$  for 10 minutes - removal of metallic impurities;
4. several rinses with DI water in an ultrasonic bath, the last one at  $90 \text{ }^\circ\text{C}$ ;
5. sample drying with  $\text{N}_2$  gas;
6. exposure to oxygen plasma for 5 minutes - removal of the remaining organic impurities and final surfaces oxidation.

Directly after cleaning procedure, in order to avoid surface contamination, the samples are packed into sealed PCV tubings and stored in ambient conditions until metallization.

## 5.2 Electrodes Fabrication

Circular pad electrodes or quadrant electrodes with inter spacing of  $\sim 140 \mu\text{m}$  (Figure 5.1 (Right panel)) are sputtered in parallel plate geometry onto the diamond surfaces using the magneto-sputtering method at the Target Laboratory of GSI.

Double-sided shadow stainless steel masks are used, allowing the metallization of both sides without interruption of the vacuum. Figure 5.1 (Left panel) shows the sample holder with a set of shadow masks. In order to remove possible surface contamination during the samples handling, before metal deposition the non-shadowed diamond surfaces are exposed to the glow discharge in argon plasma in the sputtering apparatus.

Different metals were applied, aiming to check the influence of the metal-diamond interface on the diamond detector operation. Finally, two types of diamond electrodes were chosen for standard detector metallizations:

- Al(100 nm) not annealed electrodes
- Cr(50 nm)-Au(100 nm) post-annealed at  $550 \text{ }^\circ\text{C}$  in argon atmosphere

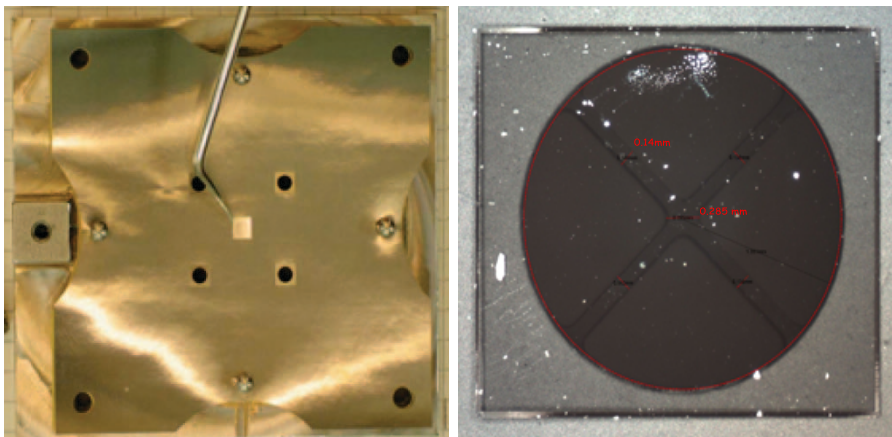


Figure 5.1: (Left panel) Double-sided shadow mask used for sputtering or evaporation of metal electrodes on diamond surfaces. Various motives can be sputtered with  $100 \mu\text{m}$  minimum spacing. (Right panel) A scCVD diamond metallized with a quadrant motif electrode made by Al(100 nm) sputtering.

Figure 5.2 (from left to right) illustrates the detector fabrication process. A raw scCVD diamond after the cleaning procedure is patterned with circular metal (Cr(50 nm) and Au(100 nm)) contacts in parallel plate geometry. The sample is glued and micro-bonded on a printed circuit board (pcb) and finally mounted in an aluminum housing. For biasing and signal read-out, a coaxial cable and SMA RF-connectors are soldered to the pcb transmission lines. The detector is then ready to use.



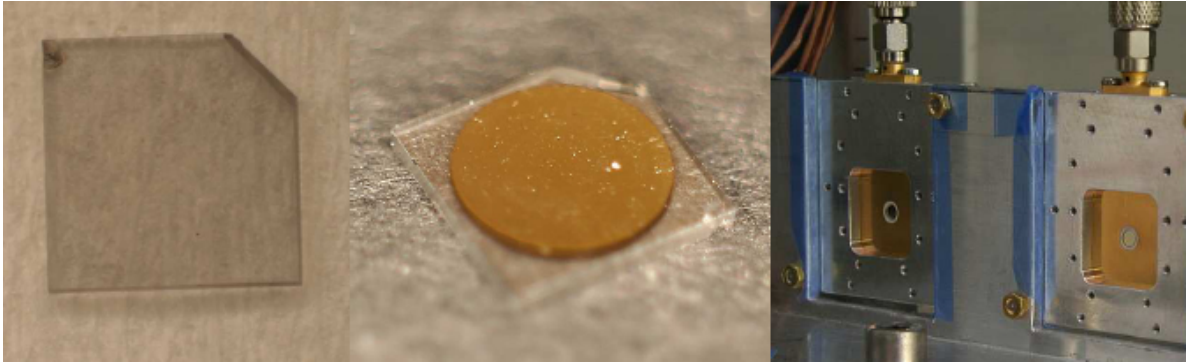


Figure 5.2: From raw diamond material (Left panel) to a ready-to-use diamond detector prototype (Right panel).



# Chapter 6

## Electronic Properties Characterization

For the optimal operation of scCVD diamonds as charged particle detector, it is important to have a detailed understanding of the charge-carrier transport as well as of the dark conductivity mechanism. This includes the determination of electron and hole drift velocities as a function of the electric field, the charge carrier lifetimes, the effective concentration of space charge in the detector bulk, as well as the dielectric strength of the film, which limits the safe range of the detector operation. In this chapter, the above parameters are directly evaluated for a wide range of applied electric fields, using the transient current technique (TCT) and measurements of the current-voltage (I-E(V)) characteristics, respectively. Using radioactive sources and low noise charge-sensitive (CS) electronics, the response of diamond detectors to 5.5 MeV  $\alpha$ -particles and to minimum ionizing  $\beta$  electrons is characterized and compared to competitive silicon detectors.

### 6.1 Dark Conductivity - I-E(V) Characteristics

According to Boltzmann statistics, the probability to find an electron at RT in the conduction band of an intrinsic, defect-free diamond (band gap 5.46 eV) as a result of thermal excitation, amounts to  $10^{-29} \text{ cm}^{-3}$ . Thus, conduction by means of intrinsic charge carrier movement is negligible. However, in the presence of crystal defects of localized energy states within the band-gap, dark conductivity may appear through defect states, e.g., by charge injection from electrodes. Shallow donor or acceptor impurities (thermally activated with low energies) causes an increase of dark current. A review of the conductivity mechanisms in defective dielectric films can be found in [Lin99].

The current-voltage (I-E(V)) characteristics is the first step in diamond-detector characterization, which allows the evaluation of the scCVD diamond dielectric strength as well as the dark conductivity mechanism. I-E(V) curves provide the definition of the safe detector operation bias range as well as a rough estimation of possible detector contributions to the electronic noise ('shot noise').

### 6.1.1 Setup and Methodology

High precision Keithley 6517 electrometers [KEI] were used to measure the leakage current of diamond detectors, typically low compared to silicon detectors.

**Parallel pad electrodes** The samples equipped with parallel pad electrodes are tested in a setup consisting of a Teflon box, containing the polarized diamond sample (Figure 6.1 top-left). The box is mounted inside an aluminum housing at ground potential. Three-pole measurements running in darkness and under dry nitrogen atmosphere avoid parasitic currents caused by humidity or air ionization and minimize distortion by electrical pick-up. To distinguish surface and bulk contributions to the measured currents, some samples were equipped with a Guard-Ring (GR) electrode at ground potential. (Figure 6.1 top-right). Thereby, surface currents are dumped to ground and may not contribute to currents into the opposing electrode kept at virtual ground. Thus only currents through the bulk of the sample do contribute.

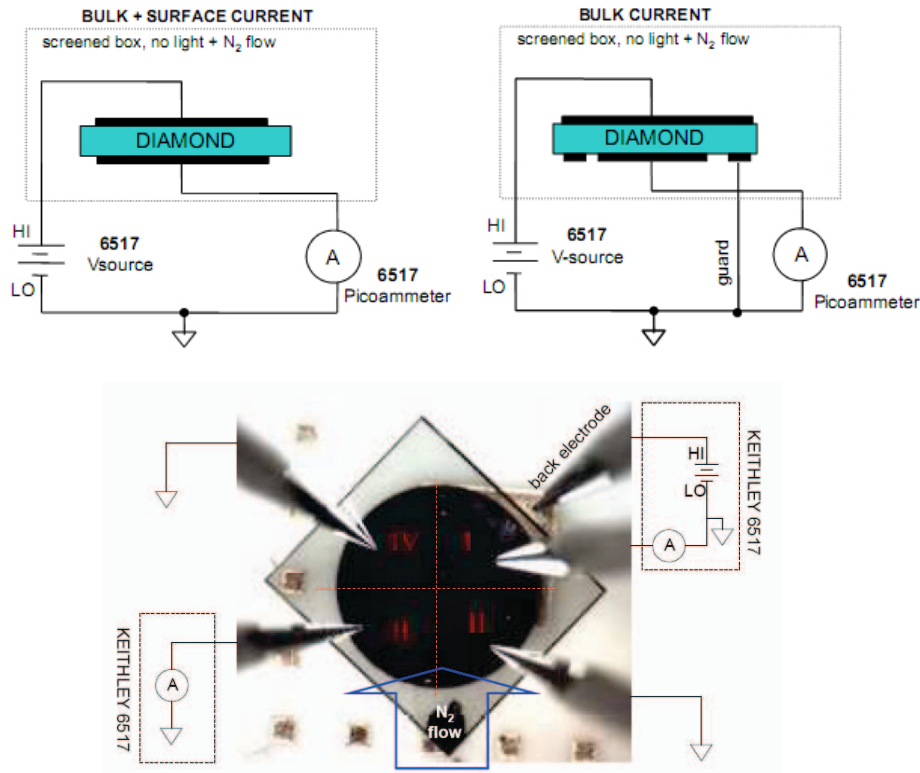


Figure 6.1: Top graphs: Setup used to probe current-voltage characteristics of pad electrodes scCVD-DDs: (Left panel) setup with sensitivity to bulk and surface currents, (Right panel) setup with sensitivity to bulk currents only. (Bottom) I-E(V) measurement configuration of scCVD-DDs, metallized with a segmented electrode.

**Quadrant electrodes** For samples metallized with a segmented electrode, a semiconductor probe station encased in a copper faraday cage was employed to measure I-E(V) characteristics on individual detector pads. Two diagonally lying quadrants are contacted

via point probes and coaxial cables to independent electrometers, while the two others are kept to ground (Figure 6.1 (bottom)). High voltage is applied to the back electrode.

**High temperature** The I-E(V) characteristics were measured as a function of temperature in vacuum of  $10^{-6}$  mbar, using a Boraelectric heater with a PID temperature controller. Temperature stability was about  $\pm 2$  °C.

**Measurement procedure** A voltage was applied to the electrodes and ramped in 10-25 V steps, cycled through a hysteresis. After each step a 2-5 minutes settling period was applied to allow measured currents to stabilize. After stabilization, the current was probed during 60 s, with 1 Hz sampling rate. Average current values per voltage step are plotted in the I-E(V) hysteresis with the standard deviation of individual measurement as error bars.

### 6.1.2 Results and Discussion

**Parallel plate geometry detectors** Figure 6.2 shows the dark-current behavior of representative scCVD diamond films from a delivery of the year 2005. The leakage current plotted as a function of the applied external electric field is normalized to the contact area. All samples in these measurements were metallized with annealed Cr(50 nm)Au(100 nm) electrodes. Persistent hysteretic behavior known from pcCVD diamond [Dir99] was found only in one out of 15 tested samples (BDS10). However, one obtained up to several orders of magnitude spread in the measured dark current for various samples. Moreover, occasionally appearing asymmetric characteristics as well as frequently an unexpected low soft-breakdown (meaning, a sudden increase in the measured current) field was found.

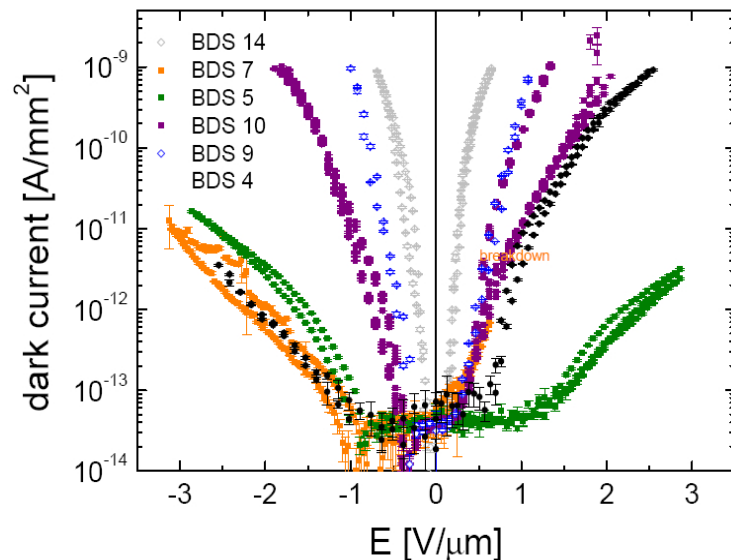


Figure 6.2: I-E(V) characteristic of six early fabricated scCVD-DDs. All samples were patterned with pad electrodes (Cr(50 nm)Au(100 nm) annealed at 550 °C ) of parallel plate geometry

To study the possible influence of surface leakage, the measurements were performed on samples equipped with a guard ring. An example is displayed in Figure 6.2 (Left panel). No significant difference in the I-E(V) characteristics was found. That indicates the diamond bulk as being the main path of leakage currents.

Several samples were re-metallized with different metal electrodes as well as with multi-layered metal electrodes. Schottky-barrier, forming metals like Al(100 nm), Au(100 nm) and Pd(100 nm), as well as reactive metals forming ohmic contacts, like Ti(50 nm) and Cr(50 nm) with a protective intermediate layer of Pt(30nm) and a top layer of Au(100 nm) were used to verify any change in detector resistivity as suggested in [Yok97]. No significant change of the dark conductivity was observed, as it is demonstrated for two scCVD samples in Figure 6.3 (Right panel).

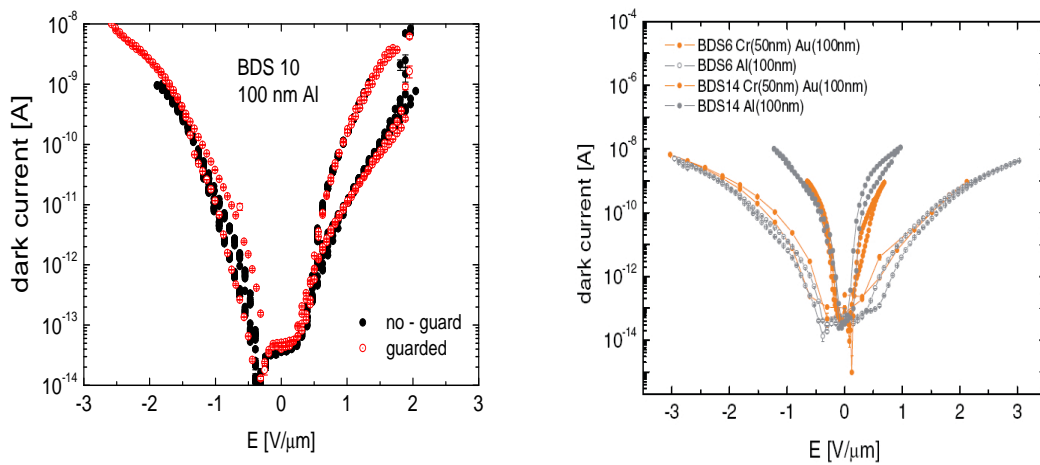


Figure 6.3: (Left panel) I-E(V) characteristics measured in the non-guarded mode (black) and in the guarded mode where surface leakage current is excluded (red). (Right panel) I-E(V) characteristics of two scCVD-DDs metallized with annealed Cr(50 nm)Au(100 nm) electrodes (yellow), and re-metallized with Al(100 nm) electrodes, respectively. No significant differences are observed.

**Quadrant electrodes** Recent samples (2007) were patterned with quadrant electrodes. The I-E(V) characteristics of four scCVD-DDs are displayed in Figure 6.4. For all samples the dark current varies significantly between different quadrants, suggesting inhomogeneous film conductivity. These samples contain a high or moderate density of structural defects, visualized as strain fields by cross-polarized light microscopy.

Figure 6.5 shows the I-E(V) characteristics of four defect-free scCVD-DDs. Here, an applied field of up to 3 V/μm yields a dark current of  $I < 0.1$  pA, which is close to the sensitivity limit of the setup. Some of these samples showed leakage currents  $I < 1$  pA up to a field of 12 V/μm.

Figure 6.6 demonstrates the correlation between defect density and leakage current for a sample of 400 μm thickness, plated with an Al(100 nm) quadrant electrode. The highest current was measured for quadrant q1, where massive structural defects are localized. Applying pixel electrodes, the origin of the significant decrease of the dielectric strength of scCVD diamond could be identified.

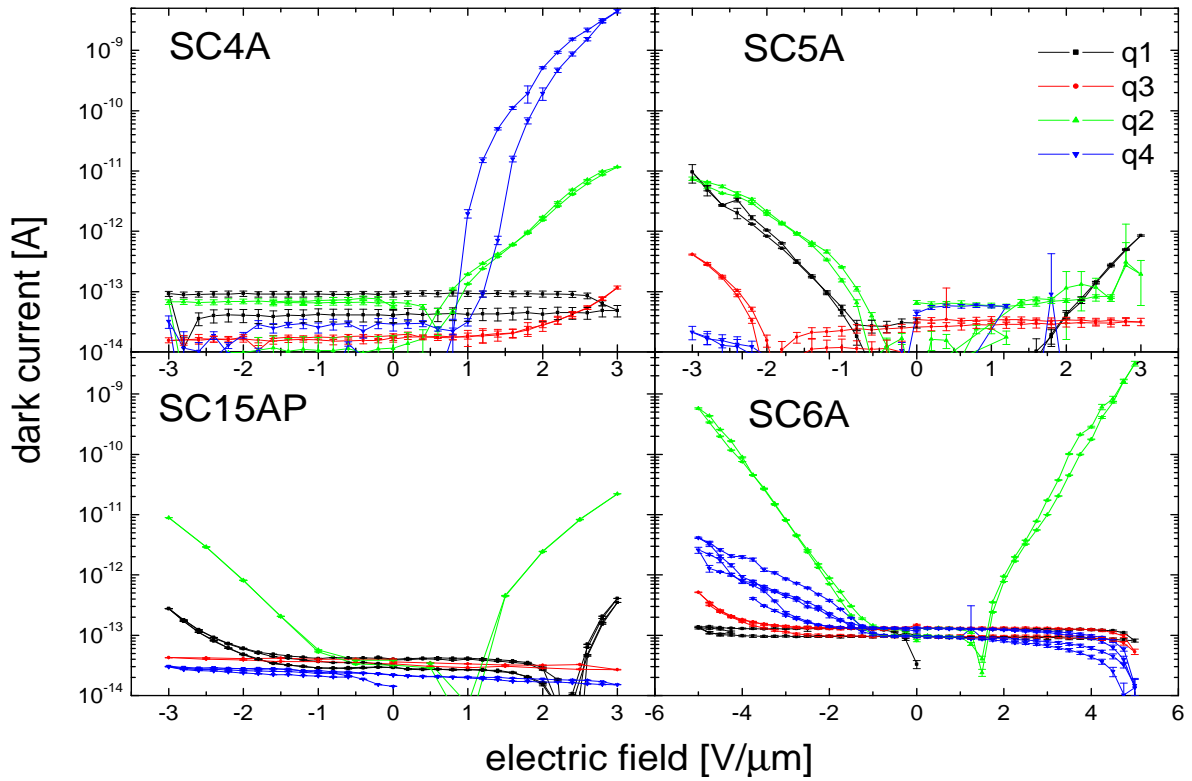


Figure 6.4: I-E(V) characteristics of scCVD-DDs plated on one side with quadrant electrodes. All four samples contain non-homogenously distributed structural defects visible in cross polarized light microscopy.

**Log-log representation** In Figure 6.7 the I-E(V) characteristics of thirteen scCVD-DDs are plotted in the log-log scale. For the majority of the samples, two regions can be distinguished: in the first the measured dark current is at the limit of the measurement sensitivity ( $I < 10^{-13}$  A), whereas in the second region soft-breakdown appears. In this region the curves can be fitted over several orders of magnitude by a single power law with an exponent  $\alpha$  ranging from 5 to 7. The coloured curves represent the I-E(V) characteristics of the samples previously tested by X-ray diffraction or/and by cross-polarized light microscopy (see Figures 4.7 and 4.9). Although the dark current of all defective samples follows a power law with similar exponent (suggesting the same mechanism of dark conductivity), the threshold electric field  $E_c$  above which soft break-down is observed, varies by two orders of magnitude. For samples with high structural defect density, the  $E_c$  is in order of only  $0.1 \text{ V}/\mu\text{m}$ , whereas samples without visible structural defects can be operated at  $10 \text{ V}/\mu\text{m}$  with leakage currents below 1 pA. In the case of the defect-free samples presented in the graph, a soft-break down appears above  $3 \text{ V}/\mu\text{m}$ . Also in this case, the slope is characterized by a power law with exponent, though exponent amounts to  $\alpha = 2.2$ .

**Electroluminescence** Figure 6.8 (Left panel) shows a photograph of a defective scCVD diamond (sample s256-02-06) during a hard breakdown ( $I > 2 \mu\text{A}$ ), revealing electroluminescence. The breakdown was induced by approaching a grounded point probe to the non-metallized top surface of the diamond, while the back electrode was kept at +400 V.

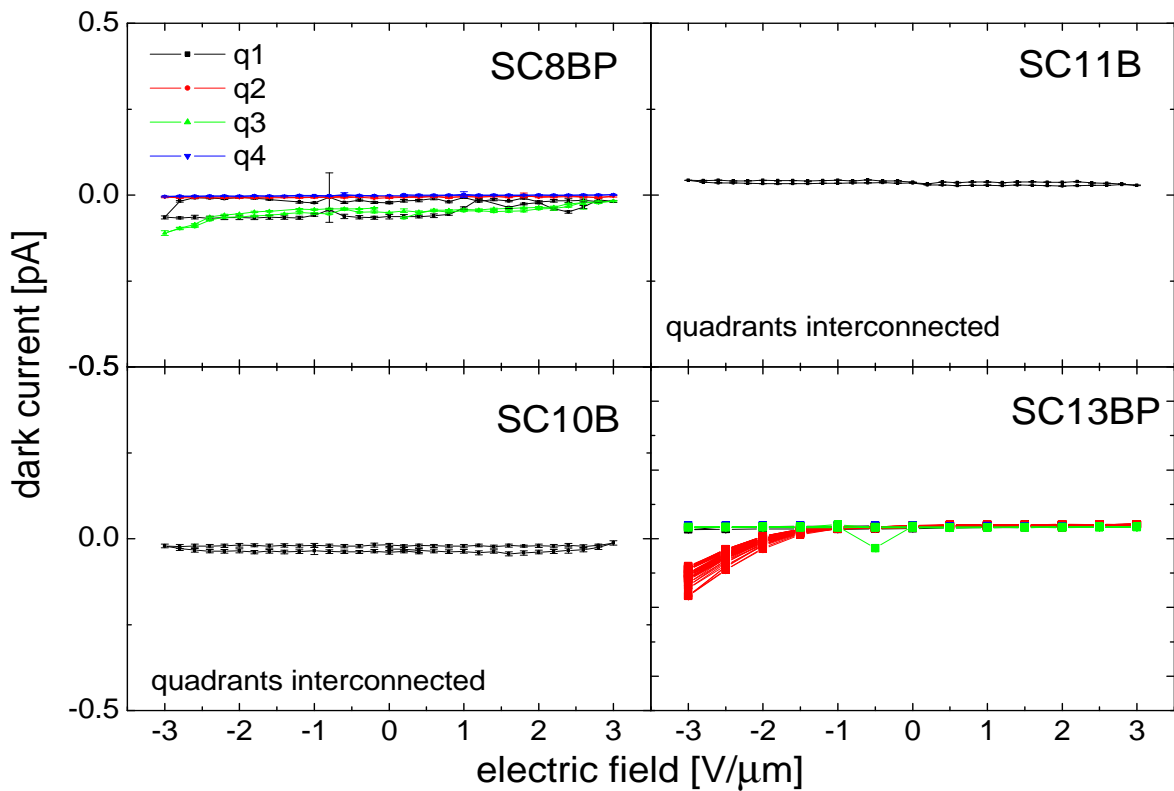


Figure 6.5: I-E(V) characteristics of scCVD-DDs plated with top quadrant electrode. Samples contain no visible structural defects as characterized by cross polarized light microscopy

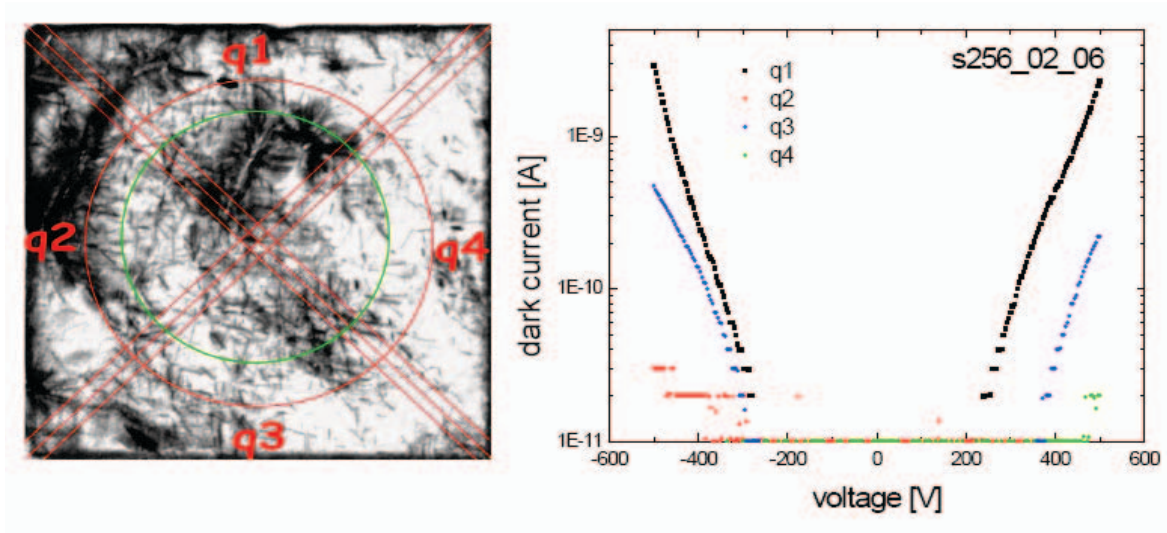


Figure 6.6: Correlation between leakage currents and structural defects of sample s256-02-06. (Left panel) The red lines mark the quadrants position on the topographic picture. (Right panel) I-E(V) characteristics of individual quadrants. A higher leakage is observed for q1 and q3, which are the regions of higher defect density.



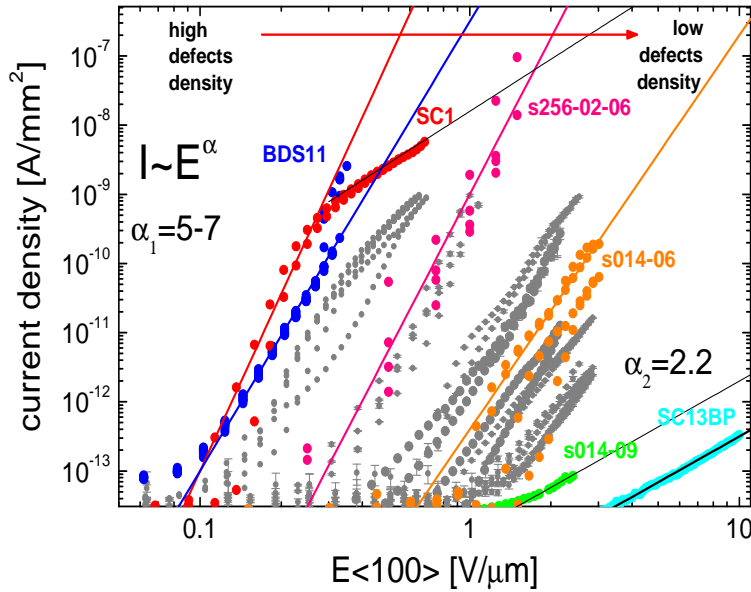


Figure 6.7: The log-log plot of the I-E(V) characteristics of thirteen scCVD-DDs. The I-E(V) characteristics of the samples previously characterized by X-ray topography or/and cross polarized light microscopy (see Chapter 4) are displayed in colour.

The observed light emission pattern matches the dislocations network of Figure 4.10. The spectrum of the emitted light (Figure 6.8 (Right panel)) was measured with a linear silicon CCD detector (Ocean Optics). The distribution of emitted light is associated with the well known band A emission, which is related to the radiative recombination of injected carriers at the dislocations [Dai01]. In order to exclude possible excitation of the defects by the UV light emission from the plasma formed in air around the point probe, the experiment was repeated in vacuum of  $10^{-6}$  mbar with the sample plated on both sides with Al(100 nm) electrodes. Also in this case, intensive blue light emission from defect sites was observed. Light emission from dislocations was observed in other two defective diamond samples, as well. In contrary, for samples (SC13BP, SC14BP or SC8BP), containing low density of structural defects, no breakdown nor electroluminescence could be induced even by as much as 10 times higher electric field applied.

**Discussion** The observed I-V characteristics in the soft-breakdown region can be described by the space charge limited current (SCLC) theory [Nes72]. The power-law behavior of I-V curves with an exponent  $\alpha > 2$  and the associated light emission is typical for double-carriers injection, which takes place via deep gap states, characterized by a Gaussian distribution of the density of states  $g(E)$  in energy [Hwa76]. Continuous band states are formed in a crystal by extended structural defects, including dislocations. Recent theoretical calculations [Fuj06, Fuj07] show that  $\langle 0\ 0\ 1 \rangle$  edge dislocations in diamond may result in band states located approximately in the mid-gap, acting as efficient radiative recombination centers. For double-carrier injection, where carrier recombination takes place, the SCLC part of the I-E(V) characteristics is expressed by a power law as a function of the applied voltage as follows [Hwa76]:

$$I = CV^{m+1} \quad \text{and} \quad m = [1 + 2\pi\sigma^2/(4k_bT)]^2 \quad (6.1)$$

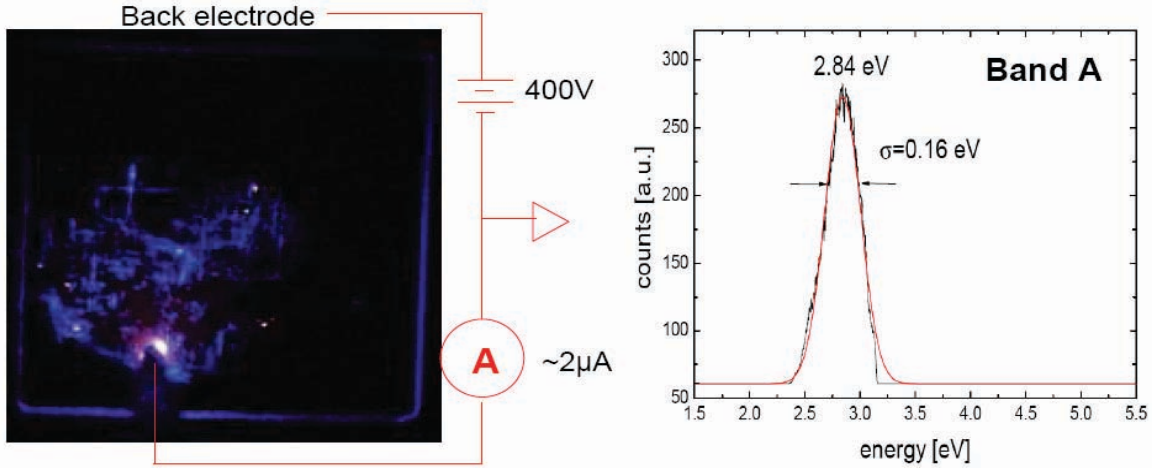


Figure 6.8: (Left panel) Electroluminescence from a defective scCVD diamond (sample s256-02-06) measured during hard-breakdown. Blue light is emitted from dislocations. (Right panel) The corresponding light emission spectrum is centered at 2.84 eV, which is known as band A emission, resulting from radiative recombination of carriers at dislocations.

where  $C$  is the pre-factor related to the defects density [Man95],  $k_bT$  is the thermal energy ( $\sim 0.025$  eV at RT),  $\sigma$  is the standard deviation of  $g(E)$ .

Fitting the experimental data with equation 6.1, the range for  $\sigma$  from 0.15 eV to 0.23 eV was obtained. This value is consistent with the width  $\sigma = 0.16$  eV of the measured band A luminescence of sample s256-02-06.

For the defect-free samples the soft-breakdown region of the I-E(V) characteristics can be fitted by a power law with exponent  $\alpha_2 = 2.2$ , which indicates a SCLC injection through defects sites of discrete energy levels, most probably atomic impurities like boron.

**Thermally activated dark current** Figure 6.9 shows the I-E(V) characteristics of two scCVD samples measured at various temperatures. From power-law fits with  $\alpha = 1$ , ohmic behavior of the applied contacts at temperatures  $T > 100$  °C may be concluded. However, if the charge-carrier transport takes place via valence band or/and conduction band, saturation of the dark current is expected at high electric field due to the decrease of the carriers mobility. Therefore, the observed non saturated linear increase of the dark current suggests charge injection through defect sites. From the Arrhenius plot of the data points in the range of 50 - 300 V, an activation energy of  $E_a = 0.37$  eV, respective  $E_a = 0.39$  eV, was obtained according to equation:

$$\sigma = \sigma_0 \cdot \exp\left(\frac{E_a}{k_bT}\right) \quad (6.2)$$

where  $\sigma$  is the current density, and  $k_bT$  the thermal energy.

In both cases, the dark current is activated with approximately the same energy before soft-breakdown occurs. The obtained values of  $\sim 0.37 - 0.39$  eV suggest an ionization of boron acceptors. Several groups have found similar  $E_a$  values for scCVD and pcCVD diamond detectors analyzing the experimental data with various thermal de-trapping methods [Lo07a, Tan02, Mar03, Wan06]. The obtained result are matches the material properties presented in the previous chapter, where the nitrogen content of E6 samples was below

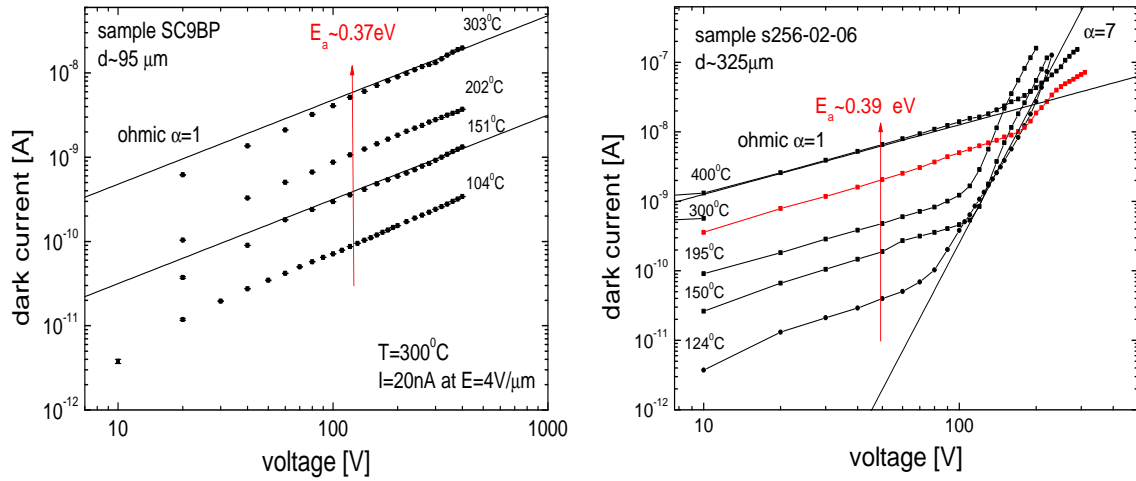


Figure 6.9: Dark conductivity at different temperatures of two scCVD-DDs as a function of applied bias. The activation energy of 0.37-0.39 eV indicates boron acceptor ionization.

the detection limit ( $N^0 < 10^{14} \text{ cm}^{-3}$ ) of the ESR, whereas the boron contamination of  $B^0 \sim 10^{15} \text{ cm}^{-3}$  was still detectable. This suggests a residual p-type conductivity of scCVD samples due to uncompensated boron acceptors.

Although the activation energy is relatively low, the measured absolute dark current for the non-defective sample SC9BP at  $4 \text{ V}/\mu\text{m}$  and  $300^\circ\text{C}$  do not exceed 20 nA, hence operation of scCVD-DDs at high temperature appears feasible. Moreover, as indicated by the red curve in Figure 6.9 (Right panel) the dark current at SCLC region of the I-E(V) characteristics of the defective sample s256-02-06 decreases above  $300^\circ\text{C}$ .

**Conclusions** The dark conductivity of scCVD-DDs is clearly affected by the presence of structural defects within the diamond lattice. The measured dark current can be described by the SCLC conductivity mechanism which, in the low-bias range and at temperatures higher than  $100^\circ\text{C}$  is characterized by the ohmic behaviour. At RT the absolute value of the current for the condition  $E < E_c$  was found at the set-up detection limit, thus, the definition of the conductivity mechanism is rather difficult in this case. At a critical electric field  $E_c$ , the ohmic regime changes to the injection regime in which the current increase follows a single power law function with an exponent of  $\alpha > 1$ . For defective samples the exponent range is  $5 < \alpha < 7$ . These values are typical for SCLC injection through gap-states of Gaussian density of states. Such gap-states are most probably formed by threading dislocations, and extended structural defects, inhomogeneous distributed within the diamond bulk. For defect-free samples the exponent amounts to  $\alpha = 2.2$ , which is a typical value for SCLC injection through discrete energy levels (most probably boron impurity). The critical field  $E_c$  defining the onset of the injection regime is clearly correlated with the structural defect density. For highly defective samples,  $E_c$  is low ( $E < 0.1 \text{ V}/\mu\text{m}$ ), whereas for high-quality films, the dark current is below 1 pA at fields as high as  $E_c > 11 \text{ V}/\mu\text{m}$ . The observed electroluminescence from defective samples suggests a double-carrier injection followed by radiative recombination at the lattice defects. Its broad spectrum, ( $\sigma = 0.16 \text{ eV}$ ) centered at 2.86 eV, corresponds to the band A emission which is related to dislocations.

Although exploitation of the conductivity mechanism of dislocations may be of a great

interest for the electronic applications because of a potential 1D transport topology [Rah07], for the detector applications, defect-free crystals are required in order to obtain reproducible and stable devices operation.

## 6.2 Transient Current Technique

The transient current technique (TCT) (often called time-of-flight (ToF) technique) is the measurement of the time  $t_{tr}$  that charge carriers, created by an ionizing source, spend to cross a sample of known thickness  $d$  under the influence of an applied electric field  $E$ . TCT is widely used to investigate the charge transport properties (drift velocity, mobility, and diffusion) in the wide bandgap semiconductors for which the extremely low concentration of free charge carriers prevent the application of more conventional characterization techniques including Hall effect measurements.

### 6.2.1 Setup and Methodology

For TCT measurements the samples are mounted in the configuration of a charged-particle sensor. A schematic of the sample mounting and the irradiation geometry is displayed in Figure 6.10. The metallized sample is clamped between two glass-ceramic printed circuit boards (pcb) with holes-via providing both, the undisturbed entrance of the particles and the electrical connection of the diamond electrodes to an external coaxial connector (SMA). The connector is used for the detector biasing and signal readout. In order to prevent pickup noise, the pcb carrying the diamond is mounted inside an aluminium box at ground potential. An  $^{241}\text{Am}$   $\alpha$ -source placed above the collecting electrode is used as a single event upset generator. The pcb apertures absorb low-energy particles, excluding events on the edges of the electrodes. The measurements are performed in ambient atmosphere, minimizing the distance between the  $\alpha$ -source and the diamond surface to about 5 mm. Nevertheless, a 5.486 MeV  $\alpha$ -particle loses  $0.762 \pm 0.04$  MeV in this layer of air. Assuming a pair-creation energy of 12.86 eV/e-h in diamond [Pom05], the generated charge corresponding to the reduced  $\alpha$ -energy of 4.724 MeV amounts to  $Q_{gen} = 59.5 \pm 0.5$  fC. The value of  $Q_{gen}$  is much smaller than the product  $U_{bias} \times C_{det}$ , where  $U_{bias} > 50$  V is the applied voltage and  $C_{det} \approx 1$  pF is the detector capacitance. In this case the injected charge is too small to significantly alter the electric field in the sample. The event rate is about 20 Hz.

**Electronics** A broadband voltage amplifier of  $50 \Omega$  impedance and 2.3 GHz bandwidth (initially developed for diamond detectors [Mor01]) and a LeCroy WP7300A digital-sampling oscilloscope (DSO) (of an analogue bandwidth of 3 GHz) were used for the measurements. The detector was connected directly to the input of the amplifier. The amplifier output signal was fed via a 0.5 m coaxial cable to the DSO, and was digitized at 20 GS/s. The DC biasing high voltage was applied to the collecting electrode, as indicated in the schematic.

The capacitance of a 300  $\mu\text{m}$  thick diamond detector, plated with full pad electrodes of 3 mm diameter, was below 1 pF. However, the overall circuit capacitance including parasitic capacitances was measured to  $C_{tot} = 2$  pF at the input of the amplifier. Assuming perfect impedance matching, the RC constant of the measurement system is equal to  $\tau_{RC} = 100$  ps. The contribution of the limited bandwidth (BW) of DSO and the DBA II to the signal rise

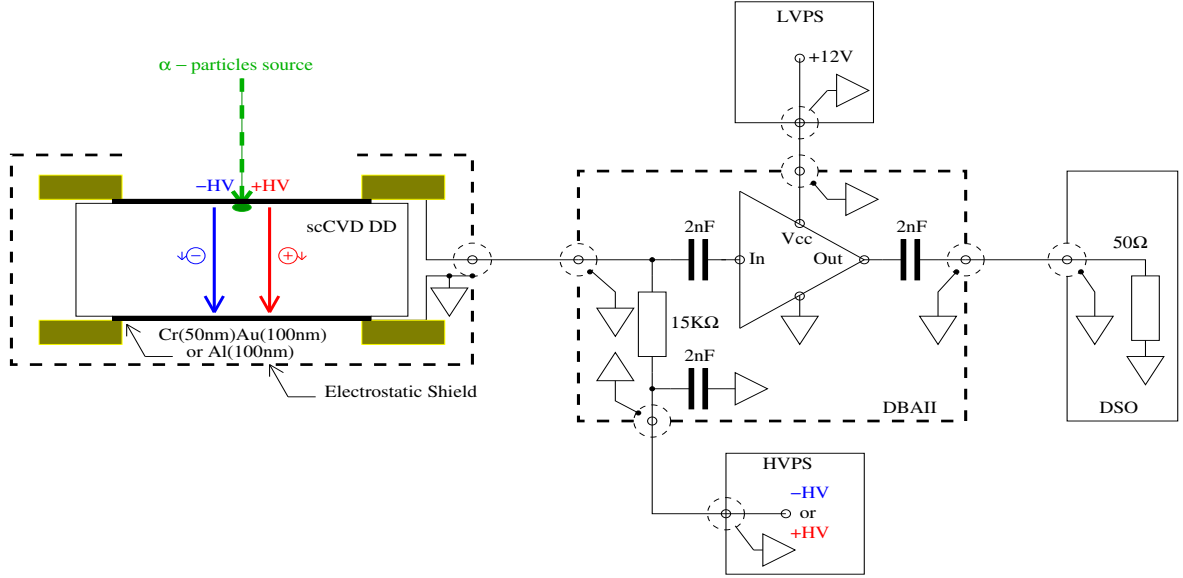


Figure 6.10: Schematic of the detector-FEE assembly used for the transient current measurements.

time ( $t_r^{10\% - 90\%}$ ) can be estimated from  $t_r^{10\% - 90\%} = 0.35/BW$ . The influence of electronics limits thus the measured rise time to approximately  $t_r^{10\% - 90\%} \approx 280$  ps.

**Waveform storage and sources of errors** The registered transient voltage signals  $U(t)$  were averaged over 20 - 100 single shots. A set of parameters of the averaged signals including, rise time  $t_r^{20\% - 80\%}$ , decay time  $t_d^{20\% - 80\%}$ , transient time  $t_{tr}$  (at FWHM), pulse area and the signal amplitude, were measured simultaneously. The standard deviation of the averaged values was used as the measurement uncertainty. The measured voltage transient signals are converted to the  $\alpha$ -particle induced current transient signals according to the formula:

$$i_{e,h}(t) = \frac{1}{R_{50}A} \left[ R_{50}C_{tot} \frac{dU}{dt} + U(t) \right] \quad (6.3)$$

where  $A$  is the gain of the amplifier ranging from 100 to 124 (individually calibrated with a pulse generator),  $R_{50} = 50 \Omega$  is the impedance of the system and  $R_{50}C_{tot} \frac{dU}{dt}$  is the signal correction due to the integrating effect of detector and the parasitic capacitances  $C_{tot}$ . The sources of errors in the TCT technique are discussed in details in [Can75]. Following this approach, the error of the drift velocity measurements in the present experiment was estimated to 5 % at low electric field ( $E < 0.3$  V/ $\mu$ m). This error is mainly due to the uncertainty in identifying the leading and trailing edges of the current pulse. For  $E > 0.3$  V/ $\mu$ m the error is about 1 %, limited mainly by the uncertainty of the sample thickness measurements.

**Methodology** The range ( $\sim 11 \mu$ m) of 4.78 MeV  $\alpha$ -particles in diamond is short compared to the typical thickness of the detectors ( $d = 300$  to  $500 \mu$ m). Hence, the carriers of one type are collected after having traveled a negligible fraction of  $d$ . The carriers of the other type, have to drift across the sample under the influence of an electric field  $E$ , with an average

velocity  $v_{dr}$  and are collected at the opposite electrode after the transit time  $t_{tr}$ . The measurement of  $t_{tr}$  at FWHM of the signals corresponds to the arrival time of the carrier cloud centroid, assuming its Gaussian distribution [Ruc68]. For the applied irradiation geometry as shown in Figure 6.10, a negative high voltage applied on the collecting electrode induces mainly electron drift, whereas for positive bias the main contribution to the signal formation have drifting holes.

According to the Shockley-Ramo theorem, charge movement induces a time-dependent current on the detector electrodes. For the parallel-plate geometry detector and assuming homogeneously distributed space charge within a scCVD-DD, the induced current is described by the simplified Equation 6.4

$$i_{e,h}(t) = \frac{Q_{gen} \cdot v(E)_{e,h}}{d} \exp^{t \tau_{eff} - t \tau_{e,h}} \quad (6.4)$$

where  $Q_{gen}$  is the generated charge,  $v(E)_{e,h}$  is the charge carriers velocity,  $d$  is the detector thickness,  $\tau_{e,h}$  denotes the lifetime of excess electrons and holes and  $\tau_{eff}$  is given by

$$\tau_{eff} = \frac{\epsilon \epsilon_0}{q \mu_{e,h} N_{eff}} \approx \frac{\epsilon \epsilon_0 t_{tr} V}{q d^2 N_{eff}}. \quad (6.5)$$

Here,  $\mu_{e,h}$  is the effective mobility of electrons or holes,  $\epsilon$  is the diamond relative permittivity,  $\epsilon_0$  is the vacuum permittivity,  $q$  is the elementary charge,  $N_{eff}$  denotes the net effective fixed space charge in the diamond bulk,  $t_r$  is the charge carriers transit time, and  $V$  is the detector bias.

According to Equation 6.4, the shape and the uniformity of the Transient-Current (TC) signals depend on the quality of the tested films. In detectors made of homogeneous monocrystalline material, where the lifetime of the excess charge is significantly longer than the transit time, the constant current is induced from each  $\alpha$ -particle hitting the detector, thus giving uniform flat-top pulses (Figure 6.11 (Left panel)). Fixed space charge on the other hand, caused by ionized impurities or trapped charge in lower-quality detectors, leads to inhomogeneous distributed build-in potentials, superimposed on the externally applied field. Depending on the net effective space charge  $N_{eff}$ , an exponential decrease or increase of the TC signals top amplitudes can be observed. An example of TCT signals affected by the negative space charge is presented in Figure 6.12. Using equations 6.4 and 6.5 a  $N_{eff} = -2.8 \times 10^{11} \text{ cm}^{-3}$  was estimated most probably produced by ionized boron acceptors.

An extreme example of the TCT are the different signal shapes as obtained from pcCVD-DD detectors (Figure 6.11 (Right panel) magenta). Due to the short lifetime of the charge-carriers and polycrystalline structure, where lattice imperfections are not homogeneously distributed, the generated charge is quenched randomly within the bulk material. In this case the limited carriers drift leads to triangular signals of various amplitudes and widths.

If a negligible amount of space charge is present ( $N_{eff} < 10^8 \text{ cm}^{-3}$ ), the internal electric field even at low external applied fields ( $E \geq 0.1 \text{ V}/\mu\text{m}$ ) is constant. Additionally, if the carriers lifetime is sufficiently long to register the trailing edge of the transient current signal, the charge carrier drift velocity can simply be calculated from Equation 6.6:

$$v_{dr} = \frac{d}{t_{tr}}. \quad (6.6)$$

If  $\tau_{e,h}$  is much longer than the transit time  $t_{tr}$ , a constant current flow is expected and Equation 6.4 reduces to Equation 6.7

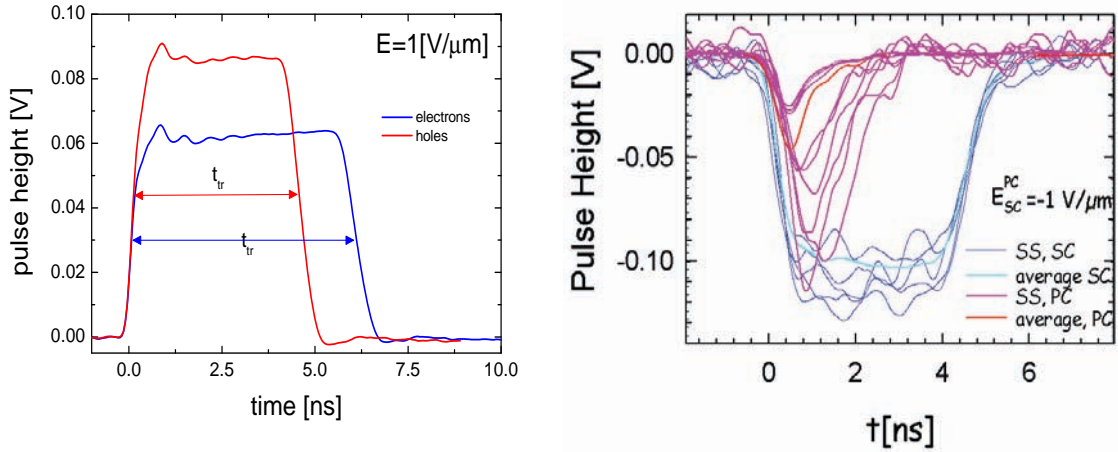


Figure 6.11: (Left panel) Averaged Transient Current (TC) signals of a scCVD diamond; drift of electrons (blue) and holes (red) measured at  $1 V/\mu m$ . The FWHM of the signals marks the transit time  $t_{tr}$ . (Right panel) A comparison between single TC signals of a pcCVD diamond (magenta) and a scCVD diamond (blue), respectively, both measured at  $1 V/\mu m$ .

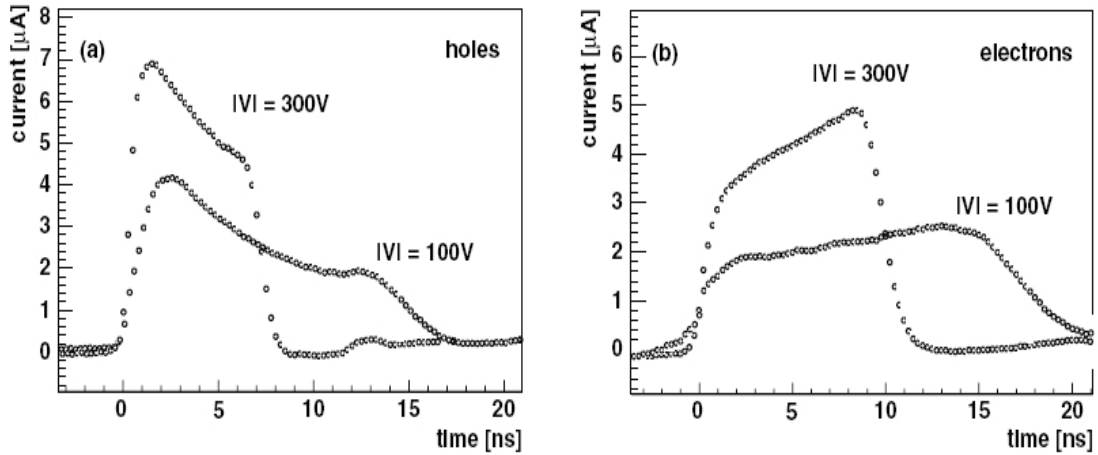


Figure 6.12: An example of TC signals of a scCVD-DD, measured for electrons (Left panel) and holes (Right panel) drift, in the presence of a negative space charge after [Per06].

$$i(t) = \frac{Q_0}{t_{tr}} = const. \quad \text{for } 0 < t < t_{tr}. \quad (6.7)$$

Note that the leading and the trailing edges are limited by the bandwidth of the electronics.

## 6.2.2 Results and Discussion

**Transient current signals at increasing electric field** Figure 6.13 shows the development of the drift-signal shape in a scCVD-DD of  $d = 480 \mu m$  at increasing detector bias. The electron-drift signals are plotted in blue (Left panel) and the hole-drift signals in red (Right panel).



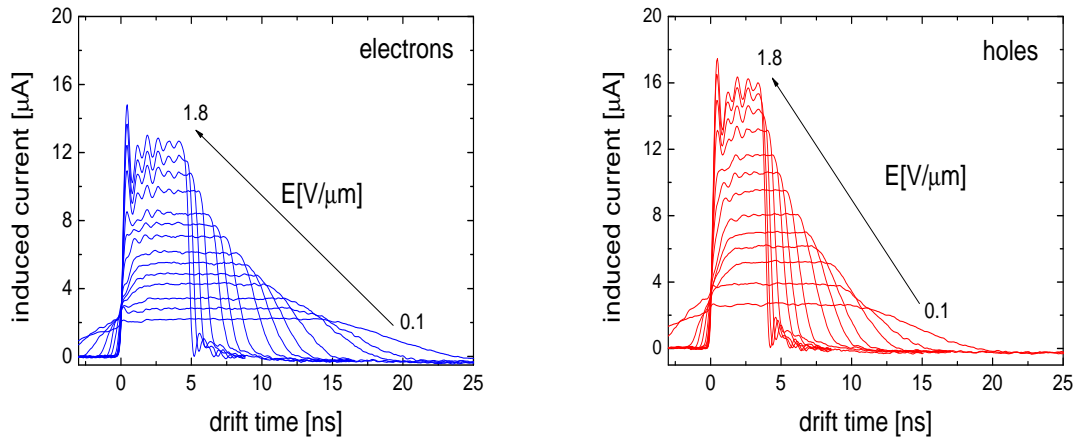


Figure 6.13:  $^{241}\text{Am}$ - $\alpha$ -induced TC signals measured at various electric fields with a scCVD-DD of  $393\ \mu\text{m}$  thickness. The electron-drift signals are shown in blue traces (Left panel) and the hole-drift signals in red traces (Right panel). The oscillations at the signals plateau are due to a weak  $50\ \Omega$  impedance mismatching.

The flat top of the signals confirms a homogeneous electric field inside the diamond bulk without detectable space charge. The lifetime of the excess charge carriers exceeds significantly the transit time. The pulse area corresponds to the collected charge  $Q_{\text{coll}}$ . Saturation to the expected  $\sim 60\ \text{fC}$  is achieved at relatively low field  $E < 0.3\ \text{V}/\mu\text{m}$ , indicating negligible charge trapping and a charge collection efficiency close to 100 %.

More than 30 scCVD samples were tested employing the TCT the obtained results were identical to those presented in Figure 6.13.

**Field dependence of the carriers drift velocity and mobility** Figure 6.14 shows the field dependence of the carriers drift velocity (Left panel) and effective drift mobility (Right panel) for electrons (blue) and holes (red) in the  $\langle 1\ 0\ 0 \rangle$  crystallographic direction. The data points were extracted from TCT measurements of 15 scCVD samples. Perfect reproducibility (within 3 %) was found for the hole drift, whereas larger dispersion (within 6 %) was determined for the electron drift. The dashed line indicates the field  $E = 1\ \text{V}/\mu\text{m}$  often considered to be the field, where the carriers drift velocity and thus the collection distance of pcCVD-DD saturates in measurements with minimum ionizing electrons [Dir99]. This is apparently not the case for scCVD-DD.

Over a wide range of the applied electric field  $E$ , the measured average drift velocity in the  $\langle 1\ 0\ 0 \rangle$  direction is lower for electrons than for holes. However for a field  $E > 10\ \text{V}/\mu\text{m}$  the electron drift velocity becomes higher than that of holes. Also at low fields  $E < 0.01\ \text{V}/\mu\text{m}$ , the velocity of electrons become higher as obtained from fit. This indicates a lower effective mass for electrons. The observed phenomenon of lower electron velocity in the range  $0.01\ \text{V}/\mu\text{m} < E < 10\ \text{V}/\mu\text{m}$  is caused by the valley repopulation effect, which results from the multi-valley band structure of diamond (Chapter 2).

An empirical formula, first proposed by Caughey and Thomas [Cau67], was used for the parametrization of the field dependence of the drift velocity and mobility:

$$v = v_{\text{sat}} \frac{E/E_c}{[1 + (E/E_c)^\beta]^{1/\beta}} \quad (6.8)$$



where  $E_c$  and  $\beta$  are fit parameters,  $v_{sat}$  - the saturation drift velocity. The effective drift mobility  $\mu_{eff}$  is the first derivative of Equation 6.8 with respect to the electric field:

$$\mu = \frac{\mu_0}{[1 + (E/E_c)^\beta]^{1+1/\beta}} \quad (6.9)$$

where  $\mu_0$  denotes the zero field mobility.

The relation between  $\mu_0$  and  $v_{sat}$  is given in Equation 6.10:

$$\mu_0 = v_{sat}/E_c \quad (6.10)$$

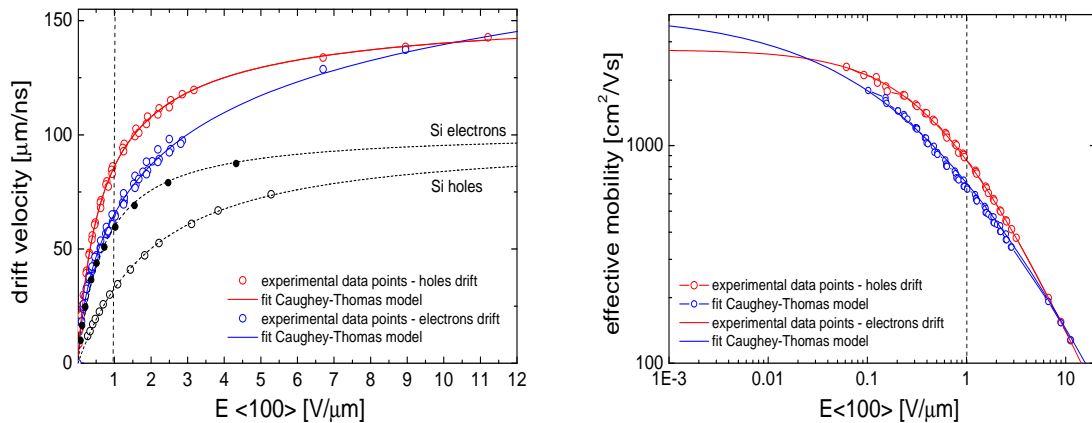


Figure 6.14: Charge carrier drift velocity (Left panel) and effective mobility (Right panel) in scCVD-DD for electrons (blue) and holes (red), drift in the  $\langle 100 \rangle$  crystallographic direction at RT. For comparison, the drift velocities in silicon [Can75] are shown (black). The data points are fitted with the empirical formulae (Equations 6.8, 6.9 and 6.10) proposed by Caughey and Thomas [Cau67].

Table 6.1 summarizes obtained parameters from fit of the experimental data with equation 6.8 (and taking into account Equation 6.10). The extrapolated low field mobility for holes ( $\mu_0^h$ ) is in good agreement with values reported recently for scCVD diamond [Per06, Tra07, Def07] and as well with theoretical calculations.

The low field mobility of electrons ( $\mu_0^e$ ) in diamond is controversially discussed in literature. The obtained value confirms the results reported in [Isb02, Per06]. However, it is almost a factor of two higher compared to the value reported by [Tra07, Def07]. The saturation velocity of both, electrons and holes, is higher than the reported values for IIA natural diamond, but in good agreement with theoretical calculations [Fer75].

The directly measured values of the effective mobilities at lowest field are for electrons  $\mu_{eff}^e = 1800 \text{ V/cm}^2\text{s}$  at  $0.1 \text{ V}/\mu\text{m}$  and for holes  $\mu_{eff}^h = 2450 \text{ V/cm}^2\text{s}$  at  $0.06 \text{ V}/\mu\text{m}$ , respectively. Experimentally measured drift velocity of electrons and holes at the highest field applied of  $11 \text{ V}/\mu\text{m}$  are equal and amounts to  $v^{e,h} = 1.43 \times 10^7 \text{ cm/s}$ .

### Drift velocity in other crystallographic directions and scattering mechanism

At present, only data from natural IIA diamond exist on this topic [Reg81] and [Nav80].

Table 6.1: Charge carrier transport parameters of scCVD-DDs obtained from fits to the experimental TCT data.

	$E_c$ [kV/cm]	$\mu_0$ [cm <sup>2</sup> /Vs]	$v_{sat}$ [cm/s]	$\beta$
<b>electrons</b>	$5.779 \pm 0.772$	$4551 \pm 500$	$(2.63 \pm 0.2) \times 10^7$	$0.42 \pm 0.01$
<b>holes</b>	$5.697 \pm 0.529$	$2750 \pm 70$	$(1.57 \pm 0.14) \times 10^7$	$0.81 \pm 0.01$

holes  $R^2 = 0.999$ , electrons  $R^2 = 0.998$

Due to the  $\langle 1\ 0\ 0 \rangle$  orientation of the available CVD diamond films, measurements of the carriers drift velocity in other crystallographic directions were not possible.

Figure 6.15 shows a comparison of the drift velocity of scCVD diamond in the  $\langle 1\ 0\ 0 \rangle$  direction (colour curves) and of natural IIa diamond in the  $\langle 1\ 0\ 0 \rangle$  and the  $\langle 1\ 1\ 0 \rangle$  directions, all measured at RT. Anisotropy is clearly visible with an up to 20 % higher  $\langle 1\ 1\ 0 \rangle$  drift velocity for electrons and about 15 % lower drift velocity for holes. The drift velocity in  $\langle 1\ 1\ 1 \rangle$  direction was studied only theoretically. The results indicate yet 3 % higher values for  $\langle 1\ 1\ 1 \rangle$  over these of the  $\langle 1\ 1\ 0 \rangle$  direction.

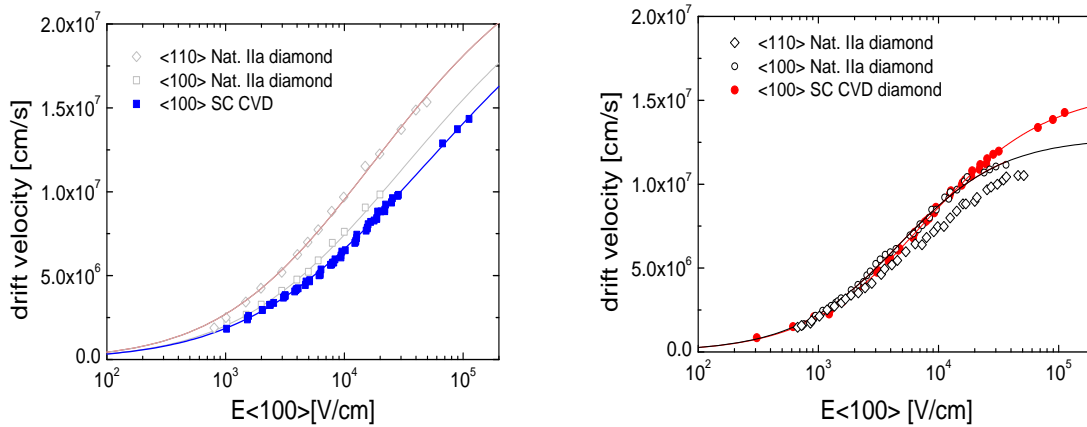


Figure 6.15: (Left panel) Electron and (Right panel) hole drift velocity as a function of the electric field in single crystal diamond measured at RT. Open symbols refer to experimental data measured along the  $\langle 1\ 1\ 0 \rangle$  and the  $\langle 1\ 0\ 0 \rangle$  crystallographic direction in IIa natural diamond [Nav80, Reg81], whereas colour full symbols refer to the drift velocity measured along the  $\langle 1\ 0\ 0 \rangle$  direction in scCVD diamond.

The carriers scattering mechanism in scCVD diamond has been studied recently by [Isb05] and [Tra07] as a function of temperature using the TCT method. In both references only acoustic phonon scattering has been observed as a main source of carriers scattering up to 400 K, indicating the high purity of the tested material.

In presence of acoustic phonon scattering, the drift velocity  $v$  of charge carriers as a function of the electric field can be expressed by a simplified model [Sze81]:

$$v = \mu_0 E = \sqrt{T/T_c} \cdot \mu_0 \cdot E \quad (6.11)$$

where  $\mu_0$  is the low field mobility,  $T$  is the temperature in  $K$  and  $T_c$  is the effective temperature of the carriers as a function of electric field  $E$ . This dependence can be written

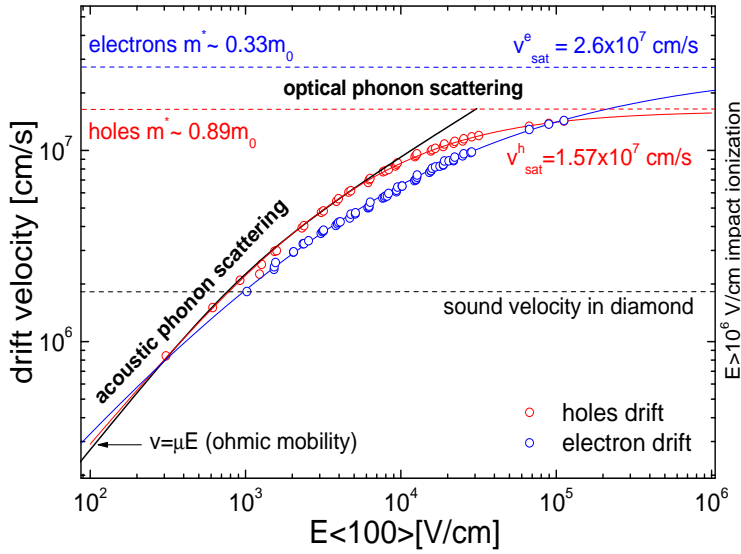


Figure 6.16: Field dependence of the charge carriers drift velocity in scCVD-DD along the  $\langle 1\ 0\ 0 \rangle$  crystallographic direction. The scattering mechanisms are indicated in the graph. The hole drift velocity at a field below  $E_c = 5.7$  kV/cm follows a simple acoustic phonon scattering model (black curve).

as [Sze81]:

$$T_c = \frac{T}{2} \left( 1 + \left[ 1 + \frac{3\pi}{8} \left( \frac{\mu_0 E}{c} \right)^2 \right]^{0.5} \right) \quad (6.12)$$

where  $c = 1.82 \times 10^6$  cm/s is the sound velocity in diamond.

In Figure 6.16 the hole-drift data are fitted with this simple model of acoustic phonon scattering, using the mobility value extracted from the data fit of Figure 6.14 ( $\mu_0 = 2750$  cm<sup>2</sup>/Vs). The model describes the behaviour of the drift velocity quite precisely up to a field  $E_{opt}$  for which onset of optical phonon scattering is expected. The electron-scattering mechanism is more complicated due to the multi-valley band structure and the associated inter-band scattering. Thus, even for relatively low fields the simple acoustic phonon model cannot be applied for the electron drift. The description of the electric field dependence of electron and hole drift in the full measured range, requires a more sophisticated approach, which includes detailed knowledge of the band structure and of the phonon dispersion curves in diamond [Nav80, Wat04].

The drift velocity saturation at high electric field in covalent semiconductors occurs due to optical phonon scattering and is described by equation [Fer82]:

$$\nu_{sat} = \sqrt{\frac{8E_{opt}}{3\pi m^*} \tanh(E_{opt}/2kT)} \quad (6.13)$$

where  $E_{opt} = 0.163$  eV is the energy of the longitudinal optical phonon (LO) in diamond,  $m^*$  is the density of states effective mass of the charge carriers in diamond, and  $\tanh(E_{opt}/2kT) \approx 1$  at RT.

Using equation 6.13 and the extrapolated saturated drift velocities, the density of states effective masses for holes and electrons were estimated to  $m_e^* = 0.33m_0$  and  $m_h^* = 0.89m_0$ , respectively.

**Longitudinal diffusion** When a plane of carriers created at the vicinity electrode by an ionization process drifts across the sample, the carriers will diffuse because of the concentration gradient. Upon their arrival at the opposite electrode, the plane of carriers will be

substantially thicker than at the entrance electrode. Assuming that the density distribution of the plane of carriers produced by  $\alpha$ -particles is Gaussian, the longitudinal diffusion coefficient  $D_l$  can be obtained from the difference between the fall time and rise time of the transient current pulse, by means of the equation

$$D_l = (t_d^2 - t_r^2)v_{dr}^3/21.6d \quad (6.14)$$

where  $t_r$  is the rise time and  $t_d$  the fall time of the transient current signal,  $v_{dr}$  is the drift velocity and  $d$  is the sample thickness. Derivation of equation 6.14 is presented in [Ruc68] and it is applicable when both  $R/v_{dr}$  and  $t_{gen}$  are much shorter than the fall time of the current pulse, where  $R$  is the range of  $\alpha$ -particles in diamond ( $\sim 12 \mu\text{m}$ ) and  $t_{gen}$  is the time of the carrier excitation and thermalization (order of a few picoseconds). A finite rise or fall time due to the readout electronic does not affect the evaluation of the diffusion constant, since the electronic contributions tend to cancel out of Equation 6.14. The measured diffusion coefficients for electrons and holes obtained using Equation 6.14 for two scCVD-DD are presented in Figure 6.17. Dashed lines mark the expected diffusion coefficient at low field calculated using the Einstein relation and the extrapolated values of  $\mu_0$  obtained from TCT measurements (Table 6.1). Solid curves represent  $D_l(E)$  as a function of  $E$  obtained from the Einstein relation using the measured effective mobility  $\mu_{eff}$  (Figure 6.14 (Right panel)). As it can be seen, the measured  $D_l$  tends to decrease with  $E$  as predicted, but it cannot be well described by the Einstein relation. At high fields, a modified Einstein relation should be used instead:  $D_l(E) = 2/3\mu_{eff}(E) \langle \epsilon \rangle / q$ , where  $\langle \epsilon \rangle$  is the mean carrier energy as a function of  $E$ . Although the distribution of  $\langle \epsilon \rangle$  is not known, one can see that it is higher than  $kT$  at RT (0.025 eV), indicating 'hot' charge carrier transport in the measured range of  $E$ .

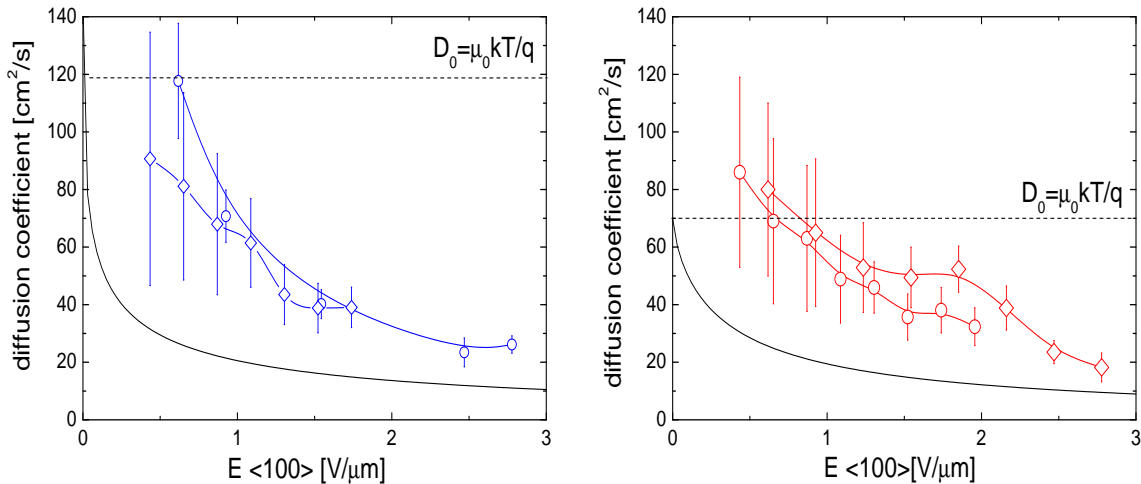


Figure 6.17: Longitudinal diffusion coefficient of electrons (Left panel) and holes (Right panel) in scCVD-DD at RT as a function of electric field  $E$ . Dashed lines mark the diffusion coefficient  $D_0$  at low field calculated from the Einstein relation and using an extrapolated values of low field mobility  $\mu_0$ . Solid curves mark the diffusion coefficient  $D_l(E)$  calculated from the Einstein relation using the measured effective mobility  $\mu_{eff}$ .

**Numerical simulation of the transient current signals** Using the 3D semiconductor device modeling software EVEREST [EVE], transient current signals induced by an  $\alpha$ -particle in a parallel plate diamond detector were simulated by solving numerically the coupled drift-diffusion and Poisson equations. Details on the simulation geometry, boundary conditions and input parameters can be found in the Appendix. The fit parameters obtained from the experimental drift velocity data were used as an input in the simulation. Figure 6.18 (Left panel) shows the intrinsic induced current signals at various biases applied to a  $320 \mu\text{m}$  thick detector; note the log scale of the time axis. The first bump corresponds to a fast collection (200-100 ps in the presented bias range) of one type of carriers. Subsequently, a constant current flow is observed, corresponding to the drift of  $e/h$  across the sample. On the right, intrinsic induced current signals were filtered through a limited bandwidth of  $\tau_{RC} = 100$  ps (thick curves), which corresponds to the experimental conditions. The simulated signals are compared to the measured TC signals of a  $320 \mu\text{m}$  thick scCVD-DD (thin curves). Perfect reproducibility can be observed in bias range employed.

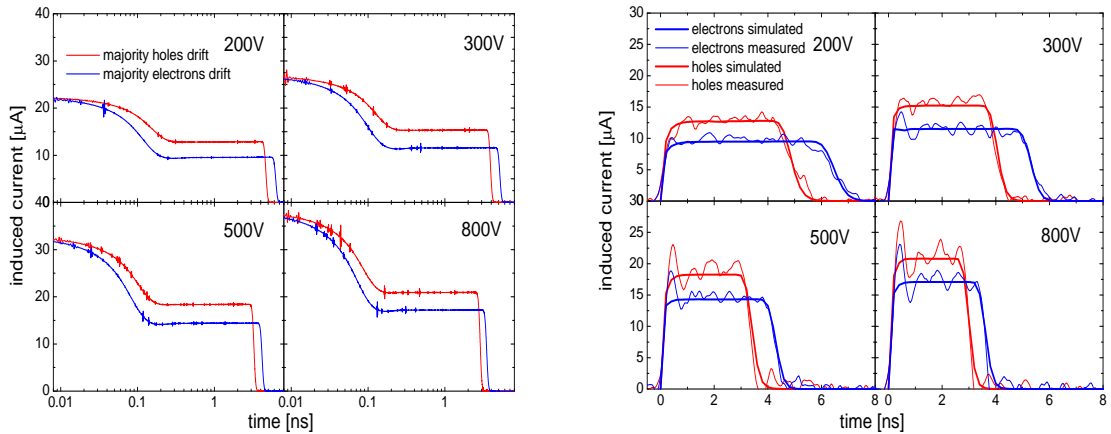
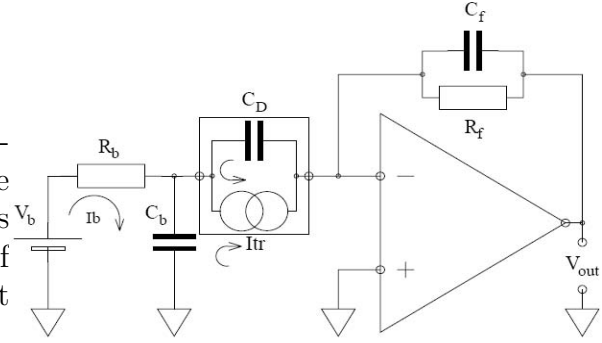


Figure 6.18: Simulated and measured transient current signals induced by  $\alpha$ -particle injection in a  $320 \mu\text{m}$  thick scCVD diamond detector. (Left panel) The simulated intrinsic induced current signal. (Right panel) The simulated signals, convoluted with the limited bandwidth of the setup of ( $\tau_{RC} \approx 100$  ps) and compared to the experimental curves.

## 6.3 Charge Collection Efficiency and Energy Resolution

An ultimate indicator of the detector's material quality in terms of purity and homogeneity of the crystal structure is the energy resolution  $\delta E/E$  measured with mono-energetic charged particles. This parameter is strongly related to the charge carrier lifetime and thus to the CCE [Tra69].

Figure 6.19: Schematic of the connection circuit for charged-particle detection: the charge sensitive (CS) readout. The scCVD-DD is replaced by equivalent circuits, consisting of the detector capacitance  $C_D$  fed by a current source  $I_{tr}(t)$ .



### 6.3.1 Set-up and Methodology

For high-precision energy measurements, classical charge sensitive electronics were used (Figure 6.20). The diamond detector (DD) is DC coupled to the low noise charge sensitive amplifier (CSA). The particle-induced current is fully integrated at the feedback capacitance  $C_f$  of CSA, and the output signal amplitude  $v_{out}$ -peak obeys the equation:

$$V_{out} = \frac{\int I_{tr}(t)dt}{C_f} = \frac{Q_{col}}{C_f} \quad (6.15)$$

The amplitude  $V_{out}$  is here a direct measure of the particle-induced charge, and - in case of complete charge collection - of the deposited energy as well.

The energy output of the CSA is fed to a shaping amplifier (SHA) and the shaped signal is digitized by a peak sensing amplitude-to-digital converter (ADC) (Silena 4418/V, 13 bit). The timing output of the CSTA2 is amplified by a timing filter amplifier (TFA) which is discriminated by a discriminator (DISCR) at lowest possible amplitude threshold. The DISCR output, fed to a gate generator (GG), provides a gate for the ADC and a trigger for the data acquisition system. The data were stored on a personal computer (PC) using the CAMDA software [CAMDA]. The chain of electronics was cross-calibrated in [pC], using a high precision spectroscopic pulse generator and a commercial PIN diode silicon detector. The pair-production energy of  $\epsilon_{Si-avg} = 3.62 \pm 0.03$  eV [Owe04a, ORT94], was assumed for silicon. The noise of the system was measured to  $\sim 320$  e (FWHM). All spectroscopic measurements were carried out in a vacuum chamber at a pressure of  $\cong 10^{-6}$  mbar.

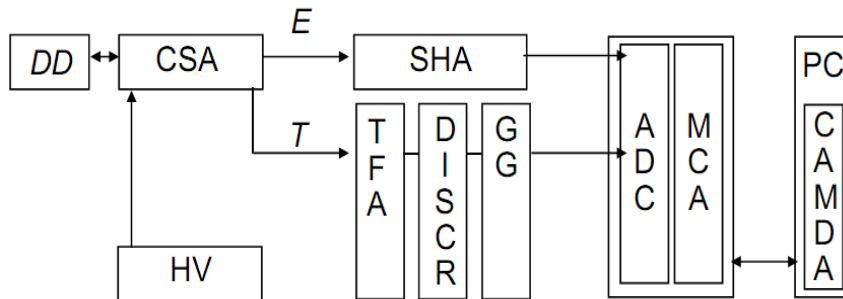


Figure 6.20: The block diagram of the electronics used for the energy loss-spectroscopy.

The measured energy resolution,  $\Delta E_{tot}$  of a detection system at energy  $E_0$  will be given by the convolution of the probability distributions of several components:

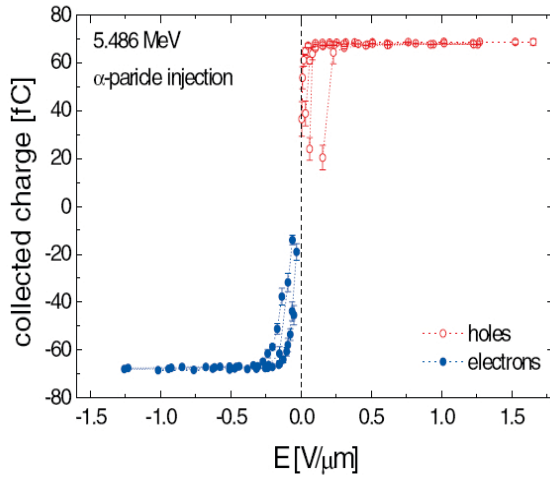


Figure 6.21: Charge collection characteristics of four scCVD-DD for a 5.486 MeV  $\alpha$ -particles measured in vacuum using CS electronics.

$$\Delta E_{tot} = f(\sigma_{loss}^2 + \sigma_{diam-intr}^2 + \sigma_{diam}^2 + \sigma_{ele}^2) \quad (6.16)$$

with  $\sigma_{loss}$  depicting the energy-loss straggling,  $\sigma_{intr-diam}$  the uncertainty introduced by intrinsic statistical fluctuations of the charge generation process in diamond,  $\sigma_{diam}$  the diamond-crystal related term, related to non-complete charge collection, and  $\sigma_{ele}$  the electronic noise contribution. Spectral lines, revealing after noise correction width in the order of the tabulated energy-loss straggling indicate thus excellent spectroscopic properties of the detector material.

### 6.3.2 Results and Discussion

Mixed-nuclide ( $^{239}\text{Pu}$ ,  $^{241}\text{Am}$ ,  $^{244}\text{Cm}$ )  $\alpha$ -spectra were recorded at different electric fields, separately for electrons and holes drift. During the continuous measurement time of more than 48 h, no decrease of the signal amplitude and no broadening of the  $\alpha$ -peaks were observed. The main line of the  $^{241}\text{Am}$  isotope (5.486 MeV) was fitted with a Gaussian. The Gaussian mean values of four detectors are plotted in Figure 6.21 versus the applied  $E$  field.

It can be observed that, the charge collection efficiency for holes drift saturates at lower field for the majority of the tested samples, suggesting that holes are less affected by trapping than electrons. However, for both drift modes, saturation occurs at relatively low field  $E < 0.3 \text{ V}/\mu\text{m}$ .

Figure 6.22 shows the measured energy spectra of the  $^{241}\text{Am}$   $\alpha$ -particles in logarithmic scale. The spectrum on the left plot was measured with a commercial  $300 \mu\text{m}$  thick silicon PIN diode, whereas the spectra in the middle and on the right plots were obtained with two scCVD-DDs of  $400 \mu\text{m}$  and  $50 \mu\text{m}$  thickness, respectively. Positive HV was applied to the collecting electrode of the diamonds (majority of holes drift). From a Gaussian fit, a FWHM of  $\delta E_{sc} = 20.5 \pm 0.6 \text{ keV}$  was obtained for the thicker diamond detector, which is comparable to the resolution of the silicon sensor ( $\delta E_{Si} = 14.5 \pm 0.4 \text{ keV}$ ). In the case of a thin diamond detector, where the trapping probability is reduced due to a shorter drift time, the energy resolution amounts to  $\delta E_{sc} = 14.7 \pm 0.2 \text{ keV}$  which is the same (within measurement uncertainty) as the measured silicon resolution at RT.



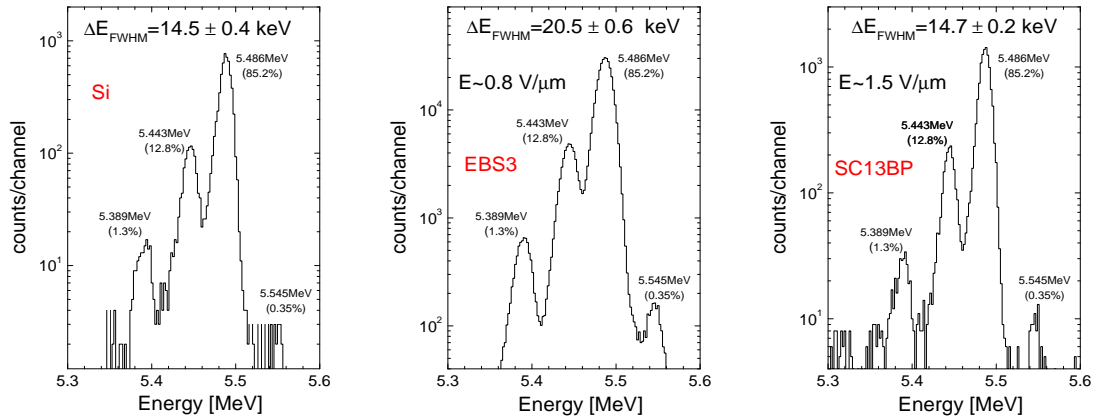


Figure 6.22: Energy resolution of two scCVD-DDs (Middle, right panels) for  $^{241}\text{Am}$   $\alpha$ -particles compared to a silicon PIN-diode detector (Left panel). All spectra measured at RT.

In general the energy resolution of thin samples (50 -100  $\mu\text{m}$ ) is higher than that of thick detectors (300-500  $\mu\text{m}$ ). The same holds when the main contribution to the signal formation have drifting electrons. These results suggest that the limiting factor of the energy-resolution in the fine energy-loss spectroscopy, is still the residual trapping of the charge carriers.

For both, hole and electron drifts the resolution  $\delta E/E$  (FWHM) of more than 30 scCVD-DDs was commonly measured below 25 keV. Comparable resolution is achievable only in very rare high quality natural IIa diamond or IIa HPHT where the selection ratio of electronic grade samples to the rest can be as high as 1:1000, making this material very expensive.

**Charge carriers lifetime - effective deep trapping time** As it was discussed in the introductory chapters, the lifetime of the excess charge carriers is mainly limited by the lattice imperfections in form of structural defects or/and atomic impurities. A collected charge measured with a resolution of 0.3 %, allows a direct estimation of the carrier lifetime in high-quality diamond detectors, where the CCE is close to 100 %. Figure 6.23 presents the CCE of four scCVD-DDs as a function of the transit time of the charge carriers. The transit time was measured with broadband electronics employing the TCT technique, whereas the collected charge was registered with high-resolution spectroscopy electronics. The data points are fitted with the Hecht equation [Hec32], where  $\tau_{e,h}$  is the effective deep trapping time.

The values  $\tau_{e,h}$  obtained vary between the samples, being in general lower for electrons than for holes. Nevertheless, for all samples the lifetime exceeds significantly the transit time in the detector operation range ( $E > 1 \text{ V}/\mu\text{m}$ ). In the best-quality scCVD films the lifetime approaches 1  $\mu\text{s}$ , that is about two orders of magnitude higher than the frequently reported values for high-quality IIa natural- or HPHT diamond [Can79, Kani96].

An estimation of the defect density is possible via the relation  $\tau_{e,h} = (N_D \sigma v_{th})^{-1}$ . Assuming a typical range of trapping cross section  $\sigma = 10^{-15} - 10^{-14} \text{ cm}^2$ , an averaged



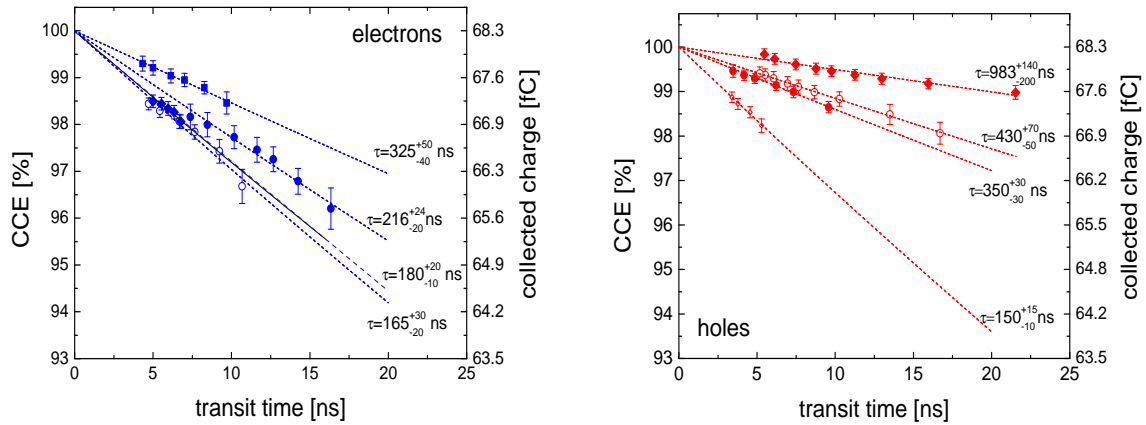


Figure 6.23: Charge collection efficiency as a function of the charge carriers transit time. The effective deep trapping / recombination time for electrons (Left panel) and holes (Right panel) was estimated from Hecht (Equation 3.38), fit to data and indicated as plot parameter on the graphs.

thermal velocity of carriers of  $v_{th} \approx 10^7$  cm/s, and by taking into account measured lifetimes, the range of the defect density for the investigated scCVD material is determined to  $10^{13} < N_D < 10^{15}$   $cm^{-3}$ . This result is in good agreement with the values obtained from the material characterization presented in Chapter 4.

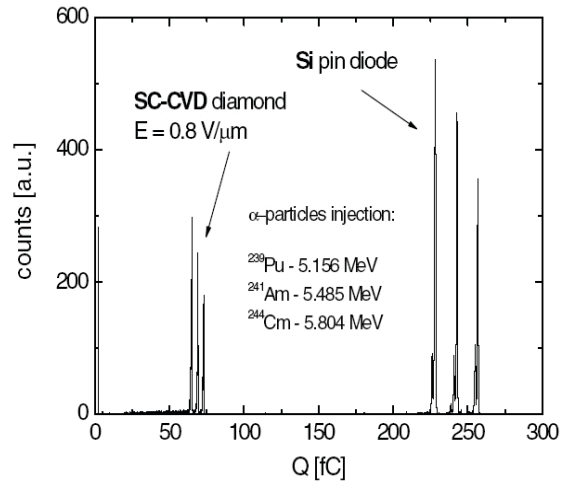
**Average pair-production energy in diamond** The average energy needed to produce an e-h pair is measured from the extrapolation of the collected charge at a charge carriers drift time approaching zero (no trapping). From Figure 6.23 at  $CCE_{t_{tr}=0} = 100\%$  a  $Q_{gen} = 68.3 \pm 0.3$  fC is obtained, which corresponds to an  $\epsilon_{avg}^{Diam} = 12.86 \pm 0.05$  eV/e-h. A cross-check was performed, comparing  $\alpha$ -spectra measured with a Si PIN diode using the identical electronics chain (Figure 6.24). The ratio of the amplitudes in both detectors amounts to  $3.55 \pm 0.01$ , that corresponds to  $\epsilon_{avg}^{Diam} = 12.84 \pm 0.05$  eV/e-h, if taking into account the e-h pair production energy in silicon  $\epsilon_{avg}^{Si} = 3.62 \pm 0.03$  eV/e-h [Owe04a, ORT94]. The measured  $\epsilon_{avg}$  is slightly less than the value of 13.1 eV/e-h [Owe04a, Kan96] reported for IIa natural diamonds and HPHT IIa diamonds and is in contradiction to the recently published values of  $17.6 \pm 2.7$  eV/e-h [Per05],  $16.1 \pm 0.5$  eV/e-h [Kan03] measured for scCVD diamond. However, theoretical calculations point out an even lower value of 11.6 eV/e-h [Ali80].

## 6.4 Detector Response to Minimum Ionizing Electrons

### 6.4.1 Set-up and Methodology

The geometrical arrangement for MIPs detection is shown in Figure 6.25 (Left panel). A  $^{90}\text{Sr}$  source emits electrons with a continuous  $\beta^-$  energy spectrum. The decay scheme as well as the parameters of the energy are given in Figure 6.25 (Right panel). In order to form a parallel electron beam, the  $^{90}\text{Sr}$  source was enclosed in a collimator made out of plexiglas. The size of the collimator aperture was about 2 mm  $\phi$ . A scintillator

Figure 6.24: Spectrum of a mixed nuclide ( $^{239}\text{Pu}$ ,  $^{241}\text{Am}$ ,  $^{244}\text{Cm}$ )  $\alpha$ -particle source, measured with a silicon PIN diode detector and a scCVD-DD. About 3.55 times more energy is needed to create an e-h pair in diamond.



counter was placed directly behind the diamond detector. Coincidence in both detectors guarantees geometrically, that signals in the diamond detector are generated from electrons that traverse the active volume of the diamond detector and have an energy beyond 1 MeV (MIP). The same kind of spectroscopy electronics as for the  $\alpha$ -particles measurements was used (section 6.3).

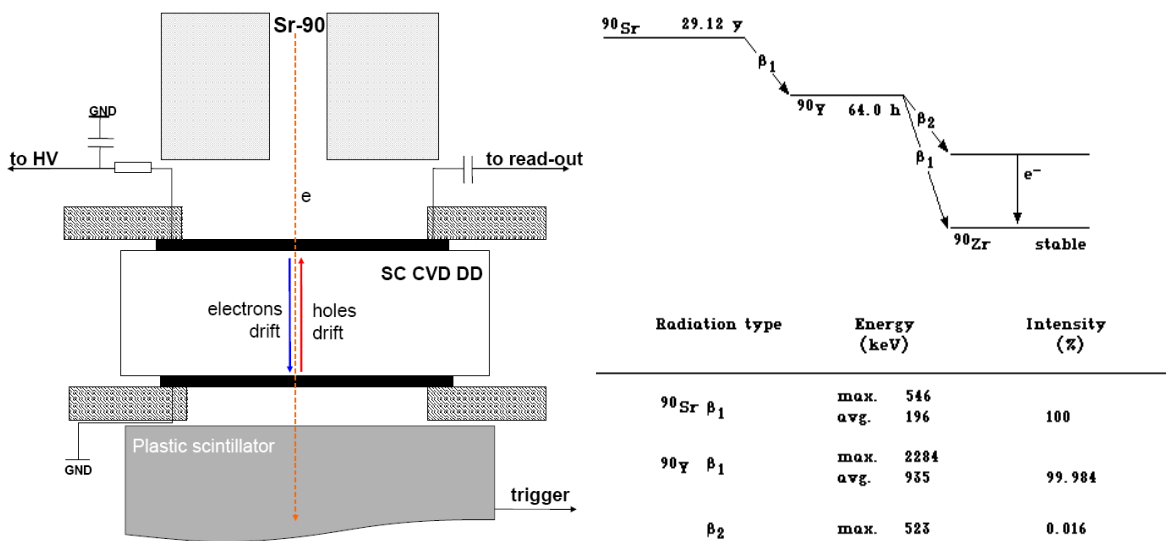


Figure 6.25: (Left panel) Geometrical arrangement for CCE measurements with  $^{90}\text{Sr}$  electrons of an energy  $E_\beta > 1$  MeV, triggered by a plastic scintillator detector. (Right panel) The decay scheme of a  $^{90}\text{Sr}$   $\beta$ -source.

Figure 6.26 (Left panel) shows a Geant4 generated spectrum of electrons emitted from a  $^{90}\text{Sr}$  source and the energy distribution of the electrons which impinge the plastic scintillator after passing 300  $\mu\text{m}$  thick diamond sample (Right panel). The majority of the low energetic electrons do not reach the active volume of the scintillator due to absorption and scattering in the diamond. The mean value of 1.2 MeV of coincident electrons reaching the diamond detector is close to the MIP energy ( $\beta \geq 0.957$ ). Additionally, an electronic threshold discriminates the plastic signals above  $\sim 1.5$  MeV, as indicated in Figure 6.27.

The measured energy distributions are fitted with a Moyal [Moy55] approximation of

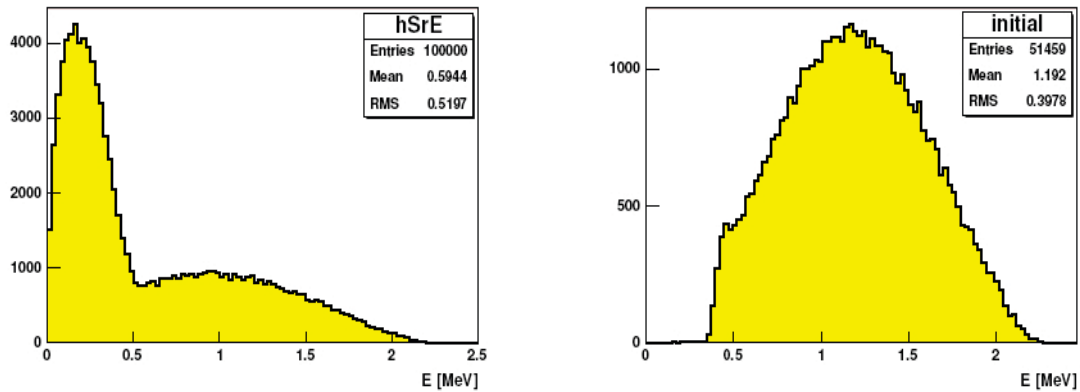


Figure 6.26: (Left panel) Geant4-generated spectrum of electrons emitted from a  $^{90}\text{Sr}$  source. (Right panel) The energy distribution of the electrons, which produce a coincident signal in the plastic scintillator and in a  $300\ \mu\text{m}$  diamond [Kuz06].

the Landau distribution (in following called 'Landau'):

$$\Psi(\lambda) = \frac{\exp[-(\lambda + e^\lambda)/2]}{\sqrt{2\pi}} \quad (6.17)$$

where  $\lambda = (E - E_p)/\sigma$ , with  $E$  the energy loss,  $E_p$  the most probable energy loss, called in following the most probable value (MPV), and  $\sigma$  the width of the distribution which depends on the type of material ( $FWHM_{\text{Landau}} \approx 3.98\sigma$ ). The electronic noise ( $\sigma = 140\ \text{e}$ ) is included in the fitting procedure by convoluting the Landau distribution with a Gaussian [langaus].

The assumption of the minimum ionizing approximation of the  $^{90}\text{Sr}$  electrons, triggered in the above setup has been confirmed with a 2.2 GeV proton beam. The measured energy loss distributions of  $^{90}\text{Sr}$  electrons and of 2.2 GeV protons are shown in Figure 6.27 (Right panel). Both measurements were performed using the same electronics chain and the spectra were fitted with the Landau distribution. As can be seen, the shape of the proton spectrum is well reproduced by the fast electrons, showing a MPV differing only by 1.4 %, and a distribution width ( $\sigma$ ) by 4 %, respectively. The low energy tail in the proton spectrum is caused by events localized at the electrode edges. The high energy tail of the proton spectrum can not be reproduced by  $^{90}\text{Sr}$  electrons due to the limited maximum energy transfer of  $\sim 0.8\ \text{MeV}$ , which is the energy difference between the maximum energy of electrons  $\sim 2.3\ \text{MeV}$  and energy needed to trigger the event  $\sim 1.5\ \text{MeV}$ .

## 6.4.2 Results and Discussion

Figure 6.28 (Left panel) shows the pulse height spectra of minimum ionizing electrons measured with three scCVD-DDs. The diamonds are 114, 324 and  $460\ \mu\text{m}$  thick, respectively. Assuming a production of  $36.7\ \text{e-h}/\mu\text{m}$ , the observed collection distances are consistent with almost complete charge collection in the sensors. The corresponding charge-collection parameters are: most probable collected charge: 4,050 e, 12,050 e and 17,300 e; FWHM: 1260 e, 3735 e, 5360 e; separation between the pedestal and the beginning of the charge distribution: 2,800 e, 9,270 e and 13,370 e. The cut-off on the low energetic side of the Landau distribution occurs at about 75 % of the charge at the MPV Landau peak,

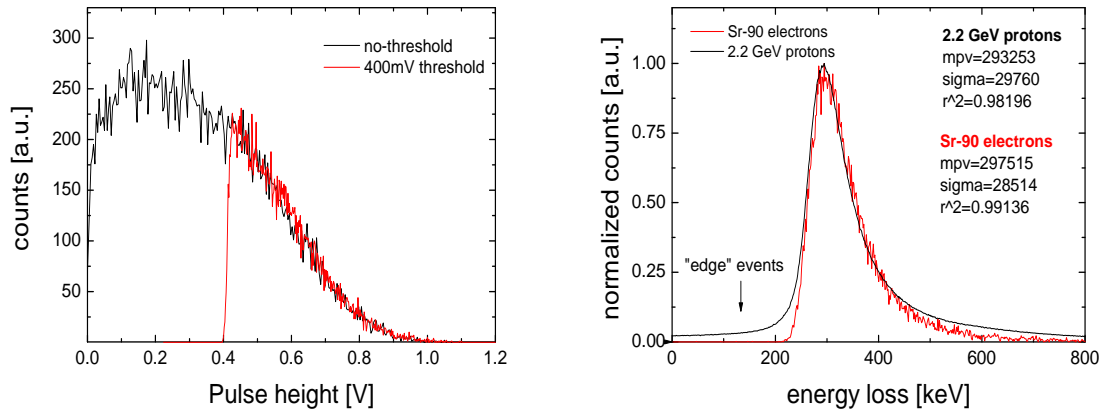


Figure 6.27: (Left panel) The total pulse height distribution of  $^{90}\text{Sr}$  electrons measured with a plastic scintillator detector: in black - without electronic threshold, in red - with electronic threshold of 400 mV. (Right panel) Comparison of the energy loss spectra obtained with  $^{90}\text{Sr}$  electrons (red curve) and with 2.2 GeV protons (black curve), respectively.

which is more favorable than in silicon - cut-off at about 50 %. The  $\sigma/\text{MPV}$  ratio for the scCVD-DDs is approximately 0.078 (Figure 6.28 (Right panel)), that corresponds to a ratio of 0.31 for FWHM/MPV. This value is one third of that obtained from high quality pcCVD-DDs [Dir99], and about two thirds that of the width of silicon detector spectra, measured with a sensor of identical thickness [Ada07].

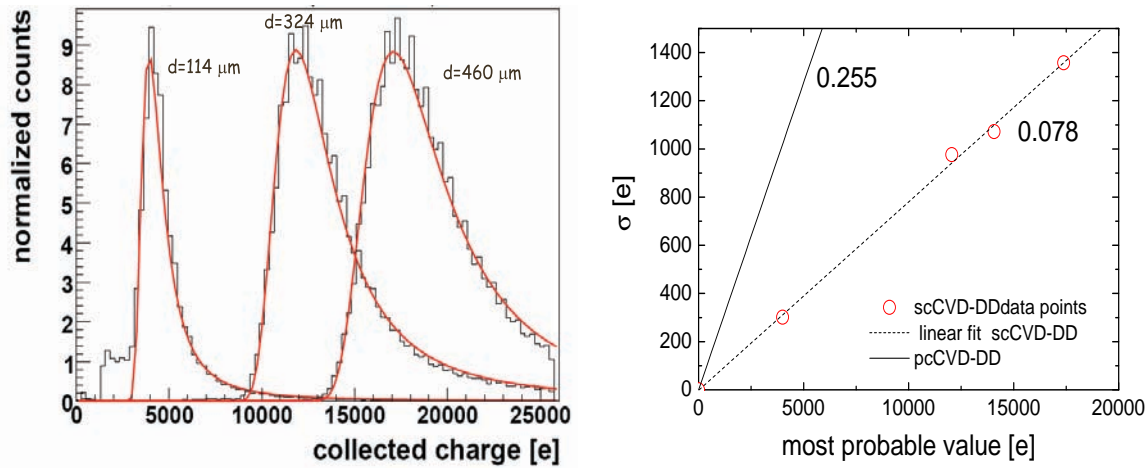


Figure 6.28: (Left panel) Spectra of minimum ionizing electrons measured with three scCVD-DDs of various thickness. (Right panel) Most probable values (MPV) as a function of the width  $\sigma$  of the Landau distributions scCVD-DDs. For comparison the same ratio is shown for measurements realized with a pcCVD-DD [Dir99].

Figure 6.29 shows the collected charge as a function of the applied electric field. For both bias polarities, the saturation of the collected charge starts at low fields ( $E < 0.1 \text{ V}/\mu\text{m}$ ) as indicated in the figure inset.

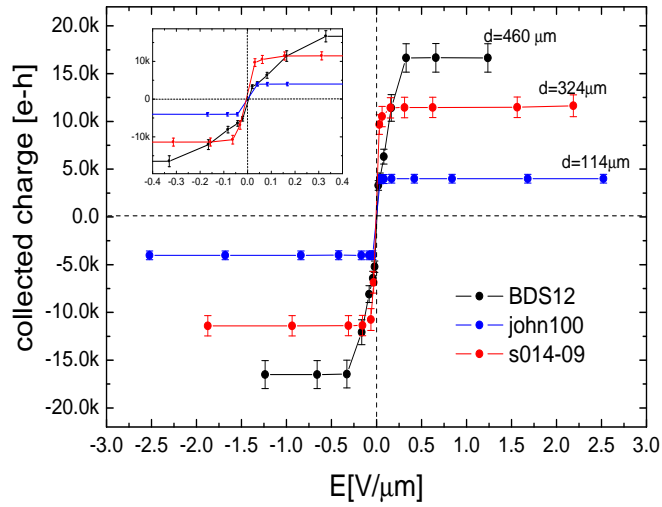


Figure 6.29: Collected charge measured with  $^{90}\text{Sr}$  electrons as a function of the applied electric field. Data from three scCVD-DDs of various thicknesses: 114, 320, 460  $\mu\text{m}$  are shown. The data points are the most probable value (MPV) of the Landau distributions with  $\sigma$  (the distribution widths) as the error bars.

## 6.5 X-ray Microbeam Mapping

### 6.5.1 Set-up and Methodology

The measurements were carried out at the European Synchrotron Radiation Facility (ESRF) using scanning X-ray microscope (SXM) of the ID21 beamline [ID21]. In a four-bunch operation mode, the ESRF synchrotron delivers X-ray beams in spills of  $\sim 100$  ps duration at 1.42 MHz repetition rate. Figure 6.30 (Left panel) shows the microstructure of the X-ray beam measured with a scCVD-DD, AC coupled to a digital oscilloscope. The presented signals are not amplified. The long-term X-ray beam structure is displayed in Figure 6.30 (Right panel), showing exponential decay of the beam with a half-life of 7.3 h. After 4 h when the beam intensity drops to about 50 % of the initial value, electrons are re-injected into the storage ring of the synchrotron.

Figure 6.31 shows the experimental setup used for the X-ray microbeam mapping investigations. The 6 keV monochromatic X-ray beam was focused into spots ranging from 1 - 100  $\mu\text{m}$  diameter (FWHM). The diamond samples were metallized with Al-sandwich electrodes. The surface impinged by the X-ray beam carried a full pad electrode at HV potential, whereas the opposite side was metallized with a quadrant motif. The samples were raster scanned upright to the beam direction using a remote controlled XY step/piezo motor. In a DC operation mode, the X-ray beam induced current (XBIC) from scCVD-DDs was first measured by feeding the signal from each quadrant electrode to a separate Keithley 485 electrometer. The signals were fed to voltage-to-frequency converters (Nova N101VTF) and averaged over different integration periods ranging from 0.1 to 1 s. The pulse response of the detectors to the X-ray micro-pulses was investigated using the synchrotron RF clock as a reference trigger. The fast Transient XBIC (TXBIC) signals, generated by the diamond detector were amplified with broadband amplifiers (DBAIII) and recorded with a LeCroy DSO of 4 GHz bandwidth. Average signals over 64 single shots were recorded. The synchronous acquisition of the photocurrent or of broadband signals with the sample position, allowed XBIC and TXBIC image formation on a pixel-by-pixel basis in both, the DC and the RF mode.

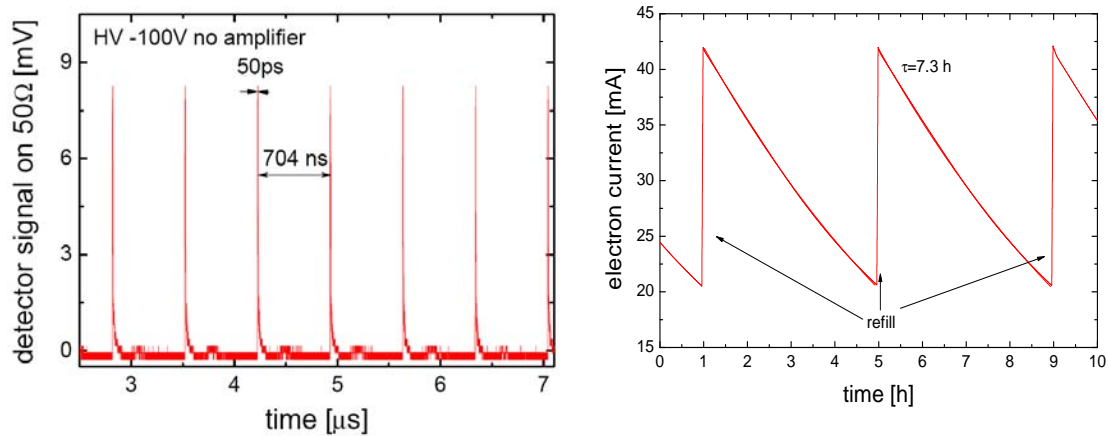


Figure 6.30: (Left panel) Micro-pulse structure of the 4-bunch mode of the X-ray beam, recorded with a scCVD-DD and a digital oscilloscope. (Right panel) The electron current in the storage ring of the ESRF synchrotron when operating in a 4-bunch mode.

In DC mode, two upstream and downstream beam monitors (silicon detectors), provided the normalization of the X-ray induced current to the beam intensity variation  $I_0$  and to the beam absorption  $I_a$  occurring in the studied samples. The  $I_0$  value was constantly measured with the upstream detector (*iodet*), consisting of an aluminium scatter / fluorescence foil and a silicon photodiode. The X-ray absorption in the studied samples was determined by the ratio of *iedet* to *iodet*. However, as a consequence of the sample holder geometry, that was only possible in a limited central region of the XBIC maps.

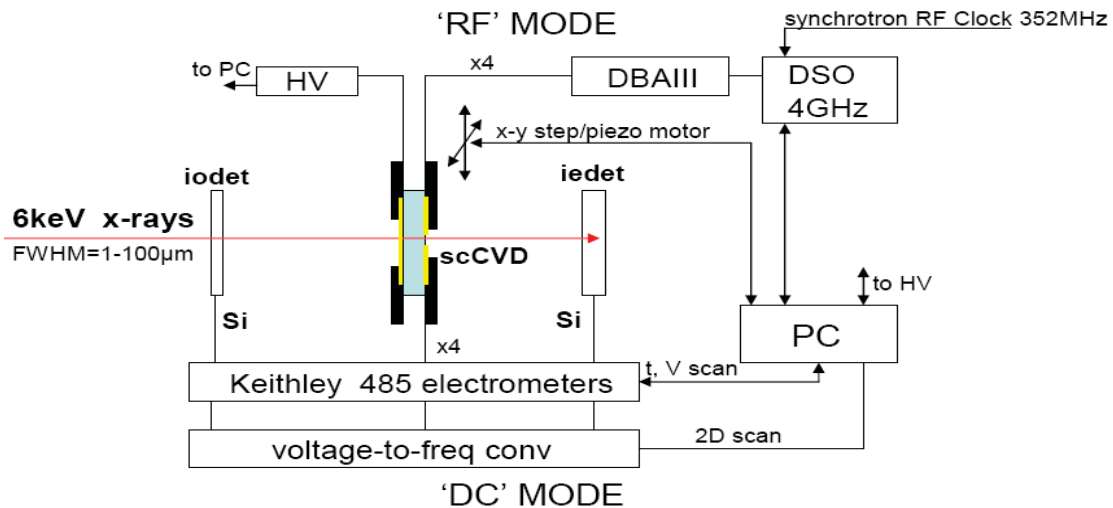


Figure 6.31: Schematic of the experimental arrangement for X-ray scanning microscopy at the ID21 line of ESRF.

The attenuation length of 6 keV X-rays in diamond amounts to  $263 \mu\text{m}$  [xray]. The charge generation by one micro-pulse was measured by integrating a single TXBIC pulse. For a maximum synchrotron current of 42 mA, the studied sample thicknesses of 50 to  $300 \mu\text{m}$  and the variation of the synchrotron current between 22 and 42 mA, the beam

induced charge ranges from 0.33 fC to 12.8 fC.

Results on three scCVD-DDs are presented. The samples were metallized with Al (100 nm) quadrant electrodes on one side and a full pad back electrode. Two samples 100  $\mu\text{m}$  (SC8BP) and 50  $\mu\text{m}$  (SC14BP) thick were found almost free of structural micro-defects with atomically flat, ion-beam polished surfaces, whereas a scaife polished 300  $\mu\text{m}$  (s256-02-06) thick film was found to have a high-density of structural defects.

### 6.5.2 Results and Discussion

In a first step, the dark-conductivity of the samples was measured in-situ. In the detector operating range from -500 V to 500 V leakage current of every quadrant of the defect-free samples was found below the sensitivity of the electrometers used ( $I_{dark} < 10$  pA). The safe bias range of operation for the sample s256-02-06 was limited by the presence of inhomogeneously distributed structural defects. The dark current characteristic of this sample is displayed in Figure 6.6.

In a second step, the XBIC-E(V) characteristics were measured varying the detector bias during the separate, individual irradiation of each of the quadrants with an incident steady state X-ray flux of  $4 \times 10^8$  photons/sec. The results are displayed in Figure 6.32. As shown in an expanded view in the right graph, the XBIC in thin samples saturates at extremely low field of  $E=0.05$  V/ $\mu\text{m}$ . Perfect operation stability is found for the sample SC14BP up to a maximum applied field  $E = \pm 6$  V/ $\mu\text{m}$ . Note that for this sample the charge is created roughly within 1  $\mu\text{m}^2$  area, with a repetition rate of 1.42 MHz. That can be translated to extremely high rates of randomly impinging minimum ionizing particles ( $\sim 10^{13}$  MIP/cm<sup>2</sup>s).

In contrast, the XBIC-E(V) characteristics of s256-02-06 is highly asymmetric, and shows unstable behaviour at negative bias. The observed current increases with time and finally, after several minutes, a hard-breakdown occurred. Looking in more detail at the XBIC-E(V) characteristics in the low field region, additionally an asymmetry was found, which indicates accumulation / trapping of the photo-generated charge in the vicinity of the electrodes in the case of high ionization rates. This effect is more pronounced for the scaif polished samples.

Assuming the current plateaus shown in Figure 6.32 correspond to the complete charge collection, the average energy needed for the creation of an e-h pair,  $\epsilon_{avg}^{Diam}$  can be calculated, taking into account the absolute value of the incident X-ray beam flux  $I_0$ , the fraction of the beam intensity absorbed by the diamond ( $I_0 - I_a$ ), and the diamond current signal. This gives an  $\epsilon_{avg}^{Diam} = 13.05 \pm 0.2$  eV/e-h, where the estimated error is mainly due to the uncertainty on the absorbed X-ray intensity. This result (within the measurement uncertainty) agrees with the value obtained for 5.5 MeV  $\alpha$ -particles.

**2D maps of the detector response** XBIC imaging was carried out on sample s256-02-06, with a beam size of 100  $\mu\text{m}$  in diameter and an applied bias of -60 V (0.2 V/ $\mu\text{m}$ ). The acquired images of four quadrants are overlaid to an X-ray white-beam topograph of the sample (Figure 6.33 (a)). The regions of 20 % lower XBIC response (dark areas) correlate with the extended structural defects visible in the diffraction imaging, indicating charge-carrier trapping at the dislocation sites. Note that, in the transmission operation mode, both electrons and holes drift across the sample. Thus, we cannot distinguish between



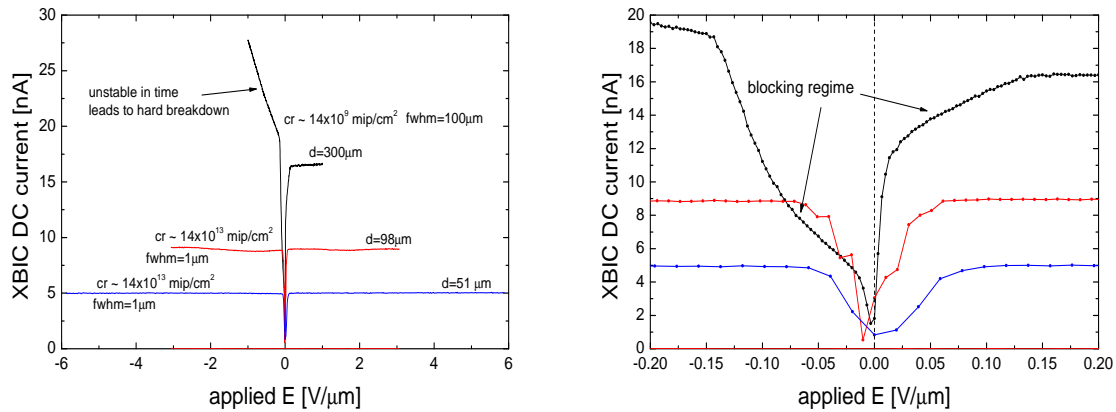


Figure 6.32: (Left panel) XBIC-E(V) characteristics of three scCVD-DDs under 6 keV X-ray beam illumination. (Right panel) Expanded view in the low-field regions. Scan parameters: beam size 100  $\mu\text{m}$ , voltage step 1 V, registration time 2 s per step.

electron and/or hole trapping. However, it was shown in [Lo07b] that the transport of both carriers is affected by the presence of dislocations.

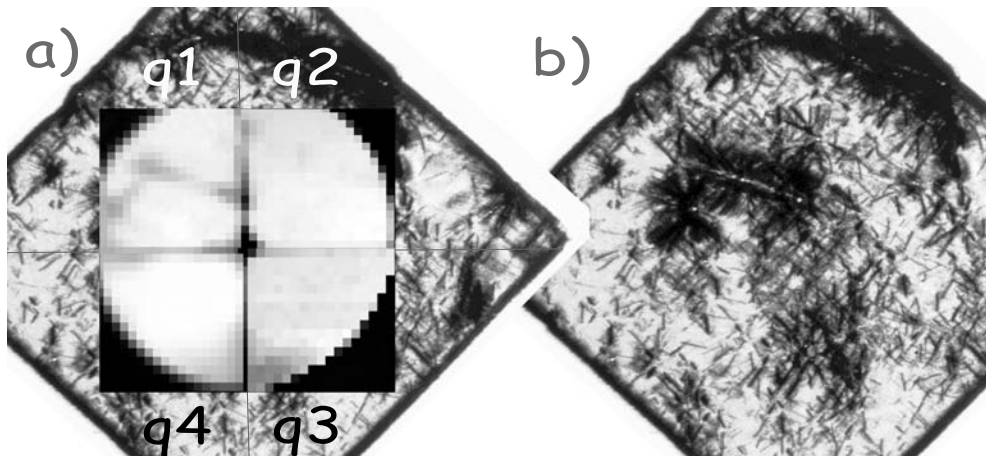


Figure 6.33: X-ray microbeam mapping of the defective scCVD-DD (s256-02-06) at 0.2 V/ $\mu\text{m}$ . a) The XBIC maps of isolated quadrants (q1, q2, q3, q4) are overlaid on the X-ray white beam topography of the sample b) s256-02-06 X-ray topography. Lower detector response is correlated with highly defective regions of the sample localized mainly under q1 and q3. Scan parameters: beam size 100  $\mu\text{m}$  (FWHM), pixel size 32  $\mu\text{m}$ , dwelling time 100 ms/pixel.

Figure 6.34 presents a high resolution XBIC scan of s256-02-06-q1 measured with a focused beam of 1  $\mu\text{m}$  diameter (FWHM) and steps of 6.6  $\mu\text{m}$ , acquired at +30 V (0.1 V/ $\mu\text{m}$ ). Dark areas correspond to lower detector response. The fine structure of the defects is clearly visible. Compared to defect-free regions, about 15 % lower response of the detector was detected at dislocations as indicated by the depth profiles in the side graphs of the figure. Unexpected increase of the current signal occurred at the strained regions surrounding the defects. This effect is particularly pronounced around the 'big-cross' defect, where the XBIC



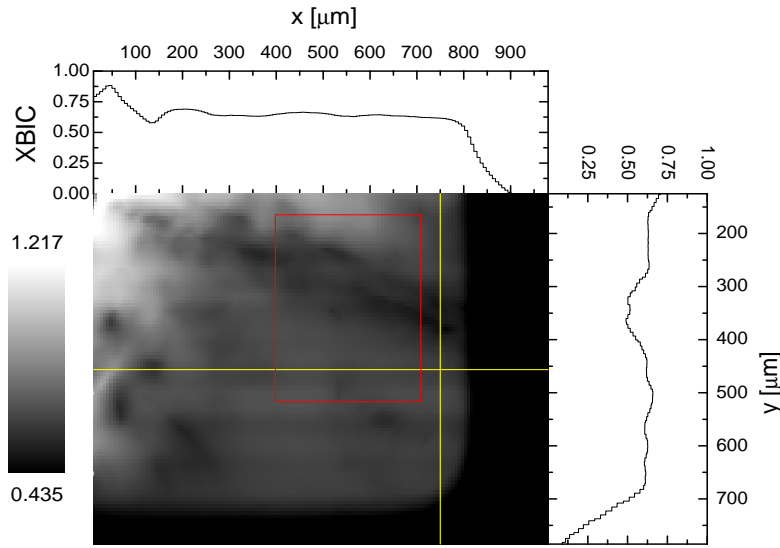


Figure 6.34: High resolution XBIC map of quadrant q1 of s256-02-05 measured at a bias voltage of +30 V ( $0.1 \text{ V}/\mu\text{m}$ ). Dark areas correspond to the lower detector response. The yellow lines mark horizontal and vertical profiles, displayed in the side graphs. Scan parameters: beam size  $1 \mu\text{m}$  (FWHM), pixel size  $6.6 \mu\text{m}$ , dwelling time  $100 \text{ ms}/\text{pixel}$ .

rose by 30 %, as indicated by the vertical profile. The charge collection at  $0.1 \text{ V}/\mu\text{m}$  is not saturated in this sample. This interesting feature may be attributed to an increased drift velocity of carriers' resulting from modification of the band structure - thus effective mass of charge carriers modification - in the strained regions, similar to those known from strained silicon [Wan00].

Figure 6.35 shows the time-voltage evolution of the XBIC response in the defective region marked in Figure 6.34 with a red rectangle. The grey scale is common for all three graphs. At first (graph a) the sample was scanned at  $-60 \text{ V}$  ( $0.2 \text{ V}/\mu\text{m}$ ); charge collection is not saturated at this applied field, whereas trapping at dislocations is visible giving about 30 % lower response. Increasing the bias to  $-120 \text{ V}$  ( $0.4 \text{ V}/\mu\text{m}$ ), the detector response became much more homogeneous (graph b) with a signal variation of only  $\sigma = 0.3 \%$  in the defect-free region. Still, a lower response can be observed at the dislocation sites; however, the signal drops by only 5 % and the region affected by trapping is limited to a smaller area. Changing the voltage to  $+60 \text{ V}$  ( $0.2 \text{ V}/\mu\text{m}$ ), a strong increase of the current signal by 300 % was observed at the defective regions. Once generated, this current persists for several seconds. The XBIC from the defect-free region stays constant at the saturated level within a variation of only  $\sigma = 0.25 \%$ . The strong enhancement of the current signal can only be explained by charge injection from the electrodes through the previously charged (by trapped charge) dislocation sites. A further increase of the applied electric field above  $\pm 1 \text{ V}/\mu\text{m}$  led to hard-breakdown, whenever the X-ray beam was scanned over the defective areas. Similar behaviour was observed for two others scCVD-DDs affected by structural defects.

The XBIC maps of the high-quality samples SC8BP and SC14BP are shown in Figure 6.36. For both detectors, the measurements were carried out at  $0.5 \text{ V}/\mu\text{m}$ , and at  $1 \text{ V}/\mu\text{m}$ , respectively. The map of the sample SC8BP is obtained by summing up the XBIC of four quadrants. Due to imperfections of the shadow mask used in metallization process the sample SC14BP possesses interconnected quadrant electrodes. Thus, only one readout channel was used in this case. Both samples were scanned with a focused beam of  $1 \mu\text{m}$  diameter (FWHM). The parameters of the scans are indicated in the figure caption. Perfect homogeneity of the response is found for both sensors in a single row measurement,

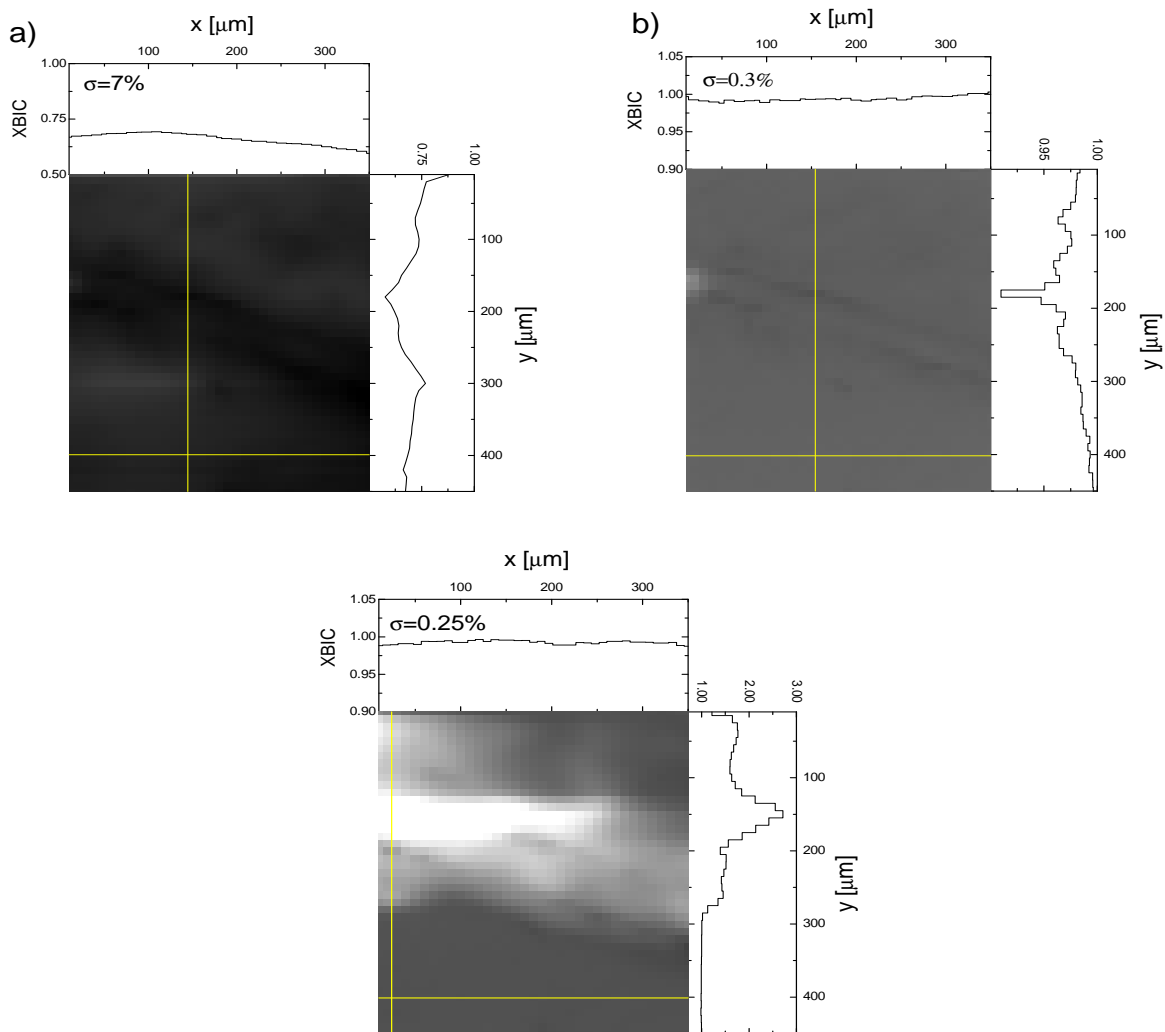


Figure 6.35: XBIC time-voltage evolution of the defective region response. a) -60 V, b) -120 V, c) +60 V. Scan parameters: beam size  $1 \mu\text{m}$ , pixel size  $10 \mu\text{m}$ , dwelling time  $100 \text{ ms/pixel}$ .

with a variation of  $\sigma = 0.1 - 0.3 \%$ . The measured overall XBIC response, represented as histograms in the figure insets, is slightly worse and ranges from  $\sigma = 0.8 \%$  to  $2.2 \%$ . The  $\sigma$ -variation is limited by the following factors: the resolution of the silicon photodiode ( $\sigma = 1 \%$ ), the thickness inhomogeneity of the diamond samples, and the presence of electrically 'dead' regions between the quadrants. However, even with such an imperfect experimental arrangement, the tiny variation of the X-ray beam intensity due to back scattering from metal parts of the pcb (order of  $0.4 \%$ ) was detected.

Figure 6.37 displays high resolution XBIC maps from two regions of the sample SC14BP's, marked with a red circle and a rectangle in Figure 6.36 (Right panel). The XBIC response in the left graph was normalized to the X-ray absorption in the sample. As can be seen, the overall homogeneity improves, leading to a  $\sigma = 0.37 \%$ . Also the fine scan Figure 6.37 (Right panel) shows the perfect XBIC homogeneity of defect-free scCVD-DD, with an overall signal variation of only  $\sigma = 0.25 \%$ .

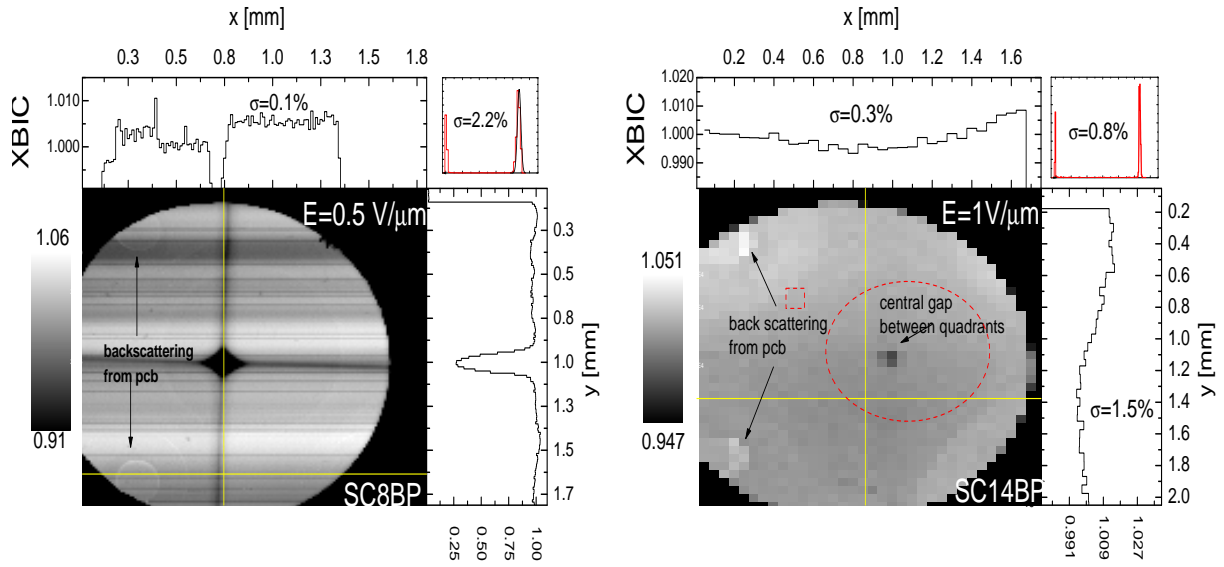


Figure 6.36: XBIC maps of defect-free scCVD-DDs (SC8BP, SC14BP). The scan parameters are: beam size  $1 \mu\text{m}$ ; pixel size  $12 \mu\text{m}$  (Left panel), and  $50 \mu\text{m}$  (Right panel), respectively; dwelling time  $100 \text{ ms/pixel}$ .

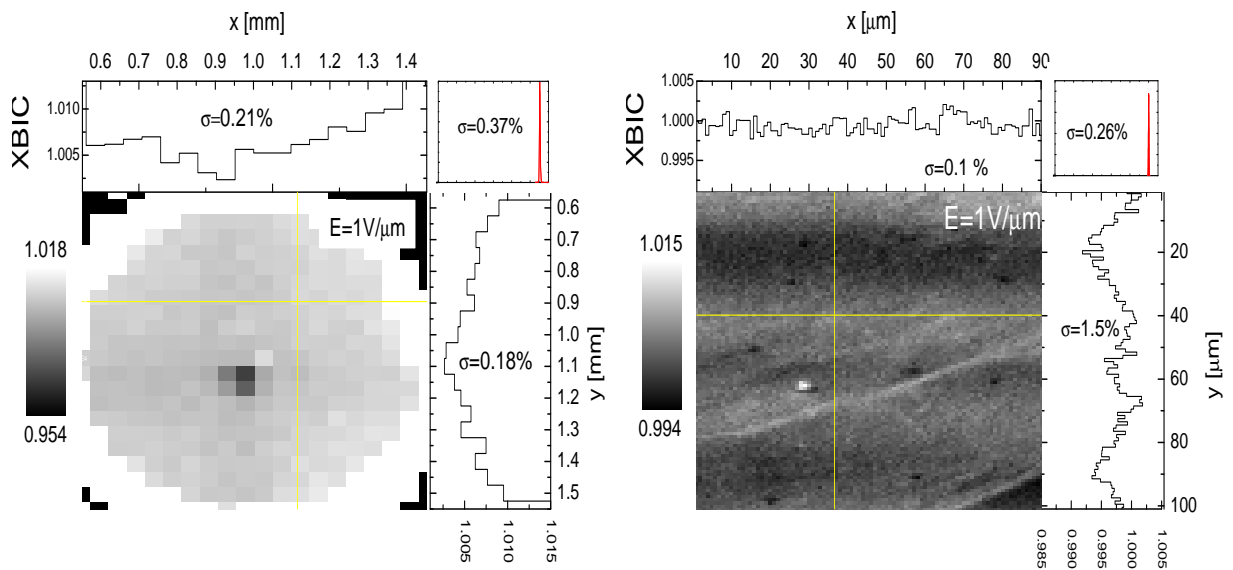


Figure 6.37: High resolution XBIC maps of sample SC14BP. (Left panel) The XBIC signal is corrected for X-ray absorption in the investigated sample. (Right panel) Fine scan of a  $70 \times 90 \mu\text{m}$  area; the scans parameters: beam size  $1 \mu\text{m}$  (FWHM), pixel size  $50 \mu\text{m}$  (Left panel),  $1 \mu\text{m}$  (Right panel), dwelling time  $100 \text{ ms/pixel}$ .

**Charge sharing in pulse mode** The response of sample SC8BP X-ray scanned at  $+400 \text{ V}$  ( $4 \text{ V}/\mu\text{m}$ ) with pulsed signal readout is shown in Figure 6.38 (Left panel). The collected charge from adjacent electrodes is plotted versus the beam position. The beam was scanned horizontally across the isolation gap of  $\sim 130 \mu\text{m}$ . The crossover response, corresponding to the charge diffusion is visible over a distance of  $18 \mu\text{m}$ . The collected charge values of the left (L) and the right (R) quadrant, are obtained by the integration of

the TXBIC signals over transit time. Despite the  $130\ \mu\text{m}$  gap between the quadrants, the sum of the signals of the L and the R quadrant corresponds to the full charge collection. Examples of TXBIC signals are shown in Figure 6.38 (Right panel). The narrow pulses correspond to the events located within the sectors L and R, whereas the double-peak signals were registered in the case of X-rays hitting exactly the mid-gap between the electrodes. The rise time of the signals is limited by the bandwidth of the electronics employed. This result is the first direct demonstration for use of a diamond detector as an ultra-fast, position sensitive detector readout in the broad-band mode.

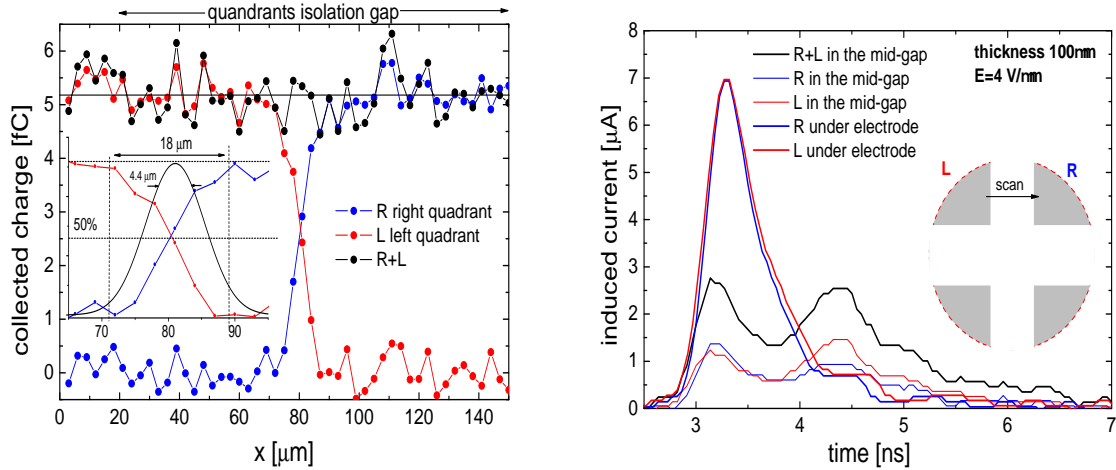


Figure 6.38: Position response of a  $100\ \mu\text{m}$  thick scCVD-DD, operated in a pulse mode at  $400\ \text{V}$ . A focussed beam ( $\text{FWHM} \sim 1\ \mu\text{m}$ ) is scanned across the insulating gap ( $\sim 130\ \mu\text{m}$ ) between the two quadrants (L and R). (Left panel) Collected charge (integral of XBIC transient signals) as a function of the beam position. (Right panel) XBIC transient signals from the electrode region and from the middle of the isolation gap.

Taking into account the beam size of  $\sigma = 0.42\ \mu\text{m}$ , broadened by the thermalization of the generated  $6\ \text{keV}$  photoelectrons in diamond to about  $\sigma_{beam} \approx 0.85\ \mu\text{m}$ , and the measured transit time of the induced charge carriers of  $\sim 2\ \text{ns}$ , a rough estimate of the transversal diffusion coefficient  $D$  may be derived. From the relation  $\Delta\sigma = \sqrt{4D t_{tr}}$ , where  $\Delta\sigma = \sigma_{obs} - \sigma_{beam}$  and  $\sigma_{obs} = 4.4\ \mu\text{m}$  are the widths of the measured charge distribution (obtained from the differentiation of XBIC signals of the L and the R quadrant) and  $\sigma_{beam} \approx 0.85\ \mu\text{m}$  is the charge distribution at the start of the carriers drift. The obtained value  $D \approx 16\ \text{cm}^2/\text{s}$  is much smaller than the value calculated from the Einstein relation  $D = \mu k_B T / q$  for the low field ( $D \approx 90\ \text{cm}^2/\text{s}$ ). This shows that the transversal carrier diffusion decreases significantly at high electric fields similar to the longitudinal diffusion [Rob73].

**Influence of the surface defects** Figure 6.39 (middle) shows the XBIC map of a resin-wheel polished scCVD-DD sample acquired at  $1\ \text{V}/\mu\text{m}$ . In the left and right panel of the figure, the optical microscope images of the electrode borders are displayed. At the left side of the sample, a high density of characteristic crescent notches was found (see Chapter 4), whereas the right side is almost free of such defects. The red areas at the edge of the electrode in the XBIC map correspond to the persistent currents which are clearly induced

at the electrode borders, where high density of surface defects was observed (left picture). The magnitude of these currents is about eight times higher than the average current values measured from the homogeneous areas of the electrode. This suggests a beam-induced charge injection from the defective surface sites. No one of the ion-beam polished scCVD-DDs has shown this 'hot electrode' effect. The circular spot on the electrode corresponds to the wire bond, causing an enhancement of the XBIC signal due to X-ray back scattering.

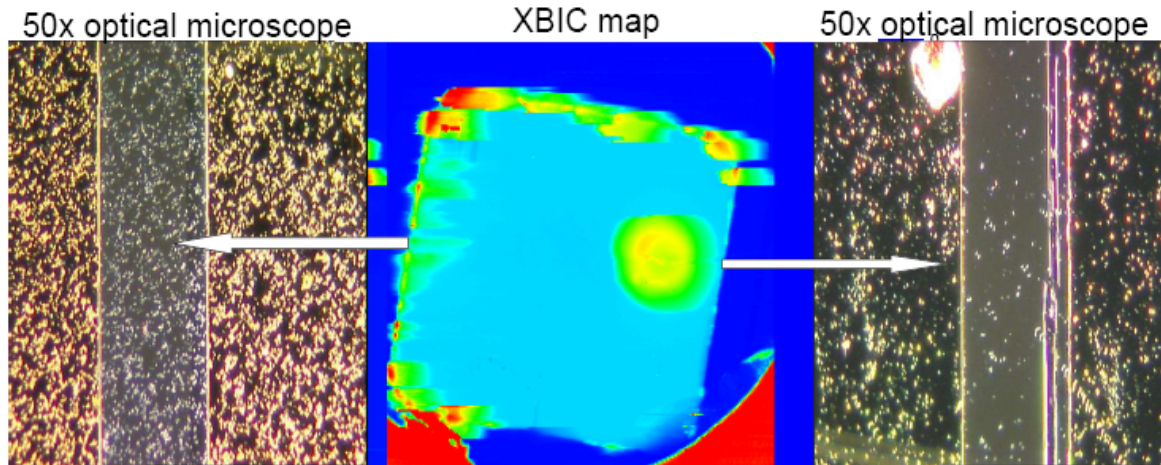


Figure 6.39: (middle) XBIC map of a resin wheel polished scCVD-DD with a damaged surface (red color represents high current). Persistent leakage currents are generated at the edge of the electrode, where a high density of surface defects is observed (Left panel) (courtesy J. Morse).

**X-ray beam monitoring application** Besides the studies concerning the homogeneity of the response scCVD-DDs to an X-ray microbeam, there is great interest to use diamond detectors as beam monitors in the present and the future generation of synchrotrons [Mor07a]. Due to the weak absorption of X-rays (i.e., for 10 keV X-rays, ten times less than in silicon) and a high thermal conductivity (i.e., at RT six times that of copper), diamond is an outstanding material for the fabrication of 'semitransparent' beam monitors. Such a device can be permanently installed into a high flux X-ray beam, providing continuous monitoring of beam-position and intensity. First tests were carried out during the experiment described above. A long-time measurement was started with the beam in the center of the isolation cross between the quadrants of sample SC8BP. The movement of the focused beam was recorded over 10 hours. The beam position was calculated applying the center of gravity algorithm to data. The shift of the beam position was traced with a precision of 13 nm ( $1\sigma$ ) using 1s integration time. The jitter of the micro-pulses versus the synchrotron RF clock was measured with a precision of 16 ps ( $1\sigma$ ). The detailed description of the measurement procedure and methods was published in [Mor07, Mor07b].

## 6.6 Summary of the Electronic Properties Characterization

In this chapter a systematic study of the electronic properties of scCVD-DDs was presented. The structural lattice defects, appearing in form of threading dislocations, govern the dark conductivity of the investigated samples. Diamonds of a high defect density exhibit significantly reduced dielectric strength, whereas the measured dark current of defect free samples is below 1 pA at fields as high as  $10 \text{ V}/\mu\text{m}$  ( $10^5 \text{ V}/\text{cm}$ ). The I-E(V) characteristics of defective samples consists of two ranges: in the first range, the measured dark current is at the limit of the setup sensitivity ( $\sim 10^{-13} \text{ A}$ ), and in the second range, space charge limited current conductivity (SCLC) takes place. The SCLC part of the I-E(V) characteristics of all measured samples can be described by a single power law with an exponent ranging from 5 to 7. The onset of the SCLC region at a field  $E_c$  is correlated with the defect density. For samples with a high defect density, charge injection occurs at only  $E = 0.1 \text{ V}/\mu\text{m}$ . The injected charge recombines radiatively at the dislocations, revealing characteristic blue light emission - the band A luminescence. For both, the defect-free and defective samples, the dark current at  $E < E_c$  is thermally activated with an activation energy of  $E_a = (0.37 \pm 0.3) \text{ eV}$ . The measured  $E_a$  suggests the presence of uncompensated boron impurities, thus a rest p-type conductivity of scCVD diamond crystals. In addition, it was demonstrated that scCVD-DDs can be operated at  $300 \text{ }^\circ\text{C}$  and  $E = 4 \text{ V}/\mu\text{m}$  with a dark current on the order of  $7 \text{ nA}/\text{mm}^2$ .

The timing properties were probed by the transient current technique using 5.5 MeV  $\alpha$ -particles as the excess charge generator. The analysis of the transient current signals allowed the direct determination of the charge-transport properties of scCVD-DDs. For the majority of the studied samples, negligible space charge and excess charge carriers trapping was found within the detector operation range. The drift velocity of the carriers in the  $\langle 100 \rangle$  crystallographic direction was measured over a wide range of applied electric fields. The extrapolated saturation drift velocity amounts to  $2.6 \times 10^7 \text{ cm/s}$  and  $1.6 \times 10^7 \text{ cm/s}$  for electrons and holes, respectively. The drift velocity of both charge carriers at  $11 \text{ V}/\mu\text{m}$  are equal, achieving a value of  $1.43 \times 10^7 \text{ cm/s}$ , which is about twice higher than the drift velocity in silicon, measured at the same applied electric field.

Using low-noise charge sensitive electronics, the detectors response to  $\alpha$ -particles was characterized. For a majority of the studied detectors, saturation of the collected charge occurs at fields  $E < 0.3 \text{ V}/\mu\text{m}$  for both electron and hole drift. The measured energy resolution  $\delta E/E = 0.35 \%$  (FWHM) obtained with 5.5 MeV  $\alpha$ -particles for scCVD-DDs' is comparable with the resolution of silicon PIN diode detectors. The measured lifetime of the excess charge carriers, exceeds significantly the carriers transit time in the detector operation range. The measured values range from 150 ns to 320 ns for electrons and from 150 ns to  $1 \mu\text{s}$  for holes, respectively. This corresponds to a remarkably high charge collection distance (CCD) on the order of several centimeters. The response to minimum ionizing particles was studied using fast electrons ( $E > 1 \text{ MeV}$ ) of a  $^{90}\text{Sr}$  source. Also in this case, the saturation of the collected charge occurs at a low field  $E < 0.3 \text{ V}/\mu\text{m}$ . The shape of the Landau distribution is superior to the shape obtained with silicon detectors with respect to the relative width and the higher cut-off energy at the low energy tail.

The excellent  $\delta E/E$  resolution measured with  $\alpha$ -particles, impinging randomly the diamond bulk were confirmed by the spatially resolved X-ray microbeam mapping at the

ESRF. The uniformity of the device response varies on a level of  $\sigma = 0.1\%$ . Perfect stability was observed for the defect-free samples, applying electric fields up to  $6\text{ V}/\mu\text{m}$  at a constant X-ray micro-pulse excitation of a rate of  $1.4\text{ MHz}$  per  $1\ \mu\text{m}^2$ . This corresponds to extremely high rates of randomly impinging minimum ionizing particles ( $\sim 10^{13}\text{ cm}^{-2}\text{s}^{-1}$ ). In contrast, scCVD-DDs containing structural defects are highly unstable. Despite a low initial dark conductivity a hard-break down of the device is induced at an applied field exceeding  $E > 1\text{ V}/\mu\text{m}$ , when the X-ray microbeam is scanned over the defective areas. Such a behavior was observed for several defective samples during the microbeam mapping experiments, as well as during the detector irradiation with high rates of charged particles. It can be attributed to a further decrease of the diamond dielectric strength as a result of the dislocations charging by charge trapping. Surface defects, caused by resin-wheel polishing, lead to carrier injection at the electrode borders. The induced current persists thereby by several seconds, and turns into a hard breakdown at high electric fields. On the other hand, ion-beam polished scCVD-DDs were shown to perform with a perfect stability.





# Chapter 7

## An Insight into Radiation Tolerance

Radiation damage studies of diamond have been carried out to a great extent in the past. The main techniques used have been optical spectroscopy in the infrared (IR) [Mit06], visible and ultraviolet (UV) ranges [Cla95] as well as electron spin resonance (ESR) [Wat01]. These studies were mainly focused on the characterization of the structure and origin of the defects created, with no relation to the electronic properties nor to the influence on the charge-carrier transport properties. On the contrary, there are only a few publications linking radiation damage with the operation of a diamond particle detector [Oh00, Mai98, Amo02]. First systematic work on this subject was performed by the RD42 collaboration [RD42], where mainly pcCVD material was investigated. It was demonstrated that pcCVD-DDs are able to operate with satisfactory signal-to-noise ratio after high-energy proton irradiation up to  $\sim 2 \times 10^{15}$  24 GeV p/cm<sup>2</sup> [Ada02b, Ada00]. At present, there are no published data available discussing the radiation tolerance of scCVD-DDs. In this chapter an attempt is made to answer the question if scCVD-DDs are able to operate after high fluency hadrons irradiation. Low-energy proton irradiations of several sc-CVD-DDs were carried out in Karlsruhe up to an integral fluence of  $1.18 \times 10^{16}$  particles/cm<sup>2</sup>. At the cyclotron in Louvain-la-Neuve, corresponding studies were performed with fast neutrons of  $E_k \sim 20$  MeV. The electronic and the optical properties of the detectors had been characterized off-line before and after the irradiations, using the detector characterization techniques introduced in the preceding chapters. The results are presented and discussed considering the present knowledge about radiation damage of diamond.

### 7.1 Non-Ionizing Energy Loss and Radiation Damage to Diamond

#### 7.1.1 Defects Creation

When charged particles traverse semiconductor devices, three main processes occur:

- **Displacement** due to non-ionizing energy loss (NIEL). When the primary particle scatters on a lattice atom, transferring enough energy to displace it, a vacancy and a primary knock-on atom (PKA) is formed. As long as, the kinetic energy of the PKA is sufficiently high, further displacements take place. The rest of the energy is dissipated by phonon creation. At high energies, nuclear reactions occur, producing

several fragments as well as secondary particles. If the produced defects are separated only by several atomic distances, they can migrate and recombine due to thermal activation. The so-called self-annealing process takes place. These rearrangements are partially influenced by the presence of impurities in the initial material, forming complex defects. Thermally stable defects influence the electric properties of the semiconductor, and thus detector operation.

- **Ionization** - this process creates electron-hole pairs and is used for radiation detection.
- **Trapping** - In insulators or wide-band gap semiconductors, the material does not return to its initial state, if the electrons and holes produced are trapped and could not be re-emitted at the operating temperature. Thus, space charge is created, which affects detector operation.

The evaluation of the non-ionizing energy-loss component is performed by computing the flux-weighted displacement cross-section  $D(\Phi, E)$ , also called the average displacement Kinetic Energy Released per unit Mass (KERMA). For a given particle flux  $\Phi(E)$ ,  $D(\Phi, E)$  is defined by Equation 7.1

$$D(\Phi, E) = \frac{\int_E \frac{d\Phi(E)}{dE} D(E) dE}{\int_E \frac{d\Phi(E)}{dE} dE} \quad (7.1)$$

where  $D(E)$  is the damage function describing the macroscopic cross section  $\sigma_k(E)$  for a specific particle interaction out of the various reactions within the solid:

$$D(E) = \sum_k \sigma_k(E) \int dE_r f_k(E, E_r) P(E_r) \quad (7.2)$$

with  $f_k(E, E_r)$  being the probability for an incident particle of energy  $E$  to produce a recoil energy  $E_r$  via a reaction of type  $k$ , and the function  $P(E_r)$  being the part of the recoil atom of energy  $E_r$  deposited by displacements.  $P(E_r)$  is called the Lindhard partition function.

The NIEL hypothesis states that the damage created in a semiconductor material is directly proportional to the non-ionizing energy loss independent of the type of impinging particle or the type of interaction. For radiation-hardness studies of silicon detectors,  $D(E)$  (expressed in MeVmb), is commonly normalized according to the ASTM standard [ASTM] to the displacement cross section of damage produced by a 1 MeV neutrons, quoted to be 95 MeVmb. Using the *NIEL* scaling hypothesis, the damage efficiency of any particle type and flux of a given kinetic energy  $E_k$ , can be described by the hardness factor  $k$ , defined by Equation 7.3

$$k(\Phi_k) = D(\Phi_k) / D_{1\text{MeVn}(95\text{MeVmb})} \quad (7.3)$$

However, such a normalization is only valid for silicon. For any other material including diamond, the damage function will be different. The NIEL for diamond damage functions have been calculated in the past for proton and pion interaction [Laz99], and more recently by a group of the University of Karlsruhe for neutrons and protons of kinetic energies

ranging from 5 MeV to 5 GeV [Boe07]. A modified FLUKA code was used, where nuclear elastic and non-elastic processes are implemented to calculate the fragment and the recoil production rates over the kinetic energy range of the impinging primary particles. The secondaries have been used as an input to the SRIM simulation software [Zie85], which calculates the lattice damage of diamond caused by slow-down fragments, as well as, PKA produced by multiple elastic Coulomb scattering. Theoretical details of damage production in solids can be found in the pioneering work of Kinchin and Pease [Kin52].

In Figure 7.1 the NIEL damage cross-sections of diamond (Right panel) are compared to silicon data (Left panel) [Huh02], both plotted versus the energy of the incoming particles.

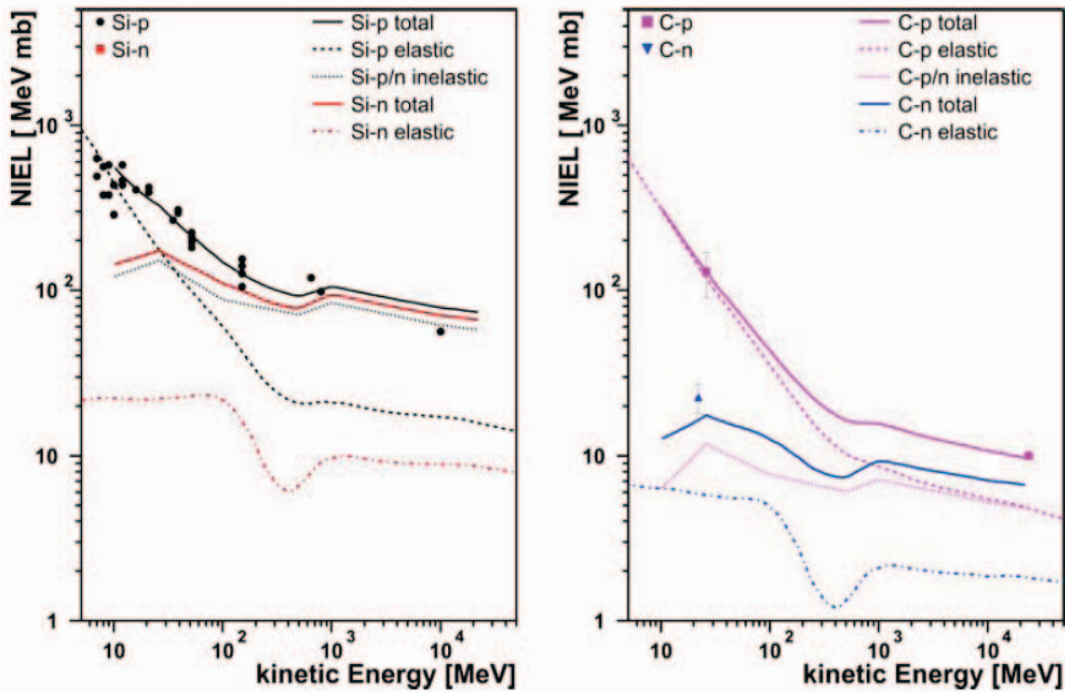


Figure 7.1: NIEL damage cross-sections for protons and neutrons as a function of the incoming particles energy after [Boe07]: (Left panel) silicon, (Right panel) diamond.

As shown in Figure 7.1, the damage cross sections are commonly lower for diamond than for silicon over the full range of the explored energies. Below 100 MeV, the cross sections for charged particles are dominated by Rutherford scattering, which increases rapidly at low energies. Due to the  $Z^2/E^2$  dependence, the radiation hardness of diamond is expected to be a factor 3.6 higher than that of silicon in this energy region. For energies higher than 100 MeV, heavier nuclear recoils are created in the silicon case ( $A_{Si} = 28$ ), leading to an amount of *NIEL* larger by a factor of ten.

The concentration of the primary-radiation induced defects (CPD) in an irradiated material can be calculated using the *NIEL* data as proposed by [Laz98] from the following relation:

$$CPD(E_k) = \frac{\rho}{2E_d}(NIEL) \quad (7.4)$$

where  $E_k$  is the kinetic energy of the incident particle, (*NIEL*) is the corresponding *NIEL* value in [keV cm<sup>2</sup>/g],  $\rho$  is the material density in [g/cm<sup>3</sup>] and  $E_d$  is the threshold energy

needed to displace a host atom from the lattice site.  $E_d$  depends on the direction of the incident particle with respect to the crystal orientation. The diamond values are:  $E_d^{100} = 37.5$  eV,  $E_d^{111} = 45.0$  eV,  $E_d^{110} = 47.6$  eV [Koi92]. In diamond, conversion from NIEL expressed in [MeVmb] to [keV cm<sup>2</sup>/g] can be made according to:

$$100 \text{ MeV mb} \times \frac{10^3 \text{ keV}}{\text{MeV}} \times \frac{10^{-27} \text{ cm}^2}{\text{mb}} \times \left( \frac{\text{mole}(C)}{12 \text{ 01g}} \right) \times \left( \frac{6 \text{ 022} \times 10^{23}}{\text{mole}(C)} \right) = 5.018 \text{ keV cm}^2/\text{g}, \quad (7.5)$$

Taking the calculated NIEL values from Figure 7.1, relation 7.4, and the conversion presented in Equation 7.1.1, the  $CPD$  value after the hadron irradiation discussed in this work is estimated for 26 MeV protons, giving a  $CPD^{26 \text{ MeV } p} = 282 \text{ cm}^{-1}$  and for  $\sim 20$  MeV neutrons  $CPD^{20 \text{ MeV } n} = 47 \text{ cm}^{-1}$

Care must be taken comparing the calculated concentration of primary defects with the experimentally measured defect density. Due to self-annealing processes, a large ratio of the primary induced defect anneals out during the irradiation. The comparison, done by [Mai98] between calculations (TRIM, GEANT) and experimental data for neutron and electron irradiated diamond suggest, that at RT more than 90 % primary created defects may recombine already during irradiation.

### 7.1.2 Types of Radiation Induced Defects in Diamond

In general, when the carbon atom is removed from the diamond lattice, a vacancy and an interstitial atom are created. Those primary defects can form a zoo of complex defects depending on the presence and the type of atomic and structural impurities within the diamond bulk. Furthermore, if the energy transfer to PKA is high enough, damage cascades may result from the original collision, producing complex defects even in a high purity diamond. These defects may not be detected as single vacancies, although they may affect the electronic properties of the diamond by trapping electrons or holes. The comprehensive study of the structure and of the origin of various radiation induced defects in diamond can be found in several publications [Dav99, Cla95, Iak02, Iak04].

**Time evolution of created defects** According to [New02], the activation energies for migration of the primary radiation induced defects in diamond namely, interstitials and mono-vacancies, are relatively high and amount to 1.6 eV and 2.3 eV, respectively. Furthermore, RT irradiation results in a rather low ( $\sim 10\%$  of primary defects) concentration of survived interstitials. A high recombination rate is explained by [New02], introducing a highly mobile form of an interstitial  $I^*$  with a migration energy of only 0.3 eV, which is active during irradiation. Therefore, in intrinsic IIa diamond irradiated at RT, the mono-vacancies are expected to be the main surviving primary defect. Figure 7.2 shows a conventional isochronal annealing of interstitials  $I_{<001>}^0$  (Left panel) and vacancies  $V^0$  (Right panel) in an irradiated IIa diamond [New02]. The residual concentration of  $I_{<001>}^0$  starts to anneal out above  $\sim 600$  K. The first slight decline around 600 K in vacancies annealing curve is due to  $V^0$  recombination with residual interstitials, whereas the second step is attributed to vacancy migration starting above 900 K.

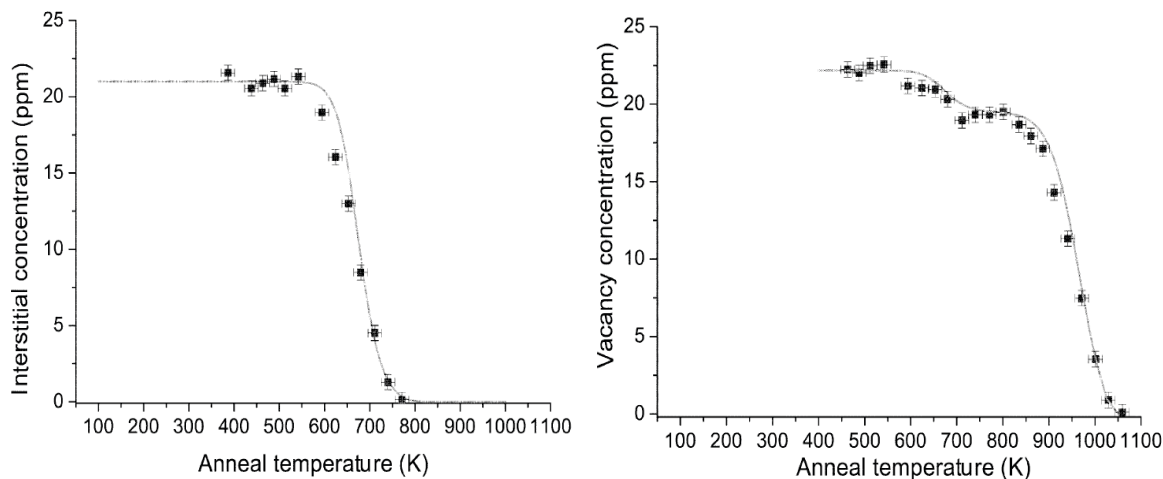


Figure 7.2: Isochronal (30 minutes) annealing of  $I_{<sup>0</sup></math> and  $V^0$  centres in an irradiated IIa diamond. The solid curve (Left panel) shows a fit to the data using mixed first and second order kinetics with an activation energy of 1.6 eV. The solid curve (Right panel) is calculated by assuming that a fraction of  $I_{<sup>0</sup></math> centres recombine with vacancies and that the vacancies also anneal out following a mixed first and second order kinetics with an activation energy of 2.3 eV [New02].$$

The kinetics of the vacancies annealing in IIa diamond has been studied by [Dav02] at 900 - 1050 K. It was shown that the decay of  $V^0$  consists of two phases. In the first short stage, an instantaneous (order of a few minutes) annealing takes place, where about 30 % - 50 % of the vacancies decays. A long term follows short stage with a decay half-life of 1.5 h and 200 h, respectively.

Concluding, in contrast to silicon, where post-irradiation defect migration takes place at RT, the damaged diamond is a much more stable system. Due to high activation energies for the migration of interstitials and vacancies, no defect evolution (annealing and/or formation of secondary defects) with time is expected after an irradiation at RT.

### 7.1.3 Effects on Diamond Bulk Properties

Figure 7.3 shows the electron re-trapping probability in diamond at RT as a function of the activation energy for defects located within the band-gap. Two regions are distinguished: the so-called 'hot' and 'cold' regions. In the hot region, shallow defects dominates, and generate an almost continuous exchange of carriers between conduction band (CB) and the trapping level. The cold region, where the emission probability is low is dominated by deep defects. In this case the trapped charge could not be effectively re-emitted to the CB. Symmetrical processes take place for holes excitation to valence band (VB) maximum.

In general, the energy levels of primary-radiation induced defects (vacancies and interstitials) are located close to the mid-gap of the semiconductor [Kin52], giving rise to the following phenomena: change of the dark current with increasing fluence (caused by the creation of generation-recombination centers), change of the effective doping concentration at large fluences, and finally, decrease of the carrier lifetimes due to an increased trapping probability at radiation-induced defects.

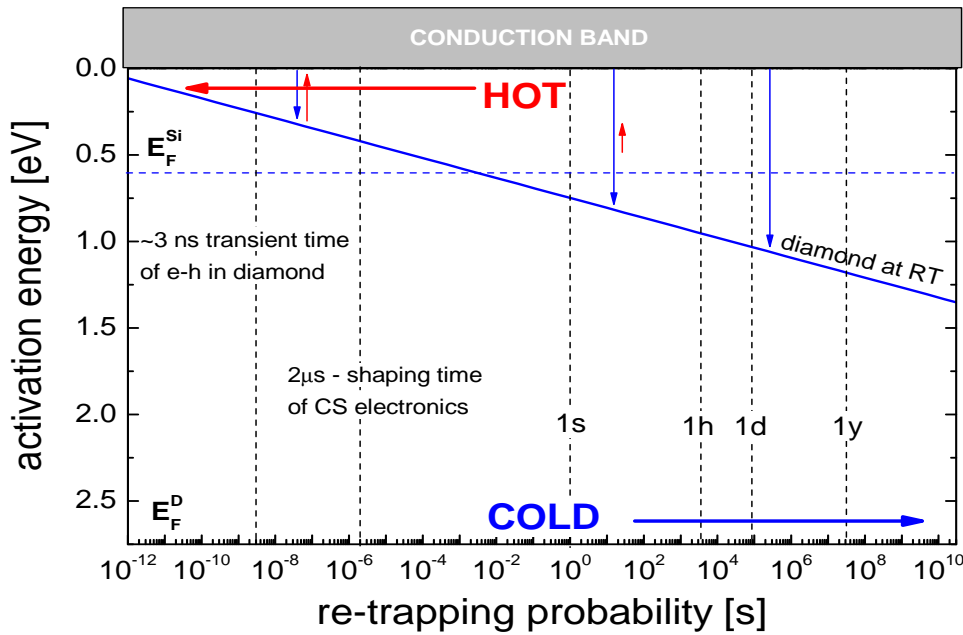


Figure 7.3: The re-trapping probability as a function of the activation energy of trapping center for diamond at RT. The Fermi levels of intrinsic silicon  $E_F^{Si}$  and diamond  $E_F^D$  are indicated in the graph. In the case of silicon, the radiation induced defects are located mainly in the 'hot' region, leading at first to an increase of the leakage current of the detector, whereas defects induced in diamond are located mainly in the 'cold' region with a low probability of re-emission.

**Dark current** When the band-gap of a semiconductor is relatively narrow (like e.g., for silicon at RT - 1.2 eV), radiation-induced defects are activated at RT, acting as generation-recombination centers. Thus a strong linear increase of the dark current is observed for this material at increased fluence [Fur06]. On the other hand, since the irradiation causes the creation of deep defects levels within the energy gap, of a wide band-gap material like diamond, such defects do not contribute to the dark current, but result in trapping centres located well below 1 eV. The dark conductivity of intrinsic wide-bandgap materials is usually governed by native dominant defects with relatively low activation energy. Thus radiation induced deep defects may lead to a partial compensation of shallow states. Consequently, the leakage current in such materials may be decreasing with increasing irradiation fluence.

**Effective doping concentration -  $N_{eff}$**  Vacancies in diamond can be considered as amphoteric impurities, acting as deep donors as well as acceptors, since their charge state depends on the position of the Fermi level [Bas01]. In high purity intrinsic IIa diamond, where the Fermi level is close to the mid-gap, neutral mono-vacancies are the major defect after irradiation. Thus, no change of the effective dopant concentration is expected after irradiation. However, as soon as free carriers are produced by ionizing radiation, the neutral mono-vacancies  $V^0$  can trap the excess carriers becoming charged. As it was shown in [Neb01] and [Pu01], neutral mono-vacancies can be positively  $V^+$  (hole trapping) and negatively charged  $V^-$  (electron trapping), respectively. Charged mono-vacancies give rise

to space charge changing  $N_{eff}$  and also (as it was suggested in [Bas01]) they can form delocalized energy bands. Hereby, the charge conduction takes place due to electron (hole) activation from an occupied donor (acceptor) to a nearest-neighboring occupied donor (acceptor). This conductivity mechanism is characterized by extremely low mobilities and thermal activation energies ranging from 0.35 to 1.15 eV (depending on the vacancies concentration). These effects may lead to the detector polarization, and consequently, to a deterioration of the charge transport within a biased device.

**Charge carrier trapping after irradiation** The lifetime of the charge carriers decreases inversely to the defect concentration. Exposing the semiconductor to a high particle fluence new defects are successively introduced. Therefore the lifetime of the excess charge carriers can be written as:

$$\frac{1}{\tau_{e,h}} = \frac{1}{\tau_{intr}} + \frac{1}{\tau_{ind}} \quad (7.6)$$

where  $\tau_{intr}$  is the charge carriers lifetime of non-irradiated device given by Equation 3.23, and  $\tau_{ind}$  is the charge carriers lifetime limited by defects introduced by NIEL during the irradiation and can be written as:

$$\tau_{ind} = \frac{1}{\Phi_p \beta_p} \quad (7.7)$$

where  $\Phi_p$  is the applied fluence, and  $\beta_p \equiv dN_p/d\Phi_p$  is the primary defects creation rate. According to Equation 7.7, a linear decrease of  $\tau_{e,h}$  with increasing particle fluence is expected in the irradiated material. An important consequence of this Matthiesen's scaling rule is the fact that radiation damage will be much more pronounced in a perfect material (like scCVD diamond) than in defective materials (like pcCVD diamond). Since, for low fluences the concentration of radiation-induced defects is often lower than the concentration of native impurities, the radiation damage effect is 'masked'.

Trapped charge can be re-emitted from a trap e.g., due to thermal or optical excitation. The probability of thermal excitation  $P(\tau_d)$  depends exponentially on the temperature as described by:

$$\tau_d = \frac{1}{\sigma \cdot v_{th} \cdot N_{CB} \cdot \exp(-\Delta E/kT)} \quad (7.8)$$

where  $N_{CB}$  is the density of states in the CB,  $\Delta E$  is the activation energy,  $k$  is the Boltzmann constant, and  $T$  is the absolute temperature.

Due to the relatively narrow band gap of silicon, the fraction of thermally re-emitted charge is high at RT. This leads to a highly increased leakage current and to a change of  $N_{eff}$ . Consequently, the charge collection in silicon detectors is decreased mainly by the reduction of the diode's depletion zone and not by the charge trapping itself. In silicon the charge loss due to the trapping starts to be important only above  $\Phi_{1MeVneq} \approx 1 \times 10^{15} \text{ n/cm}^2$  [Fur06].

For diamond the probability of re-emission at RT is small. Thus after exposure of a diamond detector containing deep trapping centers to the ionizing radiation, a partial recovery of the charge collection efficiency is observed - which is the so-called priming phenomenon or Lazarus effect known from cryogenic silicon. However, according to the Shockley-Read-Hall

Table 7.1: 26 MeV proton irradiation - samples characteristics

sample	dimensions [mm]	electrodes (diameter = 2.9 [mm])
BDS14	$4 \times 4 \times 0.49$	Cr(50 nm) Au(100 nm) annealed
EBS3	$3.5 \times 3.5 \times 0.377$	Cr(50 nm) Au(100 nm) annealed
BDS13	$4 \times 4 \times 0.473$	Cr(50 nm) Au(100 nm) annealed
s256-05-06*	$4 \times 4 \times 0.38$	Al(100 nm)

(\*)damaged surfaces

recombination (SRH) model, when the density of passivated traps increases, the probability of recombination of trapped charge increases as well. Thus, full passivation of deep traps is never possible.

## 7.2 Irradiation Procedures

### 7.2.1 26 MeV Proton Irradiation

**Samples preparation** Four scCVD diamonds (previously used as particle detectors in heavy-ion (HI) experiments) were exposed to 26 MeV proton fluence irradiation. The size of each sample and the type of electrodes applied are listed in Table 7.1. The electrodes were applied in 'sandwich' geometry. The preparation procedure of the electrode fabrication was presented in Chapter 6. The electronic properties of the samples had been measured prior to irradiation by means of I-E(V) and TCT characterization techniques. It was intended to verify any possible damage arising from the previous HI experiments. No observable changes were found comparing properties of these samples to the initial state. In addition, UV-VIS absorption spectroscopy performed at RT before the film metallization revealed full transparency in the VIS region for each sample, with the edge absorption at the band-gap energy of diamond.

**Irradiation procedure** The Kompakt-Zyklotron (KAZ) in Karlsruhe accelerates protons up to an adjustable energy ranging from 18 MeV to 40 MeV. For the irradiation of the scCVD-DDs a proton beam energy of 26 MeV was used. When an impinging particle loses its kinetic energy due to ionization processes also the NIEL cross sections changes (Figure 7.1). In order to introduce a homogenous damage profile, the impinging particles should traverse the irradiated material losing only a low fraction of their kinetic energy. Figure 7.4 (Right panel) shows the ionizing energy loss in 500  $\mu\text{m}$  diamond calculated with the SRIM software. The initial protons kinetic energy is decreased only by about 13 % giving insignificant changes in the NIEL cross-section. Therefore, homogenous damage of the diamond bulk requirement is fulfilled. Figure 7.4 (Left panel) shows the beam line and the irradiation box used for scans perpendicular to the proton beam. The aluminium box was thermally isolated with Styrodur plates and carried a 3 cm thick layer of carbide at the back to stop the protons entering the box through the double mylar foil of the front windows. The diamond samples were glued on Kapton bands and fixed on an aluminium frame, which was placed inside the box. Behind the diamonds,  $^{58}\text{Ni}$  foils were mounted



Table 7.2: 26 MeV Protons: Irradiation Conditions

sample	beam current [ $\mu\text{A}$ ]	irradiation time [min]	integral fluence $\Phi$ [26 MeVp/cm <sup>2</sup> ] scan integration	integral fluence $\Phi$ [26 MeV p/cm <sup>2</sup> ] Ni foil activation
BDS14	0.6	2	$5.35 \times 10^{13}$	$6.38 \times 10^{13}$
EBS3	6	2	$5.35 \times 10^{14}$	$6.11 \times 10^{14}$
BDS13	12	22	$1.07 \times 10^{16}$	$1.18 \times 10^{16}$
s256-05-06	0.2	$6 \times 3$	$1.07 \times 10^{14}$	-

for the verification of the integral fluence applied to the samples. During the irradiation, the aluminium box was flooded with cold nitrogen gas to avoid local overheating of the irradiated devices. The box was moved in  $y$  and  $x$  direction perpendicular to the proton beam by PC controlled step motors with constant adjustable speed and range. Only several minutes were needed to homogenously irradiate an area of 100 cm<sup>2</sup> to a fluence of  $1 \times 10^{14}$  p/cm<sup>2</sup>, using a beam current of 2  $\mu\text{A}$ . Note the maximum current applied for standard irradiations of silicon sensors is 16  $\mu\text{A}$ , above which non-linearities in damage creation had been observed [Fur06]. The summary of the irradiation conditions is given in Table 7.2

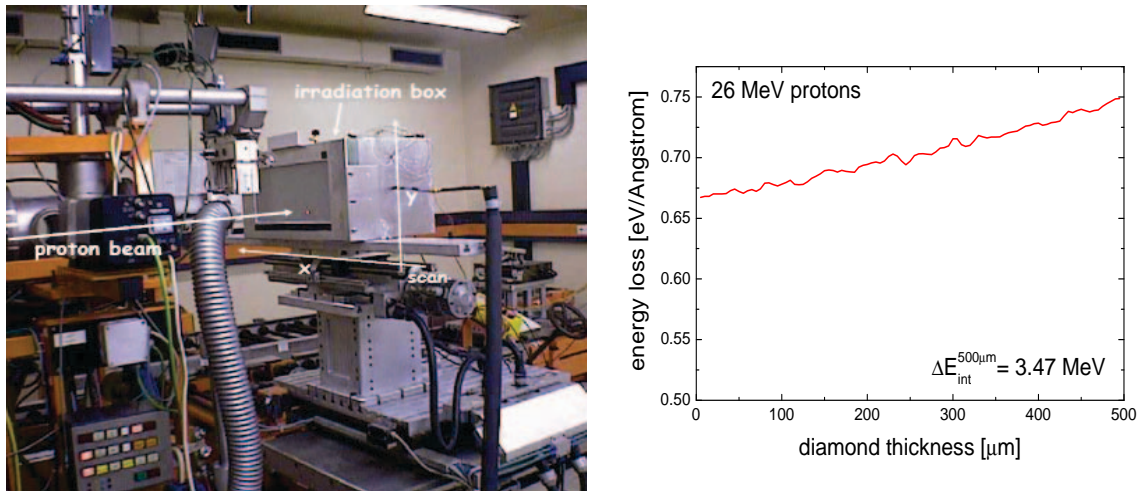


Figure 7.4: (Left panel) Photograph of the irradiation set-up at the Karlsruhe cyclotron. (Right panel) Ionizing energy loss of 26 MeV protons in diamond material. Only about 13 % of the initial kinetic energy is lost within 500  $\mu\text{m}$  of diamond. Therefore, a homogenous distribution of radiation damage through the depth of the sample is expected.

The integral fluences were estimated by means of two methods: from beam current integration over the irradiation time and scan speed. Here, the value of integral fluence was estimated before irradiation. And the more precise, <sup>58</sup>Ni foil activation measured after irradiation, which verified the pre-irradiation estimation. Details of the fluence calculations and methods can be found in [Fur06]. Approximately one week after irradiation, the activity of the diamond samples dropped to the natural background level, enabling off-line characterization of the samples.

Table 7.3:  $\sim 20$  MeV neutron irradiation - samples characteristics.

sample	dimensions [mm]	electrodes ( $\phi = 2.9$ mm)	remarks
BDS12	$5 \times 5 \times 0.46$	Al(100 nm)	2 irradiations
s014-06	$4 \times 4 \times 0.328$	Al(100 nm)	2 irradiations
s014-09	$4 \times 4 \times 0.32$	Al(100 nm)	
john100	$3.5 \times 3.5 \times 0.114$	Al(100 nm)	quadrant electrode

Table 7.4: The high flux fast neutron beam contamination. Values were evaluated using Monte-Carlo simulation by [Ber]

Particle type	% of neutron yield	Avg. energy [MeV]	Max energy [MeV]
proton	0.015	12.61	25
electron	0.016	1.57	6
gamma	2.4	1.93	10

## 7.2.2 20 MeV Neutron Irradiations

**Samples preparation** Four intrinsic scCVD diamonds were prepared for high fluence irradiation with neutrons of  $\sim 20$  MeV energy. The characteristics of the samples are given in Table 7.3. The electronic properties of samples were measured by means of I-E(V), TCT and CCD before and after neutron irradiation. The samples were mechanically clamped between two printed circuits boards (pcb) mounted in an aluminum housing. Each diamond electrode was micro-bonded to individual tracks on the pcb, providing electrical contact to the SMA connectors. For the on-line beam-induced current readout, the bipolar configuration with floating mass potential was used. The signal readout technique is discussed in the next paragraph.

**Irradiation procedure** Irradiations with 20 MeV neutrons were carried out using the high flux fast neutron beam at the cyclotron of Louvain-la-Neuve. By hitting a Beryllium target of a 2 cm thickness and a radius of 4 cm with the primary 50 MeV deuteron beam, neutrons are produced via the  ${}^9\text{Be}(d, n){}^{10}\text{B}$  reaction. To keep the charged particles and gamma contamination as low as possible, a filter stack consisting of 1 cm thick polystyrene, 1 mm cadmium and 1 mm lead, was placed right after the production target. The beam contaminations was evaluated by the accelerator group of Louvain [Ber] using Monte-Carlo simulations. The results are displayed in Table 7.4. The energy spectra of the neutrons presented in Figure 7.6 (Right panel) were obtained from the activation of the several metallic foils using an unfolding procedure. The average energy of the incoming neutron beam was around 20.4 MeV.

During the irradiations, the sensors were placed within the irradiation box, which was made of Styrodur plates. The box has a fixed position at a well defined distance from the production target. The samples were glued on plexiglass plates and inserted into the irradiation box at various distances from the target. In this way, irradiation with various neutron fluxes and thus various integrated fluences was achieved. During the irradiation,

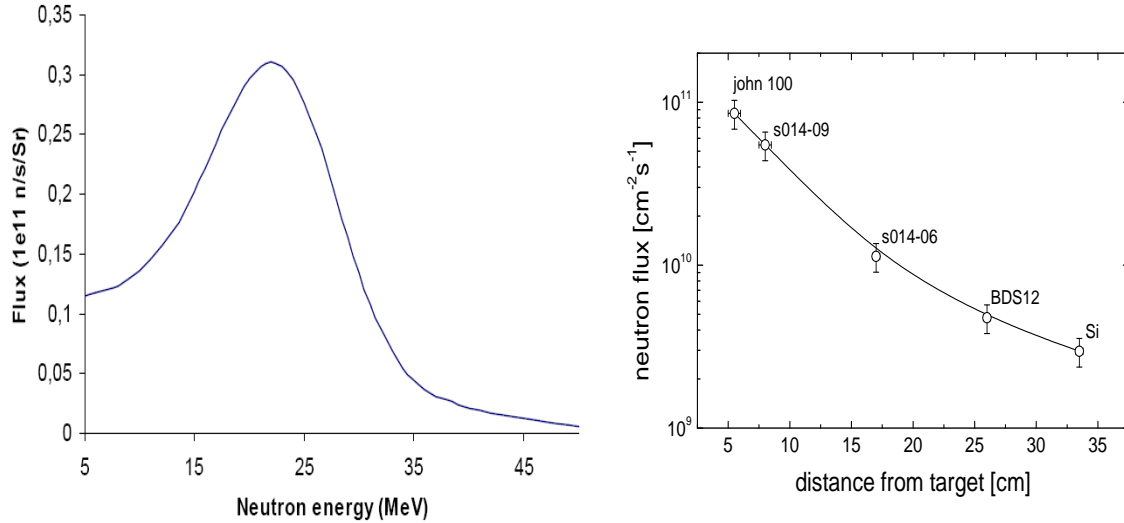


Figure 7.5: (Left panel) Energy spectrum of the incoming neutrons. The mean energy of the neutrons amounts to  $\sim 20.4$  MeV [Ber]. (Right panel) Neutron fluxes at distances from the production target.

Table 7.5: 20 MeV Neutrons: Irradiation Conditions

sample	Integrated fluence		On-line monitoring	
	PAD dosimetry	current int.	detector bias [V]	final CCD [ $\mu\text{m}$ ]
BDS12	$1.14 \times 10^{14}$	$1.16 \times 10^{14}$	200	81
BDS12	$1.97 \times 10^{14}$	-	-	-
s014-06	$2.71 \times 10^{14}$	$2.69 \times 10^{14}$	320	71
s014-06	$5.92 \times 10^{14}$	-	-	-
s014-09	$1.31 \times 10^{15}$	-	320	47
john100	$2.05 \times 10^{15}$	$2.63 \times 10^{15}$	200	17

the box was closed and flooded with cold nitrogen gas, to avoid overheating of the sensors.

A schematic of the detectors irradiation geometry is presented in Figure 7.6 (Left panel). The dimensions are given in mm. The samples s014-06 and BDS1 were placed inside the irradiation box. The others (john100 and s014-09) were mechanically fixed outside the box as close as possible to the production target in order to achieve a higher fluence within the same irradiation time. Two silicon PIN diodes placed behind the diamond detectors were irradiated in parallel. Each sample was electrically connected using 15 m long coaxial cables via a bipolar configuration with the HV source and with the readout electronics placed in the control room.

In order to evaluate the integral fluences applied, several Polymer Alanine Dosimeters (PAD) were glued as close as possible to the diamond detectors. The irradiation conditions are summarized in Table 7.5. The details of the fluence calculations are presented in [For06]. Due to the high activation, the samples were stored after irradiation at RT for two weeks at the cyclotron site.

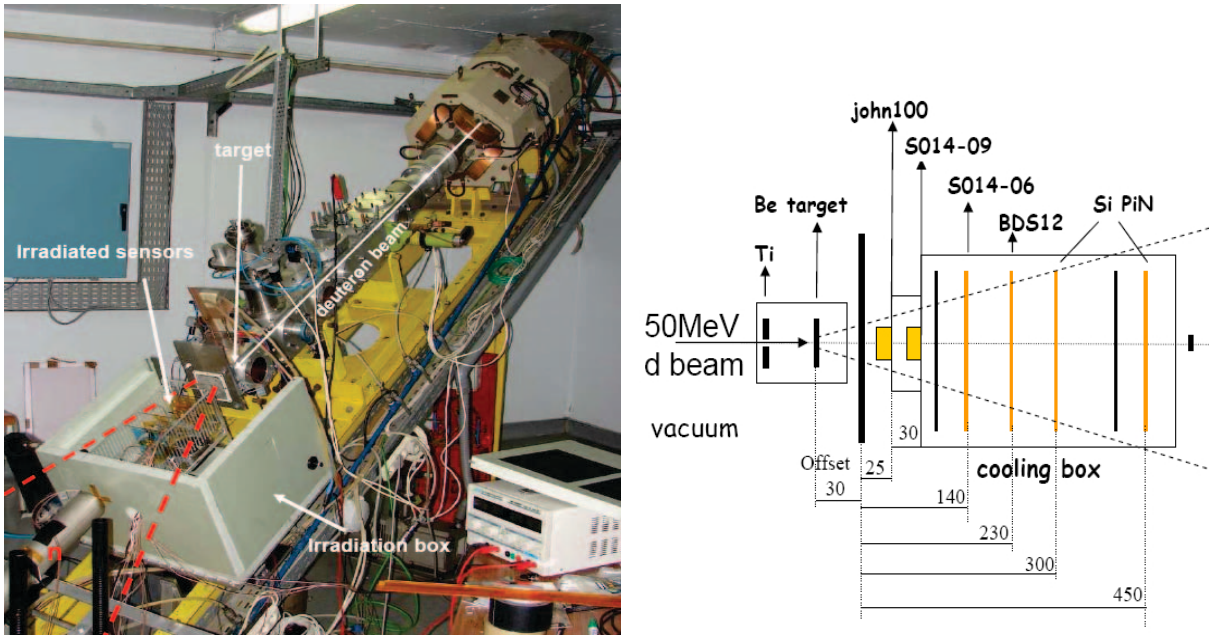


Figure 7.6: (Left panel) Photograph of the experimental environment at the high flux neutron beam line of the Louvain-la-Neuve cyclotron. (Right panel) Schematic representation of the irradiation geometry, dimensions are given in [mm].

**On-line monitoring** Because of a low gamma and charge-particle background of the neutron beam, the beam-induced current of the diamond detectors could be monitored on-line without a saturation of the readout electronics. During the neutron irradiation the diamond detectors were biased using a HV power supply. A DC current monitoring in integration intervals of 100 ms was carried out by means of a 8-channel current-to-frequency converter, designed originally for a Beam Loss Monitoring (BLM) system at the LHC [Zam05]. The detector bias conditions are listed in Table 7.5. Parallel to the diamonds irradiation, Float Zone (FZ) silicon Hamamatsu diodes [Fur06] were irradiated and monitored with the same converter.

Figure 7.7 displays the on-line current behavior of four scCVD-DDs and of a silicon diode, recorded during more than six hours of irradiation. The current values are not normalized in this plot and a logarithmic scale is used to illustrate the main differences between diamond and silicon detectors operating under high radiation fluxes. On the top, the deuteron beam current is shown (red curve), which was kept close to  $11 \mu\text{A}$  almost during the entire irradiation time.

The measured currents (including also the dark current of the devices) are before damaging proportional to the beam flux. As shown in Figure 7.7, the diamond samples beam-induced current (colour curves) decreases during irradiation, what indicates progressive creation of the bulk damage. However, no arbitrary current fluctuations are observed. When the beam was switched off for a few minutes (indicated by gray dashed lines), the diamond currents drop by three orders of magnitude. Concluding, the contribution of the leakage current to the total measured current was negligible for the damaged diamond detectors up to the end of the irradiation. In contrast, the created defects in silicon (black curve), led to a strong increase of the leakage current. Note that the silicon detectors were placed behind the diamonds inside the cooling box. Thus the beam flux was lower than for

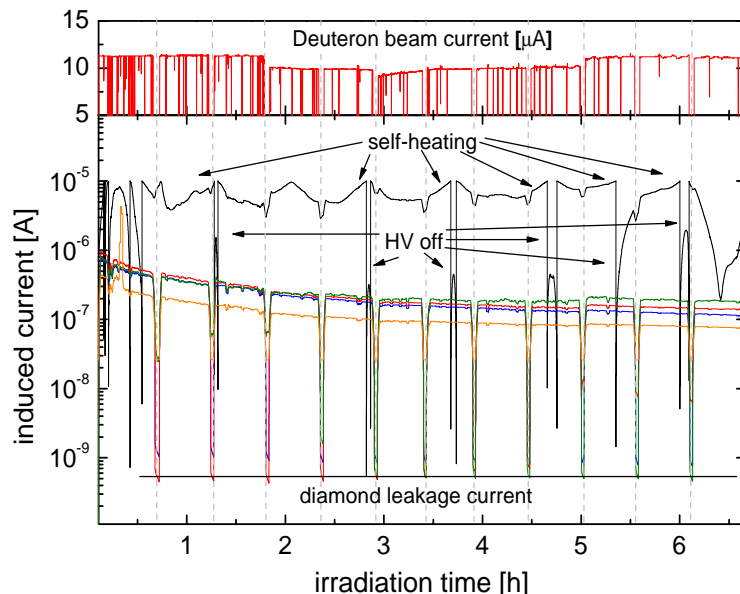


Figure 7.7: On-line monitoring of the beam-induced currents during the 20 MeV neutron irradiation (raw data). The black curve shows the response of a silicon PIN diode, the colour curves the response of four scCVD-DDs. The red curve on top represents the deuteron beam current.

any of the diamond detectors (see Figure 7.5 (Right panel)). The cooling to  $-10\text{ }^{\circ}\text{C}$ , was not sufficient to prevent self-heating of the silicon sensor, which appeared unstable. The progressive increase of the leakage current led to a thermal runaway and in order to stop this process, the detector bias was reduced (indicated by arrows). A stable operation was not possible in the case of the damaged silicon sensors. At the beam off condition, the induced signal drops only by factor of two, showing that in this case the contribution of the leakage current to the total measured signal is significant.

In order to evaluate the degradation of the charge-collection properties of diamond detectors during the irradiation, the measured beam induced currents were normalized to the initial values (assuming that the CCE was 100 % at the beginning of the irradiation). The results are plotted in Figure 7.8. A fast decay of the CCE is observed for all detectors in the first 2 - 3 hours of irradiation. Afterwards, the CCE stabilizes, tending to saturate to about 10 % of the initial value for all samples, independent of thickness and bias applied. Due to the fact that the CCE at the end of diamond irradiation was  $\ll 100\%$ , the approach  $\text{CCD} = \text{CCE} \cdot d$  can be made. The measured CCD values are indicated in the graph and listed in Table 6.5.

The unexpectedly low values of the CCD for all diamond devices result from detector bias-induced polarization (see Figure 7.17), which leads to a modification of the internal electric field and therefore to a partially depleted detector. The observed large drop of the CCD is related to the decrease of the detector active region and not only to the charge trapping by the induced defects. The measured saturation of CCE to 10 % can be explained by the fact that the width of the depleted region (where charge carrier drift takes place) is narrower than the effective CCD of the non-polarized damaged detector.

The current on-line monitoring is a powerful technique giving direct information about the degradation of the charge transport properties of a detector as a function of the applied particle fluence. However, one must be careful with the general interpretation of these data. Although the CCD values measured on-line by means of the tunnel card matches perfectly the off-line characterization obtained from in the laboratory after irradiation (see following sections), these values are strongly dependent on the conditions of the device operation,

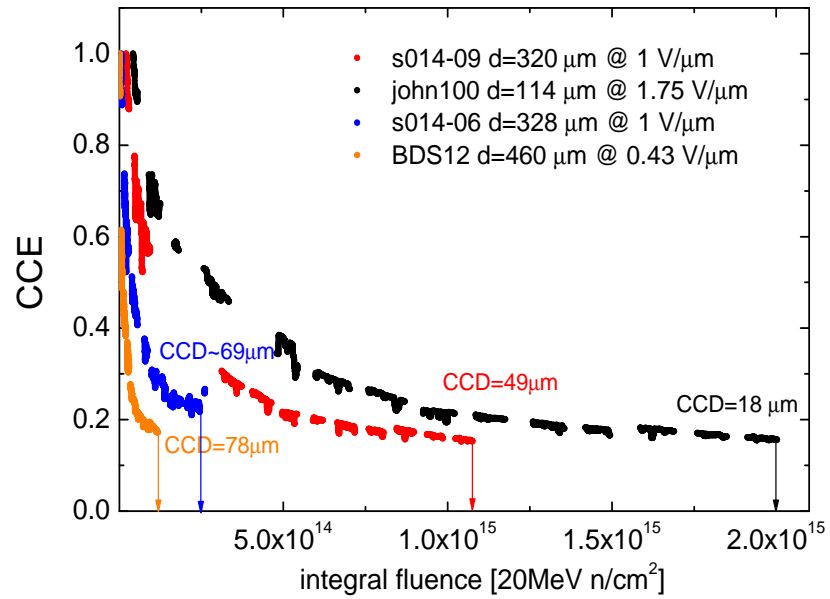


Figure 7.8: On-line monitoring of scCVD-DDs during 20 MeV neutron irradiation. The measured beam-induced current values are normalized to the initial values and presented in terms of CCE.

namely: the detector bias and the type of the metallic electrodes used.

## 7.3 Radiation-Induced Defects Identification

### 7.3.1 UV-VIS Absorbption Spectroscopy

Intrinsic, non irradiated scCVD diamonds are fully transparent in the VIS - UV range revealing an edge absorption at 224 nm, which corresponds to the electrons transition from the VB maximum to the CB minimum. Heavy irradiation induces a variety of lattice defects, depending on the radiation type and the type of diamond itself. The localized energy states introduced within the diamond band-gap lead to a modification of the intrinsic absorbption spectra. The most comprehensive review of optically active centers in diamond can be found in [Zai01].

Figure 7.9 shows UV - VIS absorbption spectra measured at RT with sample BDS13 before irradiation (black line), as well as the spectra for four diamonds irradiated with neutrons and protons (colour lines). Clear deviation from the 'edge' absorption is observed for all irradiated samples indicating the bulk damage. Two separate, irradiation induced broad absorption bands can be distinguished: the General Radiation (GR1) phonon side band (1.6 eV - 2.3 eV), and an 'ultraviolet continuum' band (2.8 eV - 5.5 eV), respectively. The latter results from charge-carrier photo-excitation from defect ground states to the CB or/and to the VB. While the shape of the spectra are similar for all samples, a spectral identification of defects at RT is difficult due to phonon washout. At low temperature where lattice vibrations are 'frozen out', zero-phonon transitions are possible, giving rise to a sharp spectral line(s) specific for a given defect.

In order to detect Zero-Phonon Lines (ZPL) of radiation-induced defects, UV - VIS absorbption spectra were measured with BDS13 at cryogenic temperatures ranging from 7 K to 77 K. Figure 7.10 shows the spectrum obtained at 7 K.

Three ZPL are observed:



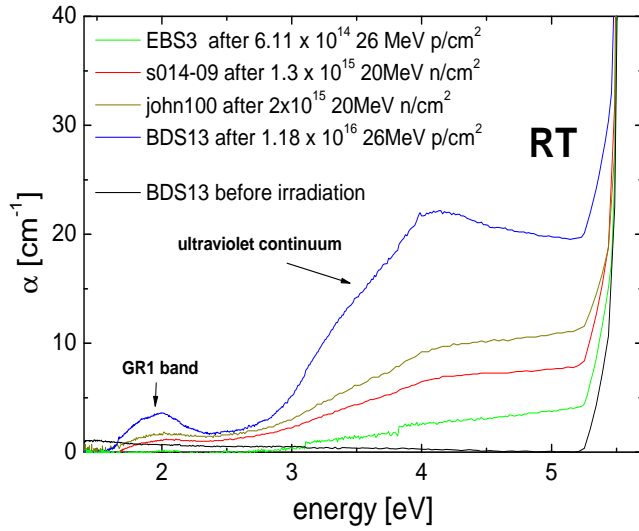


Figure 7.9: UV - VIS absorption spectra of neutron and proton irradiated diamonds, measured at RT. Two continuous bands appear after hadron irradiation: the GR1 band, related to the mono-vacancy, and a band referred as the ultraviolet-continuum, the result of a charge carriers photoexcitation from defect states to the VB or/and to the CB.

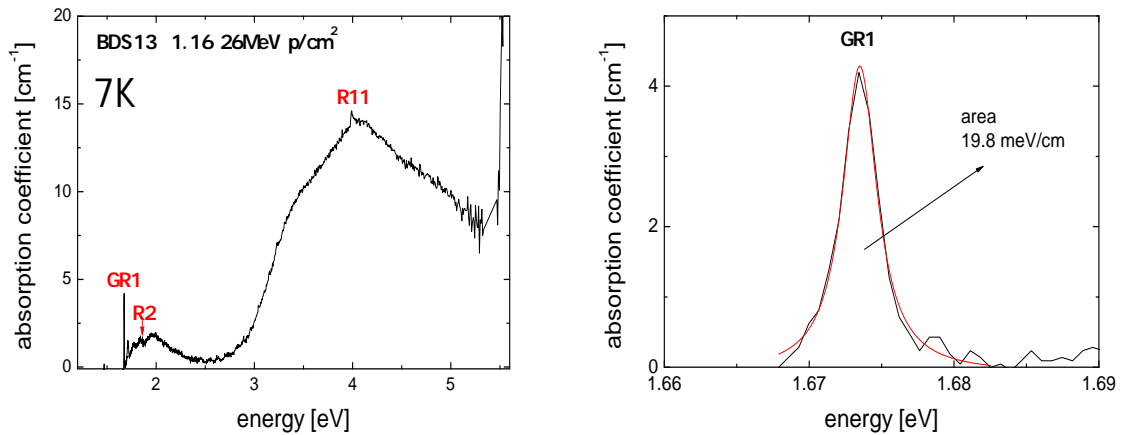


Figure 7.10: (Left panel) UV - VIS absorption spectrum of BDS13 measured at 7 K after 26 MeV proton irradiation. Three ZPL can be distinguished, related to GR1, R2 and R11 centres. (Right panel) Detailed view of the absorption spectrum around  $\sim 1.673$  eV, showing the ZPL of the GR1 center.

- at 1.673 eV (740 nm); the ZPL of the GR1 center, which is attributed to a neutral mono-vacancy defect  $V^0$  [Dav02, Lan68];
- at 1.859 eV; the ZPL of the R2 center, which is attributed to a neutral isolated  $\langle 001 \rangle$ -split self interstitial defect  $I_{\langle 001 \rangle}^0$  [New02];
- at 3.98 eV; the ZPL of the R11 center, which is produced by a transition to an excited state of the R2 center [All98].

The absence of the ND1 at 3.15 eV and other nitrogen related centers like H3 at 2.463 eV, is a proof of the low concentration of nitrogen impurities in the investigated scCVD diamonds. Furthermore, the absence of ZPL like 5RL (cluster of interstitials) at 4.581 eV, R1

(di-interstitial) or TH5 (di-vacancy) at 2.545 eV, suggests that neutral mono-vacancies are the dominant defects after the 26 MeV proton irradiation.

The concentration of neutral mono-vacancies  $N[V^0]$  and self interstitials  $N[I_{<001>}^0]$  can be calculated from the integral intensities of the GR1-ZPL and the R2-ZPL respectively, according to the following equation:

$$N[V^0] = \frac{A_{str}}{f} \quad (7.9)$$

where  $A_{str}$  is the absorption strength of the ZPL of GR1- or R2 centers given by:

$$A_{str} = \int_{ZPL} \alpha(E) dE \quad (7.10)$$

and  $f$  is the calibration constant of proportionality between the absolute defects concentration and the ZPL intensity obtained from ESR measurements by [Twi99]. The calibration constants for GR1- and R2-ZPL amount to  $f_{GR1} = 1.233 \times 10^{-16} \text{ meVcm}^2$  and  $f_{R2} = 1 \times 10^{-17} \text{ meVcm}^2$ , respectively.

From Equation 7.9 integrating the ZPL of GR1 (Figure 7.10) (Right panel) one gets the concentration of the produced vacancies for sample BDS13  $N[V^0] \approx 1.6 \times 10^{17} \text{ cm}^{-3}$ . A similar integration of the R2-ZPL center gives  $N[I_{<001>}^0] \approx 3.8 \times 10^{14} \text{ cm}^{-3}$ . Only a small part of single interstitials survive after irradiation at RT, compared to the neutral mono-vacancy concentration. The vacancy-production rate is estimated to  $\sim 13.5 \text{ cm}^{-1}$ . The obtained value is about  $\sim 20$  times lower than the value calculated from the simulated *NIEL* proton curve, indicating that due to self-annealing processes only, about 4 % of the primary created defects survive.

Assuming a constant damage rate increasing proportional with the proton fluence,  $V^0$  concentrations are estimated for the rest of the irradiated samples: BDS14 -  $N[V^0] \approx 8.65 \times 10^{14} \text{ cm}^{-3}$ , EBS3 -  $N[V^0] \approx 8.24 \times 10^{15} \text{ cm}^{-3}$  and s256-05-06 -  $N[V^0] \approx 1.44 \times 10^{15} \text{ cm}^{-3}$ .

### 7.3.2 Photoluminescence Spectroscopy

**Set-up and Methodology** Micro-photoluminescence characterization of the four neutron irradiated diamonds were carried out at a temperature of 77 K using a LabRam HR800 equipment, where the source of excitation is the 514.0 nm Argon-ion laser. The laser beam was focused in a spot of about 10  $\mu\text{m}$  and the PL light was collected by a confocal microscope, where the focal point was adjusted about 20  $\mu\text{m}$  below the diamond surface. In order to probe the homogeneity of the damage, a few spots were chosen for each sample in regions close to the edge and close to the middle of the samples.

**Results and discussion** PL spectra of all samples are plotted in Figure 7.11. The sharp line furthest to the left corresponds to the wavelength of the excitation light, the next line to the first order anti-Stokes Raman shift of the excitation light with a Raman frequency of  $1332 \text{ cm}^{-1}$ , which is the fingerprint of the diamond structure. A further strong luminescence peak is observed at 742 nm, which is the ZPL of the GR1 center, related to the excited state of the neutral mono-vacancy.

The broad background might be attributed to the surface defects arising from polishing processes - this hypothesis needs further verification. The zoomed spectra of two samples



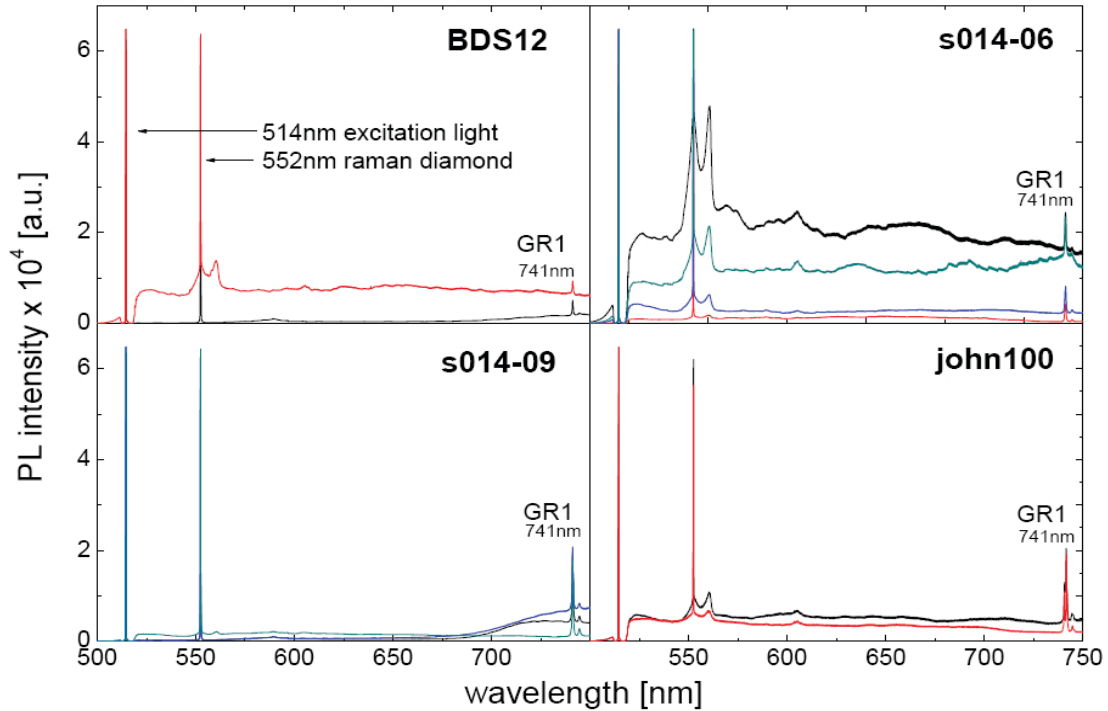


Figure 7.11: Photoluminescence (PL) spectra of neutron irradiated diamonds, measured at 77 K. One radiation induced strong PL center has been found at 741 nm (1.673 eV), which corresponds to the ZPL of the GR1 center.

(s014-09 and BDS12) are plotted in Figure 7.12. The logarithmic scale is used to demonstrate presence of the residual defects. A few sharp ZPLs of low intensity were found: the neutral nitrogen mono-vacancy complex ( $NV^0$ ) at 575 nm, and the neutral  $\langle 0\ 0\ 1 \rangle$ -split self-interstitial ( $I_{\langle 001 \rangle}^0$ ) at 664.5 nm. The origin of the other ZPLs is not known. However, comparing the intensity of those residual lines to the GR1 intensity, for example for the BDS12 sample (lowest irradiation fluence), one can see that the peak area ratio is in order of 0.001. In conclusion, as it was also the case for the 26 MeV proton irradiation, the neutral mono-vacancy is the main defect produced by the neutron irradiation.

Although photoluminescence is a very sensitive technique, it cannot give absolute number of defect concentrations. Nevertheless, by normalizing the spectra to the intensity of the first Raman line, a relative comparison of the defect concentration can be made for the four irradiated samples. Figure 7.13 (Left panel) shows the region around 741 nm with the GR1 peaks of all irradiated samples. The area below the peaks is proportional to the concentration of vacancies. The 2.4 meV split of the GR1 ground level state observed for the sample *john100*, is most probably induced by stress in the diamond lattice [Bra81].

The average values of GR1 integrals are plotted in Figure 7.13 (Right panel) as a function of the neutron fluence. Perfect linearity is found indicating a constant production rate of mono-vacancies for the range of the integral fluences applied.

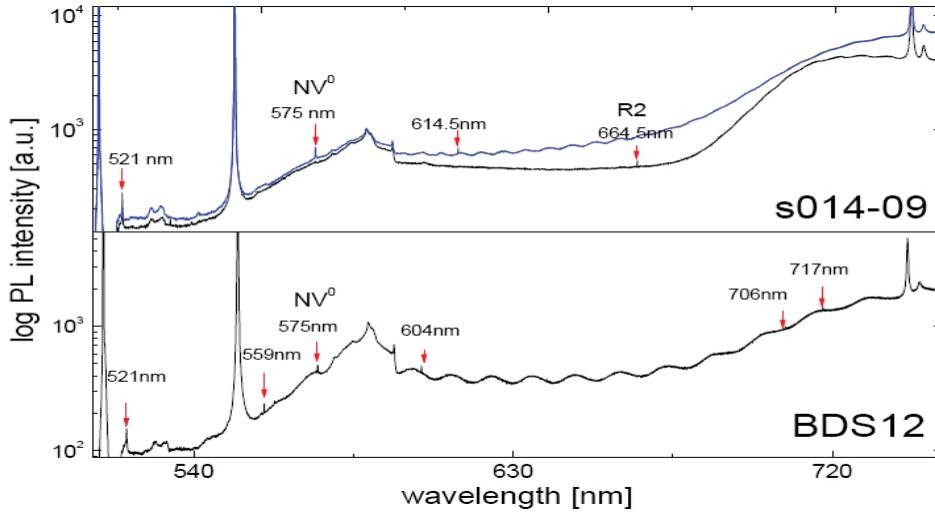


Figure 7.12: Zoomed PL spectra of two scCVD revealing residual defects. Among them, the complex of nitrogen and the neutral mono-vacancy  $NV^0$  at 575 nm and a  $\langle 001 \rangle$ -split interstitial  $I_{\langle 001 \rangle}^0$  at 664.5 nm may be identified. Comparing to the GR1 intensity, the residual defects concentration is negligible.

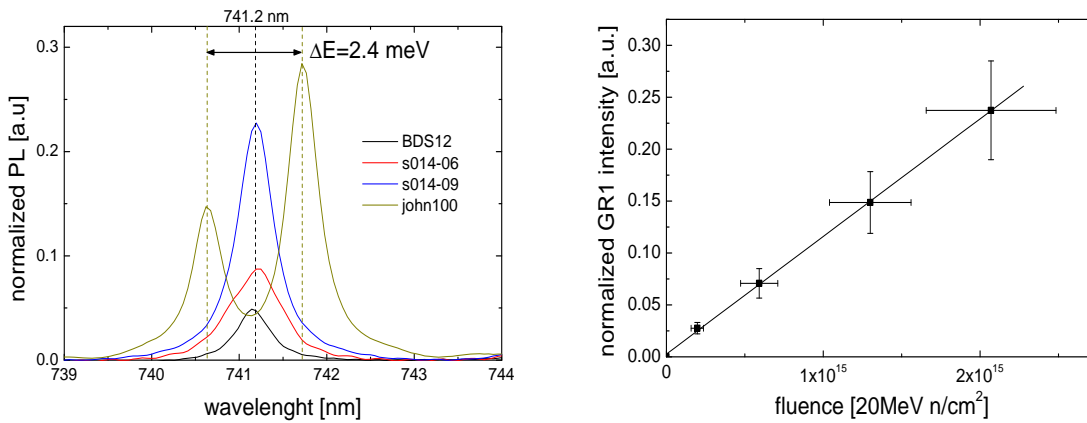


Figure 7.13: (Left panel) Normalized PL signals at 741.2 nm (ZPL of the GR1 center) from neutron irradiated scCVD diamonds. The split of the line observed from sample *john100* indicates presence of strong lattice stress [Bra81] (Right panel) Intensity of the GR1 line as a function of the integral neutron fluence.

## 7.4 Electronic Properties of Irradiated scCVD-DDs

### 7.4.1 I-E(V) Characteristics

The I-E(V) characteristics of irradiated samples were measured in the unprimed state using the set-up shown in Chapter 6. The results obtained after proton irradiation (Left panel), and after neutron irradiation (Right panel) are displayed in Figure 7.14.

Black curves represents the I-E(V) characteristic before irradiation and the red ones after irradiation. If leakage current was measurable before irradiation, it dropped strongly

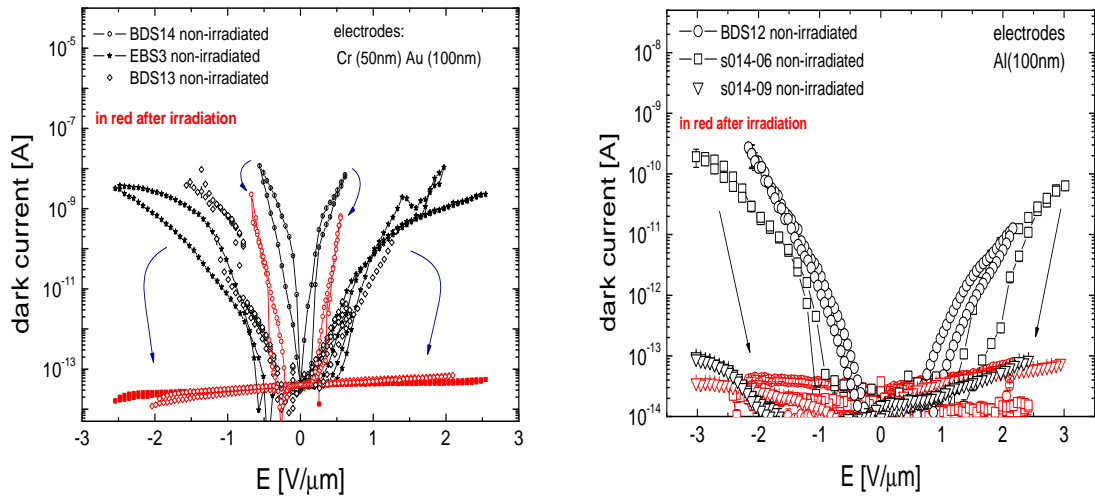


Figure 7.14: I-E(V) characteristics of irradiated diamond detectors (red curves) after 26 MeV proton irradiation (Left panel) and 20 MeV neutron irradiation (Right panel). Black data points show the corresponding leakage current before irradiation. In both cases, a strong suppression of the dark conductivity is observed after irradiation.

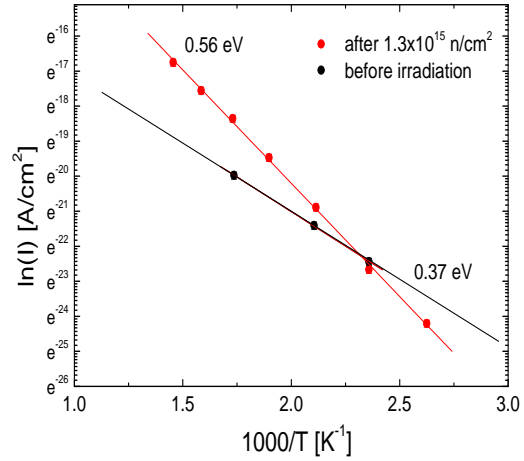
for samples irradiated above  $10^{14} \text{ cm}^{-2}$ . For the lowest particle fluence  $5.35 \times 10^{13} \text{ cm}^{-2}$  - sample BDS14 only a partial leakage current suppression takes place. Similar behavior had been measured by other authors for pcCVD diamonds as well as for IIa HPHT and natural diamond detectors [Tan05, Ale02]. This behavior can be explained by the compensation of shallow defects located at dislocations and grain boundaries (in the case of pcCVD) by deep states of neutral mono-vacancies created during the irradiation, which are located approximately in the mid-gap at 2.85 eV above VB [Pu01]. Injection and recombination of charge carriers by the shunt paths is less efficient, leading to a suppression of the 'soft-breakdown' part of the I-E(V) characteristics of intrinsic samples. After irradiation, the measured current in the region of the I-E(V) characteristic before the SCL conductivity takes place is thermally activated with higher energy. Figure 7.15 shows the Arrhenius plot of sample s014-09 measured at  $0.3 \text{ V}/\mu\text{m}$ , illustrating the differences in the dark current activation energy.

The dark current activation energy changes from 0.37 eV (residual boron impurity) before irradiation to 0.56 eV after irradiation, indicating compensation of the boron acceptors by the created neutral mono-vacancies [Pri02].

## 7.4.2 Transient Current Signals

**Set-up and Methodology** Transient current signals induced by  $\sim 5.5 \text{ MeV}$   $\alpha$ -particles in scCVD-DDs were measured before and after high fluences hadron irradiation as a function of the detector bias. The experimental setup used and the applied methodology are described in Chapter 6. Additional care had to be taken when working with irradiated samples: The radiation-induced defects act as deep trapping centers. Thus, the exposure to  $\alpha$ -particles must be short in order to avoid detector polarization. Therefore, the measurement time

Figure 7.15: Arrhenius plot of the sc-CVD (sample s014-09) dark current measured at 0.3 V/ $\mu\text{m}$  before (in black) and after (in red) the neutron irradiation. A change of the activation energy from 0.37 eV to 0.56 eV is observed after neutron irradiation.



of max. 30 s was chosen for each voltage step. During this time, about 30 - 50 events were registered, and used in the following for analysis. The bias voltage was off for about 5 minutes between each measurement step in order to minimize DC bias induced polarization (discussed in the next paragraph). In order to settle a defined state of traps population for each sample, the diamond films were annealed prior to the TCT for several seconds at 500 °C using a resistive heater.

The measured TC signals after irradiation were corrected for the charge trapping using the following relation:

$$\int_{t=0}^{t=t_{dr}} I_{irr}(E, t) \cdot \exp(t/\tau_{e,h}) dt = \int_{t=0}^{t=t_{dr}} I_{vir}(E, t) dt \quad (7.11)$$

where  $I_{irr}(E, t)$  is the TC signal at a certain applied electric field  $E$  after irradiation,  $I_{intr}(E, t)$  is the TC signal of an intrinsic detector before irradiation, and  $t$  is the drift time. The free-parameter  $\tau_{e,h}$  is the effective trapping time after the samples irradiation given in Equation 7.6.

**Transient current signals of scCVD-DDs after 26 MeV proton irradiation** Examples of TC signals of three irradiated samples are presented in Figure 7.16 (thin color curves). For the heaviest irradiated diamond BDS13, no detectable TC signal was observed. Consequently, this indicates that the charge carriers lifetime for this sample was below 100 ps. Such narrow signals could not be processed due to the limited bandwidth of the readout electronic used.

The trapping-corrected TC signals (displayed as a color thick curves) match perfectly the TC signals before irradiation (black thick curves). There is no slope observed on the curves plateau after correction and the transit time (thus the charge carriers drift velocity) remains the same after irradiation. This shows that the effective space charge produced is neutral and that carrier scattering at the created defects is negligible, most probably due to a non-charged state of the defects. This result agrees with the UV - VIS absorption as well as with the PL spectroscopy, where only  $V^0$  defects (GR1) were detected.

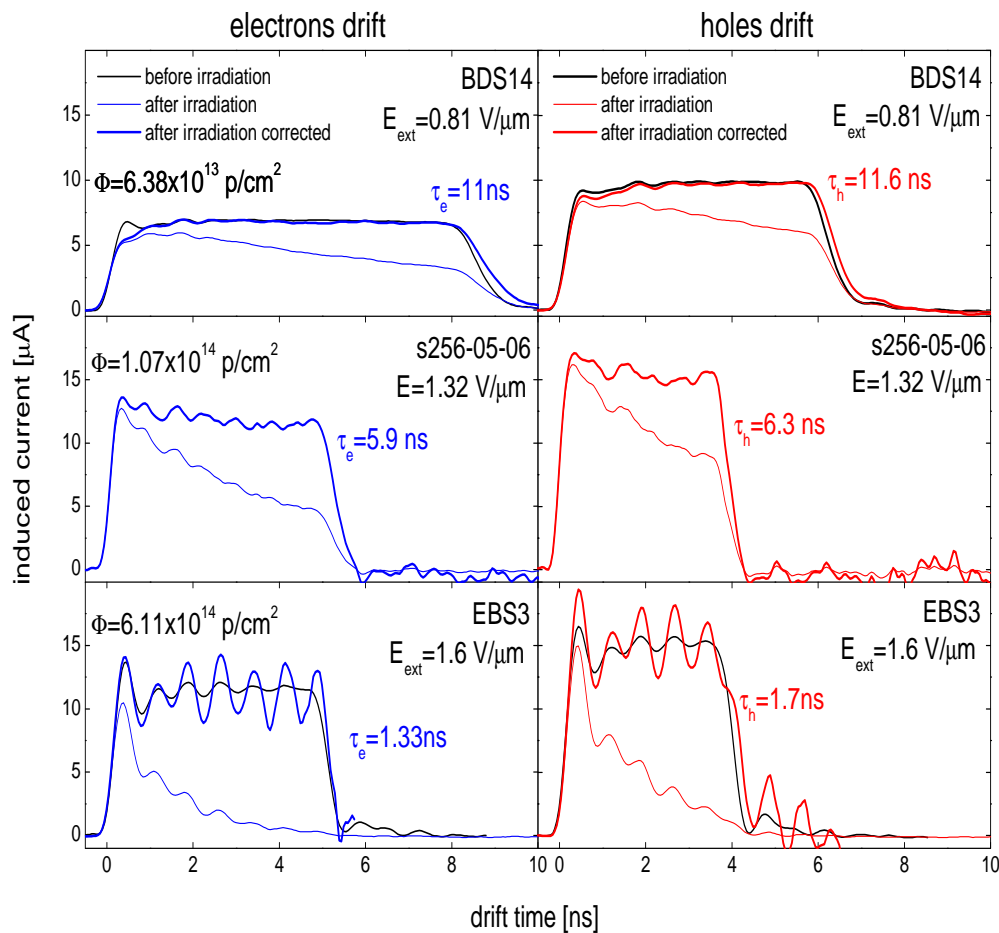


Figure 7.16: TC signals of scCVD-DD induced by 5.5 MeV  $\alpha$ -particles after irradiation with 26 MeV protons (thin colour curves). The detectors were plated with Cr(50 nm)Au(100 nm) electrodes. Prior to the measurement, the samples were shortly annealed at 500 °C. The black curves show the TC signals before irradiation. The thick colour curves are trapping-corrected signals after irradiation.

**Transient current signals of scCVD-DDs after 20 MeV neutron irradiation** In contrast to the proton irradiated samples plated with Cr(50 nm)Au(100 nm) electrodes, the characterization of the neutron irradiated samples, plated with Al(100 nm) electrodes, appeared difficult. No TC signals could be registered for electron drift measurements, and only highly distorted signals were obtained for holes drift measurements. A possible explanation is a phenomenon, which in the following is called 'DC bias-induced polarization'. Figure 7.17 shows the TCT signals at different time intervals after detector biasing. The detector is metallized with Al electrodes and was irradiated with  $\sim 10^{14}$  neutrons/cm<sup>2</sup>. An  $\alpha$ -particle injection (limited to five single events per step) was used to probe the internal electric field profile. Fast polarization of the detector is observed, where the internal electric field close to the holes collecting electrode vanishes within a few seconds after applying positive bias (A, B). For negative bias full polarization occurs after several minutes (C, D). For both bias polarities, progressive strong enhancement of the field close to the anode takes place (A,D) within several minutes. As a result, the detector is not fully depleted. A possible explanation for the deterioration of the field profile could be injection of electrons through the cathode and a subsequent time-dependent expansion of this space-charge towards the anode, where the electrons could not be effectively extracted from the diamond. The space charge transport may be related to conductivity through band states of neutral mono-vacancies [Bas01]. Switching off the bias for a few minutes neutralizes the polarization and causes the process to begin again. The 'bias-induced polarization' had been previously observed in cryogenic silicon detectors when operating detectors in reverse bias [Bor00] as well as in CdTe detectors [Fin06].

In order to avoid this problem, the samples were cleaned using the procedure presented in Chapter 6. Afterwards, they have been re-metallized with Cr(50 nm)Au(100 nm) electrodes and annealed at 500 °C for 10 minutes. The re-metallized sensors showed reduced bias-induced polarization, enabling thus TCT characterization. The TC signals of sample *john100* metallized with a quadrant motif were strongly affected by the edge events and highly reduced lifetime of the charge carriers after irradiation. Therefore, this sample was excluded from the transient current analysis. Figure 7.18 shows the results of the rest three neutron-irradiated samples obtained after re-metallization.

Due to the presence of space charge, the TC signals after correction (thick color curves) still exhibit a slightly negative slope, indicating that the diamond bulk or bulk regions close to the electrodes are not completely neutral in this case. Although the measurements were carried out within a short interval after biasing the sample, a weak bias-induced polarization was impossible to avoid. At effective trapping times below 1 ns, where the majority of the charge carriers is trapped before reaching the opposite electrode, an unavoidable amplification of the electronic oscillations was observed after signal correction. Therefore, the value  $\tau_{e,h}$  given for the sample s14-09 is only a rough estimation.

**Effective trapping times after proton and neutron irradiation** The correction procedure applied for the TC signals measured at various electric fields  $E$  allows to extract the effective deep trapping times  $\tau_{e,h}$ . The results are plotted in Figure 7.19. The error bars are within the graphical representation of the data symbols. It should be noticed that  $\tau_{e,h}$  increases slightly for all samples with increasing electric field, more pronounced for thick samples (with about 35 % increase at high field). This can be explained by a decrease of the charge carrier transversal diffusivity at high electric fields  $E > 1$  V/ $\mu$ m. The inverse

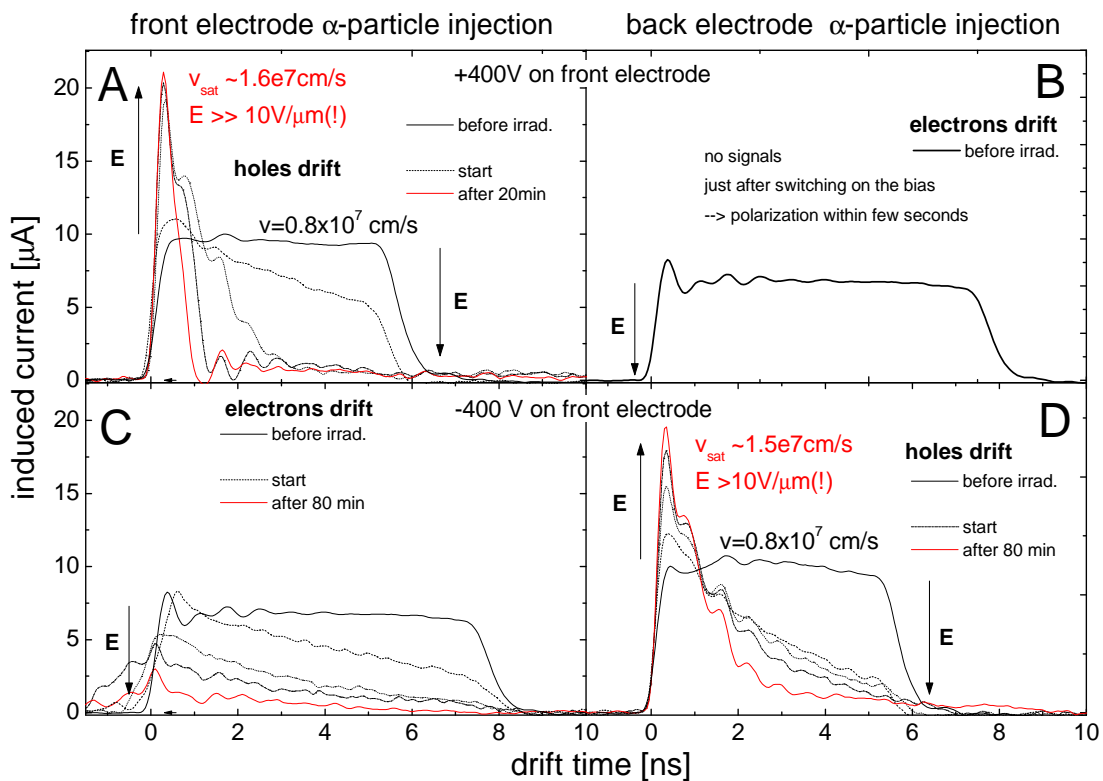


Figure 7.17: Profiling of the internal electric field of the neutron-irradiated detector BDS12 during 'DC bias-induced polarization'. The sample was metallized with Al(100 nm) electrodes. After several minutes, the internal electric field close to the cathode vanishes, whereas a strong field increase is observed close to the anode. This results in a partial depletion of the sensor.

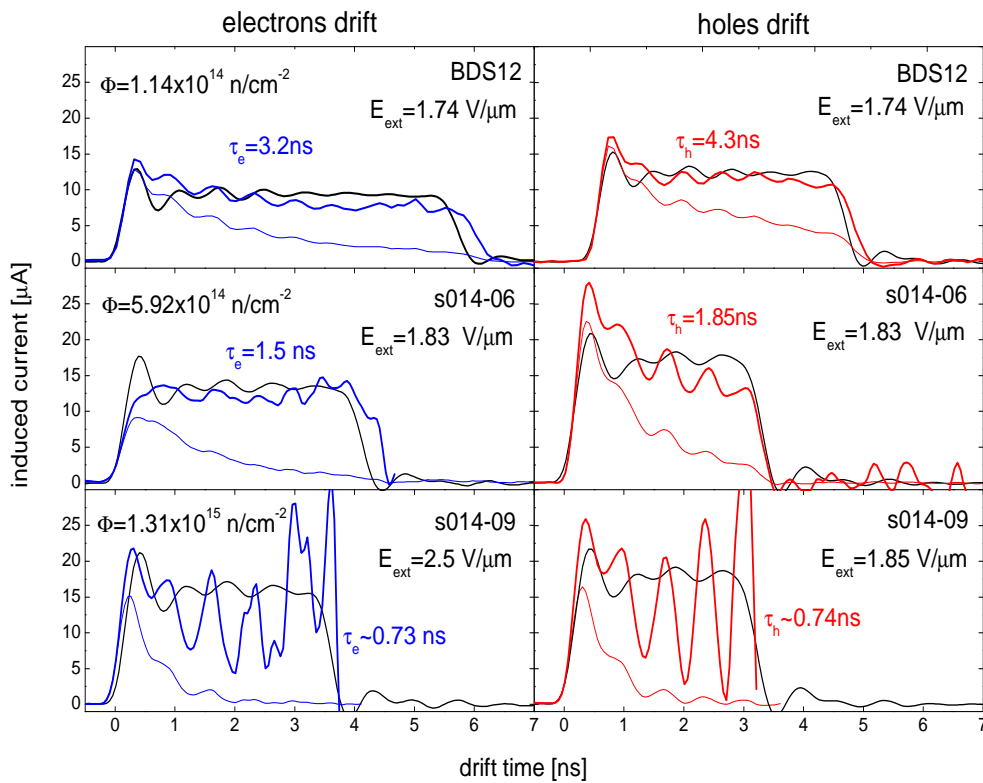


Figure 7.18: TC signals induced by 5.5 MeV  $\alpha$ -particle in scCVD-DDs after irradiation with 20 MeV neutrons, and re-metallization with Cr(50 nm)Au(100 nm) (thin colour curves). The thick black curves are signals before irradiation. The thick color curves are trapping corrected signals after irradiation.



effective deep trapping times for electrons and holes were averaged and plotted versus the incident particles fluence in Figure 7.20.

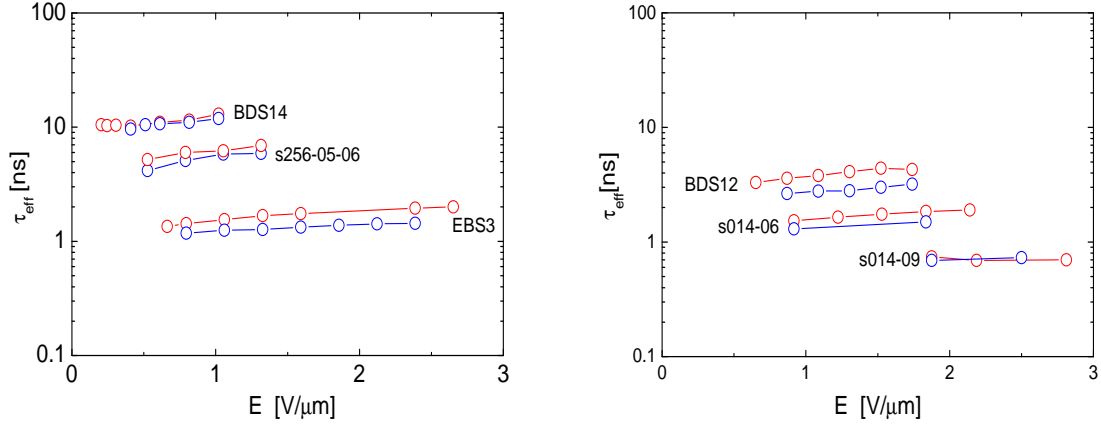


Figure 7.19: Effective deep trapping times extracted from TC signals for electrons- (blue) and holes (red) drift at various electric field  $E$ , after 26 MeV proton (Left panel) and 20 MeV neutron irradiation (Right panel), respectively.

A linear behavior with almost equal  $\beta_{e,h}$  parameter is found for both, proton and neutron irradiations.  $\beta_{e,h}$  describes the defect production rate according to  $1/\tau_{eff} = \beta_p \Phi$ . The  $\beta_{e,h}$  values are displayed in Figure 7.20. The values obtained are about twice higher than those commonly reported for silicon detectors ( $\beta_{e,h}^{Si} \approx 6 \times 10^{-16} \text{ cm}^2/\text{s}$ ) [Bat05]. The measured values for diamond reveal a higher probability of carrier deep trapping with no re-emission within the measurement time at RT.

From  $\tau_{e,h} = (\sigma v N)^{-1}$  and assuming that  $V^0$  vacancies mainly contributes to the charge trapping, the mean cross section  $\sigma_{V^0}$  for a neutral mono-vacancy is estimated to  $\sigma_{V^0} \approx 6 \times 10^{-15} \text{ cm}^2$ , which is a typical value for neutral traps in diamond [Neb03].

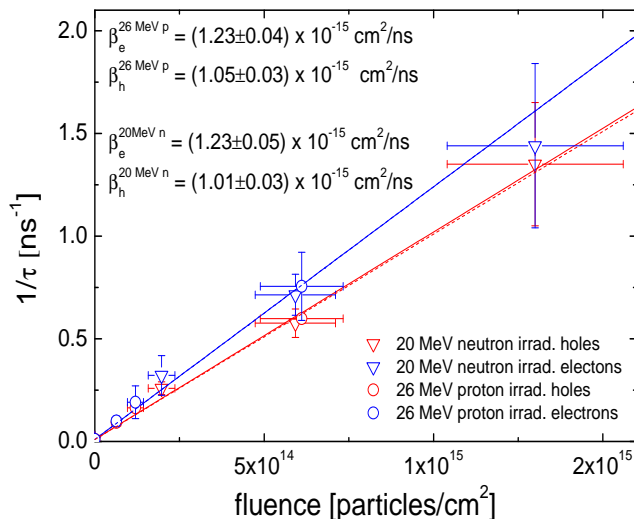


Figure 7.20: Inverse effective trapping times of de-pumped scCVD-DDs as a function of the particles integral fluence. In red holes drift, in blue electrons drift. Dashed (26 MeV protons) and solid (20 MeV neutrons) lines are linear fits to the experimental data points.

### 7.4.3 Priming and Polarization Phenomena

Due to a successive filling of deep traps, for which the release probability of trapped charge at RT is relatively low, the concentration of the active traps decreases. Consequently, the CCD of the sensors increases (priming or pumping). If however, charge is trapped in a deep trap, it contributes to the space charge. For the short-range particles, the drift of holes and electrons is disjunct, giving rise to regions with a majority of trapped electrons and others with a majority of trapped holes. A build-in internal electric field is formed, which suppresses the external electric field. Figure 7.21 shows examples of TC signals measured with proton irradiated scCVD-DDs (sample BDS14), during the formation of the build-in potential.

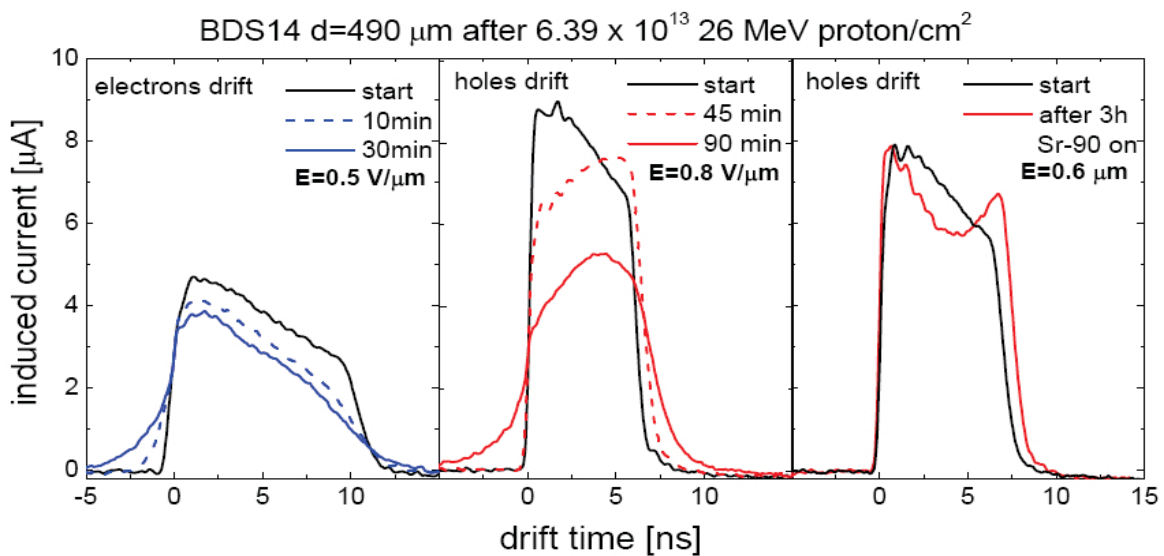


Figure 7.21: Radiation induced polarization effect in a damaged scCVD-DD (Left and middle panel) measured with short-range 5.5 MeV alpha particles. The polarization progressively suppresses the charge drift. (Right panel) After 3 hours exposure of the sample to  $\beta$ -particles from a  $^{90}\text{Sr}$  source, the signals show a quasi-symmetrical shape with a characteristic double-peak structure. However, detector operation remains stable.

The graph on the left and in the middle of Figure 7.21 illustrate the effect of polarization. When a detector is exposed to short-range 5.5 MeV  $\alpha$ -particles, a progressive degradation of the signal shape is observed with time, which indicates the internal electric field profile. After three hours no  $\alpha$ -induced signals could be registered for both, electron- and hole drift. The right graph shows data obtained after three hours exposure of the detector to a  $^{90}\text{Sr}$  source. After priming, it revealed a pronounced double peak structure, which is similar to TC signals of silicon detectors after irradiation [Ere04]. This profile indicates inhomogeneous passivation of the deep traps by electrons and holes. The signal area, corresponding to the collected charge, is already about 8 % higher after three hours priming than for the de-pumped detector. Although the drift velocity is not anymore constant and the drift time is slightly increased, stable detector operation with higher CCE is possible in this case.

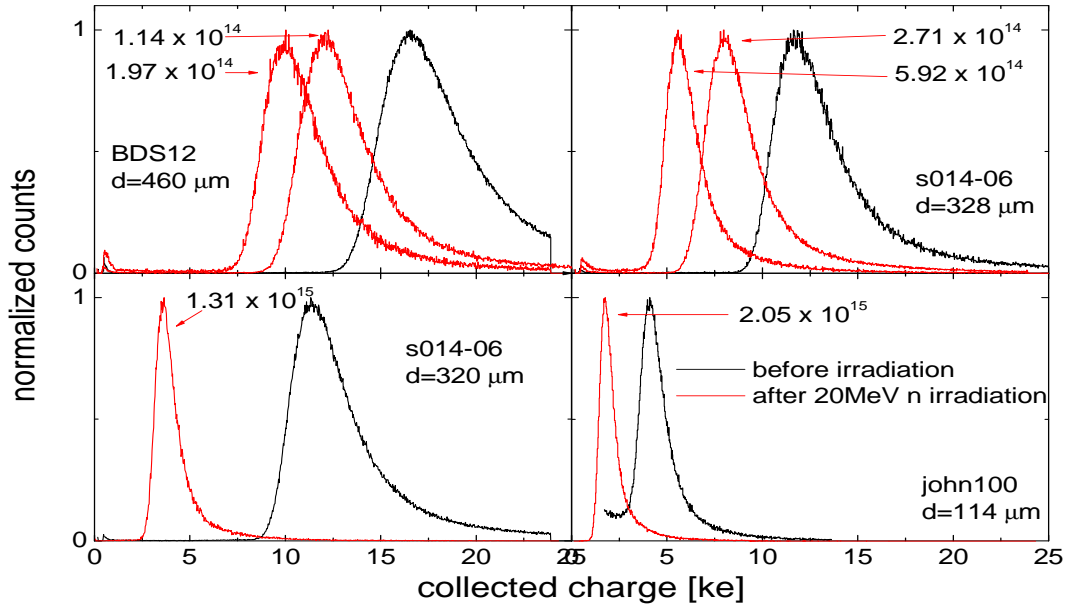


Figure 7.22: Energy-loss spectra of minimum ionizing electrons measured at RT with non-irradiated scCVD-DDs (black) and after 20 MeV neutron irradiation (red) using CS electronics. The integral neutron fluences [ $\text{n}/\text{cm}^2$ ] are indicated in the graphs.

#### 7.4.4 Charge Collection Properties of Irradiated Detectors

**Set-up and Methodology** The CCDs of irradiated diamond detectors were measured using high-energy electrons from a  $^{90}\text{Sr}$  source. The electronics and the methodology used were analogue to that presented in Chapter 6.

Prior to the measurements, the detectors were primed over night with a  $^{90}\text{Sr}$  source, biased at 50V. When the most probable value (MPV) of the electron distribution had stabilized, consecutive measurements of collected charge spectra were performed by increasing stepwise the detector bias and measuring. The spectra were fitted by the Landau distribution convoluted with a Gaussian, as described in Chapter 6. In the further analysis of the CCDs, the MPVs of the Landau distribution are used.

**Shape of the Landau distribution** In figure 7.22, pulse height distributions of fast electrons are shown, measured with four scCVD-DDs before (black) and after neutron irradiation (red). Stable detector operation was observed within the measurement time, and a clear separation of the MIP signals from the electronic noise for all irradiated samples. Although the mean value of the spectra shifts towards lower values, the overall shape of the spectrum does not change significantly after irradiation up to the highest fluence applied. The same behaviour was observed for proton irradiated samples. Figure 7.23 (Left panel) shows the pulse height distribution of sample BDS13 after irradiation with  $1.18 \times 10^{16} \text{ p}/\text{cm}^2$ . Although a low energetic tail appears, about 98 % of the events are located above the electronic noise.

The pulse-height resolution  $\sigma_{\text{Landau}}/\text{MPV}$  obtained from the fits is plotted in Figure 7.23

(Right panel) versus the applied fluence.

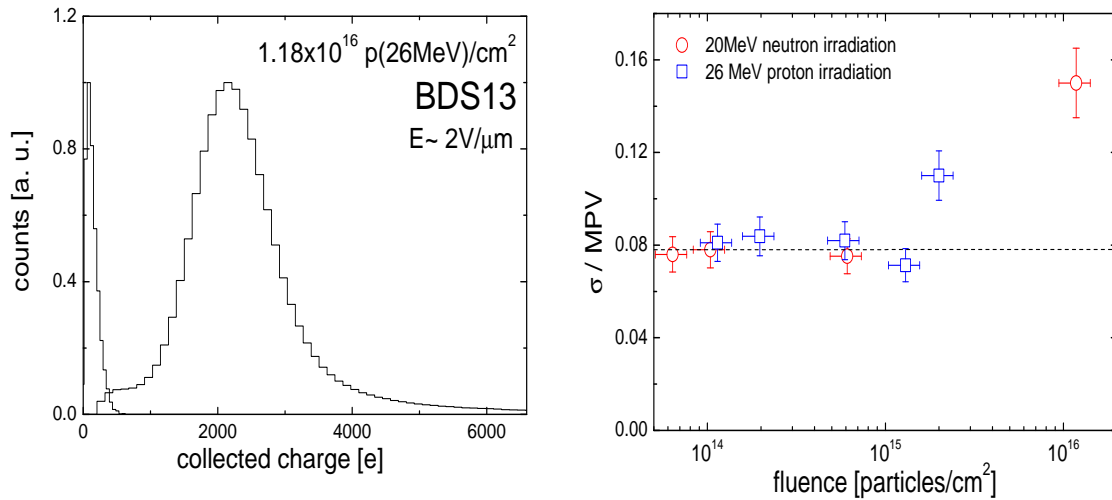


Figure 7.23: Relative  $\sigma_{Landau}/MPV$  of the Landau distribution measured for minimum ionizing electrons with irradiated scCVD-DDs as a function of the integral fluence applied.

Only a weak increase of the  $\sigma_{Landau}/MPV$  was observed for the samples which had been irradiated above  $2 \times 10^{15}$  particles/cm<sup>2</sup>. For the rest of the samples the relative widths remained unchanged and amount to 0.078, which is the same value measured for non-irradiated scCVD-DDs.

**Collected charge characteristics as a function of the applied electric field** Figure 7.24 (Left panel) presents the collected charge characteristics of proton irradiated diamonds in a primed state. Symmetrical behavior was found for both bias polarities.

The colour dashed lines represent the saturated collected charge values before irradiation, which had been measured with  $\alpha$ -particles and correspond to the full charge collection. Thin colour curves represents a compound Hecht fit to the collected charge  $Q_{coll}$  as a function of the applied electric field  $E$  with data given by Equation 7.12.

$$Q_{coll} = \frac{Q_0}{2} \frac{\tau_e}{t_{tr}^e(E)} \left[ 1 - \exp\left(\frac{-t_{tr}^e(E)}{\tau_e}\right) \right] + \frac{Q_0}{2} \frac{\tau_h}{t_{tr}^h(E)} \left[ 1 - \exp\left(\frac{-t_{tr}^h(E)}{\tau_h}\right) \right] \quad (7.12)$$

where  $Q_0$  is the generated charge,  $t_{tr}^{e,h}$  the transit time of electrons and holes as a function of the electric field  $E$ , obtained from the parametrization of the drift velocities as presented in Chapter 6 and  $\tau_{e,h}$  are effective trapping times for electrons and holes - free parameters in the fit. These fits describe the charge collection characteristics rather poorly due to the fact that the internal electric field is disturbed by the trapped charge, being inhomogeneous across the sample. Although the detailed shape of the electrons and holes transient signals is not known, for each voltage step an effective transient time  $t_{eff}^{e,h}$  and a corresponding effective electric field  $E_{eff} = \alpha E$  could be introduced, where  $\alpha$  is the field correction factor ranging from 0 to 1. The thick colour curves represent the fit of the data obtained by applying the modified compound Hecht equation, where  $E$  is replaced by  $E_{eff}$ . The  $E_{eff}$  values used in the fit are presented in Figure 7.24 (Right panel). The effective internal electric field

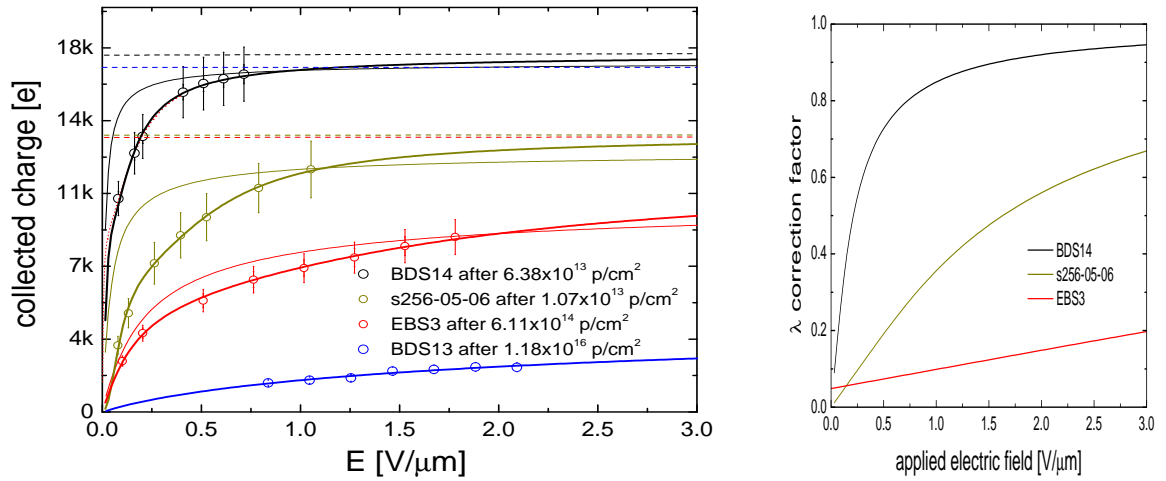


Figure 7.24: (Left panel) The collected charge characteristics of scCVD-DDs irradiated with 26 MeV protons, measured in the primed state using  $^{90}\text{Sr}$  fast electrons. The colour dashed lines mark the collected charge values before irradiation. The thin color curves are the compound Hecht (Equation 7.12) fits to the experimental data, whereas the thick colour curves are fits using a modified Hecht equation (see text). (Right panel) The correction factors, giving the best fit to the experimental data, applying the modified Hecht equation.

of irradiated and pumped samples can be much lower than the externally applied electric field (especially for low bias values). Although the experimental data can be quite precisely fitted by the modified Hecht equation using the effective  $E_{eff}$  approximation, aiming to understand qualitatively the internal field modifications, detailed numerical simulations are needed. Two samples irradiated with fluences around  $1 \times 10^{14}$  26MeV p/cm $^2$ , show a complete charge collection in the primed state and at sufficiently high  $E$ .

Figure 7.25 shows a series of collected charge characteristics of four scCVD-DDs metallized with different types of electrodes after neutron irradiation. Blue full dots represent the collected charge characteristics of the devices patterned with Al(100 nm) electrodes, measured right after neutron irradiation. No thermal treatment was applied before these measurements. Highly asymmetric behavior is observed with a linear increase of the collected charge values. A linear dependence of the CCD on the applied  $E$  is characteristic for partially depleted detectors, often observed in irradiated silicon sensors. As it was demonstrated in the previous section, DC bias-induced polarization is responsible for this process. The singular red stars represent the final CCD measured during the on-line characterization employing the current-to-frequency converter. The results agree perfectly with the later off-line characteristics and show that the on-line CCD values were measured in a strongly polarized state of the sensors.

Aiming to exclude DC bias-induced polarization, the samples were re-metallized with Cr(50 nm)Au(100 nm). In order to avoid possible defect annealing before the measurement of the charge collection characteristics, a 'cold' cleaning procedure was applied in a first step and the samples were not annealed after metallization. No significant changes in the collected charge characteristics were observed comparing with those values measured in a subsequent run with annealed CrAu electrodes. The results after re-metallization and

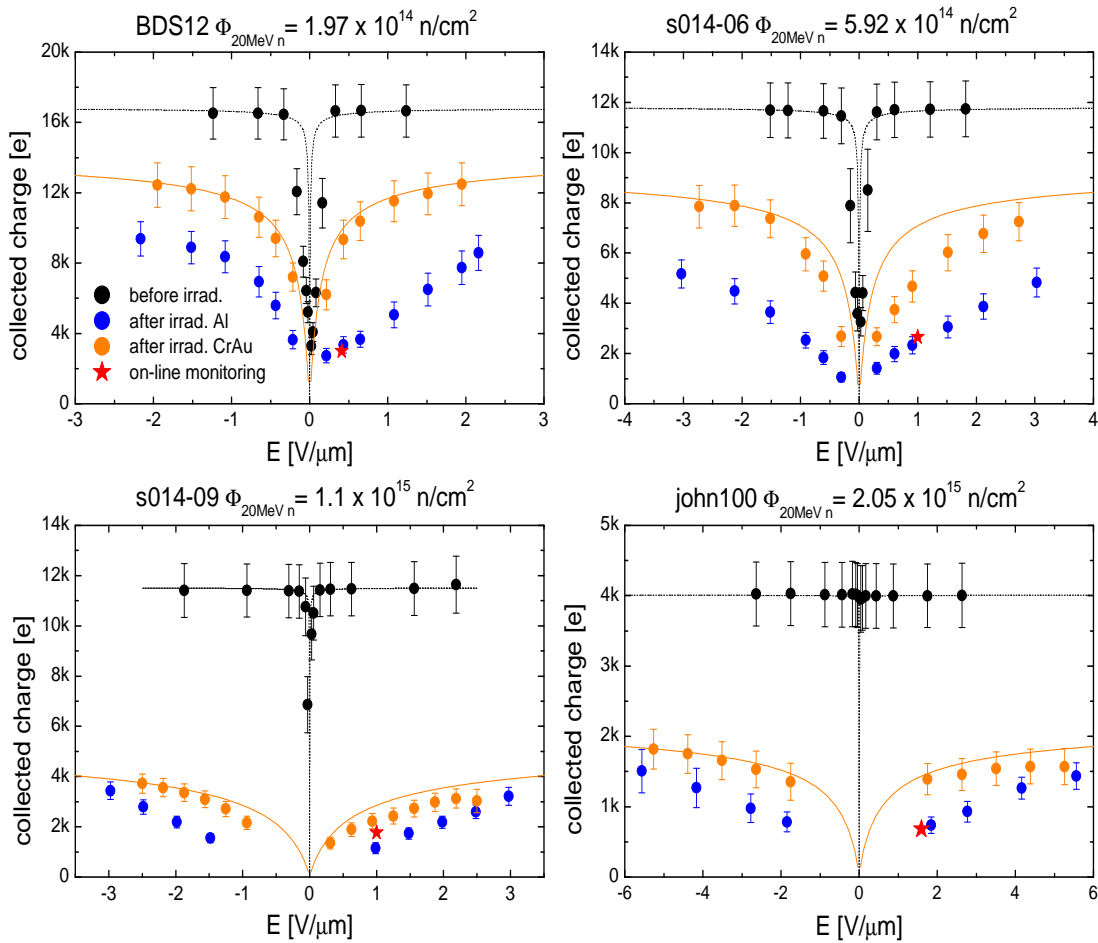


Figure 7.25: Charge-collection characteristics of scCVD-DDs after irradiation with 20 MeV neutrons, measured using fast electrons from  $^{90}\text{Sr}$  source and CS electronics with 2  $\mu\text{s}$  shaping time. In black is shown the characteristics before the irradiation. Thin yellow lines represents the compound Hecht fit to the data obtained after re-metalization.

contacts annealing are displayed in Figure 7.25 (orange dots). Clear improvement is found for both polarities, what indicates that bias induced polarization is partially inhibited.

Figures 7.26 and 7.27 present the decrease of the maximum collected charge as a function of the integral fluences of protons and neutrons applied, respectively.

- Open dots are data measured in an unprimed state by means of the TCT using 5.5  $\alpha$  particles. The CCDs were obtained by integration of the TC signals measured from electrons and holes transients.
- Full dots are data measured in the primed state using CS electronics with 2  $\mu\text{s}$  shaping time and fast electrons from a  $^{90}\text{Sr}$  source. Full stars in Figure 7.27 represent data measured after neutron irradiation with diamonds metallized with Al(100nm) electrodes.

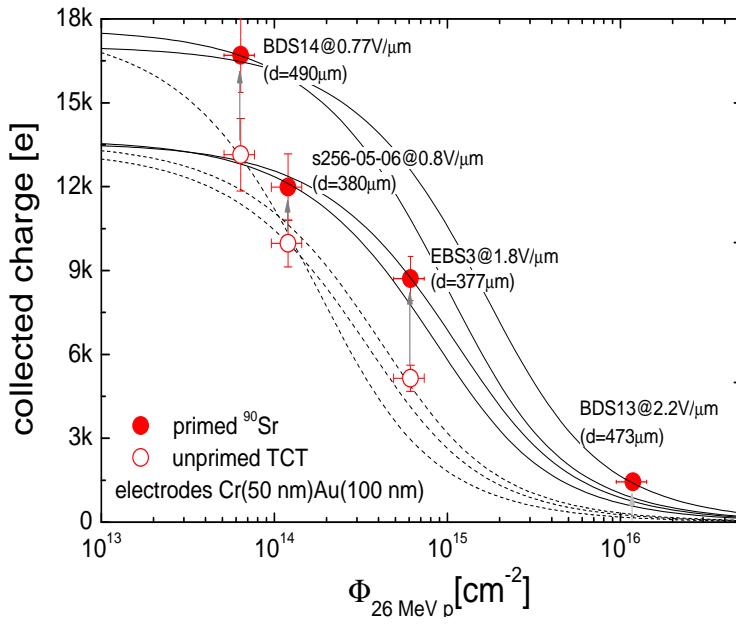


Figure 7.26: The decrease of collected charge of scCVD-DDs as a function of 26 MeV proton integral fluence. Open dots - values measured using TCT and an 5.5 MeV  $\alpha$ -particle injection detectors are in unprimed state. Full dots - measured using CS electronics with 2  $\mu$ s shaping time and minimum ionizing electrons - detectors are in primed state.

The values were recorded at the highest possible detector bias indicated in the figures. Gray arrows mark the increase of the charge collection efficiency due to the priming process.

Dashed and solid black curves in Figure 7.26 and 7.27, illustrate the degradation trend of the charge collection with the particle fluence, measured at fixed  $E$  for a given diamond detector of thickness  $d$ , assuming a constant carrier drift. The collected charge  $Q_{coll}$  values are calculated according to Equation 7.13

$$Q_{coll} = 36.7 \cdot d \cdot \frac{t_{tr}^{e,h}(E, d)}{\Phi \cdot \beta^{e,h}} \left( 1 - \exp\left(-\frac{t_{tr}^{e,h}(E, d)}{\Phi \cdot \beta^{e,h}}\right) \right) \quad (7.13)$$

where  $\Phi$  is the the integral fluence of incident particles,  $\beta$  is the parameter linking the fluence with the density of the active trapping centers,  $t_{tr}(E, d)$  is the transit time of electrons and holes in a sample of thickness  $d$ , and  $36.7d$  is the created charge  $Q_0$  in [e] produced in a detector of that thickness by one MIP.

The universal parameter which allows a direct comparison of the degradation of the charge collection properties of samples of various thicknesses is the charge collection distance (CCD). At relatively high field the drift velocity can be consider as saturated. Thus, the variance of the CCD is rather small. Using the Hecht equation, which relates the CCE ( $Q_{coll}/Q_{gen}$ ) to the CCD, the CCDs of all irradiated samples are calculated and presented in Figure 7.28. The most recent (yet unpublished) data for irradiated scCVD-DD and pcCVD-DD of the RD42 collaboration are displayed in black symbols. Black dashed lines indicate the expected linear decrease of the CCD with fluence. The CCD of primed detectors is on average about 2.3 times higher than the values measured with unprimed diamonds, indicating a partial passivation of deep trapping centers. For both proton and neutron irradiation, the CCD of primed samples decreases linearly up to an integral fluence of  $\sim 10^{15}$   $\text{cm}^{-2}$ .

The CCD, often called the mean drift length, is the distance after which the number of the drifting charge carriers, (and thus of the induced charge) is reduced to the  $1/e$  part of the generated charge. Using the data described above the expected CCE of scCVD-DDs of various thicknesses is calculated as a function of the applied particle fluence. The results are



Figure 7.27: The decrease of collected charge of scCVD-DDs as a function of 20 MeV neutron integral fluence. Open dots - values measured using TCT and an 5.5 MeV  $\alpha$ -particle injection - detectors are in unprimed state. Full dots (CrAu electrodes) and full stars (Al electrodes) - values measured using CS electronics with 2  $\mu$ s shaping time and minimum ionizing electrons - detectors are in primed state.

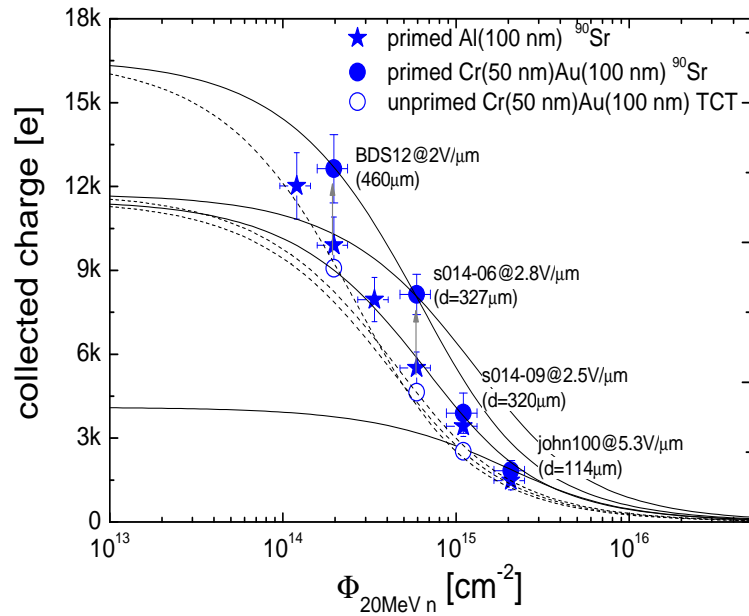
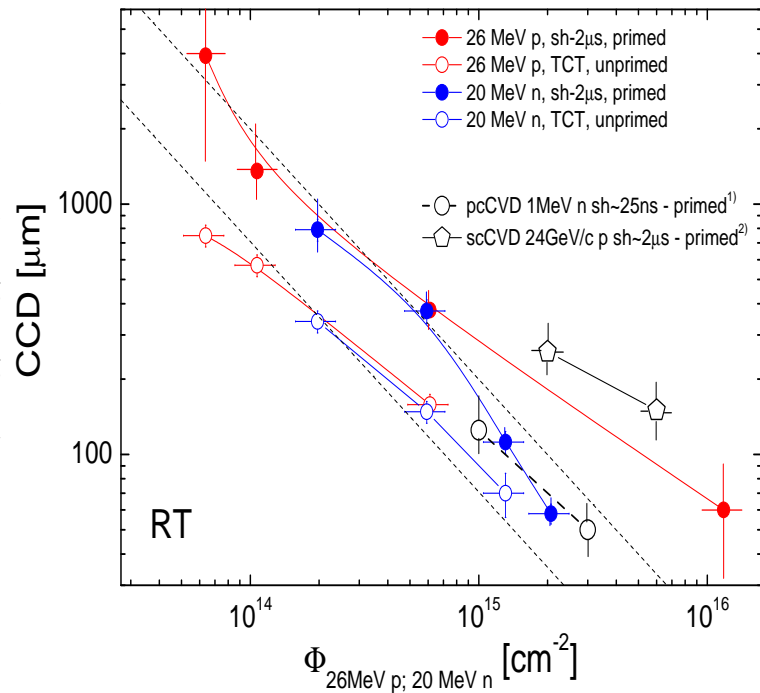


Figure 7.28: Charge collection distances of scCVD-DDs after 26 MeV proton (red) and 20 MeV neutron irradiation (blue). Full dots are data measured in the primed state, using fast electrons and charge sensitive electronics of 2  $\mu$ s shaping time. Open-dots are data measured in the unprimed state by TCT using 5.5 MeV  $\alpha$ -particles. The black dashed lines indicate the expected linear drop of the CCD. The black symbols are recent data reported by the RD42 collaboration.





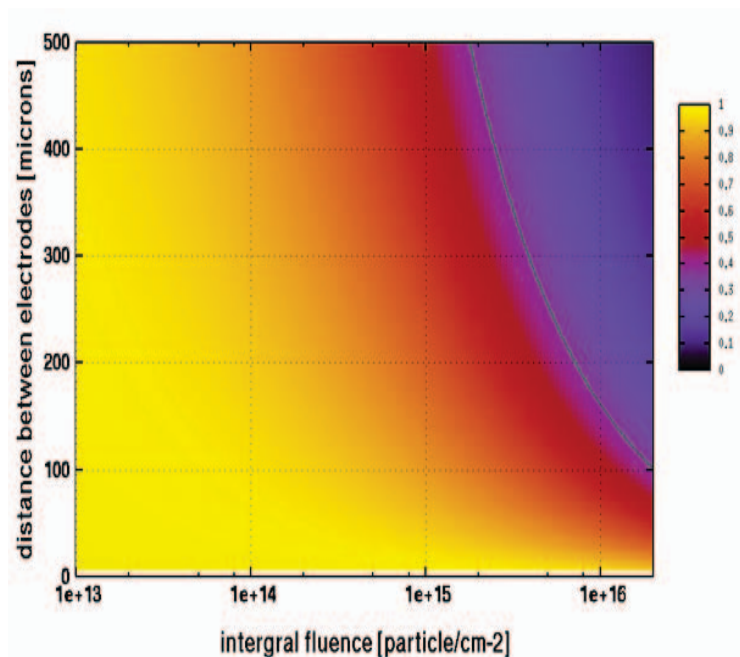


Figure 7.29: The expected charge collection efficiency (CCE) of primed scCVD-DDs as a function of electrodes interspacing and applied integral fluence. The cyan curve marks the  $1/e$  drop of the CCE.

displayed in Figure 7.29. It is evident, that the use of thin detectors is favorable. However for MIP measurements, thin diamond detectors lead to very weak signal generation and thus such detectors are not applicable. However, sensors with three-dimensional (3D) electrodes, which form a 3D array perpendicular to the surface and of spacing smaller than the sensor thickness can be considered in future developments for even more radiation hard diamond detectors.

### 7.4.5 High-Temperature Annealing

According to Figure 7.2, high temperature annealing leads to a progressive decay of interstitials and vacancies. Assuming that those defects are mainly responsible for the charge trapping in irradiated diamonds, a permanent increase of the effective charge-carriers lifetime is expected after detector annealing. However as it was shown in [Amo02], when vacancies and interstitials become mobile at high temperatures, they can form new defects with diamond impurities that also act as deep trapping centers. Due to this process, no restoration of the Ila natural diamond detector properties could be observed by this group after neutron irradiation and successive high temperature annealing up to 1200 °C.

In order to check the high temperature influence on the recovery of the charge collection properties of scCVD-DDs, the sample BDS14 was annealed in two steps, using a resistive furnace under argon flow at 1000 °C. The first step lasted one hour, the second two hours. Between the steps, the sample was characterized by TCT in the de-pumped state. Figure 7.30 shows the TC signals of the non-irradiated sample (thin curves), signals after irradiation (dashed curves), and signals after 3 hours of high temperature annealing (thick curves). A clear increase of the charge carrier lifetime is observed after annealing.

The collected charge as a function of the applied field  $E$  was obtained by the integration of the TC signals within the transit time, and the values of  $\tau_{e,h}$  were extracted from the correction to the exponential trapping loss. The results are displayed in Figure 7.31.

The lifetime  $\tau_h$  of holes is increased by approximately a factor of four after three hours

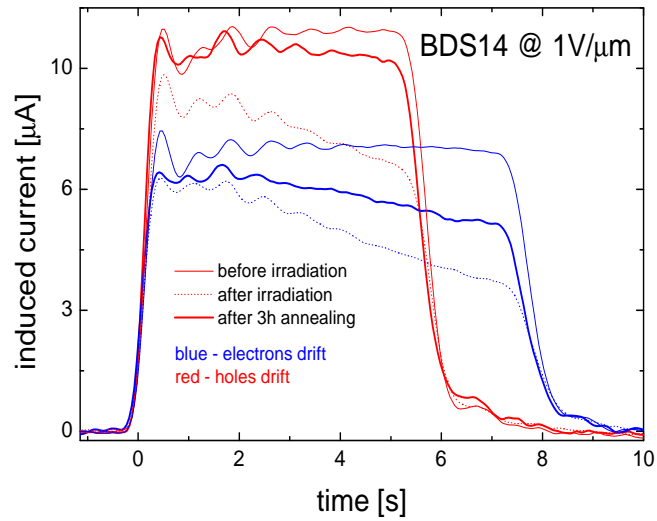


Figure 7.30: TC signals of BDS14 at  $1 \text{ V}/\mu\text{m}$  illustrating the recovery of the charge transport properties of the irradiated detector after 3h annealing at  $1000 \text{ }^\circ\text{C}$ .

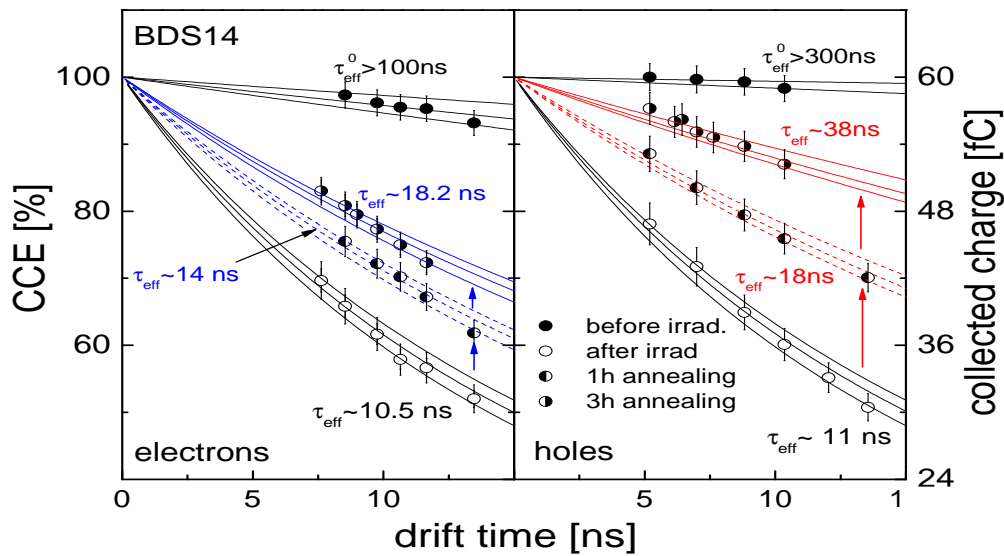


Figure 7.31: Permanent increase of the CCE after high temperature annealing at  $1000 \text{ }^\circ\text{C}$  for sample BDS14. Annealing was performed in two steps of 1 h (color dashed lines) and 2 h (solid color lines), respectively.

of annealing, leading to an almost complete recovery of the CCE with a value close to 97 % measured at  $1 \text{ V}/\mu\text{m}$  in the de-pumped state. The increase of  $\tau_e$  is in the order of two and tends to saturate after three hours annealing, giving a CCE of  $\sim 83 \%$  at  $1 \text{ V}/\mu\text{m}$ . The kinetic details as well as secondary-defects creation during annealing are not known. However, it is suggested that migrating vacancies form cluster defects, which have larger cross sections for electron trapping, could lead to the observed behavior.

### 7.4.6 Discussion

According to the NIEL hypothesis, about six times higher concentration of primary defects is expected for diamond after irradiation with 26 MeV protons comparing to 20 MeV neutrons irradiation. The optical absorption and photoluminescence spectroscopy suggest charge trapping mainly due to neutral mono-vacancies. The equal measured defects introduction rates  $\beta_p$  show that the measured collected charge characteristics do not scale with the calculated *NIEL* values. The data can be explained by differences in the self-annealing processes due to the different irradiation conditions of the diamond detectors during both tests. For instance, all detectors were biased during neutron irradiation. Although this cannot influence the primary-defect production, biasing may affect the self-annealing process by acceleration of the charged-defect migration [Zei00]. Such an effect has been observed by [Cin00, Cin98] for silicon detectors after neutron and pion irradiation, where increase by a factor of two in the effective dopants concentration ( $N_{eff}$ ) is measured for biased sensors. As soon as the bias had been reduced, this effect annealed out with time and the final state was the same as for irradiated sensors without bias. However, in the case of diamond no post-irradiation annealing takes place at RT, which can result in a permanent increase of the defect concentration of biased detectors. Furthermore, 26 MeV protons are highly ionizing particles and despite cooling, the local temperature of the diamond lattice could be rather high, leading to increased self-annealing, and finally to a lower number of stable defects. These two possible effects must be further investigated.

The observed 'bias induced-polarization' of irradiated detectors shows once more the importance of the diamond surface processing and the electrode design. Although aluminium contacts applied to intrinsic diamond sensors seem to have no negative influence on the detector operation, after lattice damage at high particle fluences, it turns into a highly blocking behaviour which deteriorates strongly the detector properties. One way to prevent this problem is to change the work function of the metal or contact energy of the surface barrier to prevent the created deep acceptor/donor levels from crossing the Fermi level e.g., applying ohmic contacts or a highly boron doped p-type diamond inter-layer. As it was demonstrated by diamond re-metallization with CrAu and successive annealing bias induced polarization was partially suppressed. Another way is to remove periodically the applied bias exploiting the different time constants for polarization and depolarization. However, the latest approach is not acceptable in particle detection from the practical point of view.

## 7.5 Summary of the Radiation-Tolerance Study

First results on the radiation tolerance of scCVD-DDs were obtained. In total eight samples have been irradiated with 26 MeV protons and with  $\sim 20$  MeV neutrons up to a highest integral fluence of  $1.18 \times 10^{16}$  p/cm<sup>2</sup>.

The optical characterization by means of PL and UV - VIS absorption spectroscopy shows that the main surviving defect produced in scCVD is the neutral mono-vacancy  $V^0$ , giving a sharp zero-phonon line at 1.638 eV after both neutron and proton irradiation. A constant defect-production rate  $\beta_p$  was found within the applied hadron fluence. Among others, residual defects present after irradiation in the diamond bulk, the  $\langle 0\ 0\ 1 \rangle$ -split single interstitial ( $I_{\langle 001 \rangle}^0$ ), and the neutral nitrogen-mono-vacancy  $NV^0$  were identified. No

indications of complex defects were observed. Integrating the GR1 ZPL from the UV - VIS absorption measurements, the absolute concentration of  $V^0$ , and the vacancies production rate were estimated for the 26 MeV proton irradiation. The values obtained are more than one order of magnitude lower than those predicted by the NIEL hypothesis, suggesting that self-annealing process takes place.

Contrary to silicon, no increase of the detector leakage current is observed after sensor irradiation. This was confirmed by on-line monitoring and off-line measurements as well. Furthermore, the shunt path conductivity found in intrinsic scCVD diamond as a consequence of structural defects is suppressed after irradiation due to a possible compensation of shallow defects by deep states of a neutral mono-vacancy. Thus, irradiated detectors can be operated at high electric field  $E$  values, which are close to the range of the drift velocity saturation. No cooling or special treatment is needed for a stable RT operation of irradiated scCVD-DDs.

The TCT was used to measure effective trapping times and the internal electric field profiles of irradiated samples. A linear scaling of the inverse effective trapping time  $1/\tau_{e,h}$ , with fluence was found as well as almost identical defects production rates  $\beta_p$  for both, neutron and proton irradiation, respectively. No space charge is found in proton irradiated diamond, confirming the neutral state of the created defects. For all neutron irradiated samples plated with Al(100 nm) electrodes, strong bias induced polarization occurs due to the blocking nature of the contacts. This effect was partially suppressed by remetallization of the samples with Cr(50 nm)Au(100 nm) electrodes, which had been annealed at 550 °C. As it was demonstrated, samples annealing above 800 °C leads to a significant permanent recovery of the charge collection efficiency of the diamond detectors due to recombination of the neutral vacancies. However, for highly segmented detectors like strip and pixel sensors, which are assembled with read-out electronics, an annealing at such high temperatures is rather difficult task.

Due to the large band-gap of diamond, deep defect levels produced by radiation can be passivated with a low probability of re-emission at RT, resulting in an increase of the CCD. The so-called Lazarus effect known from cryogenic silicon detectors is observed at RT for irradiated scCVD-DDs. This phenomenon leads to a constant increase of the CCD of primed detectors by a factor of 2.3 on average, compared to the unprimed state. Due to the passivation of deep states, an almost complete charge collection is observed for 400 - 500  $\mu\text{m}$  thick detectors at an irradiation with  $\sim 1 \times 10^{14}$  particles/cm<sup>2</sup>. For samples irradiated with 20 MeV neutrons above a fluence of  $10^{15}$  n/cm<sup>2</sup>, bias induced polarization phenomena appear. In this case the CCD does not increase significantly after priming, despite re-metallization of the samples.

The relative widths of the Landau distribution of minimum-ionizing electrons does not change after irradiation up to  $1 \times 10^{15}$  particles/cm<sup>2</sup>, and it is equal to  $\sigma/\text{MPV}=0.078$  which is the resolution obtained for intrinsic scCVD-DDs. This ratio increases slightly above this fluence but remains comparable to the value of non-irradiated silicon detectors.

Although performed characterization of irradiated scCVD-DD allowed an insight into the radiation tolerance of this novel material, the results could not be considered as a complete study of the radiation tolerance of diamond detectors. The first data does need confirmation and additionally irradiations beyond  $10^{15}$  particles/cm<sup>2</sup> will help to explore the limits of scCVD-DDs. Especially, the influence of the irradiation conditions like biasing, and particle flux on the detector CCD degradation must be clarified. At fluences below

$10^{15}$  particles/cm<sup>2</sup>, measurements of the trapping time being directly proportional to the defect density are possible using the transient current technique. This electrical characterization supported by sensitive optical measurements like photoluminescence will allow to experimentally study the NIEL hypothesis for diamond in more detail.

The priming and the bias-induced polarization of irradiated diamond detectors at RT is very similar to the behavior of silicon detectors at cryogenic temperatures [Bor01]. As it was demonstrated in [Ere07, Bor00], the field engineering by controlled charge injection (CID devices), the optimization of the readout temperature or detector illumination with visible light improves the CCD of irradiated silicon detectors at cryogenic temperatures. These techniques can be applied as well to irradiated diamond sensors. The controlled charge-injection devices based on diamond can be realized e.g., by P-I-M (p-doped, intrinsic, metal) diamond structures in forward bias operation mode. Such a structure was already fabricated and successfully operated in reverse bias as a diamond neutron detector by [Bal06, Man07], where the p-type layer consists of a highly boron doped scCVD diamond layer, followed by the active volume of intrinsic scCVD and an aluminium Schottky contact on top.

Concluding, the presented results can be considered as a worst scenario of the radiation tolerance of scCVD-DDs, which may be optimized in future developments.



# Chapter 8

## In-beam Performance

To demonstrate the functionality of scCVD diamond as a detector material for timing application and energy-loss spectroscopy, several prototypes of diamond detectors in parallel plate geometry were built. The sensors' performance with respect to energy and time resolution was tested with heavy-ion as well as with minimum-ionizing particle beams, where the dynamic range of the induced signal varied over five orders of magnitude. The most important results are presented and discussed in this chapter.

### 8.1 Timing Properties

Particles with the same momentum but different masses travel at different velocities. Therefore from the knowledge of the momentum and the time of flight,  $t$ , across a known distance  $L$ , the particle may be identified. The length  $L$  of the particle's trajectory is calculated with high accuracy from measurements in the tracking system. The velocity  $\beta$  of the particle can be calculated as  $\beta = L/ct$  and consequently the mass will be given by:

$$m = p\sqrt{\frac{c^2t^2}{L^2} - 1} \quad (8.1)$$

The time difference  $\Delta t$  between two relativistic particles ( $\beta \rightarrow 1$ ) with masses  $m_1$  and  $m_2$ , both of momentum  $p$ , is over a flight path  $L$ :

$$\Delta t_{1-2} \approx \frac{Lc}{2p^2}(m_1^2 - m_2^2) \quad (8.2)$$

The most direct way to determine the particle velocity is to measure the time that it takes to travel a certain distance. The time intervals are obtained by counting the number of oscillations of a stable oscillator that occur between the passage of the particle through two counters called 'START' and 'STOP' counters. The time spectra are created by so-called time-to-amplitude converters (TAC) or time-to-digital converters (TDC) which are fed with discriminated analogue signals of both detectors. The  $\sigma_{ToF}$  width of the time spectra are affected by the intrinsic time resolution  $\sigma_{intr}$  of both detectors  $\sigma_{ToF} = \sqrt{\sigma_{START}^2 + \sigma_{STOP}^2}$ .

The requirements for the START detector are: excellent intrinsic time resolution, high detection efficiency, ability to operate at high rates and, finally radiation hardness. The pcCVD-DD developed at GSI for heavy-ion timing applications for the HADES and the FOPI spectrometers fulfill these requirements, showing a perfect time resolution of  $\sigma_{intr} <$

50 ps [Ber01a, Kis05]. However, due to the incomplete charge collection of pcCVD-DD, these detectors cannot be used for satisfying time resolution and detection efficiency measurements with minimum-ionizing particles, or with relativistic ions lighter than Carbon.

A possible solution are scCVD diamonds which comprise the timing properties of pcCVD revealing a much better carrier collection efficiency (close to 100 %). In this section, first results of minimum ionizing particles as well as light ions timing measured with scCVD-DDs are presented.

### 8.1.1 Setup and Methodology

The ultra-fast rise time of scCVD-DDs is exploited to define the time at which a certain particle traverses the diamond sensor. Several types of discriminator units are available, which deliver a logic output pulse for each analogue detector input signal, which fulfils the discriminator requirements. Commonly, an amplitude threshold is set, defining the signal to process. The simplest discriminator type, satisfied by this one setting, is called 'leading edge' discriminator. These are the 'fastest' possible units applicable for high-rate particles timing or counting with diamond detectors.

**Limiting factors in timing with leading-edge discriminator** If a noisy analog pulse is applied to a leading-edge discriminator, the timing uncertainty can be obtained by a simple geometric transformation shown in Figure 8.1. Projecting the variance  $\sigma_n$  of the momentary signal amplitude on its rate of change  $dV/dt$  at the discriminator threshold  $V_T$  yields the variance in time  $\sigma_t$  of the output pulse called jitter :

$$\sigma_t = \frac{\sigma_n}{\left(\frac{dV}{dt}\right)_{V_T}} + \delta t \quad (8.3)$$

where  $\delta t$  is the intrinsic jitter of the discriminator and time digitizer.

If  $\sigma_n$  is determined by noise alone, it is equal to the rms noise voltage. Qualitatively, this relationship shows that increasing signal-to-noise ratio, decreasing rise time and decreasing residual jitter, lead to improved time resolution. However, if a low pass filter is applied to reduce the noise, it also slows down the pulse rise time, the slope in equation 8.3 normally decreases more rapidly than the noise diminishes, and the net result is an increase in timing jitter. Therefore, it is preferable to preserve the fastest possible rise time from the signal source i.e., in the case of diamond detectors where the rise time is in order of 100 ps, to use sufficiently fast broadband readout electronics.

A leading-edge discriminator provides a logic output when the input signal exceeds a fixed reference level. As shown in Figure 8.1, amplitude variations lead to a shift in the timing, called walk . Amplitude walk can be corrected off-line when parallel to the logic timing signal the amplitude of analog signal is registered.

**Setup** To evaluate the time resolution capability, two scCVD-DDs (D1,D2) are placed in a tandem, with the shortest possible distance between both sensors. Additionally, a reference plastic scintillator detector is placed behind the diamond stack. The amplifier signals are split by an active power divider to feed the timing chain and the energy chain with the same signal. The leading-edge discriminator is placed in the experimental area close to the detectors coupled to the amplifiers. The discriminated timing signals and the



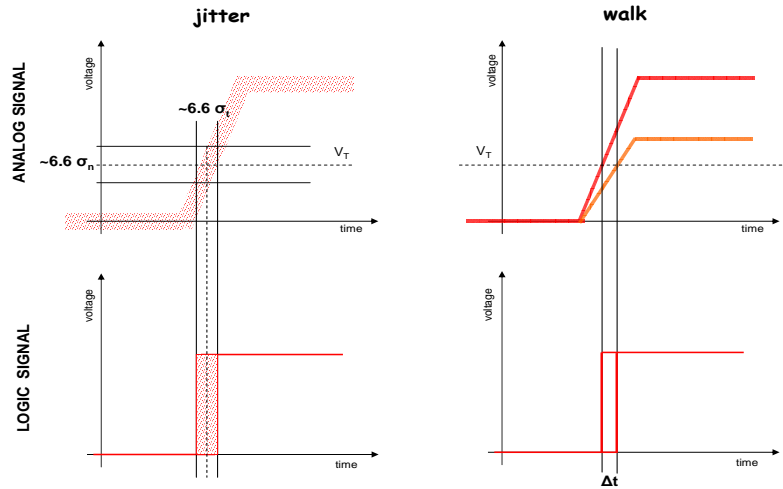


Figure 8.1: The limiting factors in timing when using leading-edge discriminator: jitter (Left panel) and walk (Right panel).

analogue energy signals are sent via  $\sim(30 - 40)$  m transmission lines to the measurement area, where they are digitalized by a time-to-digital converter (TDC) and a charge-to-digital converter (QDC), respectively. The start signals, for the TDC and for the data acquisition are provided by the overlap coincidence of the signals of both diamond detectors. The timing measurement system is sketched in Figure 8.2.

The system was calibrated before each run using an ORTEC time calibrator. The intrinsic electronics resolution  $\delta t$  was determined to  $\sigma = 15$  ps.

**The intrinsic resolution of diamond detectors** Assuming equal resolution of the START detector ( $\sigma_{start}$ ), and the STOP detector ( $\sigma_{STOP}$ ) the intrinsic time resolution of a single device is calculated according to Equation 8.4

$$\sigma_{ToF} = \frac{\sigma_{ToF}}{\sqrt{2}} \quad (8.4)$$

### 8.1.2 Results and Discussion

**Time resolution for relativistic ions** For a possible upgrade of the presently used start-detector of the FOPI spectrometer at the SIS/GSI [Rit95], the time resolution of pc- and scCVD diamonds has been tested with relativistic  $^{27}\text{Al}$  ions of  $E = 2$  AGeV. Multi-channel broadband FE-electronics (FEE1) [Cio07], developed for the RPC ToF wall of FOPI, was used to test the intrinsic resolution of  $500 \mu\text{m}$  thick pcCVD samples and of two scCVD samples, each of a  $330 \mu\text{m}$  thickness. The amplified pulses were discriminated by a leading-edge discriminator placed in the cave near the detectors. The logic output pulses were transferred over 30 m long transmission lines to the electronic setup and to the data-acquisition system placed in the measurement area. The average rate during the experiment was about 0.7 MHz.

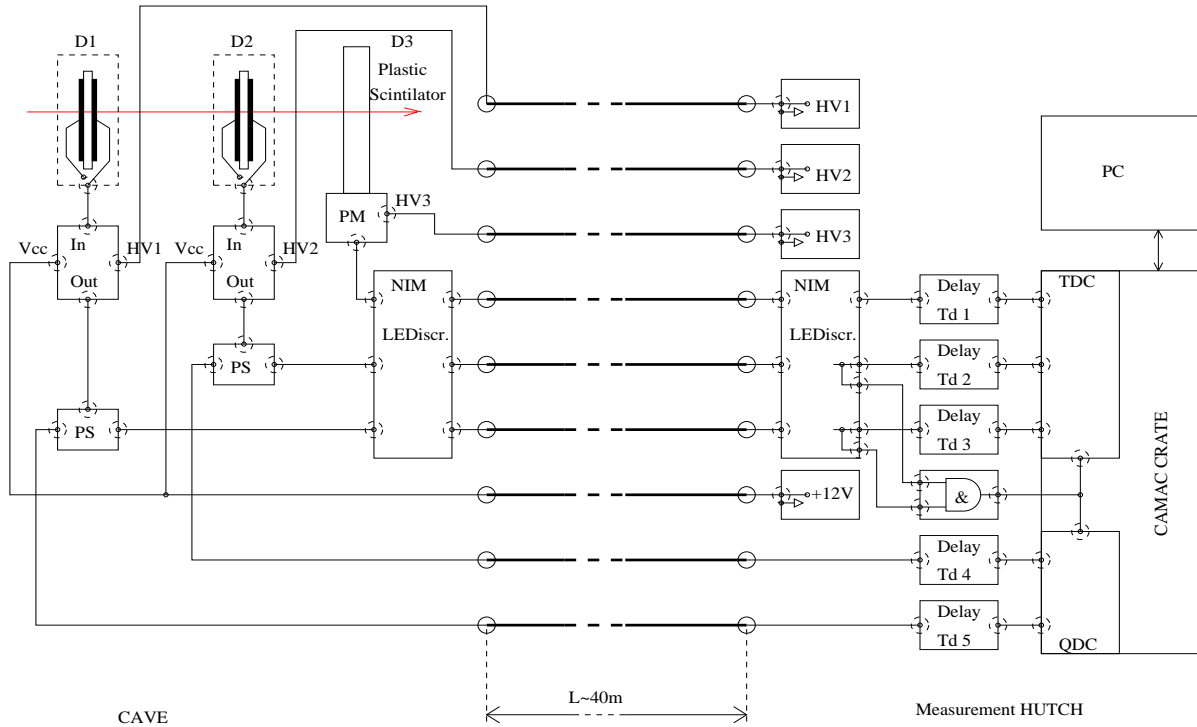


Figure 8.2: Schematic of the setup used for measurement of the intrinsic time resolution of scCVD-DDs.

Figure 8.3 shows the time spectra measured with the two pcCVD samples of  $CCE \approx 50\%$  on the left, and on the right, the time distribution measured with one of the pcCVD-DD versus the scintillator-START detector. Obviously due to this detector, the intrinsic width of 28 ps obtained with the almost identical pcCVD-DDs (left plot), is broadened by a factor of five. In the bottom plot, the time spectrum of two scCVD-DDs is shown. Surprisingly, the same intrinsic resolution as measured for the pcCVD-DDs is obtained, indicating that the widths are limited by electronic noise. A detection efficiency of  $\sim 92\%$  was estimated for the scCVD-DD-setup and of  $\sim 96\%$  for pcCVD-DDs, respectively. The lower efficiency found for scCVD arises from geometrical misalignments of the detectors, caused by the small size of the electrodes.

**Time resolution for low energy ions** The time resolution of scCVD-DDs for low-energy ions has been tested at the CNA-Seville 3 MV tandem accelerator [Gar00].  $\Delta E - E$  detector telescope consisting of a  $100\ \mu\text{m}$  and a  $300\ \mu\text{m}$  scCVD-DDs was mounted at an angle of  $90^\circ$  to the beam direction. A 6 MeV proton beam and a Pb target were used for these experiments. The energy loss of the scattered protons in the  $\Delta E$  detector is about one half of their kinetic energy and the remaining energy is fully deposited in the second diamond. For time measurements, the pulses from both detectors were fed into broadband amplifiers (DBAII). The rates in the following experiment were approaching 1 MHz. The analogue signals of both detectors registered with a DSO are shown in Figure 8.4 (Left panel). The coincidence rate was 70 % of the single rate, partially due to detector misalignment. Leading-edge discriminators were used to determine the time at which a certain particle impinged each of the counters. The telescope time correlation spectrum is shown in Figure 8.4 (Right panel). A coincident peak of only  $\sigma = 50\ \text{ps}$  was obtained, even though

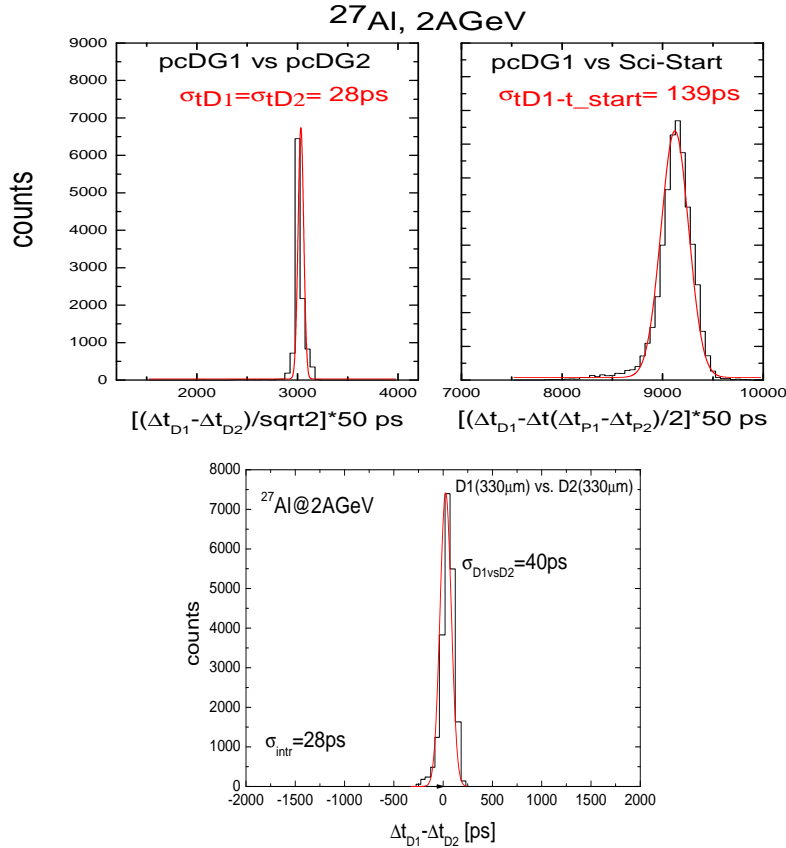


Figure 8.3: Time resolution of pc and scCVD-DDs for 2 AGeV  $^{27}\text{Al}$  ions measured with the FEE-card, developed for FOPI spectrometer. (Top-left) Intrinsic time resolution measured with two pcCVD-DD. (Top-right) Intrinsic time resolution of the plastic scintillator used in this experiment as a reference detector. (Bottom) A time resolution measured with two scCVD-DDs. The same value of the intrinsic time resolution obtained for both types of diamonds suggest electronic noise limitation.

a walk correction for such fast signals was not feasible.

To clarify the diamond detectors rate capability, the  $300\ \mu\text{m}$  scCVD-DD was exposed to direct proton and  $\alpha$ -particle beams. The minimum stable current extracted from the accelerator corresponded to a beam flux on the order of  $10^7 - 10^9$  particles/s $\cdot\text{cm}^2$ . Although the irradiation lasted several minutes, the BB-signals monitored with a fast digital oscilloscope, have not shown degradation or increased noise. In this run, the spectroscopic properties of scCVD-DDs were tested in addition. For the  $\Delta E$  detector a  $\Delta E/E = 0.7\ \%$  was obtained. This value was limited by the fluctuations of the particle energy-loss in the target foils, confirming the excellent resolution measured for  $\alpha$ -particles under laboratory conditions. More details on these beam tests can be found in [Bed07].

**Time resolution for minimum ionizing protons** The time resolution capability of scCVD-DD was tested using 3.5 GeV protons and a new low-capacitance broadband amplifier (LCBB) designed for the diamond start detectors of the HADES spectrometer. Two scCVD-DD of thickness  $d=300\ \mu\text{m}$ , equipped with 3 mm circular electrodes segmented in four quadrants, were mounted on an amplifier pcb in order to minimize stray capacitances.

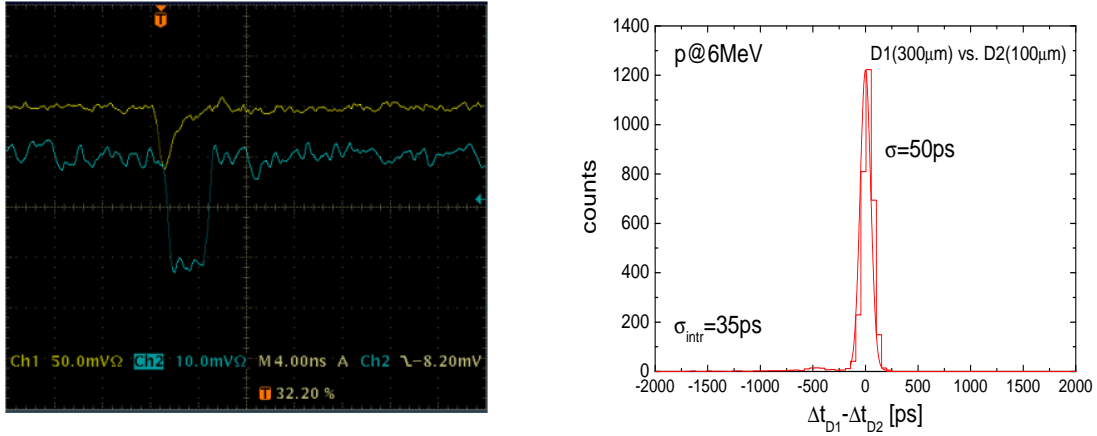


Figure 8.4: Time resolution of scCVD-DDs for 6 MeV protons. (Left panel) Analogue signals of the  $\Delta E$  sensor (a 100  $\mu\text{m}$  thick) - yellow curve and of the E sensor (300  $\mu\text{m}$  thick) - blue curve. Both amplified by DBAI amplifiers and registered with a 1 GHz DSO. (Right panel) Time spectrum.

Figure 8.5 (Left panel) shows the time spectrum obtained with two opposite diamond segments, aligned in the proton beam. The intrinsic resolution  $\sigma_{intr} = 107$  ps achieved, is a significant milestone towards the difficult goal of a  $\sigma_{intr} < 100$  ps. The tail in the time spectrum is due to edge events of longer drift time - an unavoidable experimental drawback in measurements where relativistic particles are used to test sensors smaller than the beam spots.

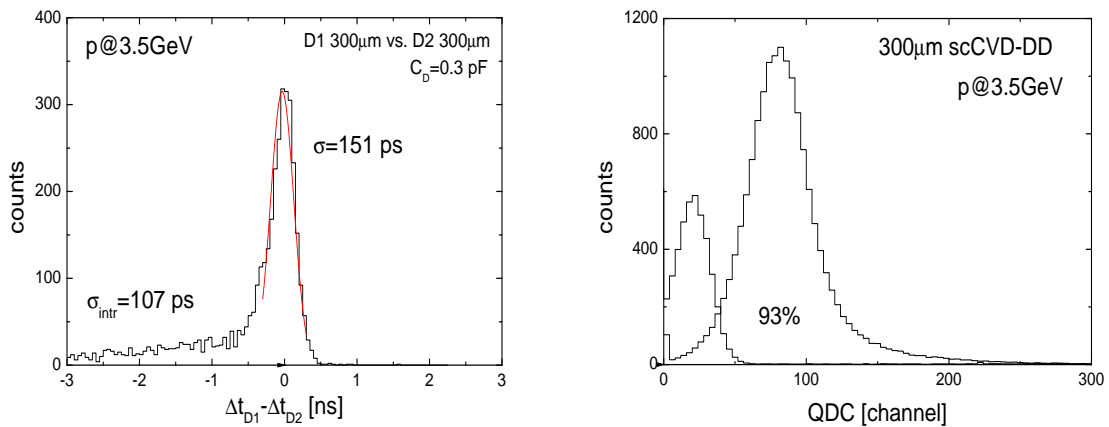


Figure 8.5: Time spectrum of scCVD-DDs for 3.5 GeV protons measured with low-capacitance broadband amplifiers, being developed for the START detector of HADES spectrometer. (Left panel) Proton time spectra. The tail to the left thought to be associated to 'edge events'. (Right panel) QDC registered pulse height spectra and the noise distribution.

Figure 8.6 summarizes the timing measurements performed with scCVD-DDs (open

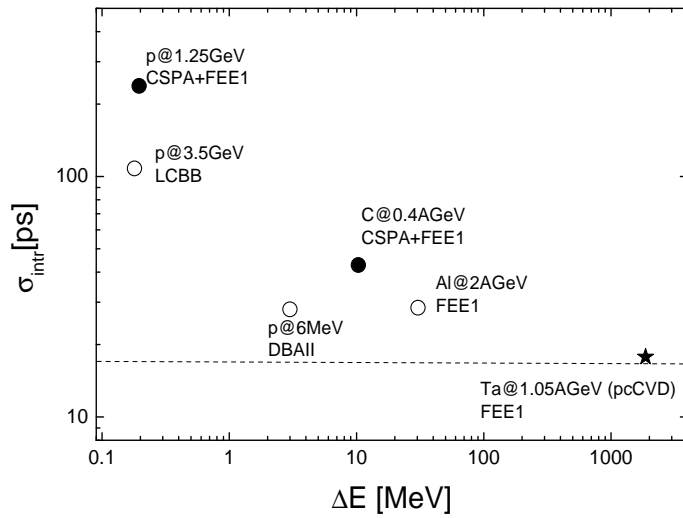


Figure 8.6: A plot, summarizing the timing measurement with scCVD-DDs. The intrinsic time resolution of diamond detectors is presented for various ions as a function of the deposited energy. Various readout electronics used in these measurements is indicated with abbreviations (see text).

dots). In addition, data points measured by the FOPI collaboration with pc- and scCVD-DDs are displayed (full dots). Due to the small intrinsic signal produced by a MIP within scCVD-DD, the signals induced by relativistic proton and carbon beams were pre-amplified with fast charge sensitive preamplifiers (CSA). The intrinsic timing resolution  $\sigma_{intr}$  obtained is plotted as a function of the energy deposition in the sensors. The general trend of deteriorating  $\sigma_{intr}$  for low ionizing particles can be concluded as a result of the decreased S/N ratio. The advantage of the broadband readout is also evident.

## 8.2 Spectroscopic Properties

In this section the performance of scCVD-DDs in measurements with relativistic heavy ions of mass around  $A=130$  and nuclear charge around  $Z=50$ , is discussed. A projectile fragmentation experiment was performed at the FRS (FRagment Separator) of GSI [Gei92], providing the unique opportunity to study in one run the energy-loss ( $\Delta E$ ), in diamond along with the particle identification potential of these novel detectors over a wide range of ions. The resulting diamond pulse height distributions are compared to those obtained from a silicon PIN diode sensor, and to the high-resolution spectra of MULTiple-Sampling-Ionization-Chambers (MUSIC detectors) [Bau97] used routinely for Particle IDentification (PID) at the FRS. Additionally, measured Transient-Current (TC) signals of a scCVD-DD produced by  $^{132}\text{Xe}$  ions of 212 AMeV, allowed an insight into the charge carriers transport properties of tested detectors at ionization densities, which are a few orders of magnitude higher than that of minimum ionizing protons or  $\alpha$ -particles.

### 8.2.1 Experimental Environment

Figure 8.7 shows a schematic of the FRS magnetic system with its four sections S1-S4, each ending in a corresponding focal plane F1 to F4. The experimental setup at F2 and F4 are sketched in a zoomed scale below the magnetic system. The target area (TA) is indicated on the left side of the picture. An independent PID was performed by coincident measurements of  $\Delta E$  spectra with two MUSIC chambers, one placed in front (MUSIC42) and the second after the test detectors (MUSIC41). In an event-by-event basis, MUSIC signals were corrected on-line, taken into account the Time-of-Flight (ToF) of the ions measured between F2 and F4 (distance F2-F4 = 36 m) with Lucite scintillation detectors. Hence, isotopes of the same magnetic rigidity  $B\rho$  are ejected in the MUSIC PID spectra. Several slits and MWPCs were serving for beam focusing and position control along the beam lines. The particles impinged the test sensors after energy loss in vacuum windows and several inhomogeneous layers of detector materials. Thus, the entrance energy of ions is always lower than the ion SIS energies. Despite a well focused beam, even for the primary Xenon ions, the beam spot was larger than the active area of the studied detectors. This led to distorted signals and to an incomplete charge collection for particles hitting the edge of the detector electrode [Ber07].

Three scCVD-DDs (D1, D2, D3) of  $4\times 4\times 0.4$  mm<sup>3</sup> in size were tested. The samples were patterned with Cr(50 nm)Au(100 nm) pad electrodes of 3 mm diameter, which had been annealed at 550 °C. As a reference detectors a 400  $\mu\text{m}$  thick silicon PIN diode (Si1) was used. The Si1 detector was characterized by an active area of  $5\times 5$  mm<sup>2</sup> surrounded by a 0.5 mm wide floating guard ring. All sensors were mounted on a remote-controlled movable platform (see Figure 8.8). For individual tests, each detector was separately moved into the beam. The induced signals were processed using charge sensitive electronic chains consisting of: a CSTA2 preamplifier and a main ORTEC amplifier with a shaping time of 0.5  $\mu\text{s}$ . Each electronic chain was calibrated by means of a high-precision pulse generator. The average energy needed for e-h pair creation in diamond was assumed to be 12.86 eV/e-h (see Chapter 6).

The ion energy loss calculations were performed in ATIMA [ATIMA] code, applying the Lindhard and Soerensen (LS) theory [Lin96]. ATIMA is running as a part of

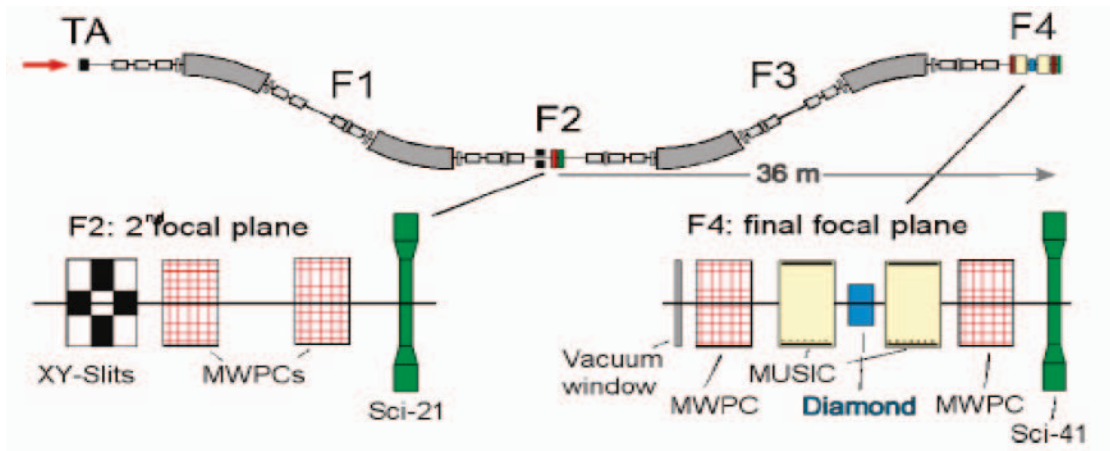


Figure 8.7: Experimental environment of the FRS with its four magnetic dipole stages. The scCVD-DDs are placed at F4, between two gaseous ionization chambers (MUSIC) used for particle identification along with two scintillator detectors providing the ion ToF between F2 and F4. The beam position is displayed by several MWPC counters and the beam profile is optionally optimized by XY-slits mounted at F2.

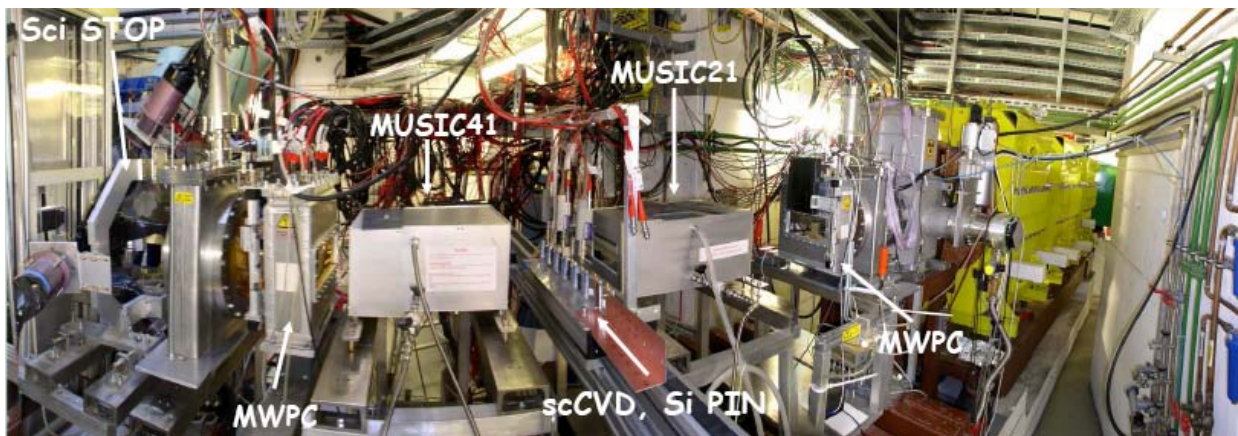


Figure 8.8: Panoramic photograph of the experimental area of the FRS at S4. Detectors used in the experiment are indicated in white. Photo courtesy M. Traeger.



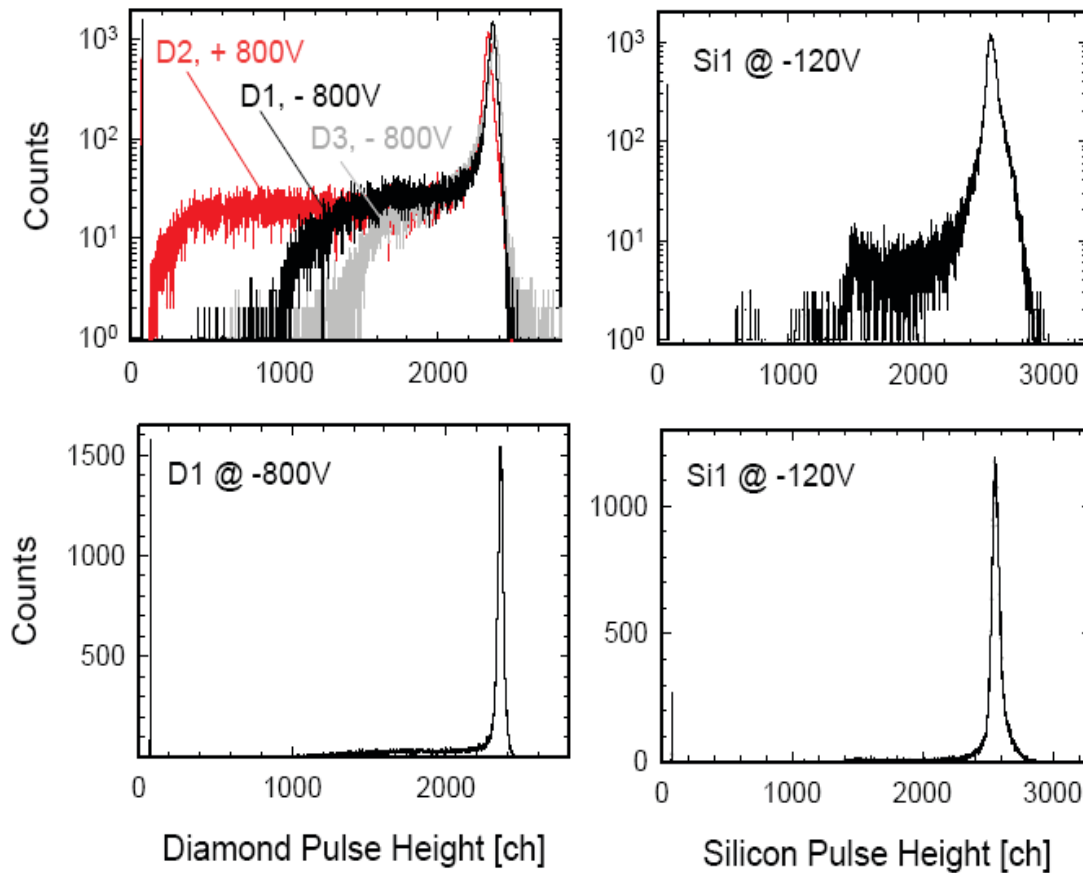


Figure 8.9: (Top left) Raw spectra of  $^{132}\text{Xe}$  projectiles of 215 AMeV measured with three scCVD-DDs at positive and negative bias. (Top right) Same measurement performed with Si1 at highest possible bias. Both spectra (top) plotted in logarithmic scale, reveal the low-energetic tails, which result from events located at the edge of the electrode.

LISE++ [LISE], the fragment separator simulation software with an implemented experimental arrangement of the GSI's FRS setup.

### 8.2.2 Detector Response to $^{132}\text{Xe}$ Projectiles at SIS Energies

#### Shape of the distribution and charge collection efficiency for primary $^{132}\text{Xe}$ ions

In Figure 8.9 raw pulse height distributions of primary  $^{132}\text{Xe}$  ions of an entrance energy of 215 AMeV ( $E_{SIS} = 334$  AMeV), measured with the scCVD-DDs at both bias polarities are compared to the corresponding spectrum obtained with the silicon detector Si1. Events of incomplete charge collection are visible in both spectra, which arise from particles impinging at the electrode edges.

Besides of the low-energetic tails in the  $^{132}\text{Xe}$  spectra of Figure 8.9, for three scCVD-DDs Gaussian line shapes of a relative width  $\delta E_{dia}/\Delta E_{dia}$  around 1.5 % were obtained. All distributions do peak within the measurement error at the ATIMA predicted mean value of the energy loss. The Si1 spectrum shows slightly worse  $\delta E_{Si1}/\Delta E_{Si1}$  at fwhm, and additional tails on the high-energetic line part.

The collected charge measured with D1 and D2 for primary  $^{132}\text{Xe}$  ions of entrance



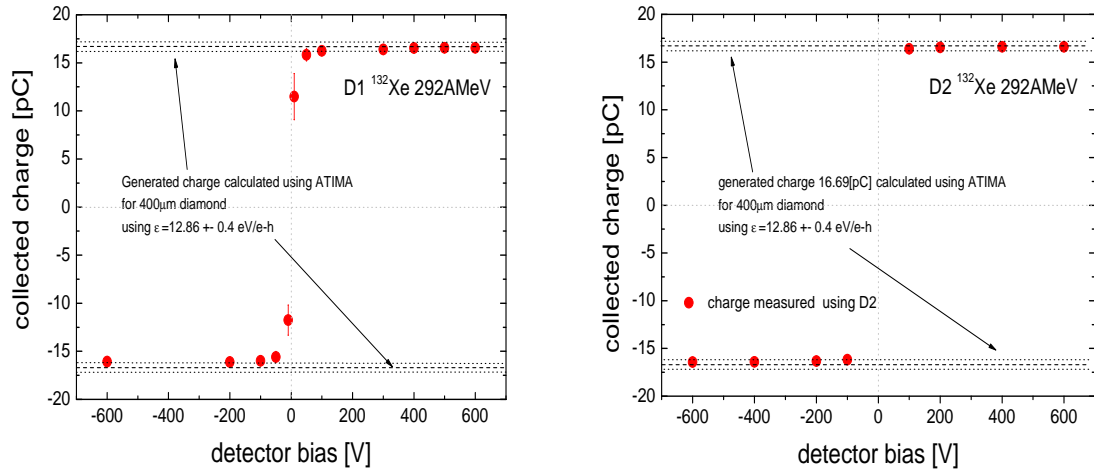


Figure 8.10: Dependence of the charge collected with D1 and D2 on the applied electric field. A quick saturation to the expected 100 % level (indicated by the dashed lines) is obtained for both detectors at very low bias.

energy 292 AMeV ( $E_{SIS} = 400$  AMeV) is plotted in Figure 8.10 as a function of the applied bias. Data points represent mean values of Gaussian fits of the experimental pulse height distributions with FWHM used as the error bars. Remarkably symmetrical characteristics and quick saturation to the expected 16.7 pC ( $1.031 \times 10^8 e$ ) level (indicated by dashed lines) are obtained for both scCVD-DDs already at  $\pm 100$  V ( $0.25$  V/ $\mu$ m).

The response of diamond detectors to Xenon ions of different kinetic energy is shown in the left graph of Figure 8.11. The expected descending trend in the energy loss for higher kinetic energies is obtained with a perfect agreement to the predicted values. At higher energies, the measured values of energy loss are slightly lower than predicted, most probably due to highly energetic  $\delta$  electrons escaping the active detector volume. The relative resolution  $\delta E/\Delta E$ , (shown in Figure 8.11 (Right panel)), deteriorates with higher entrance energies into the diamonds. For high energy deposition the relative resolution improves, showing that despite an increased ionization density the diamond detectors show no pulse height defects. The measured values do not exceed the predictions, showing that the resolution obtained is only limited by the unavoidable energy loss straggling, originating from the variation of the impact parameters involved.

### 8.2.3 Fragments Spectra

Particles, of different  $Z$  and  $A$  created by fragmentation of  $^{132}\text{Xe}$  ions of  $E_{SIS} = 740$  AMeV kinetic energy on a  $4 \text{ g/cm}^2$   $^9\text{Be}$  target were bent by the magnetic system of the FRS to hit the test sensors almost perpendicularly at F4. Figure 8.12 (top-left graph) shows the 2D correlation plot of the raw pulse height distributions of the transmitted fragments, measured with D2 at 800 V and the MUSIC41 placed before the diamond sensor. The distorted events, visible as trails on the left hand side from the correlated events, are excluded applying a polygon condition shown in red. The corresponding raw spectra of MUSIC41 and diamond D2 are shown in a zoomed scale in the top-right and in the bottom-left graph, respectively.

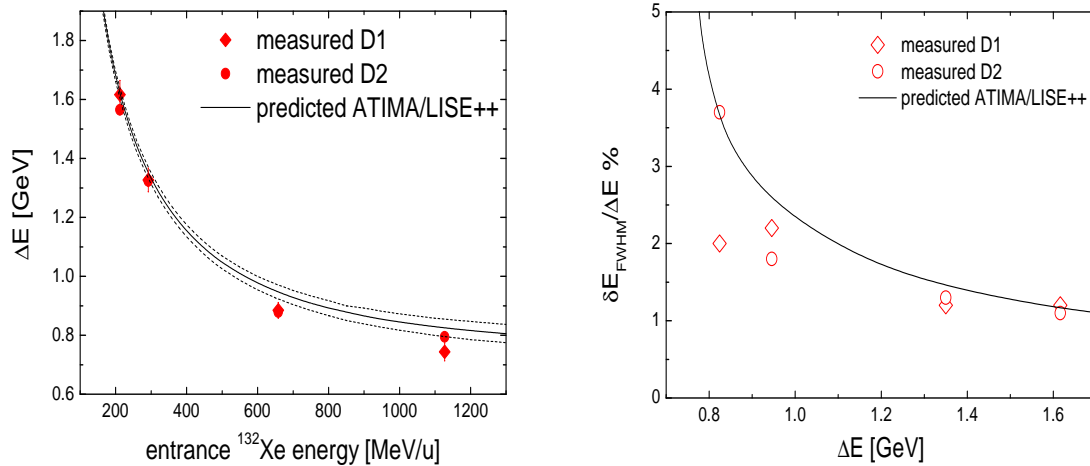


Figure 8.11: (Left panel) Response of scSCV-DDs to  $^{132}\text{Xe}$  ions of different kinetic energies. (Right panel) The relative energy resolution of scCVD-DDs as a function of deposited energy.

The D2 spectrum prior to the edge-event correction is displayed in black, and the corrected spectrum in red. About 16 fragments may be distinguished in the presented range, as shown in the MUSIC41 PID spectra (bottom-right graph). The distributions were obtained with two settings of the FRS with individual transmission profiles, chosen to cover consecutive  $Z$  regions of highest intensity transmission for elements  $Z=45$  and  $Z=48$ . In reality, the fragmentation cross-section decreases exponentially with  $Z$ . In the presented raw spectra, the line widths contain some broadening by various isotopes of the same magnetic rigidity, which arrive on the detector with slightly different velocities. Nevertheless, one can see that the  $Z$  identification power of scCVD-DDs is remarkably comparable to the property of the state-of-art high-resolution ionization chambers.

Figure 8.13(top-left) shows a plot of the energy loss  $\Delta E$  measured with D2 versus the ToF between F2 and F4 obtained with scintillator detectors. By applying the polygon condition shown in red, the broadening of the fragments spectral lines due to the spread of the ions velocities is excluded (top-right graph). The signal amplitudes measured with D2 are plotted in the bottom-left graph versus  $Z^2$ . A linear dependence is observed for  $\Delta E$ , in the measured range of  $Z^2$ . The pulse-height resolution is extracted by deconvoluting the top-right fragments spectrum with Gaussians. The results are plotted in the bottom-right graph of Figure 8.13 over the corresponding  $Z$ . The measured values follow exactly the expected widths (dotted curve) calculated with LISE++, showing that the detector performance is limited only by the statistical processes of energy loss. In contrast to the MUSIC detectors the resolution improves as  $Z$  increases [Bau97]. This shows that at least in the measured range, no pulse-height defect occurs in the case of increased ionization density. Concluding, the data demonstrate the high potential of scCVD-DDs applied for particle identification.

**Comparison with the performance of silicon detectors** The pulse-height distribution of D2, calibrated in pC is presented in Figure 8.14 (top graph) along with the

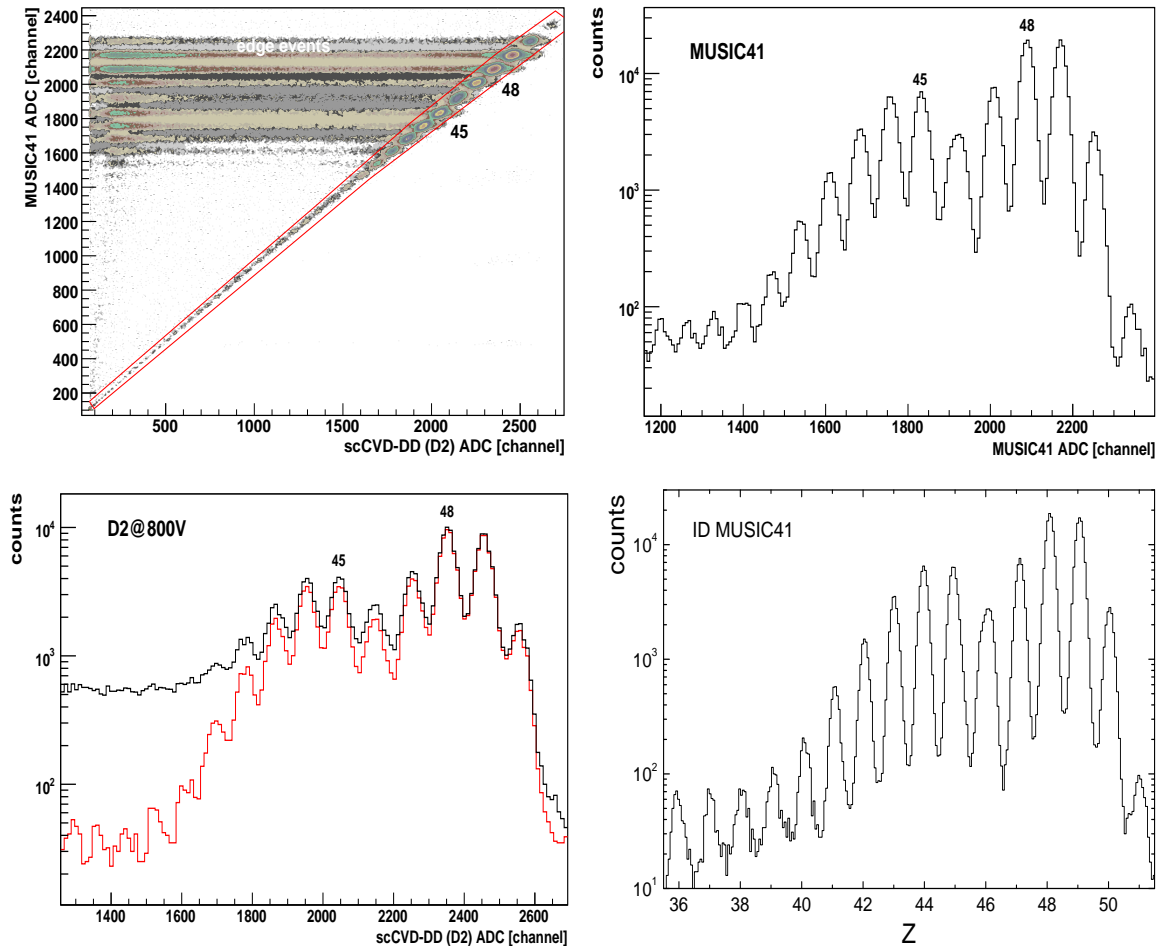


Figure 8.12: (Top-left) Pulse height scatter plot of D2 versus MUSIC4. Non-correlated 'edge events' are excluded applying the indicated polygon condition (in red); (Top-right) The corresponding raw pulse-height spectrum of MUSIC4; (Bottom-left) The corresponding raw pulse-height spectrum of D2; in black before 'edge events' correction; in red after correction; (Bottom-right) MUSIC41 PID spectrum, where data are additionally corrected considering the fragment ToF. The data have been obtained with two sets of FRS parameters, which transmitted the fragments  $Z=45$  and  $Z=48$  with highest intensity.

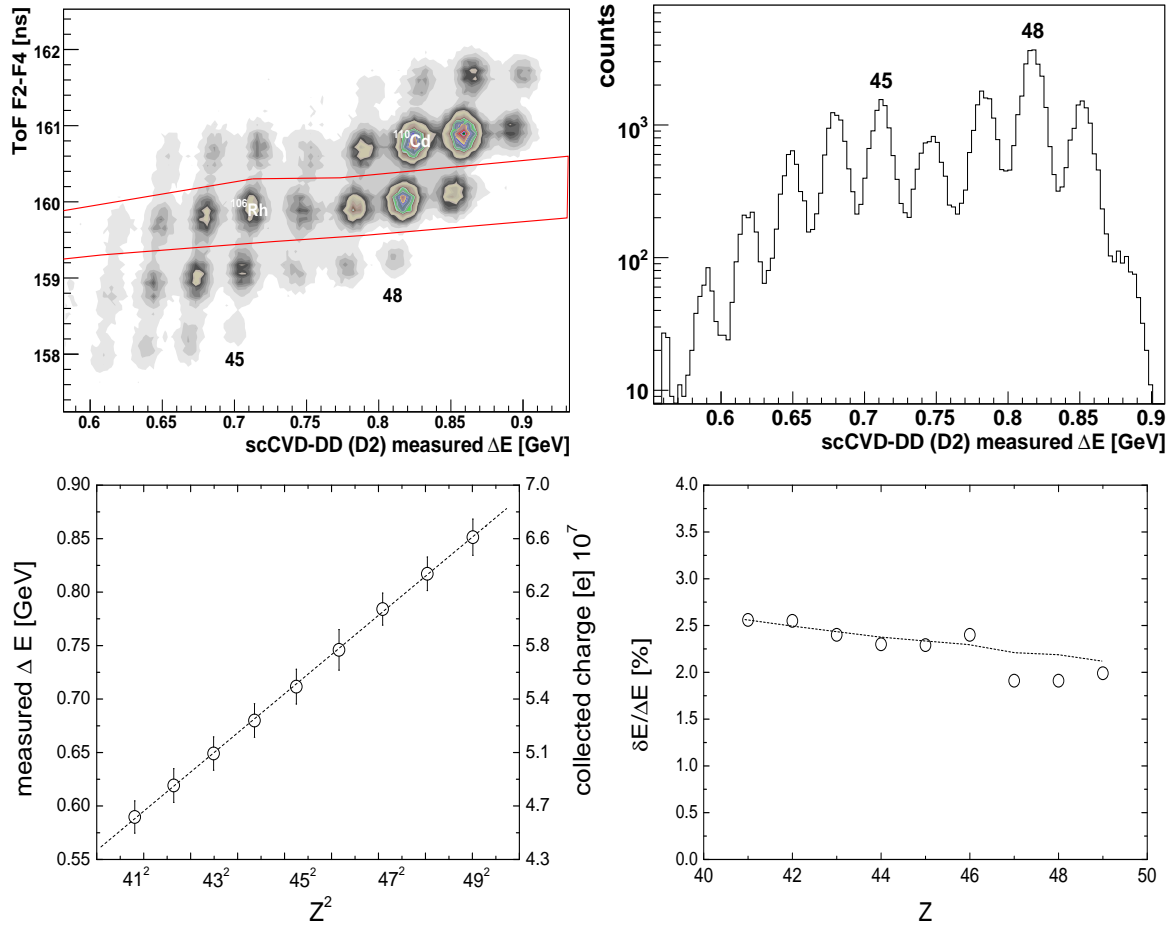


Figure 8.13: (Top-left) A plot of  $\Delta E$  versus ToF obtained with a scCVD-DD and scintillator detectors, respectively. (Top-right) The corresponding measured  $\Delta E$  of the scCVD-DD spectrum for fragments fulfilling the polygon condition. (Bottom-left) The mean  $\Delta E$  values of the fragments measured with the scCVD-DD follow the linear trend in the measured range of  $Z^2$ . (Bottom-right) The energy resolution of the scCVD-DD as a function of  $Z$ . The measured values do not exceed the predicted ones (dotted line), suggesting the unavoidable energy-loss straggling as the limiting factor of the detector performance.

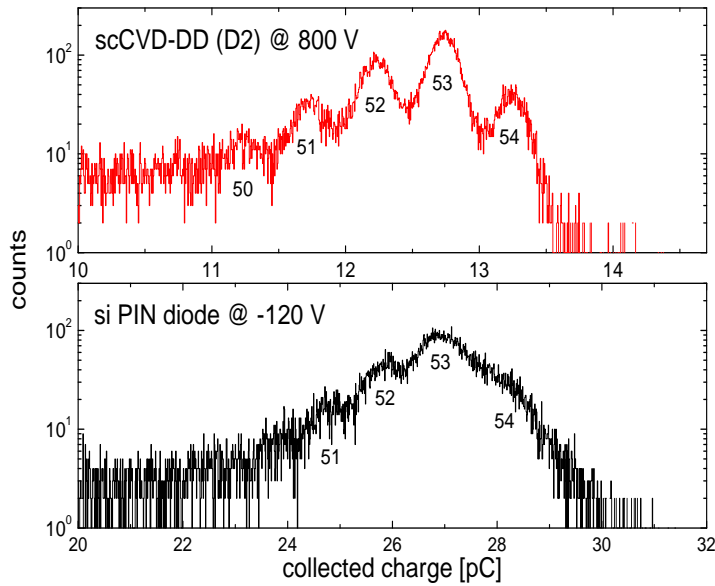


Figure 8.14: Comparison of pulse height spectra the  $^{132}\text{Xe}$  fragments obtained with a scCVD-DD (top in red) and with a silicon PIN diode (bottom in black). The transmission window of the FRS was centered at  $Z = 53$ . The spectra are not corrected for 'edge events' and variations of the ions velocity.

corresponding Si1 distribution (bottom graph), both measured in the range  $50 < Z < 54$  centered at  $Z = 53$ . The presented spectra are not corrected considering the edge events nor the different velocities of fragments of this same rigidity. The intention was to compare the performance of both detectors under same conditions. The superior performance of diamond in this experiment is evident, although before the FRS run Si1 showed slightly better resolution for 5.48 MeV  $-$ particles than the scCVD-DDs. The Si1 result cannot be explained by the beam intensity or radiation damage effects. In the performed spectroscopic measurements the rates were low ( $\sim 1$  kHz) and the total estimated fluence on Si1 was  $\sim 10^5$  p/cm<sup>2</sup> i.e., much lower than the integral rate on D2. However, due to a conversion factor  $\epsilon_{avg}^{Si} = 3.61$  eV/e-h for silicon, being about 4 times higher than for diamond ( $\epsilon_{avg}^{Diam} = 12.86$  eV/e-h), the predicted lower energy loss still leads to about twice higher generated charge in silicon counters. This advantageous property in measurements of weakly ionizing ions leads in the case of heavy ions to a highly space-charge limited (SCL) charge carriers transport. The consequence of SCL transport is extremely long drift time ( $> 500$  ns) of the excess charge carriers in silicon. Pulse height defect and deterioration of the energy resolution are observed due to the fact that the charge collection takes longer time than the shaping time of the CS electronics of  $0.5 \mu\text{s}$  in this special case. Particularly the case where a high rate capability is required, diamond detectors of superior carrier mobility and of high-field operation are preferable, since they provide quick restoration of the electric field within the detector active area.

### 8.2.4 Transient Current Signals

$^{132}\text{Xe}$  ions of 215 AMeV entrance energy produce homogeneously about  $3 \times 10^5$  e-h/ $\mu\text{m}$  in diamond. For such high ionization there is no need for signal amplification. Therefore, the transient-current signals of a  $400 \mu\text{m}$  thick scCVD-DD were registered by coupling the detector to a 1 GHz DSO, through a 30 m long high-frequency transmission line. Signals of detector D2, recorded upon a stepwise increase of the bias, are shown in Figure 8.15 (Right panel) as black solid curves. In the left panel of Figure 8.15, the measured TC sig-

nal obtained at 500 V is displayed (black curve). This signal is compared to an analytically calculated one (red curve) using Equation 3.39, where a constant internal electric field  $E_{int}$  is assumed. The significantly longer decay time of the measured signal suggests a modification of the internal field  $E_{int}$  due to the high ionization density. The charge transport is space charge limited in this case [Isb04]. Although analytical calculations do not match experimental results, numerically simulated TC signals reproduce quite precisely the measured curves as shown in red colour in Figure 8.15 (Left panel). The simulated signals in a modeled 400  $\mu\text{m}$  thick diamond detector were obtained using EVEREST semiconductor-devices simulation software [EVE]. A linear homogenous charge injection of 20.05 pC and the measured charge carriers drift velocity and mobility in scCVD (see Chapter 6) were used in the simulation. Details on the initial parameters, boundary conditions and the simulation geometry are shown in the Appendix.

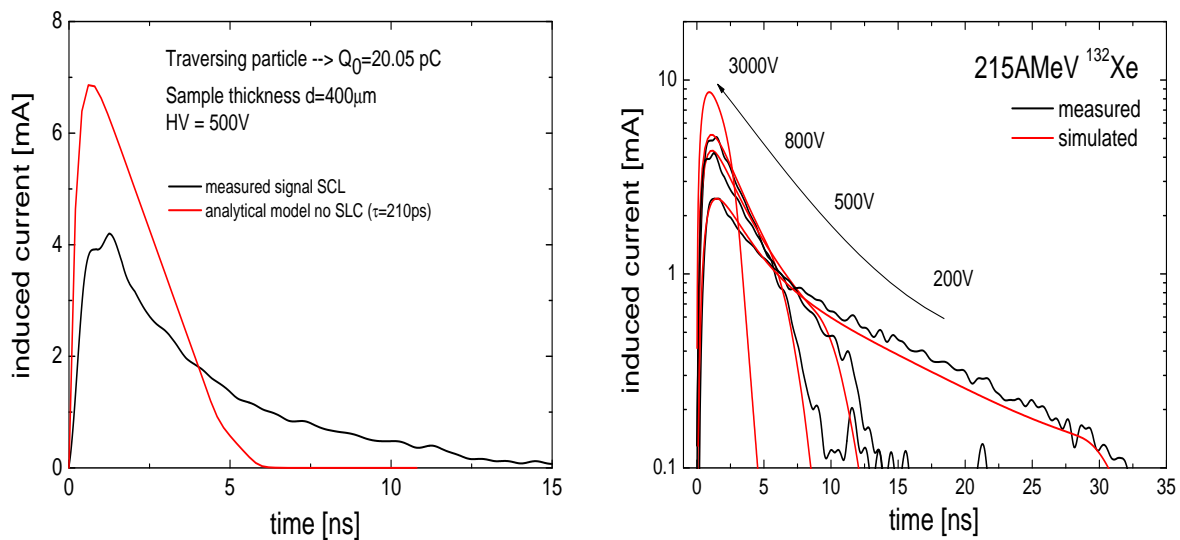


Figure 8.15: (Left panel) Transient current (TC) signals of  $^{134}\text{Xe}$  ions of 215 AMeV in D2 biased with 500 V: in red - analytically calculated assuming a constant internal electric field. in black - measured signal. The observed difference suggest a space-charge limited (SCL) transport. (Right panel) The TC signals of  $^{134}\text{Xe}$  ions of 215 AMeV for different bias, measured with a 400  $\mu\text{m}$  thick scCVD-DD (D2) (in black) and the corresponding numerically simulated TC signals (in red)

Despite the SCL charge transport, the rise time of the diamonds TC signals is not affected, preserving thus its good timing properties. The measured value of 300 ps is mainly dominated by the contributions of the 1 GHz scope and the transmission lines. Similar TC signal shapes, of an area corresponding to about 100 % of the generated charge were obtained at positive and negative bias, confirming full charge collection, as measured previously with charge sensitive electronics. At an operation bias of 800 V ( $E \sim 2 \text{ V}/\mu\text{m}$ ), the FWHM decreases below 3 ns, whereas the full charge collection requires a time of 10 ns, being significantly longer than the value measured with short-range  $\alpha$ -particles of 5.5 MeV (see Chapter 6). However, at a sufficiently high voltage of 3000 V ( $7.5 \text{ V}/\mu\text{m}$ ), the SCL transport is minimalized, giving the full charge collection within 4 ns, which is a typical transit time for the non-SCL regime.

## 8.3 Summary of the In-beam Tests

The timing and the spectroscopic properties of scCVD-DDs were studied in-beam operation. The same intrinsic time resolution of 28 ps was measured for pc- and scCVD-DDs with relativistic  $^{27}\text{Al}$  ions. This unexpected result from detectors of such strikingly different S/N ratio is attributed to the influence of the electronics. It demonstrates the high potential of CVD diamond, which is still not exploited to full advantage. For the first time the measured intrinsic time resolution of scCVD-DDs for minimum ionizing protons approached 100 ps. However, further electronics development is needed in order to improve the results obtained.

The excellent pulse height resolution  $1.5\% \leq \delta E_{\text{diam}}/\Delta E \leq 2.5\%$  obtained with scCVD-DDs in experiments with  $^{132}\text{Xe}$  projectiles and Xe fragments (limited only by the energy loss straggling) demonstrate the high potential of such sensors in HI experiments, requiring fast detectors with spectroscopic properties. These characteristics are useful for both, PID and background reduction via  $\Delta E$ . The measurements show that diamond detectors are approaching the pulse-height resolution of MUSIC chambers and are superior to silicon devices under the same experimental conditions. The transient-current signals obtained are well suited for precise heavy-ion timing of a resolution well below 50 ps up to particle rates as high as  $10^8$  pps. The temporarily screened electric field due to the high ionization density produced by heavy ions does not affect the charge collection or the timing properties at high-bias operation. Concluding, scCVD-DDs can be considered as high-rate, stand-alone detector systems for PID, with both, precise timing and energy loss measurement.





# Chapter 9

## Summary and Outlook

This work presents the study on the suitability of single-crystal CVD diamond for particle-detection systems in present and future hadron physics experiments. Different characterization methods of the electrical and the structural properties were applied to gain a deeper understanding of the crystal quality and the charge transport properties of this novel semiconductor material. First measurements regarding the radiation tolerance of diamond were performed with sensors heavily irradiated with protons and neutrons. Finally, detector prototypes were fabricated and successfully tested in various experiments as time detectors for minimum ionizing particles as well as for spectroscopy of heavy ions at the energy ranges available at the SIS and the UNILAC facilities of GSI.

Ultra-high purity with respect to atomic impurities of the material was confirmed by solid-state spectroscopic characterization techniques. Structural characterization of scCVD diamond by means of white beam X-ray topography and cross-polarized light microscopy allowed to investigate the crystal structure and to obtain topographic images, revealing isolated structural imperfections in form of threading dislocations. It was found that structural defects present in earlier received samples led to detector failures, by decreasing the diamond dielectric strength and thus inducing hard breakdown for detectors operated in high-flux radiation fields. The charge transport properties were tested by means of the transient current technique in a wide range of electric field applied. Important parameters (which characterizes the charge carrier transport in a semiconductor) like drift velocity, saturation drift velocity, low-field mobility and lifetime, were measured for the diamond samples. The electrical characterization methods include also spatially resolved measurements of the charge collection efficiency with a generation of charge carriers by X-ray micro-beam as well as non-resolving measurement methods with  $\beta$  and  $\alpha$  particles. It was found that the charge collection properties of scCVD diamond are distributed uniformly in the bulk. For the first time in diamond-detector development, the measured charge-collection distances significantly exceeded the typical sample thickness of 300-500  $\mu\text{m}$  for all investigated sensors. Full charge collection at relatively low fields and an extraordinary uniformity of the detector response on the order of 0.1 % ( $1\sigma$ ) were found for both methods of characterization applied.

The motivation to investigate the particle detection properties of scCVD diamond is its supposed radiation hardness. Therefore, the radiation hardness was tested by irradiation with 26 MeV protons and 20 MeV neutrons up to  $10^{16}$  particle/cm<sup>2</sup> integral fluence. The sample resistivity, the charge collection and the transient current signals were recorded as a function of the radiation exposure. In contrast to silicon detectors, no increase of the

leakage current was found after irradiation. Thus the contribution of irradiated diamond detectors to the electronic noise remains negligible. The registered transient current signals of irradiated detectors showed no space charge effects or degradation of the charge carriers velocity. This result is attributed to the creation of neutral mono-vacancies as the dominant defect. The lifetime of the excess charge carriers drops linearly with the applied fluence, but primed detectors were still able to operate at RT, even after the highest applied fluence  $> 10^{16} \text{ cm}^{-2}$  with a clear pulse height separation from the electronics noise.

Finally, several detector prototypes were used in heavy-ion and minimum-ionizing particle beams, which covered a dynamic range of induced signals of  $1 : 10^5$ . The stability as well as reproducibility of the detection properties were tested up to 1 GHz ion rates. It was shown that the spectroscopic properties of scCVD diamond in the relativistic HI regime are comparable to the high-resolution MUSIC gaseous ionization chamber, allowing clear particle identification in a fragmentation experiment. Furthermore, due to high carrier mobilities and the high field operation ability, performance of scCVD-DDs turned out to be superior to the silicon PIN diodes in the case heavy fragments. The outstanding timing properties are identical to pcCVD-DDs for light relativistic ions, limited only by the electronic noise of the available electronics. For the first time, the measured intrinsic time resolution of scCVD-DDs for minimum ionizing protons could be shown to approach 100 ps. However, further electronics development or/and detector engineering is needed in order to improve the obtained results.

Recapitulating, the three major subjects of this thesis are listed again: the characterization of the electrical and the structural properties of scCVD diamond, tests of the radiation tolerance with protons and neutrons, and successful in-beam tests of detector prototypes made of this novel type of diamond material.

**Perspectives for future developments of diamond detectors** At present, the main drawback of scCVD-DD is its size, limited by the size of HPHT diamond substrates used in CVD. Single crystal homoepitaxial diamond films are commercially available up to  $5 \times 5 \text{ mm}^2$ , with the option of a growth maximum of  $2 \times 2 \text{ cm}^2$  samples. However, recently realized heteroepitaxial growth of scCVD diamond on iridium substrates can overcome this limitation [Sch01]. Samples of sizes of several millimeters have already been grown by this method and have been successfully tested as particle detectors in heavy-ion beam tracking. The measured intrinsic time resolution of  $\sigma = 15 \text{ ps}$  for 78 AMeV  $^{78}\text{Kr}$  ions and the  $\Delta E/E$  resolution in order of 18 %, are promising [Sto06]. The perspectives of large size quasi-scCVD-DD are worth any effort to develop this diamond material. Iridium substrates are routinely produced in Augsburg to sizes as large as four inches in diameter as reported by [Fis08]. A new collaboration (successor of NoRHDia) aiming to develop large area advanced diamond devices based on this type of diamond is recently formed.

To improve the timing properties for minimum ionizing particles as well as the radiation tolerance of scCVD-DD, 3D structures may be considered for future diamond detector development. Such detectors (e.g., of  $100 \mu\text{m}$  electrodes interspaces and  $500 \mu\text{m}$  thickness), could be operated at RT after irradiation with fluences exceeding  $10^{16} \text{ cm}^{-2}$  with satisfying signal-to-noise ratio. Technologically, the laser cutting or graphitization by ion implantation can be considered as a tool for 3D structure of the electrodes fabrication within the diamond bulk [Sud06].

Although scCVD diamond is still not a 'commercial' material for detector fabrication,

it is considered to be employed (or already has been employed) as particle detector in the upgrades of existing experiments or in future experiments. For instance, scCVD pixel detectors are being developed at CERN for the Compact Muon Solenoid (CMS) luminosity monitors [Hal06] as well as the beam abort system [Fer05]. At GSI, scCVD diamond is considered for use as a strip START detector for the Compressed Baryonic Matter spectrometer (CBM) [CBM]. A  $\Delta E$ , E, ToF detector system for slowed-down radioactive heavy ions tracking at FAIR, is currently investigated by the NUSTAR collaboration [Bed07, NUST]. Also, outside the hadron physics community, there is great interest for using scCVD as radiation-detection material, for instance as low energy X-ray beam position monitoring of the next generation of synchrotrons at the ESRF and XFEL at DESY [Mor07a] or as radiation hard neutron detectors for nuclear reactor control and fusion experiments (ITER, OMEGA) [Mur07].

Could it be that in the future, diamond becomes not only a girl's best friend?



# Deutsche Zusammenfassung

Detektorsysteme, implementiert an zentralen Stellen zukünftiger Experimente zur Physik der Hadronen und Kerne, werden höchsten Anforderungen bezüglich Strahlungshärte und Zählratenfestigkeit genügen müssen. Die berechneten Reaktionsraten erreichen Größenordnungen bis zu  $10^8$  Ereignissen pro Sekunde. Je nach Einsatz, wird hohe Energie- Zeit- oder Ortsauflösung erwartet und in vielen Fällen, die Kombination mehrerer Eigenschaften gleichzeitig. Darüber hinaus, wird einem möglichst untergrundfreien Einsatz große Bedeutung beigemessen.

In den letzten Jahrzehnten wurden neben anderen Strahlungssensoren, sehr erfolgreich, Siliziumdetektoren eingesetzt. Insbesondere in der Schwerionenidentifizierung in Niedrigenergieexperimenten oder in der Spurensuche des Ursprungs von geladenen minimal ionisierenden Reaktionsprodukten in Hochenergieexperimenten, waren sie unverzichtbare Bestandteile der experimentellen Aufbauten. Jedoch ist die Strahlungshärte von Siliziumsensoren in vielen Fällen ungenügend. Einen Ausweg aus diesem Dilemma bietet die Vielfalt neuartiger Halbleiter großer Bandlücke, die in den letzten Jahren auf den Markt erschienen sind. Der Vielversprechendste davon ist der technisch hergestellte Diamant aus der Gasphase (CVD Diamant). Er besitzt die einzigartigen physikalischen Eigenschaften von natürlichen Diamanten und übertrifft diese in chemischer Reinheit um ein Vielfaches. Seit mehr als einem Jahrzehnt wurden die Detektoreigenschaften von polykristallinem CVD-Diamant (pcCVDD) untersucht und bewiesen, dass sich pcCVDD Detektoren hervorragend als Schwerionenzeitähler in Experimenten mit hochintensiven primären Schwerionenstrahlen eignen. Andererseits, bewirkt ihre polykristalline Struktur eine unvollständige Ladungssammlung und verhindert dadurch sowohl einen zufrieden stellenden Einsatz für Teilchenspektroskopie oder Zeitmessungen mit schwach ionisierenden Teilchen, als auch jegliche Experimente mit extrem fokussierten Strahlen.

Ziel dieser Arbeit war, die Detektoreigenschaften von neuerdings kommerziell erhältlichem monokristallinem CVD Diamant (scCVDD) in Experimenten mit hochintensiven Ionenstrahlen aller verfügbarer Ionensorten und Strahlenergien ( $E_{ion} \approx$  einige AMeV bis mehrere AGeV) aufzuzeigen, ein umfassendes Bild des Stands der Forschung und Entwicklung darzustellen und darüber hinaus, Perspektiven für die Zukunft zu beschreiben. Das untersuchte Diamantmaterial ist ausschließlich hergestellt von der Firma Element Six, Ascot, UK und bezogen von dem Exklusivvertrieb Diamond Detectors Ltd, UK. Es wurden mehr als 30 Proben verschiedener Dicke ( $50 \mu\text{m} - 500 \mu\text{m}$ ) und Größe ( $3 \times 3 \text{ mm}^2 - 5 \times 5 \text{ mm}^2$ ) untersucht, die mit verschiedener Oberflächenbehandlung präpariert waren. Die Detektoreigenschaften der Proben wurden unter verschiedenen Aspekten studiert und ihre außerordentliche Qualität wurde mit mehreren Messmethoden bestätigt. Restkonzentrationen von den im Diamant üblichen Fremdatomen Stickstoff und Bor wurden mittels optischer Absorptionsspektroskopie im sichtbaren-, infrarot- und ultra-violettem Wellenlängenbereich

ermittelt, sowie durch ESR und TYPs Messungen. Es wurden extrem niedrige Verunreinigungskonzentrationen gemessen ( $N \leq 10^{14} \text{ cm}^{-3}$  und  $B \leq 10^{15} \text{ cm}^{-3}$ ). In Anlehnung an die offizielle Klassifizierung von Diamantmaterialien, sind die untersuchten Proben als ultra-reine Typ IIa Diamanten einzuordnen. Bei Untersuchungen der Kristallstruktur wurde Difraktionstopographie unter Bestrahlung mit weißem Licht angewendet, sowie optische Mikroskopie mit gekreuzt-polarisiertem Licht. Im Gegensatz zu der hohen chemischen Reinheit, wurden hierbei in fast allen Proben, isolierte, mikroskopisch kleine Strukturdefekte gefunden, die in Form von durchgehenden gebündelten Dislokationen auftreten. Vereinzelt wurden auch etwas breitere Defekte beobachtet. Beide Defektarten erzeugen mechanische Spannungen im Kristall, die mittels Mikroskopie mit gekreuzt-polarisiertem Licht visualisiert werden können. Die Dislokationen haben ihren Ursprung an den Oberflächen von unzulänglich präparierten HPHT Substraten, die sich beim CVD Prozess in die aufwachsende Diamantschicht fortpflanzen. Die Morphologie der CVD Probenoberflächen wurde mittels AFM (Atomic Force Microscopy) studiert. Je nach Oberflächenbehandlung, variierte die gemessene Rauigkeit von 6 nm (rms), was als 'schadhaft' zu benennen ist, bis zu  $< 1$  nm (rms) was als annähernd 'perfekt' angesehen werden kann. Die rauen Oberflächen rühren von herkömmlichen mechanischen Poliermethoden her, bei welchen diamantstaubbeschichtete Scheiben eingesetzt werden, die 'zahnradartige' Rillen erzeugen, während die perfekten glatten Oberflächen der besten Proben durch Ionenstrahlpolieren gewonnen werden. Die mit Schäden behafteten Oberflächen können zu undefinierten und zeitlich veränderlichen Eigenschaften der Diamantelektrodenrenzschichten führen und somit, zu veränderten Detektoreigenschaften im Langzeitbetrieb.

Verglichen mit der aufwendigen Halbleitertechnologie, die zur Herstellung von Siliziumdetektoren erforderlich ist, ist die Herstellung von Diamantdetektoren aus den gekauften Proben einfach. Nach dem Aufbringen der Detektorelektroden durch beidseitiges Aufdampfen oder Sputtern von einzel- oder mehrlagigen Metallschichten, kann die Probe als Detektor verwendet werden. Der hohe Innenwiderstand von nicht dotiertem CVD Diamant, erwirkt auch ohne künstlich erzeugter pn-Sperrschicht, eine an freien Ladungsträgern 'verarmte' Zone, die sich über das ganze Kristallvolumen erstreckt. Darüber hinaus, verhindert die große Bandlücke von Diamant ( $E_{gap} = 5.48 \text{ eV}$ ), dass der thermisch generierte Restdunkelstrom (aufgrund seiner extremen Temperaturabhängigkeit) bei höheren Umgebungs- und Betriebstemperaturen der Detektoren steigt. Das ist ein entscheidender Vorteil gegenüber Siliziumzählern, für die die Betriebstemperaturstabilisierung auf niedrigem Temperaturniveau (Kühlung) unverzichtbar ist.

Vor der Metallbeschichtung werden die Proben in einer aus Schwefel- und Salpetersäure bestehenden Mixtur gereinigt, die bis zur Siedetemperatur erhitzt ist. Diese einstündige Prozedur dient darüber hinaus zur wichtigen Oxidation der Proben (Sättigung der freien kovalenten Bindungen der Kohlenstoffatome der äußersten Diamantschicht), die elektrisch nicht leitende Oberflächen gewährleistet. Die Standardgeometrie der Elektroden ist die Parallelplattenkonfiguration. Im Falle ortsauffösender Sensoren, wird die eine Seite entsprechend strukturiert. Feinstrukturelektroden werden photolithographisch (ähnlich wie für Siliziumdetektoren) hergestellt. Die untersuchten Testproben hingegen, wurden mit Abdeckmasken aus Edelstahl im Targetlabor der GSI beschichtet, anschließend auf Glaskeramik Platinen geklebt und mit Aluminiumdraht auf die goldbeschichteten Signalleitungen gebonded. Zum Anlegen der Spannung und zur Signalauslese wurden hochspannungs- und hochfrequenztaugliche SMA Stecker und  $50 \Omega$  Koaxialleitungen benutzt.

Für die optimale Entwicklung von Detektoren aus neuartigen Materialien (wie scCVD Diamant), ist es extrem wichtig, detailliertes Wissen über ihre Dunkelleitfähigkeit als auch über den Transport der teilcheninduzierten Ladungen im Kristall zu erwerben. Das beinhaltet die Messung von Strom-Spannungskennlinien und die Ermittlung der Durchbruchspannung die den stabilen Betriebsbereich des Detektors festlegt, Driftgeschwindigkeits- und Lebensdauermessungen beider Ladungsträger in Abhängigkeit des angelegten elektrischen Feldes und schließlich, die Bestimmung der effektiven Raumladungskonzentrationen im Zählervolumen. Die Ladungstransportparameter wurden über einen großen Spannungsbereich mit Hilfe von  $\alpha$ -Teilchen kurzer Reichweite ( $\approx 12 \mu\text{m}$  in Diamant) ermittelt, die die separate Beobachtung von Elektronen- und Löcherdrift ermöglichen. Solche Messungen sind unter dem Begriff 'Technik der transienten Ströme (TCT)' bekannt. Die Form der  $\alpha$ -induzierten Pulse wurde hinsichtlich Signalentstehung, Ausbreitung und Ladungssammlung mit hoch auflösenden Digital-Oszilloskopen und speziell entwickelten Breitbandverstärkern im Gigahertz Bereich untersucht. Die Spektroskopieeigenschaften der monokristallinen CVD Diamanten hingegen, wurden mit Nuklearspektroskopieelektronik studiert, die ursprünglich für Siliziumsensoren entwickelt wurde. Dafür wurden Pulshöhenspektren verschiedener mono-energetischer Teilchen analysiert. Der Energie- und Z-Bereich der gewählten Ionensonden erstreckte sich von mixed-nuclid - bzw.  $^{90}\text{Sr}$ -Quellen im Labor, über niederenenergetische  $^{12}\text{C}$  Ionen am UNILAC, bis hin zu relativistischen Schwerionen ( $Z > 40$ ) und minimal ionisierenden Protonen von 3.5 GeV am SIS.

Das genaue Studium der IV-Kennlinien ergab, dass die Dunkelleitfähigkeit von scCVD von den durchgehenden Dislokationen dominiert ist. Proben mit höherer Dislokationsdichte zeigen erheblich verminderte Durchschlagsfestigkeit, während die Leckströme von defektfreien Detektoren (auch bei extrem hohen angelegten Feldern von  $10 \text{ V}/\mu\text{m} = 10^5 \text{ V/cm}$ ) unter  $1 \text{ pA}/\text{mm}^2$  bleiben. Weiter zeigten die defekten Proben zwei unterschiedliche Dunkelstrombereiche: im ersten Bereich, der in etwa dem Detektorbetriebsbereich entspricht, tangiert der gemessene Leckstrom die unterste Empfindlichkeitsgrenze des verfügbaren Keithley Elektrometers ( $\sim 10^{-13} \text{ A}$ ). Im zweiten anschließenden Bereich, setzt hingegen raumladungsbegrenzte Leitfähigkeit ein (SCLC, Space-Charge Limited Current conductivity). Die Kennlinien aller Proben in dem SCLC Bereich, können durch eine einfache Potenzfunktion mit einem Exponenten zwischen 5 und 7 beschrieben werden. Der Anfang des SCLC Bereichs bei einem kritischen Feld  $E_c$ , ist mit der makroskopischen Defektdichte korreliert und setzt bei sehr schlechten Diamantstückchen schon bei  $E = 0.1 \text{ V}/\mu\text{m}$  ein. Die injizierte Ladung rekombiniert an den Dislokationen unter Emission von blauem Licht - eine Erscheinung, die als 'Band A Lumineszenz' bekannt ist. Für alle Proben (guter und schlechter Qualität) ist die Dunkelleitfähigkeit im Bereich  $E > E_c$  thermisch aktiviert, mit einer Aktivierungsenergie  $E_a = (0.37 \pm 0.3) \text{ eV}$ . Dieser Wert lässt einige unkompenzierte Borverunreinigungen vermuten. Deshalb kann für scCVD Diamant eine schwache p-Leitfähigkeit angenommen werden. Trotzdem konnte gezeigt werden, dass Detektoren aus diesem Material bei einem angelegten Feld von  $E = 4 \text{ V}/\mu\text{m}$  und bis zu einer Temperatur von  $300 \text{ }^\circ\text{C}$  mit einem Leckstrom in der Größenordnung von  $7 \text{ nA}/\text{mm}^2$  betrieben werden können.

Die Ergebnisse der TCT Messungen mit den  $\alpha$ -Teilchen überzeugen, dass die überwiegende Mehrzahl der getesteten Proben innerhalb des möglichen Betriebsspannungsbereichs sowohl vernachlässigbare fixe Raumladung als auch minimalen Ladungseinfang in tiefe Haftstellen aufweist. Die Driftgeschwindigkeit beider Ladungsträger wurde in der verfügbaren kristal-

lographischen  $\langle 100 \rangle$  Richtung der Proben über einen sehr großen Feldbereich gemessen. Die daraus extrapolierte Sättigungsdriftgeschwindigkeit betrug  $2.6 \times 10^7$  cm/s für die Elektronen bzw.  $1.6 \times 10^7$  cm/s für die Löcher. Bei einem angelegten Feld von  $11$  V/ $\mu$ m werden die Geschwindigkeiten beider Ladungsträgertypen identisch, mit einem Wert  $v_{e,h} = 1.43 \times 10^7$  cm/s, der doppelt so hoch ist wie die Driftgeschwindigkeit der Elektronen in Silizium bei gleichem Feld. Interessant jedoch für Detektoren ist die Beobachtung, dass bei normalen Betriebsbedingungen ( $E \sim 1 - 4$  V/ $\mu$ m), die Löcher in allen untersuchten Proben systematisch etwas schneller als die Elektronen driften.

Die Ladungssammeleigenschaften wurden zunächst mit 5.5 MeV -Teilchen im Labor studiert. Eine Ladungssammeleffizienz von  $\sim 100$  % wurde für alle getesteten scCVD Diamantdetektoren bestätigt. Für die überwiegende Mehrzahl, erfolgte die Sättigung der gesammelten Ladung (sowohl für Löcher- als auch für Elektronendrift) bei niedrigen Feldern  $E < 0.3$  V/ $\mu$ m. Die - Energieauflösung  $\Delta E/E = 0.35$  % (FWHM) ist vergleichbar mit der Auflösung kommerzieller Silizium PIN-Dioden Detektoren und die Lebensdauer der Ladungsträger bedeutend länger als die Driftzeit der Ladungen in den Sensoren. Die gemessenen Lebensdauern der Elektronen sind im Bereich 150 ns - 320 ns und der Löcher im Bereich 150 ns - 1  $\mu$ s. Diesen Werten entsprechen auffällig lange 'Schubwege' (mittlere Ladungssammlungsstrecken), in der Größenordnung einiger Zentimeter. Das Antwortsignal der Diamantzähler auf den Durchgang minimal ionisierender Teilchen wurde mit hochenergetischen -Teilchen ( $E_{\beta} > 1$  MeV) einer  $^{90}\text{Sr}$  Quelle untersucht. Auch in diesem Fall, sättigte die gesammelte -induzierte Ladung bei gleich niedrigen Feldwerten  $E < 0.3$  V/ $\mu$ m. Die mit scCVDD Zählern gemessenen Landau Verteilungen, übertreffen die Qualität entsprechender Siliziumspektren bezüglich relativer Breite und Separation des niederenergetischen Spektrumauslaufs vom elektronischen Rauschen. Die Homogenität der Kristallstruktur über das Detektorvolumen wurde mit extrem fokussierten 6 keV Röntgen-Mikrostrahlen am ESRF in Grenoble, sowie mit der Schwerionen-Mikrosonde am UNILAC der GSI kartographisiert und bestätigt. Die Uniformität der Antwortsignale auf den gepulsten Röntgen-Mikrostrahl variierte im  $\sigma = 0.1$  % Bereich. Die defektfreien Detektoren operierten absolut stabil bei hohen angelegten Feldern (bis zu 6 V/ $\mu$ m), bei einer konstanten Röntgen-Mikropulsrate von 1.4 MHz/ $\mu\text{m}^2$ . Das entspricht einer extrem hohen Rate von stochastisch einfallenden minimal ionisierenden Teilchen ( $\sim 10^{13}$  cm $^{-2}$ s $^{-1}$ ). Im Gegensatz dazu, waren Sensoren hoher Strukturdefektdichten extrem instabil. Trotz ihrer niedrigen Dunkelleitfähigkeit vor dem Experiment, zeigten sie starke Durchbrüche bei einem angelegten Feld  $E = 1$  V/ $\mu$ m, wann immer der fokussierte Strahl eine defekte Stelle traf. ähnliche Beobachtung wurde mit Proben defekter Oberflächen gemacht, wo anfangs über die 'zahnradähnliche' Polierstreifen am Elektrodenrand ein schwacher Dunkelstromanstieg initiiert wurde, der sich bald zu einem total harten Durchbruch entwickelte. Die Zähler mit den ionenstrahlpolierten Oberflächen, zeigten hingegen absolut stabilen Langzeitbetrieb.

Zur Bestätigung der erwarteten Strahlungshärte von scCVDD, wurden bei acht Sensoren die Änderungen der Ladungstransporteigenschaften mit niederenergetischen (26 MeV) Protonen und hochenergetischen ( $\sim 20$  MeV) Neutronen, bis zu integralen Fluenzen von  $1.18 \times 10^{16}$  p/cm $^2$  bzw.  $2 \times 10^{15}$  n/cm $^2$  studiert. Mit optischen Charakterisierungsmethoden (Photolumineszenz- und UV-VIS Licht Absorptionsspektroskopie) konnte nachgewiesen werden, dass die einzigen überlebenden Defekte, die in scCVDD durch beide Bestrahlungsarten erzeugt werden können, neutrale Leerstellen ( $V^0$  vacancies) sind, die eine scharfe single-phonon Linie bei 1.638 eV emittieren. Komplexe Defekte wurden nicht beobachtet. Es



wurden absolute  $V^0$  Konzentrationen und  $V^0$  Produktionsraten ermittelt. Die Ergebnisse sind mehr als eine Größenordnung niedriger als die erwarteten Werte, die in Anlehnung an die 'Hypothese des nicht-ionisierenden Energieverlustes' (NIEL, non-ionizing energy loss hypothesis) abgeschätzt werden können. Das legt die Vermutung nahe, dass Selbstheilungsprozesse während der Bestrahlung stattfinden.

Im Gegensatz zu Siliziumdetektoren, wurde kein Anstieg der Dunkelströme während der Bestrahlung beobachtet. Dies wurde sowohl durch die aktuellen Messungen während der Bestrahlung, als auch durch die anschließenden Labormessungen bestätigt. Die erhöhte Leitfähigkeit der Dislokationsstellen der defekten Proben, die zu Detektordurchbrüchen führt, war nach der Bestrahlung deutlich unterdrückt. Möglicherweise, können energetisch nicht zu tief liegenden Haftstellen durch tief liegende Zustände neutraler Leerstellen kompensiert werden. Dadurch können bestrahlte Diamantdetektoren in sehr hohen Spannungsbereichen arbeiten, bei welchen die Driftgeschwindigkeiten der Ladungsträger gesättigt sind. Bei Raumtemperatur arbeiten sie stabil, ohne spezielle Behandlung oder Kühlung.

Nach den Bestrahlungen wurden TCT Messungen an den Proben durchgeführt, um sowohl die effektiven Ladungseinfangzeiten in tiefe Haftstellen, als auch das Profil des elektrischen Feldes im Volumen der bestrahlten Detektoren zu messen. Die inversen effektiven Ladungseinfangzeiten  $1/\tau_{e,h}$  wachsen proportional zur Teilchenfluenz und die Defektproduktionsraten sind unabhängig von der Bestrahlungsart. Die Tatsache, dass keine Raumladung in protonenbestrahlte Proben gefunden wurde, bestätigt die Neutralität der erzeugten Punktdefekte. Alle Diamantzähler, die mit reinem Aluminium beschichtet waren, zeigten nach der Bestrahlung eine starke spannungsinduzierte Polarisation, die auf eine sperrende Wirkung von Aluminiumelektroden hinweist. Dieser Effekt konnte nach Neumetallisierung der Probe mit Cr(50 nm)Au(100 nm) Kontakten und anschließendes Erhitzen auf 550 °C reduziert werden. Es wurde demonstriert, dass das Erhitzen (Ausheilen) der Proben auf eine Temperatur über 800 °C, zu einer permanenten Wiederherstellung der Ladungssammelleffizienz der Detektoren führt, anscheinend durch Migration und Rekombination der  $V^0$  Fehlstellen.

Die große Bandlücke von Diamant ermöglicht die Konditionierung der beschädigten Detektoren durch Passivierung der tiefen Haftstellen mit überschüssigen Ladungsträgern (z.B. erzeugt durch moderate Bestrahlung mit schwach ionisierenden Teilchen (priming)). Die Reemissionswahrscheinlichkeit bei Raumtemperatur ist klein. Die Ladungssammellänge (collection distance) konnte dadurch um einen mittleren Faktor 2.3 erhöht werden. Eine vollständige Restorierung der Ladungssammlung wurde jedoch nur bei Proben erzielt, die mit  $\sim 10^{14}$  Teilchen/cm<sup>2</sup> bestrahlt waren. Die relativen Breiten der Landauverteilungen minimal ionisierender Teilchen erreichen nach  $10^{15}$  Teilchen/cm<sup>2</sup> die Auflösung hochwertiger nicht bestrahlter Proben ( $\sigma/\text{MPV} = 0.078$ ). Bei noch höheren Fluenzen ist ein schwacher Anstieg dieses Wertes zu beobachten, jedoch bleibt er immer vergleichbar zu der entsprechenden Auflösung nicht bestrahlter Siliziumzähler. Auch nach der stärksten Bestrahlung ( $1.18 \times 10^{16}$  p/cm<sup>2</sup>) sind die Verteilungen von minimal ionisierenden Teilchen klar separiert vom elektronischen Rauschen.

Obwohl diese erste Starhlungshärtungsmessungen einen Einblick in die Prozesse gewähren, die bei Bestrahlung im Kristallvolumen solch neuartiger Diamantdetektoren stattfinden, können die vorläufigen Ergebnisse nicht als eine komplette Studie dieser komplizierten Zusammenhänge oder der Resistenz dieses Materials verstanden werden. Erst nach Bestätigung der Meßdaten mit weiteren Bestrahlungen über  $10^{15}$  Teilchen/cm<sup>2</sup>, können zuverlässige

Grenzen angegeben werden. Insbesondere muss der Einfluss der Bestrahlungsbedingungen (Detektorspannung, Teilchenfluss u.a) auf die Ergebnisse untersucht werden. Die beobachtete Ausheilung und die spannungsinduzierte Polarisation des Materials sind analog zu dem Verhalten von Siliziumdetektoren bei sehr tiefen Temperaturen. Die Veränderung der Feldkonfiguration durch kontrolliertes Injizieren von Ladungen oder die Detektorbeleuchtung mit sichtbarem Licht, verbessert die Ladungssammeleigenschaften von bestrahlten Siliziumdetektoren. Solche Techniken können auch auf Diamantsensoren angewendet werden. Dadurch sind die vorgestellten Ergebnisse als der schlecht mögliche Fall anzusehen, der in zukünftigen Entwicklungen stark verbessert werden kann.

Es wurden verschiedene Detektorprototypen gebaut und mit speziell entwickelter FE Elektronik an den GSI Beschleunigern getestet. Besondere Aufmerksamkeit war auf die Schwerionenspektroskopiezähler und auf die Start-Detektoren für relativistische leichte Ionen und Protonen gerichtet. Die Prototypen wurden mit konkurrierenden Sensoren verglichen, nämlich mit polykristallinen Diamantdetektoren in Bezug auf das schnelle Zeitverhalten und mit Siliziumdetektoren in Bezug auf die spektroskopischen Eigenschaften. Es wurde mit polykristallinen und scCVDD Detektoren die gleiche intrinsische Zeitauflösung ( $\sigma_i = 28$  ps) für  $^{27}\text{Al}$  Ionen von 2 AGeV gemessen. Dieses über-raschende Ergebnis, das von zwei Sensortypen solch unterschiedlicher Qualität in Bezug auf das S/N ratio erhalten wurde, beweist, dass der limitierende Faktor der Diamantzeitauflösung, das Rauschen der zur Verfügung stehenden Elektronik ist und dass das Potential dieses einzigartigen Materials noch lange nicht ausgenutzt wird. Die beste intrinsische Zeitauflösung (bei  $\sim 98$  % Nachweiseffizienz), die mit scCVD-DD für minimal ionisierenden Teilchen gemessen wurde, war annähernd  $\sigma_i = 100$  ps - ein Wert, der für pcCVD-DD unerreichbar ist. Weitere Elektronikentwicklungen wurden begonnen, die das angestrebte Ziel ( $\sigma_i < 100$  ps) ermöglichen sollten. Als die größte Stärke dieser strahlungsharten Detektoren wird im Moment die Kombination der guten Zeitauflösung mit einem ausgezeichneten Teilchenidentifizierungspotential angesehen. Die exzellente Pulshöhenauflösung von  $1.5\% \leq \delta E_{\text{diam}}/\Delta E \leq 2.5\%$ , die in Experimenten mit schnellen  $^{132}\text{Xe}$  Projektilen und Projekttilfragmenten erzielt wurde, ist in der Größenordnung des erwarteten Energieverlust-straggling und vergleichbar mit der Auflösung der MUSIC Ionisationskammer, die im gleichen Experiment zur Identifizierung der Fragmente eingesetzt war. Der gleichzeitig getestete Silizium PIN-Dioden Zähler war schon nach einigem Xenon Beschuss stark beschädigt, nachdem er zuvor aufgrund von Pulshöhendefekten, die bei scCVDD Zählern in keiner Messung beobachtet wurden, viel schlechtere Auflösung als die Diamantsensoren zeigte. Die vielfältigen vorteilhaften Diamantzählereigenschaften sind nicht nur für die aufgeführten Messungen nützlich, sondern auch zur Untergrundsunterdrückung gut geeignet. Die gemessenen Xenon Zeitsignale sind sehr gut geeignet für Zeitmessungen bei hohen Teilchenraten. Trotz eines deutlich raumladungsbegrenzten Ladungstransports (längeren Abfallzeiten), bleiben die kurzen Anstiegszeiten der Signale erhalten und die Relaxationszeit ist kleiner als 10 ns. Es wird also auch im relativistischen Schwerionenfall, eine intrinsische Zeitauflösung  $\sigma_i \ll 50$  ps bei einer Rate von  $10^8$  Ionen/s erwartet. Mit anderen Worten, scCVD-DDs können als strahlungsharte, zählratenfeste Detektoren für Position-, Energie-, Energieverlust- und Zeitmessungen über einen großen Bereich von Ionensorten und Energien angesehen werden.

Die wichtigsten Punkte dieser Arbeit sind im Folgenden zusammengefasst:

1. Untersuchung der elektrischen Eigenschaften und der Kristallstruktur von  $\langle 1\ 0\ 0 \rangle$  orientierten scCVD Diamantplättchen verschiedener Dicken.

2. Test der Strahlungsresistenz des Materials mit Protonen und Neutronen.
3. Strahltests verschiedener Prototypen, hergestellt mit solch neuartigen Diamantplättchen als Sensormaterial und der jeweils korrespondierenden Ausleseelektronik.

Resultate:

1. Es wurde eine hohe Homogenität der Kristallstruktur, der Ladungstransportparameter und der Ladungssammlungseffizienz festgestellt. Letztere erreichte in fast allen Proben schon bei niedrigen Feldern einen Wert von annähernd 100 %. Mobilität und Driftgeschwindigkeit der Löcher im Operationsbereich der Sensoren ( $E \sim 0.2 \text{ V}/\mu\text{m}$  -  $E \geq 1 \text{ V}/\mu\text{m}$ ), sind unerwarteter Weise systematisch größer als die entsprechenden Elektronenwerte. Die normalerweise vernachlässigbare Dunkelleitfähigkeit ist gelegentlich bei hohen Feldern dominiert durch vereinzelte durchgehende Dislokationen, die die Durchschlagsfelder zu  $E = 1 - 3 \text{ V}/\mu\text{m}$  begrenzen.
2. Die gemessenen absoluten Defektkonzentrationen und Produktionsraten sind mehr als eine Größenordnung niedriger als die Werte, die in Anlehnung an die NIEL Hypothese abgeschätzt wurden. Es liegt die Vermutung nahe, daß während der Bestrahlung Selbstheilungsprozesse stattfinden. Die einzig überlebenden Defekte sind neutrale Leerstellen ( $V^0$  vacancies), die offenbar die Driftgeschwindigkeit der Ladungsträger wenig beeinflussen. Die effektiven Ladungseinfangzeiten sinken proportional mit der Teilchenfluenz und die Defektproduktionsraten sind unabhängig von der Bestrahlungsart. Der Dunkelstrom der Sensoren wird erheblich reduziert. Auch bei einer applizierten Teilchenfluenz  $> 10^{16} \text{ p}/\text{cm}^2$  sind die Verteilungen minimal-ionisierender Teilchen klar separiert vom elektronischen Rauschen. Strahlungsgeschädigte Detektoren können durch Passivieren der tiefen Haftstellen konditioniert werden und erreichen eine um den Faktor 2.3 verbesserte Ladungssammellänge. wird dadurch erreicht. Vermutlich durch Migration und Rekombination der  $V^0$  Fehlstellen bei hohen Temperaturen, wurde eine permanente und fast vollständige Wiederherstellung der Detektoreigenschaften nach Ausheilen der Defekte bei Temperaturen  $> 800 \text{ }^\circ\text{C}$  beobachtet.
3. Schwerionenzähler aus scCVD Diamant sind momentan die einzig bekannten Detektoren, die gleichzeitig sowohl eine exzellente Zeitauflösung bei hoher Teilchenraten erreichen als auch außerordentliche spektroskopische Eigenschaften aufweisen. Routinemäßig wurde eine intrinsische Zeitauflösung  $\sigma_i < 30 \text{ ps}$  and eine dicken- und kapazitätsabhängige Ratenfestigkeit von bis zu  $10^8 \text{ Hz}$  gemessen. Ihre Energieauflösung ist bei niedrigen Ionenenergien und leichten Teilchen bis etwa Kohlenstoff, vergleichbar zu der Auflösung von Siliziumdetektoren. Sie zeigen keine Pulshöhendefekte und sind daher vom Teilchenidentifizierungspotential höher als Siliziumzähler einzuschätzen und sogar vergleichbar zu MUSIC Ionisationskammern. Zeitzähler für relativistische Protonen und andere minimal-ionisierende Teilchen erreichten als besten Wert  $\sigma_i = 100 \text{ ps}$ . Generell kann geschlossen werden, daß das Rauschen der zur Zeit verfügbaren Breitbandelektronik das Zeitverhalten aller Diamantzeitdetektoren begrenzt.



# APPENDIX

**Short introduction to EVEREST** EVEREST [EVE] provides fully a three-dimensional transient device simulation suite. It comprises pre- and post-processing capabilities and a solver module which allows specification of a range of bias conditions and physical models for mobility and recombination. It has recently been extended to incorporate charge generation events. Adaptive meshing may be performed based on doping profiles, potential and current distributions, and can automatically provide accurate and efficient static solutions.

**Governing equations** Semiconductor physics are characterized by three partial differential equations in the drift-diffusion model:

$$\varepsilon \nabla^2 \Psi = -\rho \quad (\text{A-1})$$

$$q \frac{p}{t} = -\nabla J_p - qR \quad (\text{A-2})$$

$$q \frac{n}{t} = -\nabla J_n - qR \quad (\text{A-3})$$

These equations need to be solved subject to a set of boundary and initial conditions. The most important of these boundary conditions are the applied biases on the contacts. In transient simulations these can be time dependent. Poissons equation, A-1, relates the electrostatic potential  $\Psi$  to the charge concentration  $\rho$ . The carrier continuity equations, A-2 and A-3, relate the rate of change of hole concentration  $p$  and the rate of change of electron concentration  $n$  to the divergence of their respective currents  $J_p$  and  $J_n$  plus the recombination rate  $R$ . The charge concentration  $\rho$  is given by:

$$\rho = q(p - n - (N_A - N_D) + \rho_F) \quad (\text{A-4})$$

Where  $N_A$  and  $N_D$  are acceptor and donor atom concentrations,  $q$  is the electron charge and  $\rho_F$  is the interface trapped charge density. The expressions for the current densities given below are derived from the Boltzmann transport equation:

$$J_p = -q\mu_p(\nu_T \nabla p + p \nabla(\Psi - \nu_T \log(n_i))) \quad (\text{A-5})$$

$$J_n = q\mu_n(\nu_T \nabla n + n \nabla(\Psi - \nu_T \log(n_i))) \quad (\text{A-6})$$

where  $\nu_T = k_B T$ . The Fermi-Dirac function, combined with the density of states, yields expressions for electron concentration in the conduction band and the hole concentration

in the valence band. Under non-degenerate conditions they simplify to the well known Boltzmann approximations,  $p = n_i \exp(\Phi_p - \Psi)/\nu_T$  and  $n = n_i \exp(\Psi - \Phi_n)/\nu_T$

EVEREST only allows Ohmic type Dirichlet contacts, which are idealized by assuming infinite contact recombination velocities and space-charge neutrality. At an Ohmic contact:

$$\phi_n = \phi_p = V_{app} \quad (\text{A-7})$$

and charge neutrality gives:

$$p - n - (N_A - N_D) = 0 \quad (\text{A-8})$$

Using A-7 and A-8, in conjunction with Boltzmann approximations for carrier concentrations, gives Ohmic Dirichlet boundary conditions for  $\Psi$ ,  $p$  and  $n$ . The remainder of a device boundary in EVEREST is of homogeneous Neumann type, where the hole and the electron current densities and the electric field strength normal to the boundary vanish, yielding

$$\nu J_n = \nu J_p = \nu \nabla \Psi = 0 \quad (\text{A-9})$$

where  $\nu$  is the surface normal.

The drift-diffusion equations are solved using an adaptive control volume discretisation in space with variable order and variable step Gear integration in time.

**Device geometry** The device geometry was implemented in the simulation as a simple block with side ohmic contacts C1 and C2. (Figure 9.1 and 9.2 (Left panel)). Rest p-type conductivity of diamond bulk was assumed with the concentration of the ionized acceptors below  $1 \times 10^8$

**Mesh** Since the simulations use regular geometries of the devices, to ensure that the effects of mesh density on the solutions is well understood the generation of simple regular meshes was used. In order to save computation time the mesh was only refined in the x direction which is the direction of the charges drift. Therefore, the 1D approximation of the problem can be assumed.

**Initial conditions** Although EVEREST was designed for the silicon devices simulation, by adding a new input file defining physical properties of diamond, simulation of the transient current signals in scCVD-DDs was possible. The initial parameters are presented in Table 9.1.

**Charge upset events** The charge upset event for both devices is shown in Figures 9.1 and 9.2 (Right panel). The ionization profiles for 4.72 MeV  $\alpha$ -particles and 215 AMeV  $^{132}\text{Xe}$  ions were previously calculated in SRIM [Zie85] and ATIMA [ATIMA] software, respectively. In order to convert the energy deposited in diamond to e-h pairs, the average energy for e-h production  $\epsilon_{avg} = 12.86 \text{ eV}/e - h$  was used.

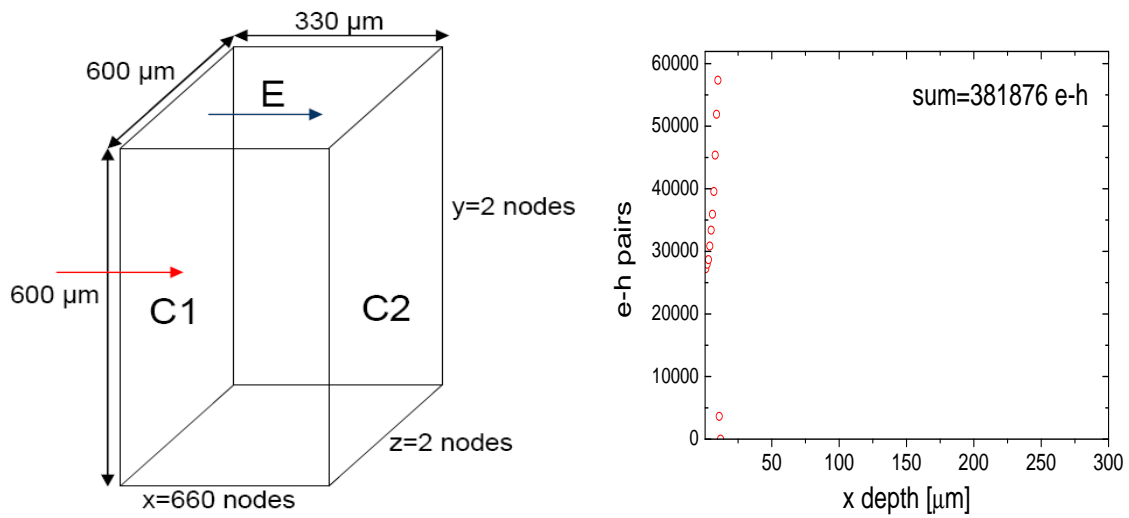


Figure 9.1: (Left panel) The device geometry with mesh parameters for 4.72 MeV  $\alpha$ -particle induced current signal simulation. Red arrow marks the charge upset event. (Right panel) Corresponding spatial distribution of the charge upset event within the device.

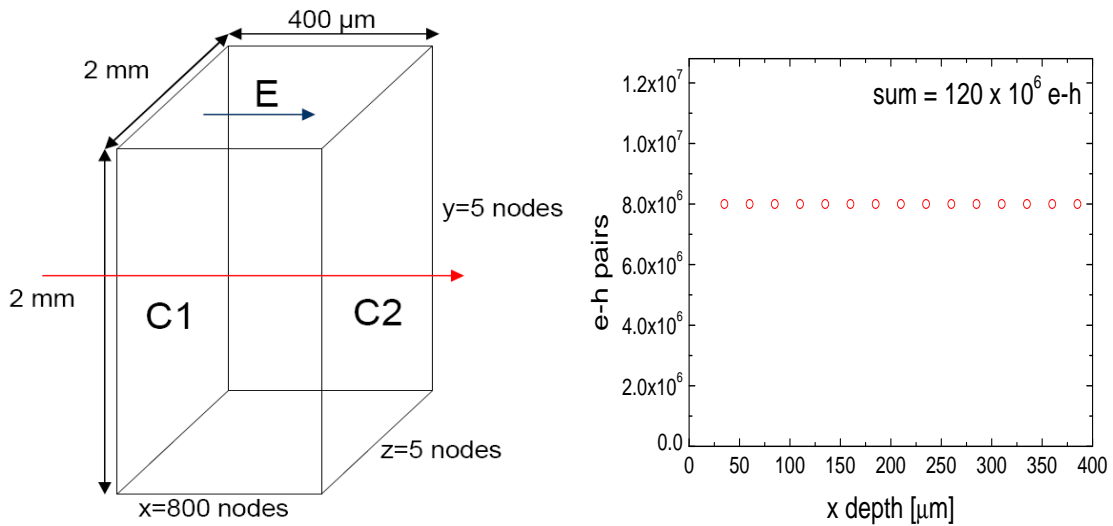


Figure 9.2: (Left panel) The device geometry with mesh parameters for 215 AMeV  $^{132}\text{Xe}$  induced current signal simulation. Red arrow marks the charge upset event. (Right panel) Corresponding spatial distribution of the charge upset event within the device.

Table 9.1: Initial parameters used in simulation (all dimensions in cm, V, s)

Process	Model	Parameters
relative permittivity	none	$\epsilon = 5.7$
intrinsic carrier concentration	constant	$n_i = 1 \times 10^3$
Bandgap	constant	$E_g = 5.46 \text{ eV}$ at 300K
Recombination	SRH	electrons $\tau_e = 0.3 \times 10^{-6}$ holes $\tau_h = 1 \times 10^{-6}$
mobility	Field dependent	electrons: $\mu_0 = 4500$ , $v_0 = 2.69 \times 10^7$ , $\beta = 0.45$ holes: $\mu_0 = 2750$ , $v_{sat} = 1.65 \times 10^7$ , $\beta = 0.78$

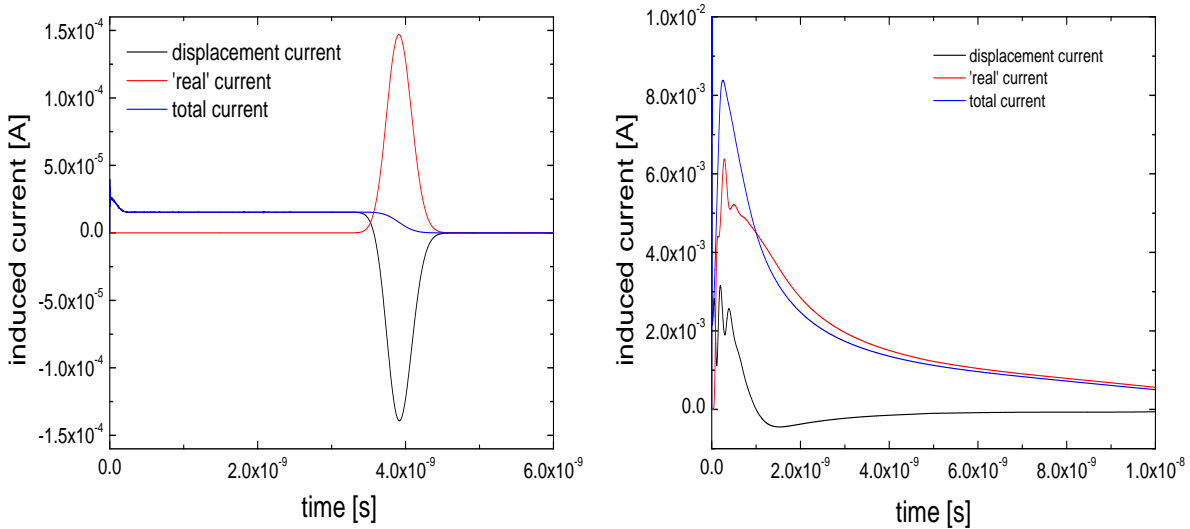


Figure 9.3: The EVEREST simulated transient current signals, in black - displacement current, in red 'real' current - current flowing through readout electrode, in blue - total current - sum of displacement and 'real' currents. (Left panel) 4.72 MeV  $\alpha$ -particle injection. (Right panel) 215 AMeV  $^{132}\text{Xe}$  ion injection.

**Solution** As with all transient simulations, it is necessary at first to perform a static simulation in order to get the initial state of the system. In this case the device is at first solved in the zero bias state and then with a successive biases applied to the one contact. The transient simulation is started from the second static solution. In transient simulation, the charge upset event takes place at  $t=0$  s. The examples of simulated intrinsic induced currents on the C2 electrode are presented in Figure 9.3 for both cases - 4.72 MeV  $\alpha$ -particle and 215 AMeV  $^{132}\text{Xe}$  ion injection.

**Electronics** The readout electronics contribution to the induced current signal formation was simulated in APLAC software [APLAC]. The corresponding electronic circuit is presented in Figure 9.4 (Left panel). The diamond detector is represented as the current source  $I1$  and capacitance  $C1$ , which is coupled through capacitor  $C3$  to the output node  $OUT$  on  $50 \Omega$ . Also the detector biasing circuit has been implemented in the schematic as a voltage source  $V1$  and corresponding components: a capacitor  $C2$  and a bias resistor



R3. The EVEREST simulated intrinsic transient current signal was used as an input signal *PULSE* in the APLAC simulation. Assuming an intrinsic detector current pulse  $I_{tr}(t)$ , with  $I_0$  the amplitude of the signal and  $t_{tr}$  the thickness-dependent transition time of the induced charge through the diamond bulk, the following equations give the input-voltage to the amplifier:

$$\begin{aligned} 0 \leq t \leq t_{tr} \quad & V_{out}(t) = I_0 \cdot R2(1 - e^{-t/R2C1}) \\ t_{tr} \leq t \leq \quad & V_{out}(t) = I_0 \cdot R2(e^{t_{tr}/R2C1} - 1) \cdot e^{-t/R2C1} \end{aligned} \quad (\text{A-10})$$

where  $R2$  amounts  $50 \Omega$  and  $C1 = C_d + C_p$  represents the sum of all circuit capacitances, with  $C_d$  the detector capacitance,  $C_p$  the parasitic capacitances.

Figure 9.4 (Right panel) shows the intrinsic induced current signal (in black) and corresponding filtered signal.

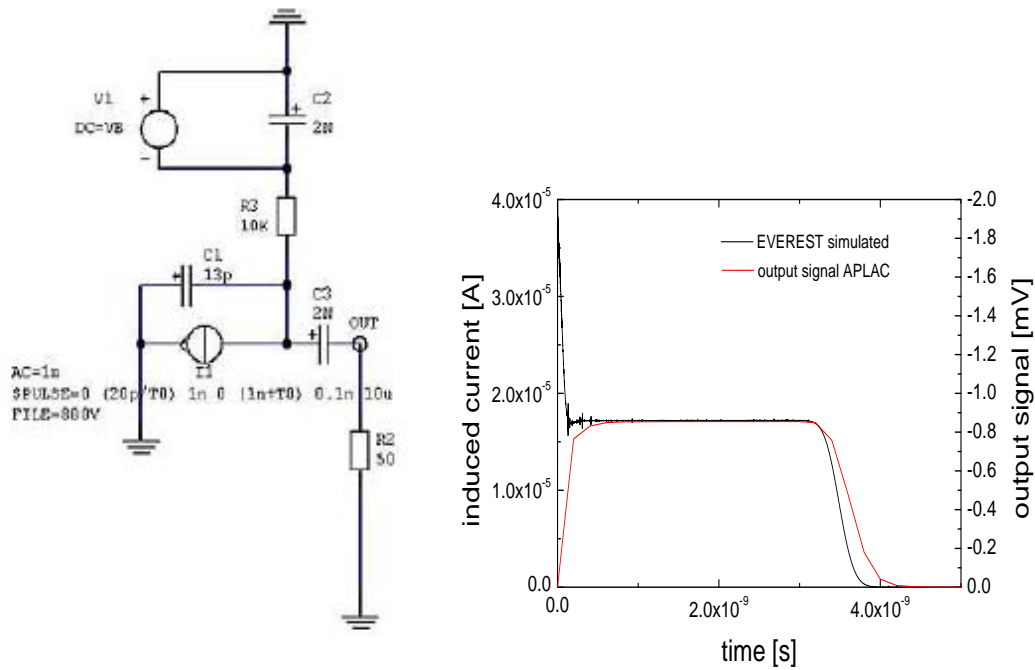


Figure 9.4: (Left panel) Schematic of the electronic readout used in simulations. (Right panel) Comparison of the intrinsic EVEREST simulated transient current signal and this signal after electronic 'filtering' simulated in APLAC.



# List of Figures

2.1	The unit cell of diamond. . . . .	6
2.2	The band structure of diamond . . . . .	7
2.3	Phonon dispersion curves of diamond. . . . .	8
2.4	Charge carriers' mobility as a function of temperature in IIa natural diamond. . . . .	12
2.5	Charge carriers drift velocity in natural IIa diamond. . . . .	12
2.6	Theoretical electromagnetic absorption spectrum of intrinsic diamond. . . . .	13
2.7	The Chemical Vapour Deposition (CVD) of diamond. . . . .	16
2.8	Schematic illustration of the H- and O-terminated (100) diamond surfaces and their properties. . . . .	18
2.9	Band diagrams of two hypothetic oxygenated diamond devices plated with aluminium Schottky contacts. . . . .	20
2.10	Electric field profiles corresponding to the band diagrams from Figure 2.9. . . . .	20
3.1	The electronic stopping power of several ions in diamond. . . . .	23
3.2	The mean energy losses of an electron in diamond (red curves) and silicon (blue curves) versus its kinetic energy. . . . .	24
3.3	The Vavilov distribution function $\Phi$ as a function of the scaled energy loss $\lambda$ for various parameter $\kappa$ and $\beta = 0.98$ . . . . .	25
3.4	Photon total cross sections as a function of energy in carbon, showing the contributions of different processes. . . . .	26
3.5	Average energy to create an e-h pair as a function of the band-gap energy for a selection of semiconductors. . . . .	28
3.6	An illustration of the Ramo theorem for a hypothetical semiconductor device surrounded by four electrodes. . . . .	30
3.7	The graphical representation of the Hecht equation, relating the charge collection efficiency (CCE) to the charge collection distance (CCD). . . . .	34
3.8	The simplified mechanism of trapping, recombination, generation re-emission of charge carriers. . . . .	34
3.9	Diagrams illustrating the space charge generation within pcCVD diamond sample. . . . .	36
4.1	ESR spectra of two scCVD diamonds and Example of IR absorption spectra of three synthetic diamonds . . . . .	39
4.2	TPYS spectra of two scCVD diamonds measured at 300 °C. . . . .	39
4.3	Absorption spectra in the VIS - UV range of an intrinsic scCVD and an Ib HPHT diamond measured at room temperature. . . . .	40
4.4	Contrast in X-ray topography. . . . .	41

---

4.5	Experimental arrangement of X-ray topography measurements at the ID19 line of ESRF. . . . .	42
4.6	'White beam' X-ray topograph of a high crystal quality IIa HPHT diamond and Quasi-3D topograph of a scCVD diamond visualizing threading dislocations. . . . .	43
4.7	'White-beam' X-ray topographs of various scCVD diamonds prepared for the use in particle detection. . . . .	44
4.8	Principle of birefringence measurement using cross polarized light. . . . .	45
4.9	Crossed-polarizer images of nine scCVD diamonds. . . . .	46
4.10	Correlation between X-ray topographs and birefringence pictures. . . . .	47
4.11	A typical example of the surface morphology of a resin wheel polished scCVD. . . . .	48
4.12	A typical example of the surface morphology of a scaife polished scCVD diamond. . . . .	49
4.13	A typical example of the surface morphology of an ion beam polished scCVD diamond. . . . .	49
4.14	The defective diamond surface showing crescent indentations, the result of resin wheel polishing process. . . . .	50
5.1	Double-sided shadow mask used for sputtering or evaporation of metal electrodes on diamond surfaces. . . . .	52
5.2	From raw diamond material to a ready-to-use diamond detector prototype. . . . .	53
6.1	Setup used to probe current-voltage characteristics of pad electrodes scCVD-DDs.; I-E(V) measurement configuration of scCVD-DDs metallized with segmented electrode. . . . .	56
6.2	I-E(V) characteristic of six early fabricated scCVD-DDs. . . . .	57
6.3	I-E(V) characteristics measured in the non-guarded mode and in the guarded mode where surface leakage current is excluded.; I-E(V) characteristics of two scCVD-DDs metallized with annealed Cr(50 nm)Au(100 nm) electrodes, and re-metallized with Al(100 nm) electrodes. . . . .	58
6.4	I-E(V) characteristics of scCVD-DDs plated on one side with quadrant electrodes. . . . .	59
6.5	I-E(V) characteristics of scCVD-DDs plated with top quadrant electrode. . . . .	60
6.6	Correlation between leakage currents and structural defects of sample s256-02-06. . . . .	60
6.7	The log-log plot of the I-E(V) characteristics of thirteen scCVD-DDs. . . . .	61
6.8	Electroluminescence from a defective scCVD diamond (sample s256-02-06) measured during hard-breakdown and corresponding light emission spectrum. . . . .	62
6.9	Dark conductivity at different temperatures of two scCVD-DDs as a function of the applied bias. . . . .	63
6.10	Schematic of the detector-FEE assembly used for the transient current measurements. . . . .	65
6.11	Averaged Transient Current (TC) signals of a scCVD diamond; Comparison between single TC signals of a pcCVD diamond and a scCVD diamond. . . . .	67
6.12	An example of TC signals of a scCVD-DD measured for electrons and holes drift, in the presence of a negative space charge. . . . .	67

6.13	$^{241}\text{Am}$ - $\alpha$ -induced TC signals measured at various electric fields with a scCVD-DD of 393 $\mu\text{m}$ thickness. . . . .	68
6.14	Charge carrier drift velocity (Left panel) and effective mobility in scCVD-DD for electrons and holes drift in the $\langle 1\ 0\ 0 \rangle$ crystallographic direction at RT. . . . .	69
6.15	Electron and (Right panel) hole drift velocity as a function of the electric field in single crystal diamond measured at RT. . . . .	70
6.16	Field dependence of the charge carriers drift velocity in scCVD-DD along the $\langle 1\ 0\ 0 \rangle$ crystallographic direction. . . . .	71
6.17	Longitudinal diffusion coefficient of electrons and holes in scCVD-DD at RT as a function of electric field $E$ . . . . .	72
6.18	Simulated and measured transient current signals induced by $\alpha$ -particle injection in a 320 $\mu\text{m}$ thick scCVD diamond detector. . . . .	73
6.19	Schematic of the connection circuit for charged-particle detection: the charge sensitive (CS) readout. . . . .	74
6.20	The block diagram of the electronics used for the energy-loss spectroscopy. . . . .	74
6.21	Collected charge characteristics of four scCVD-DD for 5.486 MeV $\alpha$ -particles measured in vacuum using CS electronics. . . . .	75
6.22	Energy resolution of two scCVD-DDs for $^{241}\text{Am}$ $\alpha$ -particles compared to a silicon PIN-diode detector. . . . .	76
6.23	Effective deep trapping / recombination time for electrons and holes in various scCVD diamond films. . . . .	77
6.24	Spectrum of a mixed nuclide ( $^{239}\text{Pu}$ , $^{241}\text{Am}$ , $^{244}\text{Cm}$ ) $\alpha$ -particle calibration source, measured using a silicon PIN diode detector as well as a scCVD-DD. . . . .	78
6.25	Geometrical arrangement for CCE measurements with $^{90}\text{Sr}$ electrons.; The decay scheme of a $^{90}\text{Sr}$ $\beta$ -source. . . . .	78
6.26	Geant4 generated spectrum of electrons emitted from a $^{90}\text{Sr}$ source. . . . .	79
6.27	Pulse height distribution of $^{90}\text{Sr}$ electrons measured with a plastic scintillator detector.; Comparison of energy loss spectra obtained with $^{90}\text{Sr}$ electrons and 2.2 GeV protons. . . . .	80
6.28	Spectra of minimum ionizing electrons measured with three scCVD-DDs of various thickness.; Most probable values (mpv) as a function of the width $\sigma$ of the Landau distributions for scCVD-DDs. . . . .	80
6.29	Collected charge measured with $^{90}\text{Sr}$ electrons as a function of the applied electric field. . . . .	81
6.30	The electron current in the storage ring of the ESRF synchrotron when operating in a 4-bunch mode.; Micro-pulse structure of the 4-bunch mode of the X-ray beam, recorded with a scCVD-DD and a digital oscilloscope. . . . .	82
6.31	Schematic of the experimental arrangement for X-ray scanning microscopy at the ID21 line of ESRF. . . . .	82
6.32	XBIC-E(V) characteristics of three scCVD-DDs measured under 6 keV X-ray beam irradiation. . . . .	84
6.33	X-ray microbeam mapping of the defective scCVD-DD (s256-02-06) at 0.2 V/ $\mu\text{m}$ . . . . .	84
6.34	High resolution XBIC map of quadrant q1 of s256-02-05 measured at a bias voltage of +30 V (0.1 V/ $\mu\text{m}$ ). . . . .	85
6.35	XBIC time-voltage evolution of the defective region response. . . . .	86
6.36	XBIC maps of defect-free scCVD-DDs (SC8BP, SC14BP). . . . .	87

6.37	High resolution XBIC maps of sample SC14BP. . . . .	87
6.38	Position response of a 100 $\mu\text{m}$ thick scCVD-DD operated in a pulse mode at 400 V. . . . .	88
6.39	XBIC map of a resin wheel polished scCVD-DD with a damaged surface. . . . .	89
7.1	NIEL damage cross-sections in silicon and diamond for protons and neutrons as a function of the incoming particles energy. . . . .	95
7.2	Isochronal annealing of $I_{<001>}^0$ and $V^0$ centres in an irradiated IIa diamond. . . . .	97
7.3	The re-trapping probability as a function of the activation energy of trapping center for diamond at RT. . . . .	98
7.4	Photograph of the irradiation set-up at the Karlsruhe cyclotron.; Ionizing energy loss of 26 MeV protons in diamond material. . . . .	101
7.5	Energy spectrum of the incoming neutrons at Louvain-la-Neuve cyclotron.; Neutron fluxes at distances from the production target. . . . .	103
7.6	Photograph of the experimental environment at the high flux neutron beam line of the Louvain-la-Neuve cyclotron.; Schematic representation of the irradiation geometry. . . . .	104
7.7	On-line monitoring of the beam-induced currents during the 20 MeV neutron irradiation (raw data). . . . .	105
7.8	On-line monitoring of scCVD-DDs during 20 MeV neutron irradiation. . . . .	106
7.9	UV - VIS absorbtion spectra of neutron and proton irradiated diamonds, measured at RT. . . . .	107
7.10	UV - VIS absorbtion spectrum of BDS13 after 26 MeV proton irradiation measured at 7 K.; Detailed view of absorbtion at $\sim 1.673$ eV the ZPL of the GR1 center. . . . .	107
7.11	Photoluminescence (PL) spectra of neutron irradiated diamonds, measured at 77 K. . . . .	109
7.12	Zoomed PL spectra of two 20 MeV neutron irradiated scCVD, revealing residual defects. . . . .	110
7.13	Normalized PL signals at 741.2 nm (ZPL of the GR1 center) from neutron irradiated scCVD diamonds.; Intensity of the GR1 line as a function of the integrated neutron fluence. . . . .	110
7.14	I-E(V)-field characteristics of irradiated diamond detectors after 26 MeV proton irradiation and 20 MeV neutron irradiation. . . . .	111
7.15	Arrhenius plot of scCVD dark current measured at 0.3 V/ $\mu\text{m}$ . . . . .	112
7.16	TC signals of scCVD-DD induced by 5.5 MeV $\alpha$ -particles after irradiation with 26 MeV protons. . . . .	113
7.17	Profiling of the internal electric field of the neutron-irradiated detector BDS12 during the 'DC bias-induced polarization'. . . . .	115
7.18	TC signals induced by 5.5 MeV $\alpha$ -particle in scCVD-DDs after irradiation with 20 MeV neutrons, and re-metallization with Cr(50 nm)Au(100 nm). . . . .	116
7.19	Effective deep trapping times extracted from the TC signals for electrons and holes drift, at various electric field E, after 26 MeV proton and 20 MeV neutron irradiation. . . . .	117
7.20	Inverse effective trapping times of de-pumped scCVD-DDs as a function of the integral particles fluence. . . . .	117

7.21	Radiation-induced polarization and priming effects in a damaged scCVD-DD measured with short-range 5.5 MeV alpha particles and fast electrons. . . . .	118
7.22	Energy-loss spectra of minimum ionizing electrons measured at RT with non-irradiated scCVD-DDs and after 20 MeV neutron irradiation using CS electronics. . . . .	119
7.23	Relative $\sigma_{Landau}/MPV$ of the Landau distribution measured for minimum ionizing electrons with irradiated scCVD-DDs as a function of the integral fluence applied. . . . .	120
7.24	The collected charge characteristics of scCVD-DDs irradiated with 26 MeV protons, measured in the primed state using $^{90}\text{Sr}$ fast electrons. . . . .	121
7.25	Charge-collection characteristics of scCVD-DDs after irradiation with 20 MeV neutrons, measured using fast electrons from a $^{90}\text{Sr}$ source and CS electronics with 2 $\mu\text{s}$ shaping time. . . . .	122
7.26	The decrease of collected charge of scCVD-DDs as a function of 26 MeV proton integral fluence. . . . .	123
7.27	The decrease of collected charge of scCVD-DDs as a function of 20 MeV neutron integral fluence. . . . .	124
7.28	Charge collection distances of scCVD-DDs after 26 MeV proton (in red) and 20 MeV neutron (in blue) irradiation. . . . .	124
7.29	The expected charge collection efficiency (CCE) of primed scCVD-DDs as a function of the electrodes interspacing and applied integral fluence. . . . .	125
7.30	TC signals of BDS14 at 1 V/ $\mu\text{m}$ illustrating the recovery of the charge transport properties of the irradiated detector after 3h annealing at 1000 $^{\circ}\text{C}$ . . . . .	126
7.31	Permanent increase of the CCE after high temperature annealing at 1000 $^{\circ}\text{C}$ for sample BDS14. . . . .	126
8.1	The limiting factors in timing when using leading-edge discriminator. . . . .	133
8.2	Schematic of the setup used for measurement of the intrinsic time resolution of scCVD-DDs. . . . .	134
8.3	Time resolution of pc and scCVD-DDs for 2 AGeV $^{27}\text{Al}$ ions measured with the FEE-card, developed for FOPI spectrometer. . . . .	135
8.4	Time resolution of scCVD-DDs for 6 MeV protons. . . . .	136
8.5	Time spectrum of scCVD-DDs for 3.5 GeV protons measured with low-capacitance broadband amplifiers. . . . .	136
8.6	A plot, summarizing the timing measurement with scCVD-DDs. . . . .	137
8.7	Experimental environment of the FRS with its four magnetic dipole stages. . . . .	139
8.8	Panoramic photograph of the experimental area of the FRS at S4. . . . .	139
8.9	$^{132}\text{Xe}$ 215 AMeV projectile raw spectra measured with three scCVD-DDs at positive and negative bias polarity.; Same measurement performed with Si1 at highest possible bias. . . . .	140
8.10	Dependence of the charge collected with D1 (left panel) and D2 (right panel) on the applied electric field. . . . .	141
8.11	Response of scSCV-DDs to $^{132}\text{Xe}$ ions of different kinetic energies.; The relative energy resolution of scCVD-DDs as a function of deposited energy. . . . .	142
8.12	Pulse height scatter plot of D2 versus MUSIC4.; Corresponding raw pulse height spectrum of MUSIC4.; Corresponding raw pulse height spectrum of D2; MUSIC41 PID spectrum. . . . .	143

---

8.13	A plot of $\Delta E$ versus ToF obtained with a scCVD-DD and scintillator detectors, respectively.; The corresponding measured $\Delta E$ spectrum of the scCVD-DD.; Mean $\Delta E$ values of fragments measured with the scCVD-DD.; The relative energy resolution of the scCVD-DD as a function of Z. . . . .	144
8.14	Comparison of pulse height spectra of the $^{132}\text{Xe}$ fragments obtained with a scCVD-DD and with a silicon PIN diode. . . . .	145
8.15	The TC signals of $^{134}\text{Xe}$ ions of 215 AMeV as a function of applied bias, measured with a 400 $\mu\text{m}$ thick scCVD-DD (D2) and corresponding numerically simulated TC signals. . . . .	146
9.1	Device geometry with mesh parameters for 4.72 MeV $\alpha$ -particle induced current signal simulation.; Corresponding spatial distribution of the charge upset event within the device. . . . .	163
9.2	Device geometry with mesh parameters for 215 AMeV $^{132}\text{Xe}$ induced current signal simulation.; Corresponding spatial distribution charge upset event within the device. . . . .	163
9.3	The EVEREST simulated transient current signals . . . . .	164
9.4	Schematic of the electronic readout used in simulations. Comparison of intrinsic EVEREST simulated transient current signal and signal after electronic 'filtering' simulated in APLAC. . . . .	165



# List of Tables

- 2.1 Properties of some semiconductor materials that could be used as detector bulk material. . . . . 15
  
- 6.1 Charge carrier transport parameters of scCVD-DDs obtained from fits to the experimental TCT data. . . . . 70
  
- 7.1 26 MeV proton irradiation - samples characteristics . . . . . 100
- 7.2 26 MeV Protons: Irradiation Conditions . . . . . 101
- 7.3 ~20 MeV neutron irradiation - samples characteristics. . . . . 102
- 7.4 The high flux fast neutron beam contamination. . . . . 102
- 7.5 20 MeV Neutrons: Irradiation Conditions . . . . . 103
  
- 9.1 Initial parameters used in simulation (all dimensions in cm, V, s) . . . . . 164



# Bibliography

- [Ada02] W. Adam et al., RADIATION TOLERANCE OF CVD DIAMOND DETECTORS FOR PIONS AND PROTONS, *Nucl. Instr. And Meth. A* , vol. 476, p. 686, 2002
- [Ada00] W. Adam et al., PULSE HEIGHT DISTRIBUTION AND RADIATION TOLERANCE OF CVD DIAMOND DETECTORS, *Nucl. Instr. And Meth. A* , vol. 447, p. 244, 2000
- [Ada07] W. Adam et al., RADIATION HARD DIAMOND NEXT TERM SENSORS FOR FUTURE TRACKING APPLICATIONS, *Nucl. Instr. And Meth. A* , vol. 565, iss. 1, p. 278, 2006
- [Ada02b] W. Adam et al., PERFORMANCE OF IRRADIATED CVD DIAMOND MICRO-STRIP SENSORS, *Nucl. Instr. And Meth. A*, vol. 476 p. 706, 2002
- [Ada00] W. Adam et al., PULSE HEIGHT DISTRIBUTION AND RADIATION TOLERANCE OF CVD DIAMOND DETECTORS, *Nucl. Instr. And Meth. A*, vol. 447, p. 244, 2000
- [Ait69] D. W. Aitken, W. L. Lakin, H. R. Zulliger, ENERGY LOSS AND STRAGGLING IN SILICON BY HIGH-ENERGY ELECTRONS, POSITIVE PIONS, AND PROTONS, *Phys. Rev.*, vol. 179, no. 2, p. 178, 1969
- [Alk67] G. D. Alkhozov, A. P. Komar, A. A. Vorob'ev, IONIZATION FLUCTUATIONS AND RESOLUTION OF IONIZATION CHAMBERS AND SEMICONDUCTOR DETECTORS, *Nucl. Instr. And Meth. A* , vol. 48, p. 1, 1967
- [Ale02] A. Alekseyev, V. Amosov, Yu. Kaschuck, A. Krasilnikov, D. Portnov, S. Tugarinov, STUDY OF NATURAL DIAMOND DETECTOR SPECTROMETRIC PROPERTIES UNDER NEUTRON IRRADIATION, *Nucl. Instr. And Meth. A* vol. 476, p. 516, 2002
- [Ali80] R. C. Alig, S. Bloom, C. W. Struck, SCATTERING BY IONIZATION AND PHONON EMISSION IN SEMICONDUCTORS, *Phys. Rev. B*, vol. 22, no. 12, p. 5565, 1980
- [All98] Lars Allers, Alan T. Collins, Jonathan Hiscock , THE ANNEALING OF INTERSTITIAL-RELATED OPTICAL CENTRES IN TYPE II NATURAL AND CVD DIAMOND, *Diam. Relat. Mater.*, vol. 7 p. 228, 1998
- [And77] H. H. Andersen, and J.F. Ziegel, HYDROGEN: STOPPING POWERS AND RANGES IN ALL ELEMENTS, *New York*, Pergamon, 1977
- [Amo02] A. Alekseyev, V. Amosov, Yu. Kaschuck, A. Krasilnikov, D. Portnov, S. Tugarinov, STUDY OF NATURAL DIAMOND DETECTOR SPECTROMETRIC PROPERTIES UNDER NEUTRON IRRADIATION, *Nucl. Instr. And Meth. A*, vol. 476 p. 516, 2002

- [APLAC] APLAC RF Design Tool, <http://www.aplac.com/>
- [ASTM] American Society for Testing and Materials (ASTM), WK1 1648, New Standard Practice for Characterizing Charged-Particle Irradiations of Materials in Terms of Non-Ionizing Energy Loss (NIEL).
- [Ash01] D. G. Goodwin, J. E. Butler, HANDBOOK OF INDUSTRIAL DIAMONDS AND DIAMOND FILMS, ed. M. A. Prelas, G. Popovici and L. K. Bigelow, Marcel Dekker, New York, p. 527, 1998
- [ATIMA] ATIMA, <http://www-linux.gsi.de/~weick/atima/>
- [Bal06] A. Balducci et al., GROWTH AND CHARACTERIZATION OF SINGLE CRYSTAL CVD DIAMOND NEXT TERM FILM BASED NUCLEAR DETECTORS, *Diam. Relat. Mater.*, vol. 15, iss. 2 – 3, p. 292, 2006
- [Bar63] W. H. Barkas, J. N. Dyer, H. H. Heckman, RESOLUTION OF THE  $\Sigma^-$ -MASS ANOMALY, *Phys. Rev. Lett.*, vol. 11, no. 1, p. 26, 1963
- [Bar64] W. H. Barkas, M. J. Berger, TABLES OF ENERGY LOSSES AND RANGES OF HEAVY CHARGED PARTICLES, *NASA Report*, SP-3013, 1964
- [Bas01] E. Baskin, A. Reznik, D. Saada, Joan Adler, R. Kalish, MODEL FOR THE DEFECT-RELATED CONDUCTIVITY IN ION-DAMAGED DIAMOND, *Phys. Rev. B*, vol. 64, p. 224110, 2001
- [Bat05] A. G. Bates, M. Moll, A COMPARISON BETWEEN IRRADIATED MAGNETIC CZOCHRALSKI AND FLOAT ZONE SILICON DETECTORS USING THE TRANSIENT CURRENT TECHNIQUE, *Nucl. Instr. And Meth. A*, vol. 555, p. 113, 2005
- [Bau97] G. Bauer et al., A MULTIPLE SAMPLING TIME PROJECTION IONIZATION CHAMBER FOR NUCLEAR FRAGMENT TRACKING AND CHARGE MEASUREMENT, *Nucl. Instr. And Meth. A*, vol. 386, iss. 2 – 3, p. 249, 1997
- [Bed07] P. Bednarczyk et al., APPLICATION OF DIAMOND DETECTORS IN TRACKING OF HEAVY ION SLOWED DOWN RADIOACTIVE BEAMS, *Acta Phys. Pol. B*, vol. 38, no. 4, p. 1293, 2007
- [Ben06] A. BenMoussa et al., PERFORMANCE OF DIAMOND DETECTORS FOR VUV APPLICATIONS, *Nucl. Instr. And Meth. A*, vol. 568, p. 398, 2006
- [Ber] K. Bernier et al, AN INTENSE FAST NEUTRON BEAM IN LOUVAIN-LA-NEUVE, *available on the web at:*  
<http://www.fynu.ucl.ac.be/themes/he/cms/neutron/beam/neutrons-beam.html>
- [Ber02] P. Bergonzo, A. Brambilla, D. Tromson, C. Mer, B. Guizard, R. D. Marshall, F. Foulon, CVD DIAMOND FOR NUCLEAR DETECTION APPLICATIONS, *Nucl. Instr. And Meth. A*, vol. 476, p. 694, 2002
- [Ber01] E. Berdermann et al., THE DIAMOND PROJECT AT GSI - PERSPECTIVES, *Proc. of the 7th Int. Conf. on Advanced Technology Particle Physics (ICATPP-7)*, Como, Italy, 2001.

- [Ber01a] E. Berdermann, K. Blasche, P. Moritz, H. Stelzer, B. Voss, THE USE OF CVD-DIAMOND FOR HEAVY-ION DETECTION, *Diam. Relat. Mater.*, vol. 10, p. 1770, 2001
- [Ber07] E. Berdermann et al., PERFORMANCE OF DIAMOND DETECTORS IN A FRAGMENTATION EXPERIMENT, Proceedings of the Nuclear Physics Conference in Bormio, 2007
- [Bic88] H. Bichsel, STRAGGLING IN THIN SILICON DETECTORS, *Rev. Mod. Phys.*, vol. 60, no. 3, p. 663, 1988
- [Bic06] H. Bichsel, D.E. Groom, S.R. Klein, PASSAGE OF PARTICLES THROUGH MATTER
- [Bla04] D. R. Black and G. G. Long, X-RAY TOPOGRAPHY, NIST, Materials Science and Engineering Laboratory April 2004
- [Blo97] REVIEW OF PARTICLE PHYSICS, *Phys. Rev. D*, vol. 54, 1997
- [Boe07] W. de Boer et al., RADIATION HARDNESS OF DIAMOND AND SILICON SENSORS COMPARED, *Phys. Status Solidi A* vol. 17, 2007
- [Bog05] G. Bogdan, et al., GROWTH AND CHARACTERIZATION OF NEAR-ATOMICALLY FLAT, THICK HOMOEPITAXIAL CVD DIAMOND FILMS, *Phys. Status Solidi A*, vol. 202, no. 11, p. 2066, 2005
- [Bol07] J. Bol, S. Müller, E. Berdermann, W. de Boer, A. Furgeri, M. Pomorski, C. Sander, DIAMOND THIN FILM DETECTORS FOR BEAM MONITORING DEVICES, *Phys. Status Solidi A*
- [Bor00] K. Borer et al., CHARGE COLLECTION EFFICIENCY OF IRRADIATED SILICON DETECTOR OPERATED AT CRYOGENIC TEMPERATURES, *Nucl. Instr. And Meth. A* , vol. 440, p. 5, 2000
- [Bor01] K. Borer et al., CHARGE COLLECTION EFFICIENCY OF AN IRRADIATED CRYOGENIC DOUBLE-P SILICON DETECTOR, *Nucl. Instr. And Meth. A*, vol. 462, p. 474, 2001
- [Bra81] S. B. Bradlow, J. D. Comms, J. E. Lov, ASYMMETRY OF THE GR1 LINE IN TYPE IIA DIAMOND, *Solid State Commun.*, vol. 38, p. 247, 1981
- [Bru02] M. Bruzzi et. al., DEEP LEVELS IN CVD DIAMOND AND THEIR INFLUENCE ON THE ELECTRONIC PROPERTIES OF DIAMOND-BASED RADIATION SENSORS, *Phys. Status Solidi A*, vol. 193, No. 3, p. 563, 2002
- [CAMDA] CAMDA, A small CAMAC Data Acquisition System, Herbert Stelzer, GSI Darmstadt, Germany
- [Can75] C. Canali, C. Jacoboni, F. Nava, G. Ottaviani, A. Alberigi-Quaranta, ELECTRON DRIFT VELOCITY IN SILICON, *Phys. rev. B*, vol. 12, no. 4, p. 2265, 1975
- [Can79] C. Canali, E. Gatt, S. F. Kozlov, P. F. Manfredi, C. Manfredotti, F. Nava, A. Quirini, ELECTRICAL PROPERTIES AND PERFORMANCES OF NATURAL DIAMOND NUCLEAR RADIATION DETECTORS, *Nucl. Instr. And Meth. A* , vol. 160, p. 73, 1979

- [Cau67] D. M. Caughey, R. E. Thomas, CARRIER MOBILITIES IN SILICON EMPIRICALLY RELATED TO DOPING AND FIELD, *Proc. of the IEEE*, vol. 55, p. 2192, 1967
- [CBM] Letter of Intent for the Compressed Baryonic Matter Experiment at the Future Accelerator Facility in Darmstadt, available at <http://www.gsi.de/fair/experiments/CBM/LOI2004v6.pdf>
- [Cin98] V. Cindro, G. Kramberger, M. Mikuz, D. Zontar, BIAS-DEPENDENT ANNEALING OF RADIATION DAMAGE IN NEUTRON-IRRADIATED SILICON  $p^+ - n - n^+$  DIODES, *Nucl. Instr. Meth. Phys. Res. A*, vol. 419, p. 132, 1998
- [Cin00] V. Cindro, G. Kramberger, M. Mikuz, M. Tadel, D. Zontar, BIAS-DEPENDENT RADIATION DAMAGE IN HIGH-RESISTIVITY SILICON DIODES IRRADIATED WITH HEAVY CHARGED PARTICLES, *Nucl. Instr. Meth. Phys. Res. A*, vol. 450, p. 288, 2000
- [Cio07] M. Ciobanu, et al., A FRONT-END ELECTRONICS CARD COMPRISING A HIGH GAIN/HIGH BANDWIDTH AMPLIFIER AND A FAST DISCRIMINATOR FOR TIME-OF-FLIGHT MEASUREMENTS, *IEEE Transactions on Nuclear Science*, vol. 54, iss. 4, p. 1201, 2007
- [Cla95] C.D. Clark, R.W. Ditchburn, H. B. Dyer, THE ABSORPTION SPECTRA OF NATURAL AND IRRADIATED DIAMONDS, *Proceedings of the Royal Society of London. Series A, Mathematical and Physical Sciences*, vol. 234, p. 363, 1995
- [Col79] A.T. Collins and E.C. Lightowers, in: THE PROPERTIES OF DIAMOND, ed. J.E. Field (Academic Press, London, ch. 3, 1979).
- [Col93] A. T. Collins, INTRINSIC AND EXTRINSIC ABSORPTION AND LUMINESCENCE IN DIAMOND, *Physica B*, vol. 185, p. 284, 1993
- [Dai01] Daisuke Takeuchia, Hideyuki Watanabe, Hidetaka Sawada, Sadanori Yamanaka, Hideki Ichinose, Takashi Sekiguchi, Hideyo Okushi, ORIGIN OF BAND-A EMISSION IN HOMOEPITAXIAL DIAMOND FILMS, *Diam. Relat. Mater.*, vol. 10 p. 526, 2001
- [Dav99] Gordon Davies, CURRENT PROBLEMS IN DIAMOND: TOWARDS A QUANTITATIVE UNDERSTANDING, *Physica B* vol. 273 – 274, p. 15, 1999
- [Dav02] G. Davies et al., VACANCY-RELATED CENTERS IN DIAMOND, *Phys. Rev. B*, vol. 46, No.20, 1992
- [Dab89] W. Dabrowski, TRANSPORT EQUATIONS AND RAMO'S THEOREM: APPLICATIONS TO THE IMPULSE RESPONSE OF A SEMICONDUCTOR DETECTOR AND TO THE GENERATION-RECOMBINATION NOISE IN A SEMICONDUCTOR JUNCTION, *Prog. Quant. Electr.*, vol. 13, p. 233, 1989
- [Dea66] P. J. Dean, E. C. Lightowers, D. R. Wight, ELECTRICAL-TRANSPORT MEASUREMENTS ON SYNTHETIC SEMICONDUCTING DIAMOND, *Phys. Rev.*, vol. 151, p. 685, 1966

- [Def07] W. Deferme, A. Bogdan, G. Bogdan, K. Haenen, W. De Ceuninck, and M. Nesldek, ELECTRICAL TRANSPORT MEASUREMENTS AND EMISSION PROPERTIES OF FREE-STANDING SINGLE CRYSTALLINE CVD DIAMOND SAMPLES, *Phys. Status Solidi A*, vol. 204, no. 9, p. 3017, 2007
- [Der75a] Derjaguin, B. V. and Fedoseev, D. V., THE SYNTHESIS OF DIAMOND AT LOW PRESSURE, *Scientific American*, vol. 233(5), p. 102, 1975
- [Der77b] Derjaguin, B. V. and Fedoseev, D. V., GROWTH OF DIAMOND AND GRAPHITE FROM THE GAS PHASE, *Jzd. Nauka* (in Russian), Ch. 4, Moscow, 1977
- [Des07] C. Descamps, et al., CLINICAL STUDIES OF OPTIMISED SINGLE CRYSTAL AND POLYCRYSTALLINE DIAMONDS FOR RADIOTHERAPY DOSIMETRY, to be published in *Rad. Meas.*, available on-line at [www.sciencedirect.com](http://www.sciencedirect.com)
- [Dev07] R. Devanathan, L. R. Corrales, F. Gao, W. J. Weber, SIGNAL VARIANCE IN GAMMA-RAY DETECTORS-A REVIEW, *Nucl. Instr. And Meth. A*, 2007
- [Dir99] Dirk Meier, CVD DIAMOND SENSORS FOR PARTICLE DETECTION AND TRACKING, Ph.D. thesis, University of Heidelberg (1999)
- [e6] <http://193.120.252.126/cvd/page.jsp?pageid=309prod=6>
- [Ere04] V. Eremin, Z. Li, S. Roe, G. Ruggiero, E. Verbitskaya, DOUBLE PEAK ELECTRIC FIELD DISTORTION IN HEAVILY IRRADIATED SILICON STRIP DETECTORS, *Nucl. Instr. And Meth. A* Vol. 535, Iss. 3, p. 622, 2004
- [Ere07] V. Eremin, J. Härkönen, Z. Li and E. Verbitskaya, CURRENT INJECTED DETECTORS AT SUPER-LHC PROGRAM, *Nucl. Instr. And Meth. A*, vol. 583, p. 91, 2007
- [Erm77] V. C. Ermilova, L. P. Kotenko, G. I. Merzon, FLUCTUATIONS AND THE MOST PROBABLE VALUES OF RELATIVISTIC CHARGED PARTICLE ENERGY LOSS IN THIN GAS LAYERS, *Nucl. Instr. And Meth. A*, vol. 145, p. 555, 1977
- [ESTAR] Stopping-power and ranges for electrons,  
<http://physics.nist.gov/PhysRefData/Star/Text/ESTAR.html>
- [EVE] <http://www.softeng.cse.clrc.ac.uk/everest/>
- [FAIR] Facility for Antiproton and Ion Research,  
[http://www.gsi.de/fair/overview/accelerator/index\\_e.html](http://www.gsi.de/fair/overview/accelerator/index_e.html)
- [Fan46] U. Fano, ON THE THEORY OF IONIZATION YIELD OF RADIATIONS IN DIFFERENT SUBSTANCES, *Phys. Rev.*, vol. 70, no. 1-2, p. 44, 1946
- [Fan47] U. Fano, IONIZATION YIELD OF RADIATIONS. II. THE FLUCTUATIONS OF THE NUMBER OF IONS, *Phys. Rev.*, vol. 72, no.1, p. 26, 1947
- [Fer75] D. K. Ferry, HIGH-FIELD TRANSPORT IN WIDE-BAND-GAP SEMICONDUCTORS, *Phys. Rev. B*, vol. 12, no. 6, p. 2361, 1975

- 
- [Fer82] Ferry, D. K., FUNDAMENTAL ASPECTS OF HOT ELECTRON PHENOMENA. IN HANDBOOK OF SEMICONDUCTORS, *North-Holland Publishing*, p. 564, 1982
- [Fer05] L. Fernandez-Hernando et al., DEVELOPMENT OF A CVD DIAMOND NEXT TERM BEAM CONDITION MONITOR FOR PREVIOUS TERM CMS NEXT TERM AT THE LARGE HADRON COLLIDER, *Nucl. Instr. And Meth. A*, vol. 552, iss. 1 – 2, p. 183, 2005
- [Fin06] J. Fink, H. Krüger, P. Lodomez, N. Wermes, CHARACTERIZATION OF CHARGE COLLECTION IN CdTe AND CZT USING THE TRANSIENT CURRENT TECHNIQUE, *Nucl. Instr. And Meth. A*, vol. 560, iss. 2, p. 435, 2006
- [Fis08] M Fischer, S Gsell, M Schreck, B Stritzker, PREPARATION OF 4-INCH IR/YSZ/Si(001) SUBSTRATES FOR THE LARGE AREA DEPOSITION OF SINGLE-CRYSTAL DIAMOND, talk presented at 18th European Conference on Diamond, Diamond-Like Materials, Carbon Nanotubes and Nitrides, Berlin 2007, to be published in *Diamond and Related Materials* 2008
- [Fre51] G. P. Freeman, H. A. Van Der Velden, SOME ASPECTS OF THE COUNTING PROPERTIES OF DIAMOND, *Physica*, vol. XVII, no. 6, p. 565, 1951
- [For06] E. Forton, RADIATION DAMAGE INDUCED BY NEUTRONS IN CMS SILICON SENSORS, PhD thesis, Universit catholique de Louvain, 2006
- [Fuj06] N. Fujita, A. T. Blumenau, R. Jones, S. öberg, and P. R. Briddon, THEORETICAL STUDIES ON  $\langle 100 \rangle$  DISLOCATIONS IN SINGLE CRYSTAL CVD DIAMOND, *Phys. Status Solidi A*, vol. 203, no. 12, p. 3070, 2006
- [Fuj07] N. Fujita, A. T. Blumenau, R. Jones, S. öberg, and P. R. Briddon, CORE RECONSTRUCTIONS OF THE  $\langle 100 \rangle$  EDGE DISLOCATION IN SINGLE CRYSTAL CVD DIAMOND, *Phys. Status Solidi A*, vol. 204, No. 7, p. 2211, 2007
- [Fur06] A. Furgeri, QUALITATSKONTROLLE UND BESTRAHLUNGSSTUDIEN AN CMS SILIZIUMSTREIFENSSENSOREN, PhD thesis, Universitaet Karlsruhe, 2006
- [Gar00] J. Garca Lpez, F. J. Ager, M. Barbadillo Rank, F. J. Madrigal, M. A. Ontalba, M. A. Respaldiza, M. D. Ynsa, CNA: THE FIRST ACCELERATOR-BASED IBA FACILITY IN SPAIN, *Nucl. Instr. And Meth. B*, vol. 161 – 163, p. 1137, 2000
- [Gau08] M.P. Gaukroger et al., X-RAY TOPOGRAPHY STUDIES OF DISLOCATIONS IN SINGLE CRYSTAL CVD DIAMOND, *Diam. Relat. Mater.*, vol. 17 (3), p.262, 2008
- [Gei92] H. Geissel et al., THE GSI PROJECTILE FRAGMENT SEPARATOR, *Nucl. Instr. And Meth. B*, vol. 70, p. 286, 1992
- [Gri97] S. E. Grillo and J. E. Field, THE POLISHING OF DIAMOND, *J. Phys. D Appl. Phys.* vol. 30, p. 202, 1997
- [Hal52] R. N. Hall, ELECTRON-HOLE RECOMBINATION IN GERMANIUM, *Phys. Rev.*, vol. 87, no. 2, p. 387, 1952



- [Hal06] E. Halkiadakis, A PROPOSED LUMINOSITY MONITOR FOR CMS BASED ON SMALL ANGLE DIAMOND PIXEL TELESCOPES, *Nucl. Instr. And Meth. A*, vol. 565, iss. 1, p. 284, 2006
- [Han07] T. Hänsel, F. Frost, A. Nickel, T. Schindler, ULTRA-PRECISION SURFACE FINISHING BY ION BEAM TECHNIQUES, *Vakuum in Forschung und Praxis*, vol. 19, iss. 5, p. 24, 2007
- [He01] Z. He, REVIEW OF THE SHOCKLEYRAMO THEOREM AND ITS APPLICATION IN SEMICONDUCTOR GAMMA-RAY DETECTORS, *Nucl. Instr. And Meth. A*, vol. 463, p. 250, 2001
- [Hec32] K. Hecht, ZUM MECHANISMUS DES LICHELEKTRISCHEN PRIMARSTROMES IN ISOLIERENDEN KRISTALLEN, 1932
- [Hib07] K. Hibino et al., THE DESIGN OF DIAMOND COMPTON TELESCOPE, *Astr. Spac. Scien.*, vol. 309, p. 541, 2007
- [Huh02] M. Huhtinen, SIMULATION OF NON-IONISING ENERGY LOSS AND DEFECT. FORMATION IN SILICON, *Nucl. Instr. And Meth. A* vol. 491, No. 194 2002
- [Hwa76] W. Hwang and K. C. Kao, STUDIES OF THE THEORY OF SINGLE AND DOUBLE INJECTIONS IN SOLIDS WITH A GAUSSIAN TRAP DISTRIBUTION, *Solid State Electron.* vol. 19, p. 1045, 1976
- [Iak02] K. Iakoubovskii and A. Stesmans, DOMINANT PARAMAGNETIC CENTERS IN  $17^O$ -IMPLANTED DIAMOND, *Phys. Rev. B* vol. 66, p. 045406 2002
- [Iak04] K. Iakoubovskii and A. Stesmans, VACANCY CLUSTERS IN DIAMOND STUDIED BY ELECTRON SPIN RESONANCE *Phys. Status Solidi A* vol. 201, No. 11, p. 2509, 2004
- [ID19] ID19 line of ESRF,  
<http://www.esrf.eu/UsersAndScience/Experiments/Imaging/ID19/>
- [ID21] ID21 line of ESRF,  
<http://www.esrf.eu/UsersAndScience/Experiments/Imaging/ID21/>
- [ioffe] Properties of semiconductors, <http://www.ioffe.rssi.ru/SVA/NSM/Semicond/>
- [Isb02] J. Isberg et al., HIGH CARRIER MOBILITY IN SINGLE-CRYSTAL PLASMA-DEPOSITED DIAMOND, *Science*, vol. 297. no. 5587, p. 1670, 2002
- [Isb04] J. Isberg, J. Hammersberg, D. J. Twitchen, A. J. Whitehead, SINGLE CRYSTAL DIAMOND FOR ELECTRONIC APPLICATIONS, *Diam. Relat. Mater.*, vol. 13, iss. 2, p. 320, 2004
- [Isb05] Jan Isberg, Adam Lindblom, Antonella Tajani, Daniel Twitchen, TEMPERATURE DEPENDENCE OF HOLE DRIFT MOBILITY IN HIGH-PURITY SINGLE-CRYSTAL CVD DIAMOND, *Phys. Status Solidi A*, vol. 202, no. 11, p. 2194, 2005

- [Jac83] C. Jacoboni, L. Reggiani, THE MONTE CARLO METHOD FOR THE SOLUTION OF CHARGE TRANSPORT IN SEMICONDUCTORS WITH APPLICATIONS TO COVALENT MATERIALS, *Rev. Mod. Phys.*, vol. 55, no. 3, p. 645, 1983
- [Jor08] D. Jordan et al., SIMPLE CLASSICAL MODEL FOR FANO STATISTICS IN RADIATION DETECTORS, *Nucl. Instr. And Meth. A*, vol. 585, p. 146, 2008
- [Kani96] R. Kania, DIAMOND RADIATION DETECTORS I. DETECTOR PROPERTIES FOR IIA DIAMOND, *Proceedings of the International Summer School of Physics Enrico Fermi Bologna Italy 1996*, 1997
- [Kan96] J. Kaneko, M. Katagiri, DIAMOND RADIATION DETECTOR USING A SYNTHETIC IIA TYPE MONO-CRYSTAL, *Nucl. Instr. And Meth. A*, vol. 383, iss. 2 – 3, p. 547, 1996
- [Kan03] J. H. Kaneko, RADIATION DETECTOR MADE OF A DIAMOND SINGLE CRYSTAL GROWN BY A CHEMICAL VAPOR DEPOSITION METHOD, *Nucl. Instr. And Meth. A*, vol 505, iss. 1 – 2, p. 187, 2003
- [Kam83] Kamo, M., Sato, Y., Matsumoto, S. Setaka, N. , DIAMOND SYNTHESIS FROM GAS PHASE IN MICROWAVE PLASMA, *J. Cryst. Growth*. vol. 62, p. 642, 1983
- [Kam88] M. Kamo, H. Yurimoto, Y. Sato, EPITAXIAL GROWTH OF DIAMOND ON DIAMOND SUBSTRATE BY PLASMA ASSISTED CVD, *Appl. Surf. Sci.*, vol. 33/34, p. 553 ,1988
- [KEI] <http://www.keithley.com/search?searchType=generalSearchableText=6517>
- [Kin52] G. H. Kinchin, R. S. Pease, THE DISPLACEMENT OF ATOMS IN SOLIDS BY RADIATION, *Rep. Prog. Phys.*, vol. 18, no. 1, , p. 1, 1952
- [Kis05] M. Kis, A DIAMOND START DETECTOR FOR FOPI, *GSI Scientific Report*, Instruments-Methods-09, 2005
- [Kle68] C. A. Klein, BANDGAP DEPENDENCE AND RELATED FEATURES OF RADIATION IONIZATION ENERGIES IN SEMICONDUCTORS, *J. Appl. Phys.*, vol. 39, p. 2029, 1968
- [Koi92] J. Koike, D. M. Parkin, T. E. Mitchell, DISPLACEMENT THRESHOLD ENERGY FOR TYPE II A DIAMOND, *Appl. Phys. Lett.* vol. 60 No. 12, 1992
- [Kon67] E. A. Konorova, S. A. Schevchenko, *Fiz. Tekh. Poluprovodn.*, vol. 1, p. 364, 1967
- [Kot05] I.V. Kotov, CURRENTS INDUCED BY CHARGES MOVING IN SEMICONDUCTOR, *Nucl. Instr. And Meth. A*, vol. 539, p. 267, 2005
- [Kuz06] Ekaterina Kuznetsova, DESIGN STUDIES AND SENSOR TESTS FOR THE BEAM CALORIMETER OF THE ILC DETECTOR, PhD thesis, Humboldt-Universitaet zu Berlin, 2006
- [Lan59] A.R. Lang, THE PROJECTION TOPOGRAPH: A NEW METHOD IN X-RAY DIFFRACTION MICORADIOGRAPHY, *Acta Cryst.* vol. 12, p. 249, 1959
- [langaus] <http://root.cern.ch/root/roottalk/roottalk02/att-3361/01-langaus.C>

- [Lan44] L.D. Landau, ON THE ENERGY LOSS OF FAST PARTICLES BY IONIZATION, *J. Phys. USSR* vol. 8, p. 201, 1944
- [Lan68] M. Lannoo, A. M. Stoneham, THE OPTICAL ABSORPTION OF THE NEUTRAL VACANCY IN DIAMOND, *J. Phys. Chem. Solids* vol. 29, p. 1987, 1968
- [Lap61] F. Lappe, THE ENERGY OF ELECTRON-HOLE PAIR FORMATION BY X-RAYS IN PbO, *J. Phys. Chem. Solids*, vol. 20, p.173, 1961
- [Laz98] I. Lazanu et al., LINDHARD FACTORS AND CONCENTRATION OF PRIMARY DEFECTS IN SEMICONDUCTOR MATERIALS FOR USES IN HEP, *Nucl. Instr. And Meth. A*, vol. 406, p. 259, 1998
- [Laz99] S.Lazanu, L.Lazanu and E.Borcht, DIAMOND DEGRADATION IN HADRON FIELDS, *Nuclear Physics B*, vol. 78 p. 683, 1999
- [Lin96] J. Lindhard, A. H. Sørensen, RELATIVISTIC THEORY OF STOPPING FOR HEAVY IONS, *Phys. Rev. A*, vol. 53, no. 4, p. 2443, 1996
- [Lin99] T. K. Lin, DEFECT MODEL AND THE CURRENT-VOLTAGE CHARACTERISTICS IN DIELECTRIC THIN FILMS, *Chinese J. Phys.*, vol. 27, no. 5, p. 351, 1999
- [LISE] LISE++, <http://groups.nsl.msui.edu/lise/lise.html>
- [Lin96] J. Lindhard, A. H. Sørensen, RELATIVISTIC THEORY OF STOPPING FOR HEAVY IONS, *Phys. Rev. A*, vol. 53, p. 2443, 1996
- [Liu88] M. Liu, D. Y. Xing, C. S. Ting, W. T. Xu, HOT-ELECTRON TRANSPORT FOR MANY-VALLEY SEMICONDUCTORS BY THE METHOD OF NONEQUILIBRIUM STATISTICAL OPERATORS, *Phys. Rev. B*, vol. 37, no. 6, p. 2997, 1988
- [Liu95] H. Liu, D. S. Dandy, DIAMOND CHEMICAL VAPOR DEPOSITION: NUCLEATION AND EARLY GROWTH STAGES, *Noyes*, New Jersey, 1995
- [Lo07a] A. Lohstroh, P. J. Sellin, S. G. Wang, A. W. Davies, J. M. Parkin, MAPPING OF POLARIZATION AND DETRAPPING EFFECTS IN SYNTHETIC SINGLE CRYSTAL CHEMICAL VAPOR DEPOSITED DIAMOND BY ION BEAM INDUCED CHARGE IMAGING, *J. Appl. Phys.*, vol. 101, p. 063711, 2007
- [Lo07b] A. Lohstroh et al., EFFECT OF DISLOCATIONS ON CHARGE CARRIER MOBILITY-LIFETIME PRODUCT IN SYNTHETIC SINGLE CRYSTAL DIAMOND, *Appl. Phys. Lett.*, vol. 90, p. 102111, 2007
- [Loh07] A. Lohstroh, P. J. Sellin, S. G. Wang, A. W. Davies, J. M. Parkin, MAPPING OF POLARIZATION AND DETRAPPING EFFECTS IN SYNTHETIC SINGLE CRYSTAL CHEMICAL VAPOR DEPOSITED DIAMOND BY ION BEAM INDUCED CHARGE IMAGING, *J. Appl. Phys.*, vol. 101, p. 063711, 2007
- [Lou78] J. H. N. Loubser, J. A. van Wyk, ELECTRON SPIN RESONANCE IN THE STUDY OF DIAMOND, *Rep. Prog. Phys.*, vol. 41, , p. 1201, 1978

- [Lon60] D. Long, SCATTERING OF CONDUCTION ELECTRONS BY LATTICE VIBRATIONS IN SILICON, *Phys. Rev.*, vol. 120, no. 6, p. 2024, 1960
- [Mai98] A. Mainwood, CVD DIAMOND PARTICLE DETECTORS, *Diam. Relat. Mater.*, vol. 7 p. 504 1998
- [Man95] C. Manfredotti, F. Wang, P. Polesello, E. Vittone, F. Fizzotti, A. Scacco, BLUE-VIOLET ELECTROLUMINESCENCE AND PHOTOCURRENT SPECTRA FROM POLYCRYSTALLINE CHEMICAL VAPOR DEPOSITED DIAMOND FILM, *Appl. Phys. Lett.*, vol. 67 iss. 23, p. 3376 , 1995
- [Man07] C. Manfredotti et al., ION BEAM INDUCED CHARGE CHARACTERIZATION OF EPITAXIAL SINGLE CRYSTAL CVD DIAMOND, *Diam. Relat. Mater.*, vol. 16, iss. 4 – 7, p. 940, 2007
- [Mar03] M. Marinelli et al, ANALYSIS OF TRAPS IN HIGH QUALITY CVD DIAMOND FILMS THROUGH THE TEMPERATURE DEPENDENCE OF CARRIER DYNAMICS, *Diamond Relat. Mater.*, vol. 12, p. 1081, 2003
- [Mat82] S. Matsumoto, Y. Sato, M. Tsutsumi, N. Setaka, GROWTH OF DIAMOND PARTICLES FROM METHANE-HYDROGEN GAS., *J. Mater. Sci.* vol. 17(11): p. 3106, 1982
- [Mar69] M. Martini, G. Ottaviani, RAMO'S THEOREM AND THE ENERGY BALANCE EQUATIONS IN EVALUATING THE CURRENT PULSE FROM SEMICONDUCTOR DETECTORS, *Nucl. Instr. And Meth.*, vol. 67, p. 177, 1969
- [May00] P. W. May, DIAMOND THIN FILMS: A 21ST-CENTURY MATERIAL, *Phil. Trans. R. Soc. Lond. A*, vol. 358, p. 473, 2000
- [Mic08] S. Michaelson, A. Hoffman, AMBIENT CONTAMINATION OF POLY-CRYSTALLINE DIAMOND SURFACES STUDIED BY HIGH-RESOLUTION ELECTRON ENERGY LOSS SPECTROSCOPY AND X-RAY PHOTOELECTRON SPECTROSCOPY, *Diam. Relat. Mater.*, doi:10.1016/j.diamond.2008.01.031, 2008
- [Mit06] Y. Mitaa, Y. Yamadaa, Y. Nisidaa, M. Okadab, T. Nakashima, INFRARED ABSORPTION STUDIES OF NEUTRON-IRRADIATED TYPE IB DIAMOND, *Physica B* vol. 376377, p. 288, 2006
- [Mol06] Michael Moll, On behalf of the RD50 Collaboration, RADIATION TOLERANT SEMICONDUCTOR SENSORS FOR TRACKING DETECTORS, *Nucl. Instr. And Meth. A*, vol. 565, Iss. 1, p. 202, 2006
- [Mor01] Moritz et al., BROADBAND ELECTRONICS FOR CVD-DIAMOND DETECTORS, *Diam. Relat. Mater.* 10, p. 1770, 2001.
- [Mor07] J. Morse, M. Salom, M. Pomorski, J. Grant, V. OShea, P. Ilinski, SINGLE CRYSTAL CVD DIAMOND DETECTORS: POSITION AND TEMPORAL RESPONSE MEASUREMENTS USING A SYNCHROTRON MICROBEAM PROBE, Paper Submitted to Proceedings of Symposium P, MRS 2007 Fall Meeting, Boston 10 December 2007

- [Mor07a] J. Morse, M. Salom, E. Berdermann, M. Pomorski, W. Cunningham, J. Grant, SINGLE CRYSTAL CVD DIAMOND AS AN X-RAY BEAM MONITOR, *Diam. Relat. Mater.*, vol. 16, iss. 4 – 7, p. 1049, 2007
- [Mor07b] J. Morse, M. Salom, E. Berdermann, M. Pomorski, W. Cunningham, J. Grant, V. OShea, SINGLE CRYSTAL CVD DIAMOND FOR SYNCHROTRON X-RAY BEAM MONITORING, proceedings of Diamond at Work conference, Rome 2007
- [Moy55] Moyal J. E., THEORY OF IONIZATION FLUCTUATIONS, *Phil. Mag.*, vol. 46, p. 263, 1955
- [Mue06] S. Mueller, Diploma thesis, University of Karlsruhe, 2006
- [Mur07] A. Murari et al., PROGRESS IN ITER-RELEVANT DIAGNOSTIC TECHNOLOGIES AT JET, *EFDA-JET-CP(06)05-12* available at: <http://www.iop.org/Jet/fulltext/EFDC060512.pdf>
- [Nav80] F. Nava, C. Canali, C. Jacoboni, L. Reggiani, S.F. Kozlov, ELECTRON EFFECTIVE MASSES AND LATTICE SCATTERING IN NATURAL DIAMOND, *Solid State Commun.* vol. 33, p. 475, 1980
- [Neb98] C.E. Nebel, M. Stutzmann, F. Lacher, P. Koidl, R. Zachai, CARRIER TRAPPING AND RELEASE IN CVD-DIAMOND FILMS, *Diam. Relat. Mater.*, vol. 7, p. 556, 1998
- [Neb00] C.E. Nebel, A. Waltenspiel, M. Stutzmann, M. Paul, L. Schaefer, PERSISTENT PHOTOCURRENTS IN CVD DIAMOND, *Diam. Relat. Mater.*, vol. 9, p. 404, 2000
- [Neb01] C.E. Nebel et al., SPACE CHARGE SPECTROSCOPY OF DIAMOND, *Diam. Relat. Mater.* vol. 10 p. 639, 2001
- [Neb03] C. E. Nebel, ELECTRONIC PROPERTIES OF CVD DIAMOND, *Semicond. Sci. Technol.*, vol. 18, p. S1, 2003
- [Neb04] Ch. E. Nebel, J. Ristein, THIN-FILM DIAMOND II, *Semiconduct. Semimet.*, vol. 77, p. 82, 2004
- [Nes72] S. Nespurek, P. Smejtek, SPACE-CHARGE LIMITED CURRENTS IN INSULATORS WITH THE GAUSSIAN DISTRIBUTION OF TRAPS, *Czech. J. Phys. B* vol. 22, p. 160, 1972
- [New02] M.E. Newton, B.A. Campbell, D.J. Twitchen, J.M. Baker, T.R. Anthony, RECOMBINATION-ENHANCED DIFFUSION OF SELF-INTERSTITIAL ATOMS AND VACANCY INTERSTITIAL RECOMBINATION IN DIAMOND, *Diam. Relat. Mater.*, vol. 11, p. 618, 2002
- [Nok01] S. Nokhrin, J. Rosa, M. Vanecek, A. G. Badalyan and M. Nesladek, EPR STUDY OF PREFERENTIAL ORIENTATION OF CRYSTALLITES IN N-DOPED HIGH QUALITY CVD DIAMOND, *Diam. Relat. Mater.*, vol. 10, 3 – 7, p. 480, 2001
- [NoR] Novel Radiation Hard CVD Diamonds for Hadron Physics (NoRHDia) collaboration, <http://www-norhdia.gsi.de>

- [NUST] H. Geissel, TECHNICAL REPORT ON THE DESIGN, CONSTRUCTION, COMMISSIONING AND OPERATION OF THE SUPER-FRS OF FAIR, available at [http://www-linux.gsi.de/wwwnusta/tech\\_report/02-super-frs.pdf](http://www-linux.gsi.de/wwwnusta/tech_report/02-super-frs.pdf)
- [Oh00] Alexander Oh,U, Michael Moll, Albrecht Wagner, Wolfram Zeuner, NEUTRON IRRADIATION STUDIES WITH DETECTOR GRADE CVD DIAMOND, *Diam. Relat. Mater.* vol. 9 p. 1897, 2000
- [ORT94] EG G ORTEC, MODULAR PULSE-PROCESSING ELECTRONICS AND SEMICONDUCTOR RADIATION DETECTORS, 95 (1994).
- [Owe04a] A. Owens, A. Peacock, COMPOUND SEMICONDUCTOR RADIATION DETECTORS, *Nucl. Instr. And Meth. A*, vol. 531, iss. 1 – 2, p. 18, 2004
- [Pai71] G. S. Painter, D. E. Ellis, A. R. Lubinsky, AB INITIO CALCULATIONS OF THE ELECTRONIC STRUCTURE AND OPTICAL PROPERTIES OF DIAMOND USING THE DISCRETE VARIATIONAL METHOD, *Phys. Rev. B*, vol. 4, p. 3610, 1971
- [Per05] H. Pernegger, CHARGE-CARRIER PROPERTIES IN SYNTHETIC SINGLE-CRYSTAL DIAMOND MEASURED WITH THE TRANSIENT-CURRENT TECHNIQUE, *J. Appl. Phys.*, vol. 97, p. 073704, 2005
- [Per06] H. Pernegger, HIGH MOBILITY DIAMONDS AND PARTICLE DETECTORS, *Phys. Status Solidi A* vol. 203, No. 13, p. 3299 2006
- [Pie68] T. E. Pierce, M. Blann, STOPPING POWERS AND RANGES OF 5-90-MeV  $S^{32}$ ,  $Cl^{35}$ ,  $Br^{79}$ , AND  $I^{127}$  IONS IN  $H_2$ ,  $He$ ,  $N_2$ ,  $Ar$ , AND  $Kr$ : A SEMIEMPIRICAL STOPPING POWER THEORY FOR HEAVY IONS IN GASES AND SOLIDS, *Phys. Rev.* vol. 173, p. 390, 1968
- [Pil07] M. Pillon et al., NEUTRON DETECTION AT JET USING ARTIFICIAL DIAMOND DETECTORS, *Fusion Eng. Des.*, vol. 82, p. 1174, 2007
- [Pom05] M. Pomorski et al., CHARACTERISATION OF SINGLE CRYSTAL CVD DIAMOND PARTICLE DETECTORS FOR HADRON PHYSICS EXPERIMENTS, *Phys. Status Solidi A*, vol. 202, no. 11, p. 2199, 2005
- [Pom06] M. Pomorski et al., DEVELOPMENT OF SINGLE-CRYSTAL CVD-DIAMOND DETECTORS FOR SPECTROSCOPY AND TIMING, *Phys. Status Solidi A*, vol. 12, no. 12, p. 3152, 2006
- [Pri02] J. F. Prins, IMPLANTATION-DOPING OF DIAMOND WITH  $B^+$   $C^+$ ,  $N^+$  AND  $O^+$  IONS USING LOW TEMPERATURE ANNEALING, *Diam. Relat. Mater.*, vol. 11, p. 612, 2002
- [Pu01] A. Pu, V. Avalos, S. Dannefaer, NEGATIVE CHARGING OF MONO-AND DIVACANCIES IN IIA DIAMONDS BY MONOCHROMATIC ILLUMINATION, *Diam. Relat. Mater.*, vol. 10, p. 585, 2001
- [Rah07] A. Rahman, M. K. Sanyal, FORMATION OF WIGNER CRYSTALS IN CONDUCTING POLYMER NANOWIRES, <http://www.citebase.org/abstract?id=oai:arXiv.org:cond-mat/0702009>, 2007

- [rd39] Criogenic silicon detectors,  
<http://www.hip.fi/research/cms/tracker/RD39/php/home.php>
- [rd42] Development of Diamond Tracking Detectors for High Luminosity Experiments at the LHC, <http://greybook.cern.ch/programmes/experiments/RD42.html>
- [RD42] <http://greybook.cern.ch/programmes/experiments/RD42.html>
- [rd50] Radiation hard semiconductor devices for very high luminosity colliders,  
<http://rd50.web.cern.ch/rd50/>
- [Red54] A. G. Redfield, ELECTRONIC HALL EFFECT IN DIAMOND, *Phys. Rev.*, vol. 94, p. 526, 1954
- [Reg81] L. Reggiani, S. Bosi, C. Canali, F. Nava, S. F. Kozlov, HOLE-DRIFT VELOCITY IN NATURAL DIAMOND, *Phys. Rev. B*, vol. 23, no. 6, p. 3050, 1981
- [Reb07] M. Rbisz, B. Voss, A. Heinz, E. Usenko, M. Pomorski, CVD DIAMOND DOSIMETERS FOR HEAVY ION BEAMS, *Diam. Relat. Mater.*, vol. 16, p. 1070, 2007
- [Rit95] FOPI Collaboration Ritman J., THE FOPI DETECTOR AT SIS/GSI, *Nucl. Phys. B*, vol. 44, no. 1, p. 708, 1995
- [Ris01] J. Ristein, F. Maier, M. Riedel, M. Stammer, L. Ley, DIAMOND SURFACE CONDUCTIVITY EXPERIMENTS AND PHOTOELECTRON SPECTROSCOPY, *Diam. Relat. Mater.*, vol. 10, p. 416, 2001
- [Rob73] R. E. Robson, DIFFUSIVITY OF CHARGE CARRIERS IN SEMICONDUCTORS IN STRONG ELECTRIC FIELDS, *Phys. Rev. Lett.*, vol. 31, no. 13, 1973
- [rose] The ROSE collaboration, <http://rd48.web.cern.ch/RD48/>
- [Ruc68] J.G. Ruch, G. S. Kino, TRANSPORT PROPERTIES OF GAAS, *Phys. Rev.*, vol. 174, no. 3, p. 921, 1968
- [Sch74] B. Schorr, PROGRAMS FOR THE LANDAU AND THE VAVILOV DISTRIBUTIONS AND THE CORRESPONDING RANDOM NUMBERS, *Comput. Phys. Commun.* vol. 7 p. 215, 1974
- [Sch01] M. Schreck, F. Hörmann, H. Roll, J. K. N. Lindner, B. Stritzker, DIAMOND NUCLEATION ON IRIDIUM BUFFER LAYERS AND SUBSEQUENT TEXTURED GROWTH: A ROUTE FOR THE REALIZATION OF SINGLE-CRYSTAL DIAMOND FILMS, *Appl. Phys. Lett.*, vol. 78, p. 192, 2001
- [Sec07] Aurlia Secroun et al., DISLOCATION IMAGING FOR ELECTRONICS APPLICATION CRYSTAL SELECTION, *Phys. Status Solidi A*, vol. 204, no. 12, p. 4298, 2007
- [Sen02] P. Senger, THE COMPRESSED BARYONIC MATTER EXPERIMENT, *J. Phys. G: Nucl. Part. Phys.*, vol. 28, p. 1869, 2002
- [Sho52] W. Shockley, W. T. Read Jr., STATISTICS OF THE RECOMBINATIONS OF HOLES AND ELECTRONS, *Phys. Rev.*, vol. 87, no. 5, 1952

- [Sho61] W. Shockley, PROBLEMS RELATED TO P-N JUNCTIONS IN SILICON, *Solid State Electron.*, vol. 2, p. 35, 1961
- [SimWi] David W. Winston, SIMWINDOWS SEMICONDUCTOR DEVICE SIMULATION PROGRAM, <http://ece-www.colorado.edu/~bart/ecen6355/simwindows/>
- [Spi81] Spitzyn, B. V., Bouilov, L. L., and Derjaguin, B. V., VAPOR GROWTH OF DIAMOND ON DIAMOND AND OTHER SURFACES, *J. of Crystaal Growth*, 52:219-226 (1981)
- [Sto06] A. Stolz, M. Behravan, M. Regmi, B. Golding, HETEROEPITAXIAL DIAMOND NEXT TERM DETECTORS FOR HEAVY ION BEAM TRACKING, *Diam. Relat. Mater.*, vol. 15, iss. 4 – 8, p. 807, 2006
- [Sud06] S. K. Sudheer, V. P. Mahadevan Pillai, V. U. Nayar, CHARACTERIZATION OF LASER PROCESSING OF SINGLE-CRYSTAL NATURAL DIAMONDS USING MICRO-RAMAN SPECTROSCOPIC INVESTIGATIONS, *J. Raman Spectrosc.*, vol. 38, iss. 4 , p. 427, 2006
- [Sze81] S. M. Sze, PHYSICS OF SEMICONDUCTOR DEVICES, *Wiley-Interscience*, 2nd edition, 1981
- [Tac05] M. Tachiki et al., CHARACTERIZATION OF LOCALLY MODIFIED DIAMOND SURFACE USING KELVIN PROBE FORCE MICROSCOPE, *Surf. Sci.* vol. 581, p. 207, 2005
- [Tan02] Y. Tanimura, J. Kaneko, M. Katagiri, Y. Ikeda, T. Nishitani, H. Takeuchi, and T. Iida, HIGH-TEMPERATURE OPERATION OF A RADIATION DETECTOR MADE OF A TYPE IIA DIAMOND NEXT TERM SINGLE CRYSTAL SYNTHESIZED BY A HPHT METHOD, *Nucl. Instr. And Meth. A* vol. 443, p. 325, 2002
- [Tan05] T. Tanaka et al., RADIATION TOLERANCE OF TYPE IIA SYNTHETIC DIAMOND DETECTOR FOR 14 MEV NEUTRONS, *Diam. Relat. Mater.* vol. 14 p. 2031 2005
- [Tok06] Tokuyuki Teraji, CHEMICAL VAPOR DEPOSITION OF HOMOEPITAXIAL DIAMOND FILMS, *Phys. Status Solidi A*, vol. 203, no. 13, p. 3324, 2006
- [Tom04] Tomokatsu Watanabe, Tokuyuki Teraji, and Toshimichi Ito, MONTE CARLO SIMULATIONS OF ELECTRON TRANSPORT PROPERTIES OF DIAMOND IN HIGH ELECTRIC FIELDS USING FULL BAND STRUCTURE, *J. Appl. Phys.*, vol. 95, No. 9, p. 4866, 2004
- [Tra69] R. Trammell, F. J. Walter, THE EFFECTS OF CARRIER TRAPPING IN SEMICONDUCTOR GAMMA-RAY SPECTROMETERS, *Nucl. Instr. And Meth. A*, vol. 76, p. 317, 1969
- [Tra03] E. Trajkov, S. Prawer, P. Spizzirri, THE EFFECT OF ION IMPLANTATION ON THERMALLY STIMULATED CURRENTS IN POLYCRYSTALLINE CVD DIAMOND, *Diam. Relat. Mater.*, vol. 12, p. 1738, 2003
- [Tra07] N. Tranchant, M. Nesladek, D. Tromson, Z. Remes, A. Bogdan, P. Bergonzo, TIME OF FLIGHT STUDY OF HIGH PERFORMANCE CVD DIAMOND DETECTOR DEVICES, *Phys. Status Solidi A*, vol. 204, no. 9, p. 3023, 2007
- [Tsh72] Guido R. Tschulena, ANISOTROPY OF WARM ELECTRONS IN GERMANIUM AND SILICON, *Z. Physik*, vol. 256, p. 113, 1972



- [Twi99] D.J. Twitchen, D.C. Hunt, V. Smart, M.E. Newton, J.M. Baker, CORRELATION BETWEEN ND1 OPTICAL ABSORPTION AND THE CONCENTRATION OF NEGATIVE VACANCIES DETERMINED BY ELECTRON PARAMAGNETIC RESONANCE (EPR), *Diam. Relat. Mater.* vol. 8, p. 1572, 1999
- [Vav57] P. V. Vavilov, IONIZATION LOSSES OF HIGH-ENERGY HEAVY PARTICLES, *Zh. Eksp. Teor. Fiz.*, vol. 32, p. 920, 1957
- [Wan00] Xin Wang et al. , MONTE CARLO SIMULATION OF ELECTRON TRANSPORT IN SIMPLE ORTHORHOMBICALLY STRAINED SILICON, *J. Appl. Phys.*, vol. 88, p. 4717, 2000
- [Wan06] S. G. Wang, P. J. Sellin, and A. Lohstroh, TEMPERATURE-DEPENDENT HOLE DETRAPPING FOR UNPRIMED POLYCRYSTALLINE CHEMICAL VAPOR DEPOSITED DIAMOND, *Appl. Phys. Lett.* vol. 88, p. 023501, 2006
- [Wat01] G.A. Watta, M.E. Newtonb, J.M. Bakera, EPR AND OPTICAL IMAGING OF THE GROWTH-SECTOR DEPENDENCE OF RADIATION-DAMAGE DEFECT PRODUCTION IN SYNTHETIC DIAMOND, *Diam. Relat. Mater.*, vol. 10, p. 1681, 2001
- [Wat04] Tomokatsu Watanabe, Tokuyuki Teraji, Toshimichi Itoa, Yoshinari Kamakura and Kenji Taniguchi, MONTE CARLO SIMULATIONS OF ELECTRON TRANSPORT PROPERTIES OF DIAMOND IN HIGH ELECTRIC FIELDS USING FULL BAND STRUCTURE, *J. Appl. Phys.*, vol. 95, no. 9, 2004
- [xray] X-Ray Attenuation Length calculator, [http://henke.lbl.gov/optical\\_constants/atten2.html](http://henke.lbl.gov/optical_constants/atten2.html)
- [Yan05] J. Yang, W. Huang, T.P. Chow, J. E. Butler, FREE-STANDING DIAMOND SINGLE CRYSTAL FILM FOR ELECTRONICS APPLICATIONS, *Proceedings of MRS 2005 Fall Symposium*, paper no. 0905-DD06-09 available at <http://www.mrs.org>
- [Yok97] M. Yokoba, Yasuo Koide, A. Otsuki, F. Ako, T. Oku, Masanori Murakami, CARRIER TRANSPORT MECHANISM OF OHMIC CONTACT TO P-TYPE DIAMOND, *J. Appl. Phys.*, vol. 81, no. 10, p. 6815, 1997
- [Zai01] A. Zaitsev, OPTICAL PROPERTIES OF DIAMOND; A DATA HANDBOOK, Springer-Verlag Berlin Heidelberg 2001
- [Zam05] C. Zamantzas, B. Dehning, E. Effinger, G. Ferioli, G. Guaglio, R. Leitner, THE LHC BEAM LOSS MONITORING SYSTEMS REALTIME DATA ANALYSIS CARD, *Proceedings of DIPAC*, Lyon, France, 2005
- [Zei00] R. Zeisel, C.E. Nebel, M. Stutzmann, CAPACITANCE-VOLTAGE PROFILING OF DEUTERIUM PASSIVATION AND DIFFUSION IN DIAMOND SCHOTTKY DIODES, *Diam. Relat. Mater.*, vol. 9, p. 413, 2000
- [Zha94] S. Zhao, CHARACTERIZATION OF THE ELECTRICAL PROPERTIES OF POLYCRYSTALLINE DIAMOND FILMS, Ph.D. Thesis, The Ohio State University, 1994.
- [Zhu95] W. Zhu, DIAMOND: ELECTRONIC PROPERTIES AND APPLICATIONS, p. 175, Kluwer Academic Publisher, 1995

[Zie85] THE STOPPING AND RANGE OF IONS IN SOLIDS, edited by J. F. Ziegler, J. P. Bier-sack, and U. Littmark *Pergamon Press*, New York, 1985. The corresponding program package SRIM can be found at <http://www.srim.org/>.

# Acknowledgements

First, I want to thank Eleni Berdermann for giving me the opportunity to continue my work on diamond detector development as a PhD student and Prof. Dr. Joachim Stroth who agreed to supervise my PhD work at the Frankfurt University. I'd like also to thank Hadron Physics Community for financial support (RII3-CT-2004-506078).

I appreciate sincerely the support of Eleni Berderman while writing the thesis. Thanks to her patience and time the 'hard copy' of my work could be presented finally to the world.

My thesis is multidisciplinary so during four years stay at GSI, I visited several scientific institutes and met, worked with a dozen or so scientist, whom I want to thank below:

**Detector Laboratory of GSI** - For introducing me to the basics of detector design and FE electronics during my first year of the stay, I'm grateful to Eleni Berdermann, Dr. Mircea Ciobanu, Dr. Alexander Martemiyarov and Dr. Andrei Caragheorghopol. I also would like to thank Michael Traeger, Dr. Bern Voss, Dr. Christian Schmitd, Dr. Mladen Kis for helping me in daily work.

**Target Laboratory of GSI** - For fruitful cooperation and diamond samples metallization, annealing and other processes: Dr. Bettina Lommel, Dr. Birgit Kindler, Willi Hartmann, and special thanks to Annett Hübner .

**Materials Research of GSI** - Prof. Dr. Reinhard Neumann, who made available my access to the Materials Research's chemical laboratory for several months. Special thanks to Prof. Dr. Kurt Schwartz for helping me with the optical characterization of the samples and Dr. Dobri Dragov Dobrev for introducing me to the 'real world' of a chemist ('This substance is not dangerous, you can pour it into the sink directly').

**Karlsruhe University** - Without their help the 'radiation hardness' part of my thesis would be never born: Prof. Dr. Wim de Boer, Dr. Alexander Furgeri, Dr. Johannes Bol and Steffen Mueller.

**ESRF group** - Special thanks to Dr. John Morse, Dr. Jurgen Heartwig, and crew of the ID19 and ID21 lines.

**NoRHDia collaboration** - all the members for scientific discussions and knowledge sharing during the NoRHDia workshops. Special thanks to the experts of the 'diamond physics' Dr. Christoph Nebel, Dr. Milos Nesladek and Dr. Philippe Bergonzo.

For happy time spent together while drinking beer and eating 'Bifteki' in one of two well known restaurant in Wixhausen I'd like to thank all my friends: Gosia, Alex, Darek, Katarzyna, Jacek, Dorota, Adam, Sergiy, Markus, Georgios, Diego and many others which I simply forgot at the moment. Special thanks to Piotr for showing me the underwater world and organizing the beam-time in Seville.

For supporting me in this difficult time very special thanks to Monika, my future wife.

To everyone who helped me in carrying out this work, many thanks!



## LEBENS LAUF

Name und Vorname: Pomorski Michal  
Geburtsdatum: 21. März 1978  
Geburtsort: Skarzysko-Kamienna, Polen

## SCHULISCHER WERDEGANG:

**1985 - 1993** Besuch der Grundschule in Skarzysko-Kamienna, Polen

**1993 - 1997** Besuch der Adam-Mickiewicz-Gymnasiums mit Math.-Phys. Schwerpunkt in Skarzysko-Kamienna

**1997 Abitur**

## UNIVERSITÄRER WERDEGANG WS:

**1997-2000** Beginn des Studiums der Physik an der Universität AGH Science and Technology, Krakow, Poland (ursprünglich University of Mining and Metallurgy) Fakultät Physics and Nuclear Techniques

**2000 Ingenieur / Bachelor of Science (BSc)**

**2000 - 2002** Anfertigung der Diplomarbeit mit dem Titel: 'Measurement of the entrance dose in the X-ray diagnostic densitometry of lumbar spine with the use of thermoluminescence detectors'

bei dr. hab., Prof. AGH Marta Wasilewska-Radwaska

**2002 Master of Physics** (Universität AGH Science and Technology, Krakow)

**2002 - 2004** UFR de Sciences Physiques de la Terre, Université Paris 7 Denis Diderot, Paris arbeit mit dem Titel: 'Detectors of thermal neutrons and sensors of temperature based on CVD diamond'

bei Prof. Dr. Jean-Pierre Frangi

**2004 Diplôme de Recherche Technologique (DRT)** (Université Paris 7 Denis Diderot, Paris)

seit **2005** Beginn der Promotion am Institut für Kernphysik der Johann Wolfgang Goethe-Universität Frankfurt und der Gesellschaft für Schwerionenforschung (GSI) Darmstadt.

bei Prof. Dr. Joachim Stroth